




**ADVERTIMENT.** L'accés als continguts d'aquesta tesi queda condicionat a l'acceptació de les condicions d'ús establertes per la següent llicència Creative Commons:  <https://creativecommons.org/licenses/?lang=ca>

**ADVERTENCIA.** El acceso a los contenidos de esta tesis queda condicionado a la aceptación de las condiciones de uso establecidas por la siguiente licencia Creative Commons:  <https://creativecommons.org/licenses/?lang=es>

**WARNING.** The access to the contents of this doctoral thesis it is limited to the acceptance of the use conditions set by the following Creative Commons license:  <https://creativecommons.org/licenses/?lang=en>



# Advanced Thin Film Electrode Materials for Application in Solid Oxide Cells

*Juan de Dios Sirvent Verdú*

**Tesi doctoral**

Programa de doctorat en Ciència de Materials

**Directors:** Prof. Albert Tarancón Rubio, Dr. Federico Baiutti

**Tutor:** Prof. Albert Tarancón Rubio

Institut de Recerca en Energia de Catalunya

2023



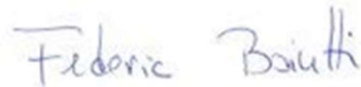
El Prof. Albert Tarancón Rubio y el Dr. Federico Baiutti investigadores de l'Institut de Investigació en Energia de Catalunya (IREC), certifiquen:

Que la memòria titulada *Advanced Thin Film Electrode Materials for Application in Solid Oxide Cells* presentada per Juan de Dios Sirvent Verdú per optar al grau de Doctor en el Programa de Ciència de Materials de la Universitat Autònoma de Barcelona ha estat realitzada sota la seva direcció a l'Institut de Investigació en Energia de Catalunya (IREC).

Barcelona, a 24 d'octubre de 2023



ICREA Prof. Albert Tarancón Rubio



Dr. Federico Baiutti

**UAB**  
Universitat Autònoma  
de Barcelona

**IREC<sup>R</sup>**  
Shaping Energy for a Sustainable Future



*Defender la alegría como una trinchera  
defenderla del escándalo y la rutina  
de la miseria y los miserables  
de las ausencias transitorias  
y las definitivas*

*defender la alegría como un principio  
defenderla del pasmo y las pesadillas  
de los neutrales y de los neutrones  
de las dulces infamias  
y los graves diagnósticos*

*defender la alegría como una bandera  
defenderla del rayo y la melancolía  
de los ingenuos y de los canallas  
de la retórica y los paros cardiacos  
de las epidemias y las academias*

*defender la alegría como un destino  
defenderla del fuego y de los bomberos  
de los suicidas y los homicidas  
de las vacaciones y del agobio  
de la obligación de estar alegres*

*defender la alegría como una certeza  
defenderla del óxido y la roña  
de la famosa pátina del tiempo  
del relente y del oportunismo  
de los proxenetas de la risa*

*defender la alegría como un derecho  
defenderla de dios y del invierno  
de las mayúsculas y de la muerte  
de los apellidos y las lástimas  
del azar  
y también de la alegría*

*Defensa de la Alegría, Mario Benedetti*



## *Acknowledgements*

I started writing these words one year ago and I have finished writing them right before submitting the thesis. It was important to me to proceed like this because first and foremost, and despite all the frustration experienced in the last year, I am grateful for having done this PhD.

Two of the people that have had the most impact during this PhD are, of course, my supervisors. Albert, let me tell now a few words on the influence that you had on me as I got to know you more. I have seen how passionate you are about our research, but also about fostering a nice and funny environment within the group. You have pushed me forward so that I could go further in my research and you have given me advice and guidance when I was more in need of it. For all of these reasons I want to say thank you.

Federico, I have a serious concern on finding proper and finite words to express how lucky I feel for having you as my supervisor, I am sure I could fill several pages of gratitude. You have been my guide throughout all this time, teaching me that 'no result is also result', that 'no measurement is no result' and that it is good that 'we' try different things. In times of doubt you have either helped me or encouraged me to keep on going, and with time I have got to grow as an independent researcher. I am extremely grateful for all of this.

What to say about the rest of the amazing Nanoionics team? I have met too many wonderful people that have accompanied during these years, in one way or another. Allow me to do a quick review: Arianna, Lorena, Jose, Carolina, Natalia, Maritta, Marina, Yunqing, Valerie, Marco, Simone, Iria, Marc N., Alex, Marc T., Francesco, Kosova, Nerea, Fjorelo, Gianfranco, Juan Carlos, Lucile, Philipp, Paul, Fernanda, Ismael, Ana, Toni, Daiana, Natasha, Santiago, Beatrice, Carlota, Lisa and Marlene. Special thanks go to Marc N., thank you for your immense help in the lab, your (not always) patience and for your particular kind of humor. Francesco, thank you for always being there ready to discuss some results, offer advice, and particularly for all your help during my first year. Marc T. and Nat, I owe you for all your help and discussion on printing the device holders. Lucile, thank you so much for your help in the lab, for being always so nice and willing to help and of course, for entering the Committee, it felt so great having you there. Jose, thank you for your friendship, all the discussions in the office and for encouraging me to be more independent. Fjorelo, thank you for being always so nice, it was great to share this time with you. Maritta, thank you as well for your friendship, your positive post-it messages, for being so irritably nice and for your stickers at coffee time. Kosova, thank you for great friendship, for always being there when I needed anything (so many things!). Juancar, thank you for your friendship, for listening to me every time I needed to blow off steam and specially for being how you are, full of joy and good vibes, and overall a great friend.



I would also like to thank all the people I met during my stay at Imperial College, it was such a nice experience. John, thank you so much for having me there, for all your help and discussions on the topic, and specially for being much more involved and present than I had initially expected. I want to say special thanks to Sarah F. as well, for all your guidance with LEIS, for helping me so I could make the most out of my short time there and for the extra assistance during these last months, you made my work so much better. Jerry, thank you for being so kind and for all your help, having you as a friend is one of the best things that I got from my time there. To all the rest of fantastic people I met: Apostolos, Ritika, Maria, Siva, Nomaan and Yao, thank you all.

I would also like to briefly thank all the nice collaborators that I have met during these years. Special thanks to Mónica, Guilhem, Giulio, Alex and Oskar, it was great to collaborate with you all, you enriched my thesis experience and my research.

Last but not least, I want to thank my family and friends, who made these demanding years much more bearable and helped me to put the thesis on perspective. Thank you Sarah for accompanying me during all this time, for being understanding during my most stressful days and nights of working until late, and for being the best life partner one could ever have.

## *Abstract*

The energy industry is currently on the verge of transitioning into a sustainable paradigm powered by renewable energies. Among the alternatives to fossil fuel-driven technologies, the use of solid oxide cell (SOC) systems is a promising candidate. SOCs are the most efficient technologies for electrical power generation and hydrogen production, making them an interesting solution for reversible energy systems. Nonetheless, the expansion of SOC technologies into real life applications is often hindered by the presence of thermally activated processes, restricting the operation to the high temperature regime. Consequently, thermally-driven degradation is regularly experienced in these devices. There is a clear interest then in the discovery of new materials that i) present enhanced electrochemical activity at lower temperatures and ii) keep their performance over time. The use of thin film electrodes based on engineered nanostructures has been demonstrated to improve the performance at much lower operational temperatures. This thesis is then focused on the development of thin film-based highly functional materials for SOC electrode application. The research carried out has been divided in three main parts: i) development of  $\text{La}_{0.75}\text{Sr}_{0.25}\text{Cr}_{0.5}\text{Mn}_{0.5}\text{O}_3$  (LSCrMn) and  $\text{Ce}_{0.8}\text{Sm}_{0.2}\text{O}_2$  (SDC) nanocomposites for application in fuel and symmetric electrodes; ii) characterization of the functional properties of the  $\text{La}_{0.8}\text{Sr}_{0.2}\text{Mn}_x\text{Co}_y\text{Fe}_{1-x-y}\text{O}_3$  (LSMCF) library for application as oxygen electrodes; iii) implementation of thin film electrode materials under different cell architectures.

The first part of the thesis deals with the development of thin film-based nanocomposite electrodes. First, Ni-Ce<sub>0.9</sub>Gd<sub>0.1</sub>O<sub>2</sub> (NiCGO) cermet nanocomposites were studied as promising fuel electrodes. Additionally, all-ceramic LSCrMn-SDC heterostructures were also investigated. Specifically, a dense LSCrMn-SDC nanocomposite was found to present remarkable electrochemical activity under both reducing and oxidizing conditions, with no significant degradation observed. Further studies were carried out for the optimization of the heterostructures microstructure, leading to enhanced performance for hydrogen oxidation.

The second part of this thesis investigated the LSMCF library for application as oxygen electrodes. The complete library was fabricated in a single process by means of combinatorial deposition. LSMCF was then studied by high-throughput methodologies for full characterization of the structural and electrocatalytic properties. The results showed high oxygen kinetics for the Fe- and Co-rich regions and remarkable low activation energy for the intermixed co-doped compositions studied. Studies on degradation performance showed distinctive behaviour with remarkable stability of the co-doped LSMCF and  $\text{La}_{0.8}\text{Sr}_{0.2}\text{MnO}_3$  (LSM) with respect to single  $\text{La}_{0.8}\text{Sr}_{0.2}\text{CoO}_3$  (LSC) and  $\text{La}_{0.8}\text{Sr}_{0.2}\text{FeO}_3$  (LSF). Analyses beyond the subsurface revealed the presence of highly off-stoichiometric regions and apparent overall increase of defect size and defect density.

In the final part of the thesis, the integration of thin film electrode materials in full SOC devices have been studied. Specifically, the use of  $\text{La}_{0.9}\text{Sr}_{0.1}\text{CrO}_3$  (LSCr) thin films as symmetric electrodes has been analysed by operating a cell under redox cycling conditions. The use of thin film LSC and SDC in reversible SOC systems was studied under fuel cell and electrolysis operation modes. Finally, the integration of all-ceramic thin film materials in micro-SOCs was explored, with successful fabrication of proof-of-concept devices supported in silicon.

This manuscript offers a thorough study for the development of thin film-based functional materials aimed to overcome the limitations affecting SOC electrodes. The use of nanoengineering processes and combinatorial methods for material research are presented as promising routes for the discovery of electrode materials with enhanced performance. The successful integration of these type of materials in different device architectures is proposed as validation of the versatility in application of the thin film materials investigated.

## Resumen

La industria energética está actualmente al borde de una transición hacia un paradigma sostenible potenciado por las energías renovables. Entre las alternativas a los combustibles fósiles, el uso de sistemas basados en celdas de óxido sólido (SOC) es un candidato prometedor. Las SOC son las tecnologías más eficientes de generación eléctrica y producción de hidrógeno, cosa que las hace una solución interesante para sistemas de energía reversibles. No obstante, su aplicación en soluciones reales se encuentra normalmente limitada por la presencia de procesos activados térmicamente, lo cual restringe su operación al rango de altas temperaturas. Por consiguiente estos dispositivos sufren regularmente de degradación inducida por procesos térmicos. Esto hace que haya un claro interés por descubrir nuevos materiales que i) presenten actividad electroquímica mejorada a bajas temperaturas y ii) mantengan su rendimiento en el tiempo. Se ha demostrado que el uso de electrodos de capa fina basados en nanoestructuras mejora el rendimiento a temperaturas mucho más bajas. Esta tesis se ha enfocado en el desarrollo de materiales altamente funcionales basados en capa fina como electrodos SOC. La investigación llevada a cabo se ha dividido en tres partes principales: i) desarrollo de nanocompuestos de  $\text{La}_{0.75}\text{Sr}_{0.25}\text{Cr}_{0.5}\text{Mn}_{0.5}\text{O}_3$  (LSCrMn) y  $\text{Ce}_{0.8}\text{Sm}_{0.2}\text{O}_2$  (SDC) para su aplicación en electrodos de combustible y simétricos; ii) la caracterización de las propiedades funcionales de la librería  $\text{La}_{0.8}\text{Sr}_{0.2}\text{Mn}_x\text{Co}_y\text{Fe}_{1-x-y}\text{O}_3$  (LSMCF) para aplicación como electrodos de oxígeno; iii) la implementación de materiales de electrodo de capa fina en diferentes arquitecturas de celda.

La primera parte de la tesis cubre el desarrollo de electrodos nanocompuestos basados en capa fina. En primer lugar, nanocompuestos cermet de  $\text{Ni-Ce}_{0.9}\text{Gd}_{0.1}\text{O}_2$  (NiCGO) se han estudiado como electrodos de combustible. Se ha encontrado un nanocompuesto denso de LSCrMn-SDC que presenta alta actividad electroquímica bajo condiciones tanto reductoras como oxidantes, sin apreciación de degradación significativa. Más estudios se han realizado para la optimización de la microestructura, consiguiendo mejorar el rendimiento frente a la oxidación de hidrógeno.

La segunda parte de la tesis investiga la librería de LSMCF para su aplicación en electrodos de oxígeno. El LSMCF se ha estudiado por medio de metodologías de alto rendimiento para la caracterización completa de las propiedades estructurales y electrocatalíticas. Los resultados muestran alta cinética de transporte de oxígeno para las regiones ricas en Fe/Co, así como baja energía de activación para los compuestos co-dopados. Estudios del rendimiento frente a la degradación han mostrado un comportamiento con alta estabilidad para el LSMCF co-dopado y el  $\text{La}_{0.8}\text{Sr}_{0.2}\text{MnO}_3$  (LSM) en comparación con el  $\text{La}_{0.8}\text{Sr}_{0.2}\text{CoO}_3$  (LSC) y el  $\text{La}_{0.8}\text{Sr}_{0.2}\text{FeO}_3$  (LSF).

En la parte final de la tesis se ha estudiado la integración de materiales de capa fina para electrodos en dispositivos SOC completos. El uso de capas finas de  $\text{La}_{0.9}\text{Sr}_{0.1}\text{CrO}_3$  (LSCr) como electrodos simétricos se ha analizado por medio de la operación bajo condiciones de ciclado redox. El uso de capas finas de LSC y SDC en sistemas reversibles SOC se ha estudiado bajo operación en modos de celda de combustible y de electrólisis. Finalmente, la integración de materiales de capa fina en micro-SOCs se ha estudiado, consiguiendo fabricar dispositivos a nivel de prueba de concepto sobre sustratos de silicio.

Este manuscrito ofrece un estudio exhaustivo del desarrollo de materiales funcionales basados en capa fina destinados a superar las limitaciones que afectan a los electrodos de las SOC. El uso de procesos de nanoingeniería y metodologías combinatoriales para la investigación en materiales se presentan como aproximaciones prometedoras para el descubrimiento de materiales de electrodo de alto rendimiento. La integración exitosa de este tipo de materiales en distintas arquitecturas se propone como validación de la versatilidad en los ámbitos de aplicación de los materiales de capa fina investigados.

## Resum

La indústria energètica està actualment a la vora d'una transició cap un paradigma sostenible potenciat per les energies renovables. Entre les alternatives als combustibles fòssils, l'ús de sistemes basats en cel·les d'òxid sòlid (SOC) és un candidat prometedor. Les SOC són les tecnologies més eficients de generació elèctrica i producció d'hidrogen, cosa que les fa una solució interessant per sistemes d'energia reversibles. No obstant, la seva aplicació en solucions reals es troba normalment limitada per la presència de processos activats tèrmicament, la qual cosa restringeix la seva operació al rang d'altres temperatures. Per conseqüent, aquests dispositius pateixen regularment de degradació induïda per processos tèrmics. Això fa que hi hagi un clar interès per descobrir nous materials que i) presentin activitat electroquímica millorada a baixes temperatures i ii) mantinguin el seu rendiment en el temps. S'ha demostrat que l'ús d'elèctrodes de capa fina basats en nanoestructures millora el rendiment a temperatures molt més baixes. Aquesta tesi s'ha focalitzat en el desenvolupament de materials altament funcionals basats en capa fina com a elèctrodes SOC. La investigació portada a terme s'ha dividit en tres parts principals: i) desenvolupament de nanocompòsits de  $\text{La}_{0.75}\text{Sr}_{0.25}\text{Cr}_{0.5}\text{Mn}_{0.5}\text{O}_3$  (LSCrMn) i  $\text{Ce}_{0.8}\text{Sm}_{0.2}\text{O}_2$  (SDC) per a la seva aplicació en elèctrodes de combustible i simètrics; ii) la caracterització de les propietats funcionals de la llibreria  $\text{La}_{0.8}\text{Sr}_{0.2}\text{Mn}_x\text{Co}_y\text{Fe}_{1-x-y}\text{O}_3$  (LSMCF) per aplicació com elèctrodes d'oxigen; iii) la implementació de materials d'elèctrode de capa fina en diferents arquitectures de cel·la.

La primera part de la tesi cobreix el desenvolupament d'elèctrodes nanocompòsits basats en capa fina. En primer lloc, nanocompòsits cermet de  $\text{Ni-Ce}_{0.9}\text{Gd}_{0.1}\text{O}_2$  (NiCGO) s'han estudiat com elèctrodes de combustible. S'ha trobat un nanocompòsit dens de LSCrMn-SDC que presenta alta activitat electroquímica baix condicions tant reductores com oxidants, sense apreciació de degradació significativa. Més estudis s'han realitzat per la optimització de la microestructura, aconseguint millorar el rendiment front l'oxidació d'hidrogen.

La segona part de la tesi investiga la llibreria de LSMCF per la seva aplicació en elèctrodes d'oxigen. L'LSMCF s'ha estudiat per mitjans de metodologies d'alt rendiment per la caracterització completa de les propietats estructurals i electrocatalítiques. Els resultats mostren alta cinètica de transport d'oxigen per les regions riques en Fe/Co, així com baixa energia d'activació pels compostos co-dopats. Estudis del rendiment front la degradació han mostrat un comportament d'alta estabilitat per l'LSMCF co-dopat i l' $\text{La}_{0.8}\text{Sr}_{0.2}\text{MnO}_3$  (LSM), en comparació amb l' $\text{La}_{0.8}\text{Sr}_{0.2}\text{CoO}_3$  (LSC) i l' $\text{La}_{0.8}\text{Sr}_{0.2}\text{FeO}_3$  (LSF).

A la part final de la tesi s'ha estudiat la integració de materials en capa fina per elèctrodes en dispositius SOC complets. L'ús de capes fines de  $\text{La}_{0.9}\text{Sr}_{0.1}\text{CrO}_3$  (LSCr) com elèctrodes simètric s'ha analitzat per mitjà de l'operació baix condicions de ciclat redox. L'ús de capes fines d'LSC i SDC en sistemes reversibles SOC s'ha estudiat baix operació en modes de

cel·les de combustible i electròlisi. Finalment, la integració de materials en capa fina en micro-SOCs s'ha estudiat, aconseguint fabricar dispositius a nivell de prova de concepte sobre substrats de silici.

Aquest manuscrit ofereix un estudi exhaustiu del desenvolupament de materials funcionals basats en capa fina destinats a superar les limitacions que afecten als elèctrodes de les SOC. L'ús de processos de nanoenginyeria i metodologies combinatorials per la recerca en materials es presenten com aproximacions prometedores per al descobriment de materials d'elèctrode d'alt rendiment. La integració exitosa d'aquest tipus de materials en diferents arquitectures es proposa com a validació de la versatilitat en els àmbits d'aplicació dels materials en capa fina investigats.

# *Index*

<b>1. Introduction .....</b>	<b>1</b>
1.1 Motivation .....	5
1.2 Solid Oxide Cells .....	7
1.2.1 Working principles.....	7
1.2.2 State of the art materials for solid oxide cells.....	9
1.2.3 Mechanisms of degradation in solid oxide cells .....	13
1.3 Types of solid oxide cell devices.....	14
1.3.1 Cell geometry and operation models.....	14
1.3.2 Thin film solid oxide cells.....	17
1.3.2.1 Thin film functional electrode materials .....	17
1.3.2.2 Ceramics for micro solid oxide cells.....	19
1.4 Advanced tools for materials search.....	21
1.5 Scope of this thesis .....	23
References.....	25
<b>2. Experimental Methods .....</b>	<b>39</b>
2.1 Introduction.....	43
2.2 Fabrication and processing.....	43
2.2.1 Deposition of thin films by physical methods.....	43
2.2.2 Combinatorial deposition of material libraries .....	45
2.2.3 Si-based devices: micro- and nanofabrication.....	48
2.3 Morphological and structural characterization techniques .....	50
2.3.1 Scanning Electron Microscopy .....	50
2.3.2 Transmission Electron Microscopy .....	51
2.3.3 X-Ray Diffraction.....	51
2.3.4 Atomic Force Microscopy .....	52
2.3.5 Spectroscopic Ellipsometry.....	53
2.4 Advanced characterization techniques.....	55



2.4.1 Low Energy Ion Scattering .....	55
2.4.2 X-Ray Photoelectron Spectroscopy .....	57
2.4.3 Tip Enhanced Raman Spectroscopy.....	58
2.4.4 Positron Annihilation Spectroscopy .....	59
2.4.4.1 Doppler Broadening Variable Energy Positron Annihilation Spectroscopy.....	60
2.4.4.2 Variable Energy Positron Annihilation Lifetime Spectroscopy .....	62
2.5 Functional characterization .....	63
2.5.1 In-plane conductivity measurements .....	63
2.5.2 Electrochemical Impedance Spectroscopy.....	64
2.5.2.1 Electrochemical characterization of thin film electrodes .....	64
2.5.2.2 Electrochemical characterization of thin film electrodes during thermal ageing in oxidizing conditions .....	69
2.5.3 Electrochemical characterization in full device architectures .....	69
2.5.3.1 Conceptualization of the measurement setup .....	69
2.5.3.2 Electrical characterization .....	72
2.6 Characterization tools for studying material libraries .....	72
2.6.1 High throughput X-Ray Fluorescence .....	72
2.6.2 High throughput X-Ray Diffraction.....	73
2.6.3 High throughput Spectroscopic Ellipsometry.....	74
2.6.4 Raman Spectroscopy .....	74
2.6.5 Electrochemical test station.....	75
2.6.6 Isotope Exchange Depth Profiling coupled with Secondary Ion Mass Spectrometry .....	79
References.....	83
<b>3. Thin film nanostructures for symmetrical and fuel electrodes in solid oxide cells ....</b>	<b>87</b>
3.1 Motivation .....	89
3.2 Ceria-based state-of-the-art all-ceramic hydrogen electrode.....	92
3.3 NiCGO thin films for hydrogen electrode application in thin film SOCs .....	94
3.3.1 Microstructural characterization of the NiCGO thin film hydrogen electrodes.....	94
3.3.2 Electrochemical performance of the NiCGO thin film hydrogen electrodes.....	96
3.4 Functional layers based on LSCrMn-SDC heterostructures .....	99

3.4.1 Development of dense LSCrMn-SDC functional layers for hydrogen and symmetric electrodes .....	99
3.4.1.1 Microstructural characterization of the thin film heterostructures.....	99
3.4.1.2 Measurement of the sheet conductivity under reducing and oxidizing conditions.....	105
3.4.1.3 Electrochemical performance of the heterostructures.....	107
3.4.1.4 Evolution of the electrochemical performance of the LSCrMn-SDC nanocomposite on thermal degradation.....	113
3.4.2 Optimization of LSCrMn-SDC thin film microstructure for anode application.....	114
3.4.2.1 Structural characterization of microstructure-variant LSCrMn-SDC thin films .....	115
3.4.2.2 Electrochemical performance of microstructure-variant LSCrMn-SDC heterostructures on hydrogen oxidation .....	118
3.5 Conclusions .....	123
References.....	125
<b>4. Study of the <math>\text{La}_{0.8}\text{Sr}_{0.2}\text{Mn}_x\text{Co}_y\text{Fe}_{1-x-y}\text{O}_3</math> perovskite family as suitable cathodes in solid oxide fuel cells.....</b>	<b>131</b>
4.1 Motivation .....	133
4.2 Optimization of the deposition procedure .....	135
4.3 Development of high throughput characterization methods .....	138
4.3.1 Structural, compositional and optical characterization.....	138
4.3.1.1 Distribution of the B-cation by high throughput X-Ray Fluorescence .....	138
4.3.1.2 Characterization of the crystallographic structure by X-Ray Diffraction.....	140
4.3.1.3 Structural characterization by Raman Spectroscopy .....	142
4.3.1.4 Analysis of the optical properties by spectroscopic ellipsometry .....	145
4.3.2 Functional characterization .....	147
4.3.2.1 Analysis of the mass transport properties by Isotopic Exchange Depth Profiling-Secondary Ion Mass Spectrometry.....	147
4.3.2.2 Electrochemical characterization by impedance spectroscopy mapping.....	152
4.4 Study of the evolution of LSMCF thin films facing thermal degradation .....	156
4.4.1 Electrochemical performance during thermal degradation .....	156
4.4.2 Structural and chemical evolution of the thin film surface and subsurface.....	157

4.4.2.1 Evolution of surface microstructure and appearance of segregated phases....	158
4.4.2.2 A-site cation structural and chemical evolution at the surface and sub-surface level .....	161
4.4.2.3 Effect of the surface evolution with degradation of the electrochemical performance.....	174
4.4.3 Evolution of the distribution and nature of B-site cations and vacancy-defects beyond the surface and subsurface.....	175
4.4.3.1 Compensation of the B-site cations upon thermal annealing.....	175
4.4.3.2 Evolution of vacancy-related defects and their correlation with cation.....	178
4.5 Guidelines for the selection of a thin film LSMCF compound .....	186
4.6 Conclusions .....	188
References.....	190
<b>5. Integration of thin film electrode materials in highly functional solid oxide cells...</b>	<b>197</b>
5.1 Motivation .....	199
5.2 Symmetric solid oxide fuel cells.....	202
5.2.1 Thin film characterization and cell configuration.....	202
5.2.2 Electrochemical characterization.....	204
5.2.3 Microstructural characterization after operation .....	210
5.3 Single crystal supported thin film solid oxide cells.....	211
5.3.1 Characterization in fuel cell mode .....	212
5.3.2 Characterization in electrolysis mode.....	214
5.4 Integration of thin film solid oxide fuel cells in silicon supported devices: micro solid oxide fuel cells.....	218
5.4.1 Cell architecture and device setup .....	219
5.4.2 Electrochemical characterization.....	221
5.4.3 Post-mortem structural characterization .....	222
5.5 Remarks on the experimental limitations for the operation of thin film-based solid oxide cells .....	227
5.6 Conclusions .....	230
5.7 Future work .....	232
<b>6. Conclusions.....</b>	<b>237</b>

<b>A. Direct observation of Sr segregated species in oxygen electrodes by Tip-Enhanced Raman Spectroscopy .....</b>	<b>241</b>
A.1 Motivation .....	245
A.2 Characterization of strontium species in $\text{La}_{0.8}\text{Sr}_{0.2}\text{Mn}_{0.42}\text{Co}_{0.19}\text{Fe}_{0.39}\text{O}_3$ by Tip-Enhanced Raman Spectroscopy.....	246
A.3 Conclusions and future work.....	249
References.....	250



## *List of Acronyms*

3YSZ	$(\text{ZrO}_2)_{0.97}(\text{Y}_2\text{O}_3)_{0.03}$
8YSZ	$(\text{ZrO}_2)_{0.92}(\text{Y}_2\text{O}_3)_{0.08}$
ACOM	Automated Crystal Phase and Orientation Mapping
AFM	Atomic Force Microscopy
ALD	Atomic Layer Deposition
ASR	Area Specific Resistance
BE	Binding Energy
BL	Bilayer
CC	Current Collector
CC <sub>hy</sub>	Current Collector – hydrogen electrode side
CC <sub>ox</sub>	Current Collector – oxygen electrode side
CGO	$\text{Ce}_{1-x}\text{Gd}_x\text{O}_2$
DB-VEPAS	Doppler Broadening Variable Energy Positron Annihilation Spectroscopy
DPB	Double Phase Boundary
DRT	Distribution of Relaxation Times
E <sub>a</sub>	Activation Energy
EDS,EDX	Energy-dispersive X-ray Spectroscopy
EIS	Electrochemical Impedance Spectroscopy
FT	Fourier Transform
GDC	Gadolinium-doped Ceria
HF	High Frequency
HOR	Hydrogen Oxidation Reaction
HRTEM	High Resolution Transmission Electron Microscopy
IEDP	Isotope Exchange Depth Profiling
KE	Kinetic Energy
LA-PLD	Large Area Pulsed Laser Deposition
LCO	$\text{LaCrO}_3$
LEIS	Low Energy Ion Scattering
LF	Low Frequency
LSC	$\text{La}_{1-x}\text{Sr}_x\text{CoO}_3$ , $\text{La}_{0.8}\text{Sr}_{0.2}\text{CoO}_3$
LSC64	$\text{La}_{0.6}\text{Sr}_{0.4}\text{CoO}_3$
LSC82	$\text{La}_{0.8}\text{Sr}_{0.2}\text{CoO}_3$
LSCr	$\text{La}_{0.9}\text{Sr}_{0.1}\text{CrO}_3$
LSCF	$\text{La}_{1-x}\text{Sr}_x\text{Co}_{1-y}\text{Fe}_y\text{O}_3$
LSCrMn	$\text{La}_{1-x}\text{Sr}_x\text{Cr}_{1-y}\text{Mn}_y\text{O}_3$ , $\text{La}_{0.75}\text{Sr}_{0.25}\text{Cr}_{0.5}\text{Mn}_{0.5}\text{O}_3$
LSMC	$\text{La}_{0.8}\text{Sr}_{0.2}\text{Mn}_x\text{Co}_{1-x}\text{O}_3$
LSMCF	$\text{La}_{0.8}\text{Sr}_{0.2}\text{Mn}_x\text{Co}_y\text{Fe}_{1-x-y}\text{O}_3$

LSF	$\text{La}_{1-x}\text{Sr}_x\text{FeO}_3$
LSM	$\text{La}_{1-x}\text{Sr}_x\text{MnO}_3$
LSMC	$\text{La}_{0.8}\text{Sr}_{0.2}\text{Mn}_x\text{Co}_{1-x}\text{O}_3$
MIEC	Mixed Ionic Electronic Conductor
ML	Machine Learning
NC	Nanocomposite
NiCGO	$\text{NiO}:\text{Ce}_{0.9}\text{Gd}_{0.1}\text{O}_2$
OCV	Open Circuit Voltage
ORR	Oxygen Reduction Reaction
PLCVD	Plasma Laser Chemical Vapor Deposition
PALS	Positron Annihilation Lifetime Spectroscopy
PAS	Positron Annihilation Spectroscopy
PLD	Pulsed Laser Deposition
PVD	Physical Vapor Deposition
RIE	Reactive Ion Etching
$R_{\text{ms}}$	Mean Square Roughness
RP	Ruddlesden-Popper
RSOC	Reversible Solid Oxide Cell
SAED	Selected Area Electron Diffraction
SDC	Samarium-doped Ceria, $\text{Ce}_{0.8}\text{Sm}_{0.2}\text{O}_2$
SEM	Scanning Electron Microscopy
SIMS	Secondary Ion Mass Spectrometry
SOC	Solid Oxide Cell
SOEC	Solid Oxide Electrolysis Cell
SOFC	Solid Oxide Fuel Cell
SSOC	Symmetric Solid Oxide Cell
SSZ	Scandia-Stabilized Zirconia
STEM	Scanning Transmission Electron Microscopy
TEM	Transmission Electron Microscopy
TERS	Tip Enhanced Raman Spectroscopy
TF-SOC	Thin Film Solid Oxide Cell
ToF	Time-of-Flight
TPB	Triple Phase Boundary
VAN	Vertically Aligned Nanostructure
VEPALS	Variable Energy Positron Annihilation Lifetime Spectroscopy
XPS	X-Ray Photoelectron Spectroscopy
XRD	X-Ray Diffraction
XRF	X-Ray Fluorescence
YSZ	Yttria-Stabilized Zirconia

$\mu$ SOFC

Micro Solid Oxide Fuel Cell





# *1. Introduction*



1.1 Motivation .....	5
1.2 Solid Oxide Cells .....	7
1.2.1 Working principles.....	7
1.2.2 State of the art materials for solid oxide cells.....	9
1.2.3 Mechanisms of degradation in solid oxide cells .....	13
1.3 Types of solid oxide cell devices.....	14
1.3.1 Cell geometry and operation models.....	14
1.3.2 Thin film solid oxide cells.....	17
1.3.2.1 Thin film functional electrode materials.....	17
1.3.2.2 Ceramics for micro solid oxide cells.....	19
1.4 Advanced tools for materials search.....	21
1.5 Scope of this thesis .....	23
References.....	25



## 1.1 Motivation\*

Solid oxide electrolysis and fuel cells are the most efficient technology for hydrogen generation and clean electricity production from hydrogen, respectively. This makes them one of the most promising technologies for facing the upcoming challenges for industry decarbonization. Solid oxide cells (SOCs) are characterized by high efficiency, power density and applicability –from portable devices to large-scale stacks– and have therefore sparked the interest of the research and of the technology communities during the last decades.

The presence of thermally activated processes –particularly critical for the oxygen electrode– represents one of the bottlenecks of the technology for operation at more convenient low-to-intermediate temperatures. An additional limitation commonly observed is the degradation of the materials electrochemical performance due to formation of secondary phases at the interfaces. These effects result in blockage of electrochemically active sites for the surface reactions and ion transport through the device. Among the possible solutions to overcome these limitations, employing electrodes based on engineered nanostructures have demonstrated an improvement of the performance at much lower operation temperatures<sup>3,4</sup>. Interestingly, the use of nanostructured materials have also been proven to counter degradation effects related to segregation of dopant species<sup>5</sup>. Materials with increased entropy (co-doped systems) have also been reported to present resilient behavior for facing degradation<sup>6</sup>. The origin of electrochemical enhancement and long-term stability often found in such nanostructured electrodes is still under debate. This thesis is therefore aimed at investigating these phenomena, focusing on the study of nanostructured and co-doped electrode materials, and their application in thin film solid oxide cells (TF-SOCs).

This chapter introduces the main concepts and ideas covered throughout the development of the work presented in this thesis. In section 1.2 a general overview of SOCs is given. This includes the basic principles of the electrochemical phenomena involved in their functionality, a review of the classical materials utilized for the fabrication of each cell component and a brief presentation of the different types of SOCs existing and main

---

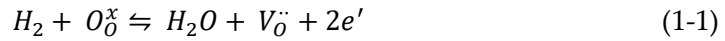
\*This introduction is adapted from Sirvent, J. de D.; Buzi, F.; Baiutti, F.; Tarancón, A. Advances in Nanoengineered Air Electrodes: Towards High-Performance Solid Oxide Cells. In *Nanoengineered Materials for Solid Oxide Cells*; Develos-Bagarinao, K., Ed.; IOP Publishing, 2023; pp 1-1-1–35. <https://doi.org/10.1088/978-0-7503-4064-9ch1>, with the permission of IOP Publishing<sup>1</sup> and from Sirvent, J. de D.; Carmona, A.; Rapenne, L.; Chiabrera, F.; Morata, A.; Burriel, M.; Baiutti, F.; Tarancón, A. Nanostructured  $\text{La}_{0.75}\text{Sr}_{0.25}\text{Cr}_{0.5}\text{Mn}_{0.5}\text{O}_3\text{-Ce}_{0.8}\text{Sm}_{0.2}\text{O}_2$  Heterointerfaces as All-Ceramic Functional Layers for Solid Oxide Fuel Cell Applications. *ACS Appl. Mater. Interfaces* **2022**, *14* (37), 42178–42187. <https://doi.org/10.1021/acsami.2c14044>, under Creative Commons Attribution 4.0 International Public License<sup>2</sup>.

architectures employed. Focus is particularly given to the materials and systems most relevant to the studies discussed throughout the thesis. Section 1.3.2 focuses in introducing the field of TF-SOCs. This section provides a brief review on promising functional materials fabricated by thin film methods and their functional properties. Additionally, the advantages and feasibility of integrating ceramic materials in micro solid oxide cells ( $\mu$ SOCs) is discussed. Section 1.4 is focused on the discussion of advanced tools for materials search. The use of high-throughput experimental methods is discussed, highlighting successful cases found in the literature and commenting the advantages of implementing these methodologies. The identification of material performance descriptors and their combination with the use of machine learning-based analysis methods is briefly introduced. Finally, specific details on the scope of this thesis are described in Section 1.5.

## 1.2 Solid Oxide Cells

### 1.2.1 Working principles

SOCs are devices which are able to either produce electricity (fuel mode - SOFC) or store chemical energy (electrolysis mode - SOEC) coming from the result of an electrochemical reaction. The most well-known SOC device is the one operated in fuel cell mode with hydrogen as the fuel. In this case, the hydrogen oxidation reaction (HOR) takes place in the anode:



while the oxygen reduction reaction (ORR) takes place in the cathode:



The resulting product of the electrochemical reaction is water, as it can be observed in the simplified balanced reaction:



The electrochemical potential of the fuel cell is given by the Nernst equation:

$$E_{eq} = E^0 - \frac{RT}{nF} \ln \left( \frac{p_{H_2O}}{p_{H_2} p_{O_2}^{1/2}} \right) \quad (1-4)$$

This equation relates the cell potential under equilibrium conditions ( $E_{eq}$ ) with the electrochemical reaction potential in standard conditions ( $E^0$ ), the universal gas constant ( $R$ ), the number of electrons involved per unit of mole of fuel, the Faraday constant ( $F$ ), the temperature ( $T$ ) and the fraction of partial pressures of the product and reactants of the reaction. The amount of hydrogen consumed during the operation of the cell can be calculated directly –assuming a single chemical reaction– through the measurement of the current, according to equation (1-5).

$$x_{consumed/produced} = \frac{|i|}{nF} \quad (1-5)$$

In general terms, the efficiency of SOCs is determined by the energy losses that are present in the device<sup>7,8</sup>: (i) ohmic resistance coming from ionic conduction, (ii) mass transport at the electrode (bulk or surface ambipolar diffusion) and in the gas phase (concentration polarization) (iii) activation polarization related to electrode reactions. Figure 1-1 shows a schematic of the voltage vs current density plot of a prototypical SOFC showing all three contributions to the energy loss. It should be noted that the cell potential  $E_{eq}$  normally coincides with the experimental Open Circuit Voltage (OCV) of the device, although it



might not be the case in the case of large activation. As the operation temperature decreases, the electrode overpotentials play a more significant role in the performance of the cell due to their high thermal activation.<sup>9</sup> Therefore, decreasing the activation energy and polarization resistance of the electrodes is of foremost importance for lowering the operation temperatures of the whole SOCs.

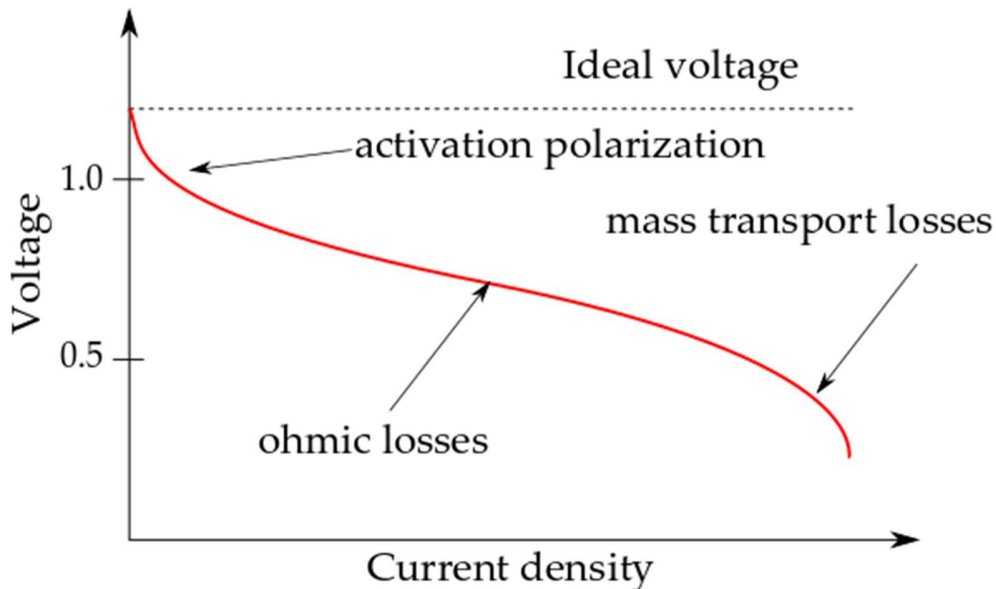


Figure 1-1. Schematic representation of the voltage vs current density ( $j$ - $V$ ) plot of a SOFC.

One of the most important factors involved in the performance of SOCs is related to the surface reaction. In conventional systems –i.e. in which porous electrodes allowing for gas diffusion are employed– the reaction takes place favorably in specific electrochemically active sites. This active region is commonly referred to as triple phase boundary (TPB), as is the junction between the electrolyte, the electrode (either for the hydrogen<sup>10,11</sup> or the oxygen electrode<sup>12</sup>) and the gas phases. In the case of oxygen electrodes, the TPB reaction occurs via dissociation of the molecular oxygen at the electrode-electrolyte interface, the insertion of the oxide ion into the electrolyte layer and the transport of the electronic charge through the air electrode. The exact mechanism of the electrochemical reaction depends on the material employed and its microstructure, thus more than one process might play a role (e.g. additional transport of adsorbed oxygen through the electrode surface into the TPB)<sup>13</sup>.

The reaction area can be extended beyond the TPB by employing mixed ionic-electronic conducting (MIEC) electrode materials. These materials allow to move from a TPB-based into a double phase boundary (DPB) geometry, in which the electrochemical reaction occurs at the whole surface of the air electrode. This mechanism extends the reaction active region, as the oxygen transport can be carried out across the electrode bulk or surface. This makes MIEC electrodes highly interesting for dense electrode applications, as in the cases studied

in this thesis. A scheme of the general transport mechanism taking place for both TPB and DPB-based oxygen electrodes is presented in Figure 1-2.

The parameters that describe the kinetics of the electrochemical performance of MIEC oxygen electrode materials are the oxygen surface exchange coefficient ( $k^*$ ) and the oxygen diffusion coefficient ( $D^*$ ). An approximately linear correlation between these two parameters has been experimentally demonstrated for perovskite-based MIECs employed as air electrodes<sup>14-17</sup>, highlighting the strong influence of the ionic transport properties (in particular, oxygen vacancy availability and mobility) on the surface electrochemical activity. However, additional factors including surface chemical composition or the presence of secondary phase aggregates, may lead to a strong variability in the surface exchange coefficient.

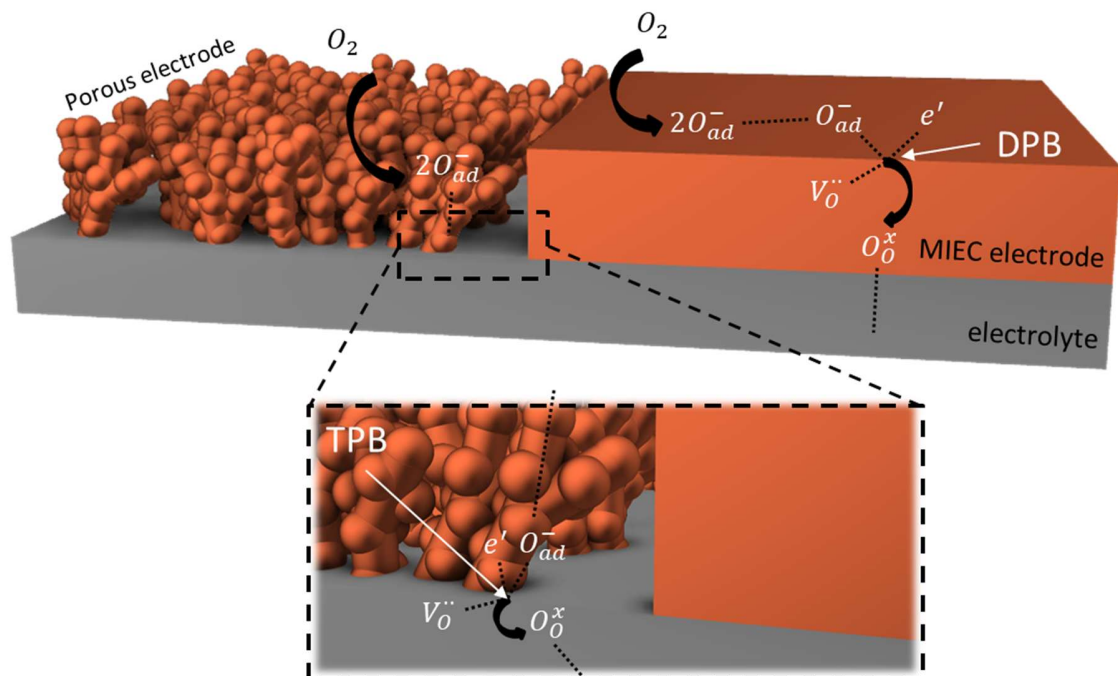


Figure 1-2. TPB and DPB oxygen incorporation mechanisms in both porous and dense (mixed ionic-electronic conductor) oxygen electrodes. Reproduced from Ref.<sup>1</sup> with permission of IOP Publishing.

### 1.2.2 State of the art materials for solid oxide cells

As a general basis, all the components of a SOC are made of ceramic oxides with different functional properties depending on their role in the cell (i.e. hydrogen and oxygen electrodes, electrolyte or interconnectors). In some cases, metallic components can be included and utilized as interconnectors or as catalysts (cf. later in the text). There is a large variety of ceramic materials that can be employed in SOC systems –some of the most commonly known will be discussed in this chapter–, but in the majority of cases they can be differentiated by their crystallographic structure, normally perovskites and fluorites. Figure

1-3 shows the basic structure of perovskite (in its cubic form) and fluorite materials. Perovskites structures are characterized by the general formula  $ABX_3$ , where A and B are cations and X is the anion. In the simplest case of a cubic structure with application in SOCs A is typically a large size cation from the family of the lanthanides (trivalent) or the alkali earth (divalent) metals with 12-fold cuboctahedral coordination, B is a transition metal cation (tri/tetravalent) with 6-fold octahedral coordination and X is the oxygen anion  $O^{2-}$ . Fluorite materials crystallize in a cubic geometry with the formula  $AX_2$ , which for the case of application in SOCs the A position is filled with a tetravalent lanthanide or transition metal cation (e.g. Zr, Ce) and X corresponds to the oxide ion. In SOCs, perovskite materials have been employed in all the components, oxygen and hydrogen electrodes<sup>18</sup>, electrolytes<sup>19</sup> and even interconnectors<sup>20</sup>. Regarding fluorites, they are typically employed as electrolytes<sup>21</sup> and hydrogen electrodes<sup>22,23</sup>, although they can also be utilized as functional layers<sup>24-26</sup> and as constituent phases in composites for oxygen electrodes<sup>27,28</sup>. A more detailed description of the materials employed for the different SOC components is given in the next paragraphs, with particular interest in the materials investigated throughout this thesis, i.e. electrode materials.

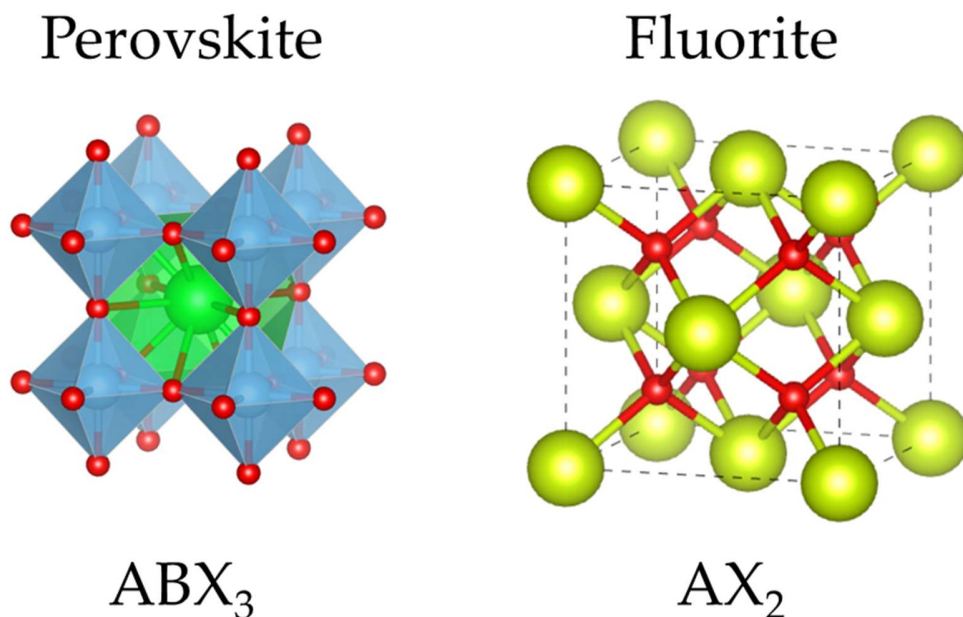


Figure 1-3. Crystallographic structure of cubic perovskite ( $ABX_3$ ) and fluorite ( $AX_2$ ) materials. The structures have been obtained using the VESTA software utilizing CIFs of reference materials: perovskite  $SrTiO_3$ <sup>29</sup> and fluorite  $CeO_2$ <sup>30</sup>.

Historically, oxide-based oxygen electrodes in SOCs consisted in a porous ceramic layer of an electronic conductor. The porosity of the material facilitates the transport of oxygen gas through the electrode surface to the interface with the electrolyte, in which the electrochemical reaction takes place. Typically employed oxygen electrodes were based on manganite perovskites such as  $La_{1-x}Sr_xMnO_3$  (LSM)<sup>31</sup>, which limited the oxygen reduction

reaction at the TPB. More recently, the introduction of composites was carried out for improving the performance, fabricating two-phase systems that combine materials with good oxygen affinity (e.g. LSM) and fast ionic conductivity such as yttria-stabilized zirconia (YSZ) or gadolinium doped-ceria (GDC)<sup>27,32,33</sup>. Finally, the use of MIECs for expanding the electrochemically active area to the whole electrode surface became the most employed solution. Among them, lanthanum cobalt- and iron-based oxides (e.g.  $\text{La}_{1-x}\text{Sr}_x\text{Co}_{1-y}\text{Fe}_y\text{O}_3$  - LSCF-) were rapidly considered the most promising oxygen electrode materials, representing the current technological state-of-the-art.<sup>34</sup> Despite this, perovskite-based MIECs still present limitations caused by secondary reactions with the electrolyte (e.g. generation of strontium zirconates)<sup>35</sup> and by structural instabilities (i.e. surface Sr segregation),<sup>36</sup> which might result in the formation of insulating phases at the electrode-electrolyte or electrode-gas interface (cf. section 1.2.3).

Regarding the hydrogen electrode, state of the art materials are mainly based on porous metallic phases<sup>37</sup> and metal-electrolyte composites (cermets)<sup>10,11,38</sup>. Nevertheless, such structures present several limitations in terms of structural stability at high temperatures and sulphur poisoning<sup>39</sup>. Moreover, their implementation in some cell systems (planar configurations, thin-film based devices, cf. later in the text) is hindered by the poor in-plane percolation of porous layers and by fabrication incompatibilities of the metallic phases with typical thin film deposition techniques. As a result, there is an increasing effort in developing novel all-oxide materials that may reach the high performance of metallic-based hydrogen electrodes while retaining long-term stability. State-of-the-art full ceramic fuel electrodes are based on ceria doped with Gd (as in GDC-CGO) or Sm (SDC)<sup>22,23,40</sup>. Despite doped-ceria presents an excellent catalytic activity upon the HOR as well as a certain degree of mixed ionic electronic conductivity in reducing conditions, it is characterized by limited electronic conductivity<sup>41</sup> causing current percolation losses. This limitation makes the implementation of ceria-based, metal-free anodes deeply challenging. Potential alternatives consist in the use of novel anode formulations, such as double perovskites  $\text{Sr}_2\text{MMoO}_6$ <sup>42-44</sup>,  $\text{Sr}_{2-x}\text{La}_x\text{CoMoO}_6$ <sup>45</sup> and  $\text{SrFe}_{0.2}\text{Co}_{0.4}\text{Mo}_{0.4}\text{O}_{3-\delta}$  perovskite<sup>46</sup>. This is also the case of the perovskite family of chromites, and in particular Sr-doped lanthanum chromite manganites ( $\text{La}_{1-x}\text{Sr}_x\text{Cr}_{1-y}\text{Mn}_y\text{O}_3$  - LSCrMn)<sup>47-50</sup>, which presents high mixed ionic electronic conductivity and excellent thermal stability in reducing conditions<sup>51</sup>. While  $(\text{La,Sr})\text{CrO}_3$  is a predominant hole conductor even in reducing atmospheres, a decrease of the B-site oxygen coordination and formation of oxygen vacancies is achieved by doping with multivalence transition elements (e.g Mn)<sup>49,50,52</sup>. Mn-doped  $(\text{La,Sr})\text{CrO}_3$  has therefore extensively been used in the past as an anode material due to the combination of high electronic and oxygen vacancy conductivity. Particularly, equimolar Cr:Mn ratio has been shown to exhibit the best trade-off between phase stability and electrochemical activity<sup>49,53,54</sup>. Nonetheless, the electrochemical performance of LSCrMn-based systems as standalone anode materials is far behind ceria and cermet based anodes, so new chromite formulations and doping strategies have been explored<sup>55-60</sup>.

To date, the most commonly employed electrolyte materials for SOCs are the ones based on zirconia. In particular, YSZ is the most established electrolyte. The addition of  $\text{Y}_2\text{O}_3$  to  $\text{ZrO}_2$  stabilizes the cubic structure of the material (only present at high temperatures for pure zirconia) and increases its oxygen conductivity<sup>61</sup>. In particular, 3% doped YSZ presents particularly good mechanical stability<sup>62</sup>. An additional electrolyte materials based on zirconia is scandia stabilized zirconia (SSZ) which is reported to present higher ion conductivity and mechanical stability, despite it suffers from phase transition resulting in aging of the performance and also presents higher cost<sup>63</sup>. Other materials have been proposed as promising electrolytes, although none of them has been able to surpass the overall suitability of YSZ. This is the case of doped-ceria materials, which are characterized by higher ionic conduction and therefore have been proposed as promising electrolyte materials for lower temperature SOCs<sup>64</sup>. Nevertheless, doped-ceria presents electronic conductivity in reducing conditions, leading to a reduction of the cell potential. Other alternative electrolyte materials with high ionic conductivity are  $\text{La}_{0.8}\text{Sr}_{0.2}\text{Ga}_{0.8}\text{Mg}_{0.2}\text{O}_3$  and  $\text{La}_{0.8}\text{Sr}_{0.2}\text{Ga}_{0.8}\text{Mg}_{0.2-x}\text{Ni}_x\text{O}_3$ <sup>65</sup>, and the Bimevox<sup>66,67</sup> series of materials.

Other components of interest in SOCs are interconnectors. Given the conditions in which SOCs operate, there are not many materials that are suitable for their use as interconnectors. Although metallic interconnects are desirable from a structural and robustness point of view, these are normally discarded or limited to lower temperatures due to the differences in the thermal expansion coefficient with respect to the ceramic components. With respect to ceramics, there are few oxides that present high electrical conductivity under both reducing and oxidizing conditions. These restrictions are the reason why interconnects are typically made of the perovskite chromite  $\text{LaCrO}_3$  (LCO)<sup>61,68</sup>. Sealing materials suppose another field of investigation that is key for the successful operation and integration of SOC systems<sup>69</sup>. Several materials can be employed for sealing SOCs, such as compression sealants, metallic gaskets, glasses, ceramic sealants and glass-ceramic combinations<sup>63,68</sup>. Nevertheless, compression sealants often show a certain amount of gas leakages while metallic gaskets –often made of gold– are expensive and hence are normally limited to lab-scale prototyping. From the point of view of thermomechanical stability, glass and hybrid sealants seem to be the most promising approaches for accommodating the mechanical stresses and structural mismatch of SOCs<sup>70</sup>. In summary, Figure 1-4 shows a collection of the most commonly employed materials in conventional SOFCs –i.e. the main materials discussed in this section–, reproduced from Wincewicz et al.<sup>63</sup>.

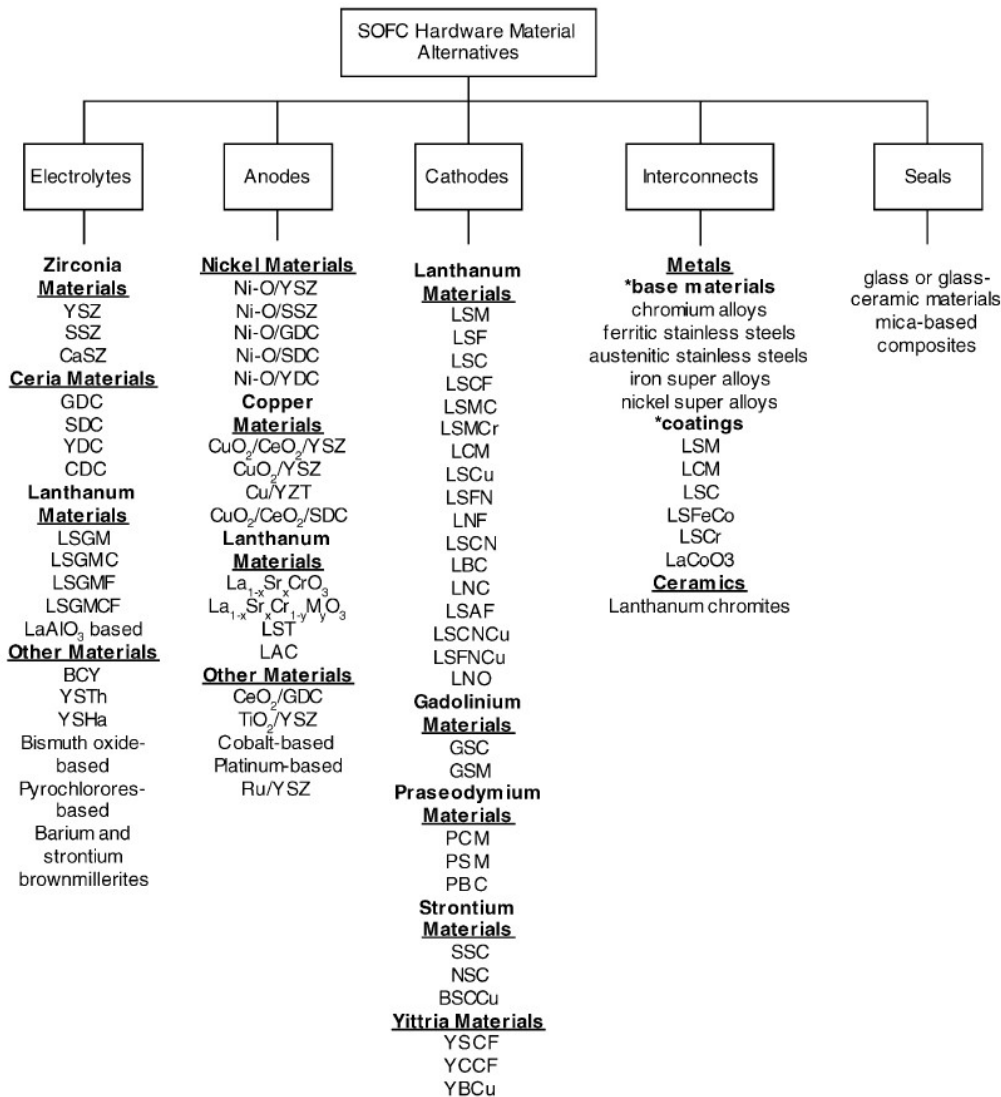


Figure 1-4. Summary of the main materials employed for the different components of SOCs. Reproduced from Wincewicz, K.; Cooper, J. Taxonomies of SOFC Material and Manufacturing Alternatives. *Journal of Power Sources* 2005, 140 (2), 280–296. <https://doi.org/10.1016/j.jpowsour.2004.08.032>, with permission from Elsevier<sup>63</sup>.

### 1.2.3 Mechanisms of degradation in solid oxide cells

Despite the high efficiency of SOCs, there are some limitations that hinder their widespread application. The high temperatures employed for their operation typically result in the evolution of the materials present in their components through different degradation mechanisms. As briefly commented in the previous section, typical phenomena involved in the degradation of SOCs are the appearance of secondary phases in the electrolyte-electrode interface<sup>71</sup>, migration of chromium from the interconnects towards the electrodes<sup>72</sup>, sulfur poisoning<sup>39</sup> and the segregation of dopant elements towards the electrode surface in the

form of secondary phases<sup>73</sup>. Some of these degradation phenomena are better understood while some others remain a difficult challenge to be solved. For instance, incompatibilities in the electrolyte-electrode interface leading to the formation of strontium zirconate insulating species has been partially solved with the use of diffusion barrier layers based on doped-ceria<sup>24,26,71</sup>.

In this thesis, particular focus has been given to degradation phenomena related to dopant segregation processes in MIEC materials, in particular Sr-doped lanthanum perovskite oxides. Segregation of Sr species in the surface of oxygen electrodes is a phenomenon commonly observed in SOCs. Materials with particularly high electrochemical activity for ORR like LSC and LSCF are reported to be more prone to suffer from these processes<sup>74-76</sup>. Nonetheless, the appearance of segregated Sr-rich particles in the electrode surface has also been observed in other materials such as manganites<sup>77,78</sup> and chromites<sup>79,80</sup>. This type of degradation has been also observed under different operation conditions. It has been observed under regular thermal treatment<sup>81</sup>, and also under cathodic/anodic DC biases, depending on the dopant employed<sup>82</sup>. Additional studies have reported the reinsertion of Sr into the perovskite lattice showing performance recovery after carrying out thermal treatments at temperatures beyond the operation temperature<sup>83,84</sup>. Recent studies have also pointed to the formation of SrSO<sub>4</sub> species in the surface as specific phase involved in the detriment of the electrochemical performance<sup>85,86</sup>. Several strategies have been proposed for blocking Sr migration towards the surface, like inducing lattice strain<sup>87,88</sup>, increasing the entropy of the oxygen electrode materials<sup>5,6</sup> or the use of heterostructures<sup>87</sup>.

## 1.3 Types of solid oxide cell devices

### 1.3.1 Cell geometry and operation modes

SOCs can be fabricated following different designs and geometries. These are classified in (i) tubular, (ii) segmented-cell-in-series, (iii) monolithic and (iv) planar configurations, although tubular and planar are the most commonly employed ones<sup>61,70</sup>. The tubular geometry cell consists in a porous support tube in which the different cell layers are sequentially deposited on top of it. The flat cell design allows for more variability in the scale of the final device, ranging from the implementation in large stacks to miniaturization in the form of  $\mu$ SOCs (cf. later in the chapter). Additionally, the planar design results in compatibility with a vast amount of fabrication processes, e.g. slurry based methods<sup>27</sup>, printing techniques<sup>89</sup> and vacuum-assisted deposition processes<sup>90,91</sup>. Figure 1-5 shows the schematic representation of a planar SOFC built up for a two cell stack configuration, reproduced from Ref<sup>92</sup>.

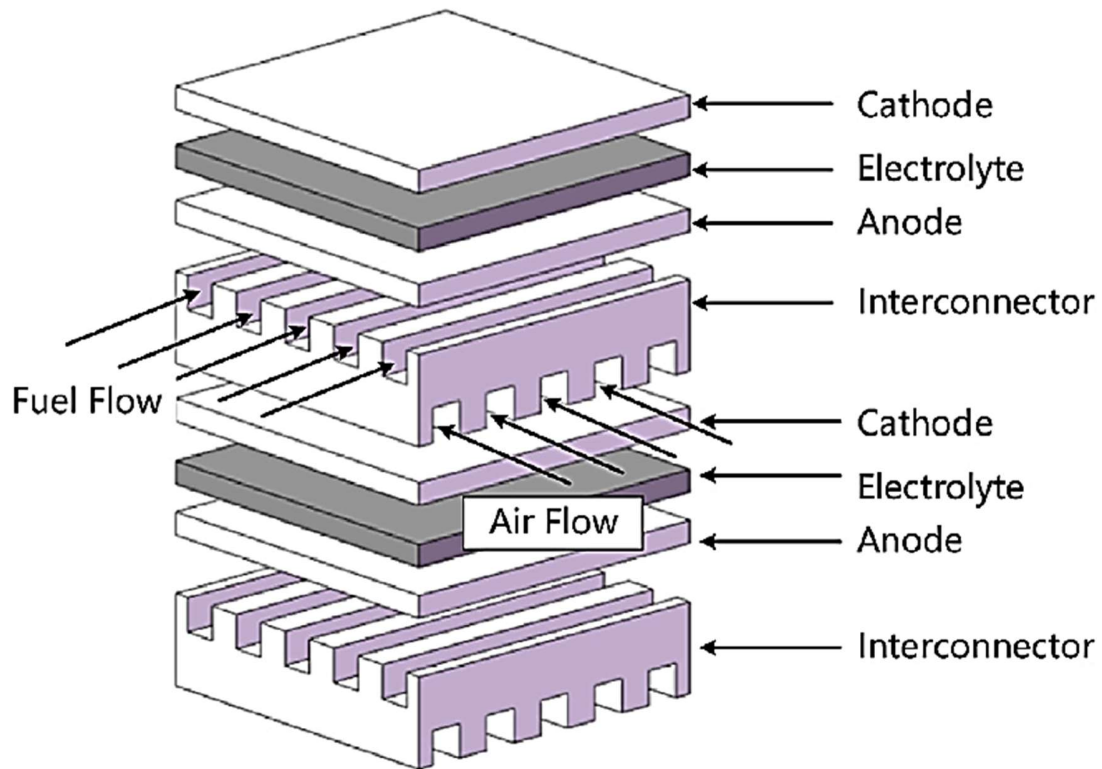


Figure 1-5. Concept design of a planar SOFC assembled in a cross-flow stack configuration. Reproduced from Wu, X.; Jiang, J.; Zhao, W.; Li, X.; Li, J. *Two-Dimensional Temperature Distribution Estimation for a Cross-Flow Planar Solid Oxide Fuel Cell Stack*. *International Journal of Hydrogen Energy* **2020**, 45 (3), 2257–2278. <https://doi.org/10.1016/j.ijhydene.2019.11.091>, with permission from Elsevier<sup>92</sup>.

SOCs offer more complex functionalities than operating them in single fuel or electrolysis modes, being able to operate under different work conditions depending on the materials selected. Examples of these applications are schematized in Figure 1-6. One of them –panel (a)– consists in employing SOCs as reversible cells (RSOCs), in which the fuel and electrolysis modes are alternated in view of the energy needs. The implementation of RSOCs is particularly interesting for modulating the energy demand. This is done by storing the excess of electrical energy in the form of chemical energy (i.e. hydrogen formation by electrolysis) and then supply the demand of electrical energy by consuming such hydrogen (fuel cell mode). As RSOCs operate in both electrolysis and fuel cell modes, it is of uttermost importance that the materials employed present high electrochemical activity in both modes and withstand the possible degradation mechanisms favored in each configuration<sup>93,94</sup>.



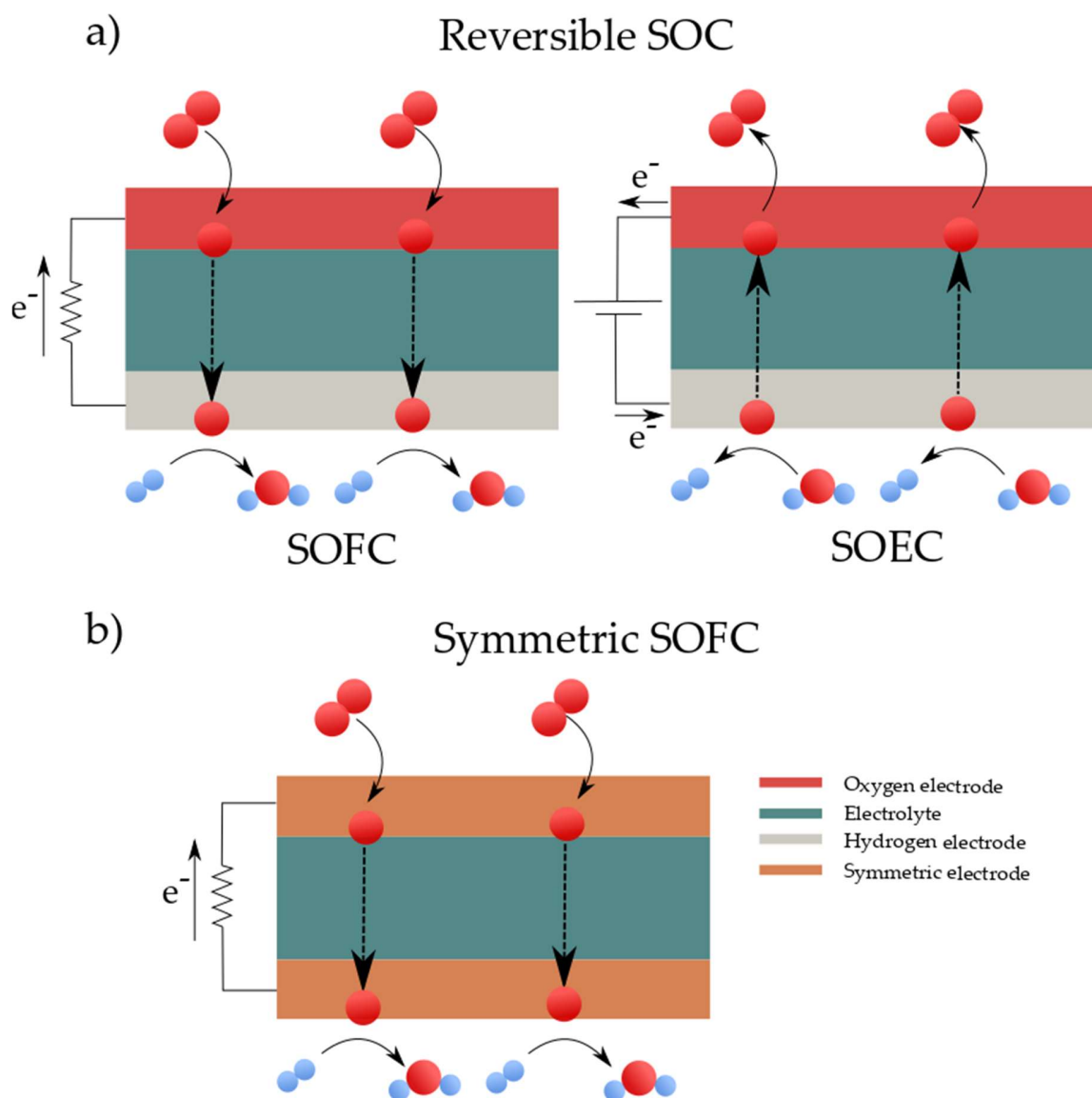


Figure 1-6. Schematic of the operation modes and geometries of the SOC devices studied in this thesis: reversible SOC (a) and symmetric SOFC (b).

Figure 1-7 shows an example of a SOC operated under both electrolysis and fuel cell modes<sup>95</sup>. In particular, SOFC operation with 100 % H<sub>2</sub> is represented, while reversible SOFC/SOEC characterization is shown for a 50 % H<sub>2</sub>/ H<sub>2</sub>O mixture. The second case depicted in Figure 1-b is the case of symmetric SOCs (SSOCs). These type of devices present several advantages that make them appealing for application in electrochemical systems<sup>18,96</sup>. The use of the same material for both electrodes can result in decreasing the cost associated to material fabrication and production, due to reduced processing steps. Additionally, the thermomechanical stresses are expected to be alleviated due to the use of a single electrode material. Because of their use as interconnectors, perovskite chromites have gained interest for their use as promising symmetrical electrodes<sup>58,97,98</sup>.

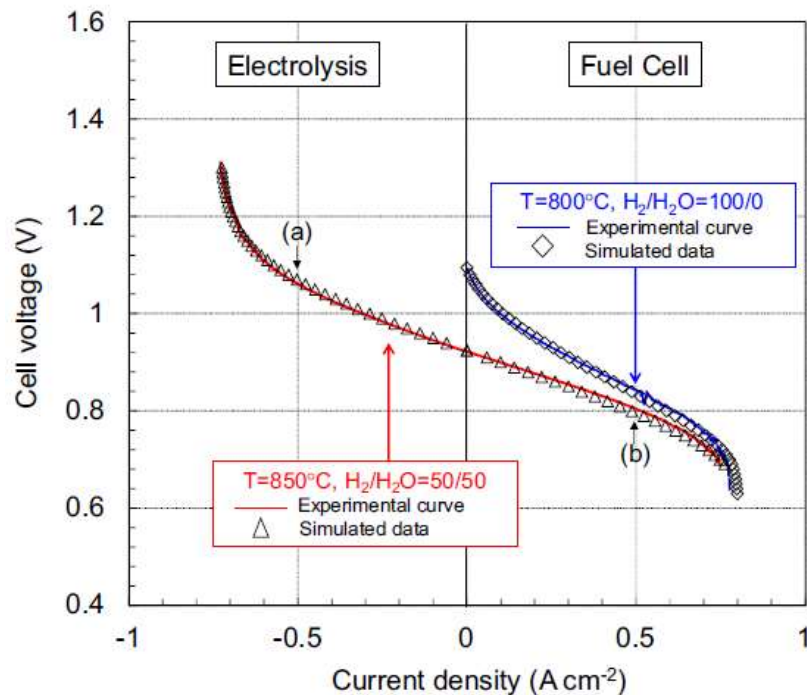


Figure 1-7. Example of a SOC operated under electrolysis and fuel cell conditions. Reproduced from Laurencin, J.; Hubert, M.; Sanchez, D. F.; Pylypko, S.; Morales, M.; Morata, A.; Morel, B.; Montinaro, D.; Lefebvre-Joud, F.; Siebert, E. Degradation Mechanism of  $\text{La}_{0.6}\text{Sr}_{0.4}\text{Co}_{0.2}\text{Fe}_{0.8}\text{O}_{3-\delta}/\text{Gd}_{0.1}\text{Ce}_{0.9}\text{O}_{2-\delta}$  Composite Electrode Operated under Solid Oxide Electrolysis and Fuel Cell Conditions. *Electrochimica Acta* **2017**, *241*, 459–476. <https://doi.org/10.1016/j.electacta.2017.05.011> with the permission from Elsevier<sup>95</sup>.

### 1.3.2 Thin film solid oxide cells

Among the variety of SOC technologies and architectures, the ones based on thin film materials suppose a promising field of research. The use of thin film layers in the components of SOCs present several advantages and interesting features with respect to conventionally fabricated materials. For instance, reducing the thickness of the electrolyte layer decreases the ohmic losses generated through the oxide ion conduction, maximizing the power extracted from the cell. This would also facilitate lowering the operational temperature of SOCs, hence reducing costs by allowing the use of a wider and more cost competitive range of materials for interconnects and sealing components. Additionally, fabrication of thin-film based materials allows for the achievement of unique materials with enhanced electrochemical activity and functional properties (cf. next sections).

#### 1.3.2.1 Thin film functional electrode materials

In the last years, advances in vacuum assisted physical and chemical deposition methods for the deposition of thin film oxides opened the possibility to the fabrication of functional layers for electrode applications<sup>99,100</sup>, e.g. in the development of novel micro solid oxide

systems<sup>101–103</sup>. The implementation of thin-film based electrodes allows to fabricate nanostructured SOC materials and devices with enhanced electrochemical properties not reachable at the bulk level. Examples of the advantages of these nanostructured electrodes include enhanced oxygen conduction at phase contact<sup>104,105</sup>, faster electrochemical activity for the surface reaction<sup>106</sup>, or improved stability<sup>5,107</sup>. These are interesting features that nanoengineered materials offer for the improvement in performance with respect the oxygen reaction in SOCs, in particular thin films materials. Ultimately, research on the use of nanostructured solid oxide air electrodes may lead in the upcoming years to the next generation of nanostructured enhanced solid oxide cells.

Nanostructuring oxygen electrode materials through thin-film approaches like strain<sup>108</sup> and grain boundary<sup>104,105,109</sup> engineering, and the fabrication of complex structures including ultrathin coatings<sup>107,110</sup>, multilayers<sup>111,112</sup> and vertically aligned nanostructures<sup>113</sup> (VANs) are some of the proposed strategies to enhance the solid-gas reaction kinetics and the cell stability (see Figure 1-8). In particular, the development of new self-assembled thin-film nanocomposites is a promising strategy for engineering the electrode-electrolyte interface, arguably a key area during SOC operation, as commented in the previous sections. Here, high electrochemical activity, in-plane electronic percolation and stability against cationic diffusion should be ensured. VANs offer a fully dense structure, favourable out-of-plane geometry for mass transport and the possibility of taking advantage of interface nanoionics effects for tuning the local chemistry<sup>114–116</sup>. In VANs, the intimate alternation of the single phase materials at the nanoscale allows to fully exploit strategies of electrode fabrication based on maximization of the TPB density<sup>3,113</sup>. Perovskite-fluorite based VANs have already been explored as novel functional layers in SOFCs. Early studies carried out by Yoon et al.<sup>99</sup> introduced the use of VANs based on LSC and CGO at the electrolyte-electrode interface. The application of such heterostructure increased the TPB density, leading to reduced polarization resistance. GDC/YSZ VANs were later proposed by Su et al. for boosting the ionic conductivity of electrolytes in SOFCs, resulting in a significant increase of the power output<sup>117</sup>. Develos-Bagarinao et al. have also recently reported high electrochemical performance on a system with a LSCF-GDC VAN functional layer<sup>118</sup>. Dense thin films also enhance the cell stability by providing a barrier against cation migration. A LSM-SDC VAN cathode for SOFC application has been proven by our group to suppress dopant segregation on the film's surface.<sup>5</sup> Morales et al. have shown that, by implementing a thin-film ceria layer at the electrolyte/electrode interface, continuous SOFC operation over 4500 h can be achieved with low degradation and high power  $> 1\text{W.cm}^{-2}$  at 750 °C.<sup>100</sup>

Regarding the hydrogen electrode, advanced structures relying on the utilization of heterointerfaces and nanocomposites have also been proposed recently – after the seminal works by Chueh and Jung on ceria-based electrodes<sup>22,23,40,119</sup> – including  $\text{La}_{0.2}\text{Sr}_{0.7}\text{TiO}_{3-\delta}$ - $\text{Gd}_{0.1}\text{Ce}_{0.9}\text{O}_{1.95-\delta}$  composites<sup>120</sup>, and a NiCGO cermet with extremely low content of Ni<sup>121</sup>, achieving remarkable HOR activity. Furthermore, LSCrMn/ceria-based composites have

been proposed as SOFC anodes in the past<sup>122,123</sup>, combining the electrical properties and stability of LSCrMn with the superior electrochemical properties of doped-ceria with respect to HOR. Such promising results demonstrate the potential of using LSCrMn-SDC advanced materials and heterointerfaces –i.e. one of the goals of this thesis, see Chapter 3– for functional layer application in SOCs technologies.

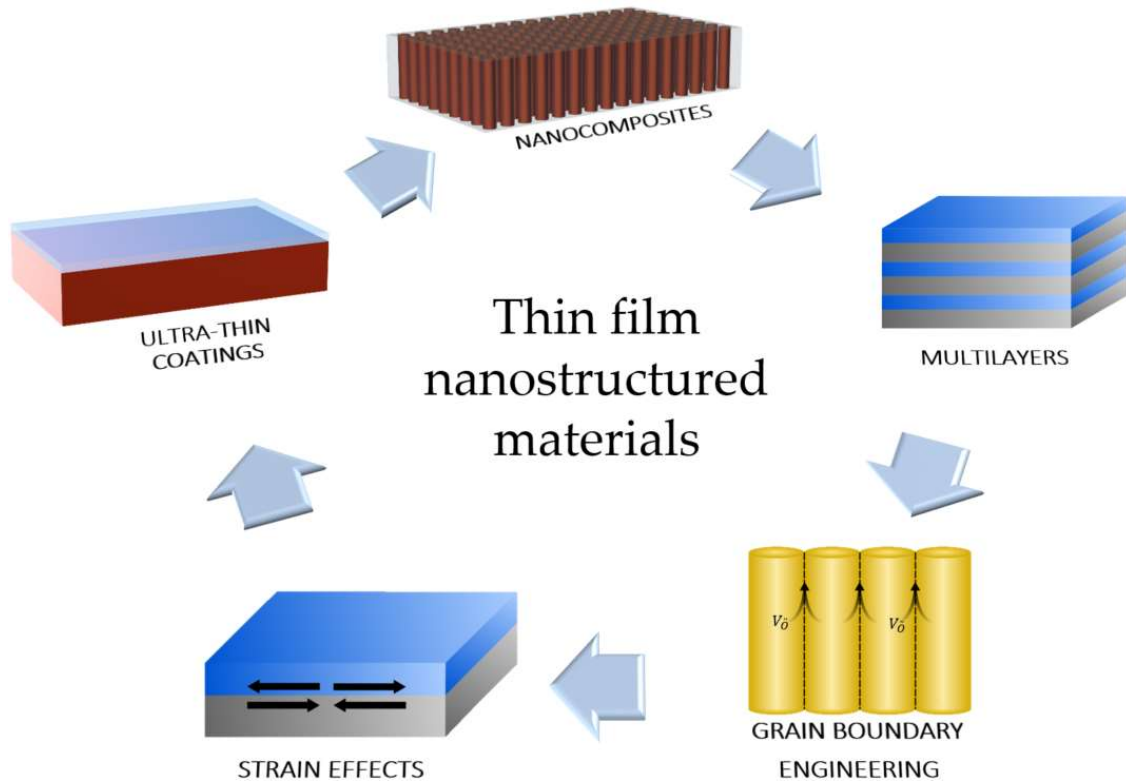


Figure 1-8. Schematic of different thin film nanostructured materials for SOFC application.

### 1.3.2.2 Ceramics for micro solid oxide cells

Miniaturized SOCs, or  $\mu$ SOCs, represent a promising technology for the transition to a sustainable, wireless grid of energy devices. These microreactors could potentially power the information and communication technology sector and their spread as Internet of Things nodes, as well as act as microenergy storers. The reduced scale of  $\mu$ SOCs suppose a feasible approach to overcome some of the limitations of classical SOCs. In particular, reducing the thickness of the device to the nanometer scale would lower the ohmic resistance of the electrolyte. This widens the operational temperature range in which the device can be applied towards a lower limit ( $< 500\text{-}600\text{ }^{\circ}\text{C}$ )<sup>90,91,102</sup>. Moreover, integration into a microdevice limits the use of conventional SOCs such as cermets, as they are not easily integrated with thin film fabrication techniques. The microstructure of the materials employed are then normally restricted to planar geometries, given the combination with semiconductor processing techniques such as wet/dry etching and photolithography

processes for patterning the device. In general terms,  $\mu$ SOFCs can be fabricated following different designs and structures (keeping the planar geometry) and onto several substrates<sup>103</sup>. In particular, it can be either fabricated on top of a porous electrode substrate<sup>124</sup> or as a free-standing membrane released from a silicon substrate<sup>102,103,125</sup>. The latter is the most commonly employed architecture when referring to  $\mu$ SOFCs. More recent studies propose the use of metallic substrates as support for  $\mu$ SOFCs<sup>126</sup>. This approach would facilitate device electrical integration facilitating the percolation of current from the ceramic layers to the connections.

Figure 1-9 shows a schematic of the architecture of silicon-based  $\mu$ SOFCs employed in this thesis. The main difference between this architecture and the observed in other works lays on the use of a zirconia layer fabricated by Atomic Layer Deposition (ALD) before the deposition of the electrolyte layer. This approach was applied based in previous experience from the group<sup>127</sup>, and has proven to be a promising strategy for preventing pinhole formation in the electrolyte, one of the most common detrimental effects observed in these types of devices<sup>128</sup>. This is due to the high degree of conformality reached during the ALD deposition, in contrast to the more directional growth observed in techniques like pulsed laser deposition (PLD). It is worth mentioning that there is not a lot of information in the literature on sealant optimization for application in  $\mu$ SOFCs. Some examples of sealants reported in the literature are silver O-rings (Garbayo et al.<sup>101</sup>), ceramic glue (Evans et al.<sup>125</sup>) and gold gaskets (Li et al.<sup>129</sup>), while many works do not mention the sealant employed in their systems<sup>130,131</sup>. This is quite relevant since the successful integration of all the layers involved in these types of devices will be in the end determined by the thermomechanical compatibility of all the materials involved (i.e. ceramic, semimetallic and metallic).

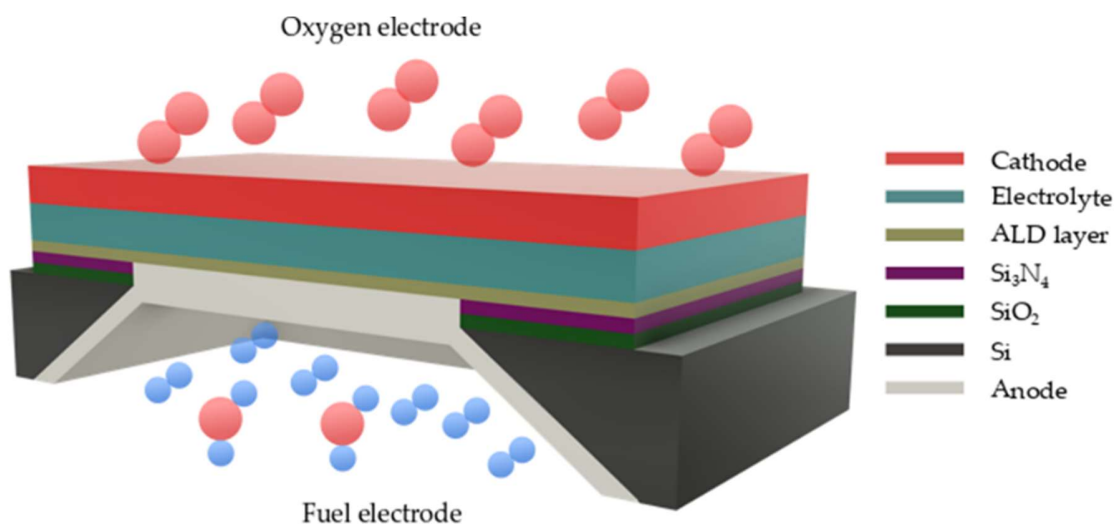


Figure 1-9. Cross-section schematic view of the  $\mu$ SOFC design employed in this thesis.

## 1.4 Advanced tools for materials search

There is growing interest in the use of advanced methodologies for the discovery of new materials and formulations in a wide span of research fields. Investigations dealing with drug discovery and drug combination are already making use of combinatorial methodologies and computational analyses<sup>132,133</sup>. Focusing on material science, the use of combinatorial methods for the simultaneous growth of composition graded materials is an emerging field reaching disciplines like photovoltaics<sup>134</sup>, electrochemistry<sup>135,136</sup> and many more<sup>137</sup>. In particular for the case of oxides with application in solid state energy systems, previous studies from the group opened lines of investigation dealing with binary systems of LSMC and LSM<sub>x</sub> deposited by combinatorial PLD<sup>138-140</sup>. Recent works developed by Papac et al. have reported the fabrication of the Ba(Co,Fe,Zr,Y)O<sub>3-δ</sub> library of electrode materials for protonic ceramic fuel cells. In one of their works<sup>141</sup> they present a promising electrochemical station for the automatized characterization of the electrochemical properties of the system by impedance spectroscopy. They have also developed an analysis procedure based on Distribution of Relaxation Times (DRT) processing in combination with Bayesian methods that allows the automatic extraction of impedance relevant features along the library studied<sup>142,143</sup>. Related lines of research focus on the study of specific descriptors of the functional properties of electrochemically active materials. These descriptors consist in parametric features generally obtained by structural and chemical characterization, as well as modelling processes, and they establish a correlation with the chosen performance parameter. Examples of these methodologies can be found in literature related to heterogeneous catalysis, where relationships between binding energies and catalyst activity are often described<sup>144</sup>. In the particular case of SOC oxide materials, some studies have found a correlation between the position of the oxygen p-band center (the descriptor) with obtained values for surface oxygen exchange coefficients or oxygen evolution reaction activities<sup>145,146</sup>.

Ultimately, the use of combinatorial methods and high-throughput processes represents a promising approach for accelerated research and material discovery. Beyond these methodologies, the implementation of machine learning (ML) analyses for the extraction of performance descriptors and prediction of optimal material compositions is expected to be the real game-changer in materials science<sup>147</sup> and in particular energy solutions<sup>148,149</sup>. In particular, ML methodologies are already being pursued for the prediction of SOFC performance evolution on operation<sup>150</sup>. Beyond this, it can be expected that the development of ML analyses procedures would make use of the large datasets generated by high throughput experimental techniques. The coupling of large experimental datasets with ML models will result in one of the key directions that research will follow in the next years. In the case of this thesis, part of the work developed has focused in the implementation of high-throughput techniques for the characterization of a perovskite material library

resulting from the combination of three well-known oxygen electrodes, i.e. LSC, LSF and LSM. The goal behind this work is not exclusively focused on the direct extraction of optimal electrochemical features within the system studied, but also serve as an experimental database for the prediction and analysis of non-evident experimental features. This could end up facilitating the comprehension of the mechanisms behind the electrochemical performance of these materials. Even so, this could allow to translate the same reasoning and identification of similar descriptors in other materials. Figure 1-10 shows a schematic on the main concept behind the development of high-throughput methodologies for materials search, in comparison to conventional materials science. Combining the use of high-throughput methodologies with ML models would accelerate the search of new materials beyond the limits of traditional research.

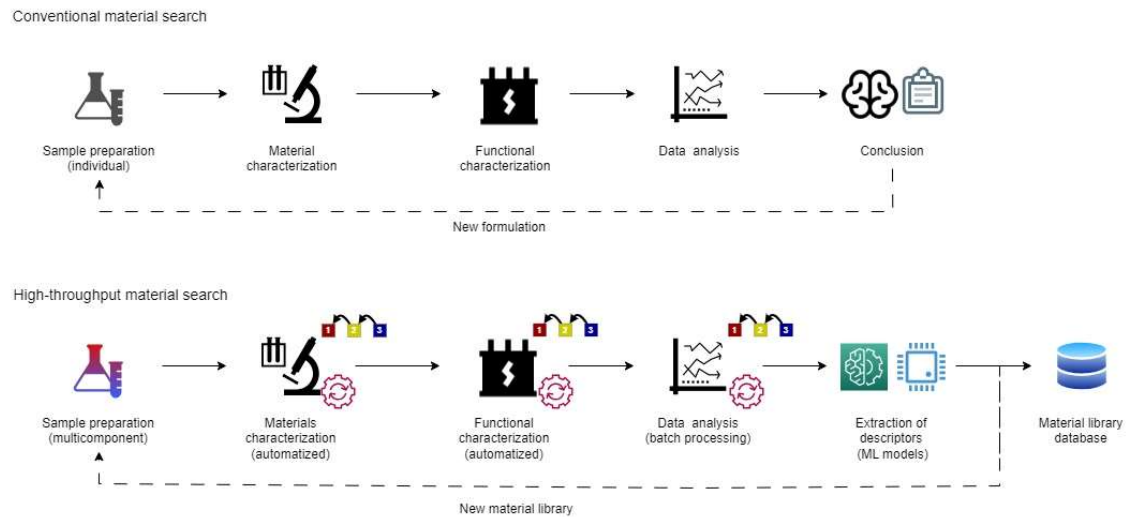


Figure 1-10. Schematic of the workflow followed for materials search based on high-throughput methods and compared to conventional methodologies.

## 1.5 Scope of this thesis

The work presented in this doctoral thesis aims to investigate the use of thin film based functional electrodes in SOCs and their integration in full device architectures. Thin film electrode materials have been studied under different approaches. Doped-ceria based thin film cermet presenting low levels of Ni have been studied for their application as hydrogen electrodes. Nanostructured all-oxide electrodes based on LSCrMn and SDC have been studied as promising materials for both hydrogen and symmetric electrode applications. Combinatorial studies and high throughput characterization of the LSMCF perovskite family have been pursued in order to gain knowledge on the electrochemical properties of oxygen electrodes as well as their behavior on thermal degradation within a self-sustained dataset. For this, development of high-throughput methodologies as well as automatic data processing routines were explored. Integration of thin film materials in functional devices have been tested in symmetric and reversible configurations on single crystal supported cells. The symmetric thin film cells have been studied with focus on their performance evolution facing redox cycling processes. Reversible cells were studied under both fuel and electrolysis modes. Integration with silicon technologies in the form of  $\mu$ SOFCs have been achieved as proof-of-concept cells. Experimental limitations on the characterization and operation of these devices are also discussed.

This thesis is organized as follows:

- Chapter 2 describes all the experimental description and methodologies employed on the work behind this thesis. The chapter includes details on single and combinatorial thin film fabrication carried out by PLD. The characterization techniques utilized in this thesis are also described, with particular emphasis given to the surface characterization techniques utilized and the high throughput approaches developed. Experimental details of the integration and operation of the materials studied in functional devices are also reported.
- Chapter 3 describes the development of nanostructured functional layers for their application in symmetric and hydrogen electrodes in SOCs. Research on LSCrMn, SDC and NiCGO based electrode materials is reported in this chapter. Several nanostructuring approaches as well as variation in the microstructures are discussed as strategies for achieving high performance electrode materials.
- Chapter 4 focuses on the combinatorial study of the perovskite family of  $\text{La}_{0.8}\text{Sr}_{0.2}\text{Mn}_x\text{Co}_y\text{Fe}_{1-x-y}\text{O}_3$  oxygen electrodes. The work includes the development of high-throughput techniques for the complete characterization of the material library. These techniques involve compositional and structural analyses, as well as functional characterization of the mass oxygen transport properties and the electrochemical performance. Additionally, a series of selected material library compositions have been studied in terms of their stability facing thermal



degradation. Microstructural characterization, surface chemical analyses, reconstruction of cation depth profiles and material defect characterization techniques have been utilized for analyzing film degradation in terms of migration of strontium and formation of secondary species.

- Chapter 5 presents different approaches for the integration of thin film-based oxygen and hydrogen electrodes in functional SOC devices. The chapter explores the use of all-ceramic thin film electrodes in single crystal electrolyte supported devices both in symmetric and reversible architectures, as well as the integration with silicon technologies in order to fabricate  $\mu$ SOFCs. The work presented unveils the promising properties of chromite-based symmetric electrodes for cell activity recovery after performing redox cycling processes. Additionally, thin film reversible SOCs operated in both fuel and electrolysis modes are presented. The electrochemical characterization of fully assembled  $\mu$ SOFCs and a detailed discussion on the experimental limitations for their operation is also discussed.

## References

- (1) Sirvent, J. de D.; Buzi, F.; Baiutti, F.; Tarancón, A. Advances in Nanoengineered Air Electrodes: Towards High-Performance Solid Oxide Cells. In *Nanoengineered Materials for Solid Oxide Cells*; Develos-Bagarinao, K., Ed.; IOP Publishing, 2023; pp 1-1-1–35. <https://doi.org/10.1088/978-0-7503-4064-9ch1>.
- (2) Sirvent, J. de D.; Carmona, A.; Rapenne, L.; Chiabrera, F.; Morata, A.; Burriel, M.; Baiutti, F.; Tarancón, A. Nanostructured  $\text{La}_{0.75}\text{Sr}_{0.25}\text{Cr}_{0.5}\text{Mn}_{0.5}\text{O}_3\text{-Ce}_{0.8}\text{Sm}_{0.2}\text{O}_2$  Heterointerfaces as All-Ceramic Functional Layers for Solid Oxide Fuel Cell Applications. *ACS Appl. Mater. Interfaces* **2022**, *14* (37), 42178–42187. <https://doi.org/10.1021/acsami.2c14044>.
- (3) Acosta, M.; Baiutti, F.; Tarancón, A.; MacManus-Driscoll, J. L. Nanostructured Materials and Interfaces for Advanced Ionic Electronic Conducting Oxides. *Adv. Mater. Interfaces* **2019**, *6*, 1900462. <https://doi.org/10.1002/admi.201900462>.
- (4) Zhang, J.; Ricote, S.; Hendriksen, P. V.; Chen, Y. Advanced Materials for Thin-Film Solid Oxide Fuel Cells: Recent Progress and Challenges in Boosting the Device Performance at Low Temperatures. *Adv. Funct. Mater.* **2022**, *32* (22), 2111205. <https://doi.org/10.1002/adfm.202111205>.
- (5) Baiutti, F.; Chiabrera, F.; Acosta, M.; Diercks, D.; Parfitt, D.; Santiso, J.; Wang, X.; Cavallaro, A.; Morata, A.; Wang, H.; Chroneos, A.; MacManus-Driscoll, J.; Tarancón, A. A High-Entropy Manganite in an Ordered Nanocomposite for Long-Term Application in Solid Oxide Cells. *Nat. Commun.* **2021**, *12* (1), 2660. <https://doi.org/10.1038/s41467-021-22916-4>.
- (6) Yang, Y.; Bao, H.; Ni, H.; Ou, X.; Wang, S.; Lin, B.; Feng, P.; Ling, Y. A Novel Facile Strategy to Suppress Sr Segregation for High-Entropy Stabilized  $\text{La}_{0.8}\text{Sr}_{0.2}\text{MnO}_{3-\delta}$  Cathode. *J. Power Sources* **2021**, *482*, 228959. <https://doi.org/10.1016/j.jpowsour.2020.228959>.
- (7) Chan, S. H.; Khor, K. A.; Xia, Z. T. A Complete Polarization Model of a Solid Oxide Fuel Cell and Its Sensitivity to the Change of Cell Component Thickness. *J. Power Sources* **2001**, *93* (1–2), 130–140. [https://doi.org/10.1016/S0378-7753\(00\)00556-5](https://doi.org/10.1016/S0378-7753(00)00556-5).
- (8) Kim, J.; Virkar, A. V.; Fung, K.; Mehta, K.; Singhal, S. C. Polarization Effects in Intermediate Temperature, Anode-Supported Solid Oxide Fuel Cells. *J. Electrochem. Soc.* **1999**, *146* (1), 69–78. <https://doi.org/10.1149/1.1391566>.
- (9) Gao, Z.; Mogni, L. V.; Miller, E. C.; Railsback, J. G.; Barnett, S. A. A Perspective on Low-Temperature Solid Oxide Fuel Cells. *Energy Environ. Sci.* **2016**, *9* (5), 1602–1644. <https://doi.org/10.1039/C5EE03858H>.
- (10) Doppler, M. C.; Fleig, J.; Bram, M.; Opitz, A. K. Hydrogen Oxidation Mechanisms on Ni/Yttria Stabilized Zirconia Anodes: Separation of Reaction Pathways by Geometry Variation of Pattern Electrodes. *J. Power Sources* **2018**, *380*, 46–54. <https://doi.org/10.1016/j.jpowsour.2018.01.073>.
- (11) Doppler, M. C.; Fleig, J.; Bram, M.; Opitz, A. K. Comparison of Electrochemical Hydrogen Oxidation on Different Metal/Ceramic Model Anodes and Mechanistic Implications. *J. Phys. Energy* **2019**, *1* (3), 035001. <https://doi.org/10.1088/2515-7655/ab1ece>.

- (12) Zhang, X.; Zhang, W.; Zhang, L.; Meng, J.; Meng, F.; Liu, X.; Meng, J. Enhanced Electrochemical Property of  $\text{La}_{0.6}\text{Sr}_{0.4}\text{Co}_{0.8}\text{Fe}_{0.2}\text{O}_{3-\delta}$  as Cathode for Solid Oxide Fuel Cell by Efficient in Situ Polarization-Exsolution Treatment. *Electrochimica Acta* **2017**, *258*, 1096–1105. <https://doi.org/10.1016/j.electacta.2017.11.163>.
- (13) Jung, W.; Tuller, H. L. A New Model Describing Solid Oxide Fuel Cell Cathode Kinetics: Model Thin Film  $\text{SrTi}_{1-x}\text{Fe}_x\text{O}_{3-\delta}$  Mixed Conducting Oxides—a Case Study. *Adv. Energy Mater.* **2011**, *1* (6), 1184–1191. <https://doi.org/10.1002/aenm.201100164>.
- (14) Kilner, J. Surface Exchange of Oxygen in Mixed Conducting Perovskite Oxides. *Solid State Ion.* **1996**, *86–88*, 703–709. [https://doi.org/10.1016/0167-2738\(96\)00153-1](https://doi.org/10.1016/0167-2738(96)00153-1).
- (15) Wang, L.; Merkle, R.; Mastrov, Y. A.; Kotomin, E. A.; Maier, J. Oxygen Exchange Kinetics on Solid Oxide Fuel Cell Cathode Materials—General Trends and Their Mechanistic Interpretation. *J. Mater. Res.* **2012**, *27* (15), 2000–2008. <https://doi.org/10.1557/jmr.2012.186>.
- (16) De Souza, R. A.; Kilner, J. A. Oxygen Transport in  $\text{La}_{1-x}\text{Sr}_x\text{Mn}_{1-y}\text{Co}_y\text{O}_{3\pm\delta}$  Perovskites. *Solid State Ion.* **1999**, *126* (1–2), 153–161.
- (17) De Souza, R. A. A Universal Empirical Expression for the Isotope Surface Exchange Coefficients ( $K^*$ ) of Acceptor-Doped Perovskite and Fluorite Oxides. *Phys. Chem. Chem. Phys.* **2006**, *8* (7), 890. <https://doi.org/10.1039/b511702j>.
- (18) Zhang, M.; Du, Z.; Zhang, Y.; Zhao, H. Progress of Perovskites as Electrodes for Symmetrical Solid Oxide Fuel Cells. *ACS Appl. Energy Mater.* **2022**, *5* (11), 13081–13095. <https://doi.org/10.1021/acsaem.2c02149>.
- (19) Skinner, S. J.; Kilner, J. A. Oxygen Ion Conductors. *Mater. Today* **2003**, *6* (3), 30–37. [https://doi.org/10.1016/S1369-7021\(03\)00332-8](https://doi.org/10.1016/S1369-7021(03)00332-8).
- (20) Anderson, H. Review of P-Type Doped Perovskite Materials for SOFC and Other Applications. *Solid State Ion.* **1992**, *52* (1–3), 33–41. [https://doi.org/10.1016/0167-2738\(92\)90089-8](https://doi.org/10.1016/0167-2738(92)90089-8).
- (21) Chronos, A.; Yildiz, B.; Tarancón, A.; Parfitt, D.; Kilner, J. A. Oxygen Diffusion in Solid Oxide Fuel Cell Cathode and Electrolyte Materials: Mechanistic Insights from Atomistic Simulations. *Energy Environ. Sci.* **2011**, *4* (8), 2774. <https://doi.org/10.1039/c0ee00717j>.
- (22) Jung, W.; Dereux, J. O.; Chueh, W. C.; Hao, Y.; Haile, S. M. High Electrode Activity of Nanostructured, Columnar Ceria Films for Solid Oxide Fuel Cells. *Energy Environ. Sci.* **2012**, *5* (9), 8682–8689. <https://doi.org/10.1039/c2ee22151a>.
- (23) Chueh, W. C.; Hao, Y.; Jung, W.; Haile, S. M. High Electrochemical Activity of the Oxide Phase in Model Ceria-Pt and Ceria-Ni Composite Anodes. *Nat. Mater.* **2012**, *11* (2), 155–161. <https://doi.org/10.1038/nmat3184>.
- (24) De Vero, J. C.; Bagarinao, K. D.; Kishimoto, H.; Ishiyama, T.; Yamaji, K.; Horita, T.; Yokokawa, H. Effect of Gd-Doped Ceria Interlayer Microstructure on the Interdiffusion Behavior Between  $\text{La}_{0.6}\text{Sr}_{0.4}\text{Co}_{0.2}\text{Fe}_{0.8}\text{O}_{3-\delta}$  Cathodes and Ytria-Stabilized Zirconia Electrolytes. *ECS Trans.* **2017**, *78* (1), 971–981. <https://doi.org/10.1149/07801.0971ecst>.
- (25) Bernadet, L.; Baiutti, F.; Martinelli, F.; Torrell, M.; Morata, A.; Montinaro, D.; Tarancón, A. Thin Film Barrier Layers with Increased Performance and Reduced Long-Term Degradation in SOFCs. *ECS Trans.* **2021**, *103* (1), 1177–1185. <https://doi.org/10.1149/10301.1177ecst>.

- (26) Knibbe, R.; Hjelm, J.; Menon, M.; Pryds, N.; Søgaard, M.; Wang, H. J.; Neufeld, K. Cathode-Electrolyte Interfaces with CGO Barrier Layers in SOFC: Cathode-Electrolyte Interfaces in IT-SOFCs. *J. Am. Ceram. Soc.* **2010**, *93* (9), 2877–2883. <https://doi.org/10.1111/j.1551-2916.2010.03763.x>.
- (27) Murray, E. P.; Barnett, S. A. (La,Sr)MnO<sub>3</sub>-(Ce,Gd)O<sub>2-x</sub> Composite Cathodes for Solid Oxide Fuel Cells. *Solid State Ion.* **2001**, *143* (3–4), 265–273. [https://doi.org/10.1016/S0167-2738\(01\)00871-2](https://doi.org/10.1016/S0167-2738(01)00871-2).
- (28) Druce, J.; Téllez, H.; Ishihara, T.; Kilner, J. A. Oxygen Exchange and Transport in Dual Phase Ceramic Composite Electrodes. *Faraday Discuss.* **2015**, *182*, 271–288. <https://doi.org/10.1039/C5FD00028A>.
- (29) Al-Shakarchi, E. K.; Mahmood, N. B. Three Techniques Used to Produce BaTiO<sub>3</sub> Fine Powder. *J. Mod. Phys.* **2011**, *02* (11), 1420–1428. <https://doi.org/10.4236/jmp.2011.211175>.
- (30) Artini, C.; Pani, M.; Carnasciali, M. M.; Buscaglia, M. T.; Plaisier, J. R.; Costa, G. A. Structural Features of Sm- and Gd-Doped Ceria Studied by Synchrotron X-Ray Diffraction and  $\mu$ -Raman Spectroscopy. *Inorg. Chem.* **2015**, *54* (8), 4126–4137. <https://doi.org/10.1021/acs.inorgchem.5b00395>.
- (31) Jiang, S. P. Issues on Development of (La,Sr)MnO<sub>3</sub> Cathode for Solid Oxide Fuel Cells. *J. Power Sources* **2003**, *124* (2), 390–402. [https://doi.org/10.1016/S0378-7753\(03\)00814-0](https://doi.org/10.1016/S0378-7753(03)00814-0).
- (32) Hart, N. T.; Brandon, N. P. Functionally Graded Cathodes for Solid Oxide Fuel Cells. *J. Mater. Sci.* **2001**, *36*, 1077–1085.
- (33) Jørgensen, M. J.; Mogensen, M. Impedance of Solid Oxide Fuel Cell LSM/YSZ Composite Cathodes. *J. Electrochem. Soc.* **2001**, *148* (5), A433. <https://doi.org/10.1149/1.1360203>.
- (34) Takeda, Y.; Kanno, R.; Noda, M.; Yamamoto, O. Perovskite Electrodes for High Temperature Solid Electrolyte Fuel Cells. *Bull. Inst. Chem. Res.* **1986**, *64* (4).
- (35) Lu, Z.; Darvish, S.; Hardy, J.; Templeton, J.; Stevenson, J.; Zhong, Y. SrZrO<sub>3</sub> Formation at the Interlayer/Electrolyte Interface during (La<sub>1-x</sub>Sr<sub>x</sub>)<sub>1- $\delta$</sub> Co<sub>1-y</sub>Fe<sub>y</sub>O<sub>3</sub> Cathode Sintering. *J. Electrochem. Soc.* **2017**, *164* (10), F3097–F3103. <https://doi.org/10.1149/2.0141710jes>.
- (36) Willy Poulsen, F.; van der Puil, N. Phase Relations and Conductivity of Sr- and La-Zirconates. *Solid State Ion.* **1992**, *53–56*, 777–783. [https://doi.org/10.1016/0167-2738\(92\)90254-M](https://doi.org/10.1016/0167-2738(92)90254-M).
- (37) Setoguchi, T.; Okamoto, K.; Eguchi, K.; Arai, H. Effects of Anode Material and Fuel on Anodic Reaction of Solid Oxide Fuel Cells. *J. Electrochem. Soc.* **1992**, *139* (10), 2875–2880. <https://doi.org/10.1149/1.2068998>.
- (38) Kan, W. H.; Samson, A. J.; Thangadurai, V. Trends in Electrode Development for next Generation Solid Oxide Fuel Cells. *J. Mater. Chem. A* **2016**, *4* (46), 17913–17932. <https://doi.org/10.1039/C6TA06757C>.
- (39) Matsuzaki, Y. The Poisoning Effect of Sulfur-Containing Impurity Gas on a SOFC Anode: Part I. Dependence on Temperature, Time, and Impurity Concentration. *Solid State Ion.* **2000**, *132* (3–4), 261–269. [https://doi.org/10.1016/S0167-2738\(00\)00653-6](https://doi.org/10.1016/S0167-2738(00)00653-6).
- (40) Jung, W.; Gu, K. L.; Choi, Y.; Haile, S. M. Robust Nanostructures with Exceptionally High Electrochemical Reaction Activity for High Temperature Fuel Cell Electrodes. *Energy Environ. Sci.* **2014**, *7* (5), 1685–1692. <https://doi.org/10.1039/c3ee43546f>.

- (41) Joo, J. H.; Choi, G. M. Electrical Conductivity of Thin Film Ceria Grown by Pulsed Laser Deposition. *J. Eur. Ceram. Soc.* **2007**, *27* (13–15), 4273–4277. <https://doi.org/10.1016/j.jeurceramsoc.2007.02.135>.
- (42) Skutina, L.; Filonova, E.; Medvedev, D.; Maignan, A. Undoped Sr<sub>2</sub>MMoO<sub>6</sub> Double Perovskite Molybdates (M = Ni, Mg, Fe) as Promising Anode Materials for Solid Oxide Fuel Cells. *Materials* **2021**, *14* (7), 1715. <https://doi.org/10.3390/ma14071715>.
- (43) Xu, Z.; Hu, X.; Wan, Y.; Xue, S.; Zhang, S.; Zhang, L.; Zhang, B.; Xia, C. Electrochemical Performance and Anode Reaction Process for Ca Doped Sr<sub>2</sub>Fe<sub>1.5</sub>Mo<sub>0.5</sub>O<sub>6-δ</sub> as Electrodes for Symmetrical Solid Oxide Fuel Cells. *Electrochimica Acta* **2020**, *341*, 136067. <https://doi.org/10.1016/j.electacta.2020.136067>.
- (44) Alvarado Flores, J. J.; Ávalos Rodríguez, M. L.; Alcaraz Vera, J. V.; Rutiaga Quiñones, J. G.; Guevara Martínez, S. J.; Zarraga, R. A. Advances in the Knowledge of the Double Perovskites Derived from the Conformation and Substitution of the Material Sr<sub>2</sub>MgMoO<sub>6-δ</sub> as Anode with Potential Application in SOFC Cell. *Int. J. Hydrog. Energy* **2021**, *46* (51), 26152–26162. <https://doi.org/10.1016/j.ijhydene.2021.03.030>.
- (45) Kumar, P.; Jena, P.; Patro, P. K.; Lenka, R. K.; Sinha, A. S. K.; Singh, P.; Singh, R. K. Influence of Lanthanum Doping on Structural and Electrical/Electrochemical Properties of Double Perovskite Sr<sub>2</sub>CoMoO<sub>6</sub> as Anode Materials for Intermediate-Temperature Solid Oxide Fuel Cells. *ACS Appl. Mater. Interfaces* **2019**, *11* (27), 24659–24667. <https://doi.org/10.1021/acsami.9b03481>.
- (46) Stanley, P.; Hussain, A. M.; Huang, Y.; Gritton, J. E.; Wachsman, E. D. Defect Chemistry and Oxygen Non-Stoichiometry in SrFe<sub>0.2</sub>Co<sub>0.4</sub>Mo<sub>0.4</sub>O<sub>3-δ</sub> Ceramic Oxide for Solid Oxide Fuel Cells. *Ionics* **2020**, *26*, 5641–5649. <https://doi.org/10.1007/s11581-020-03674-7>.
- (47) Vernoux, P.; Djurado, E.; Guillodo, M. Catalytic and Electrochemical Properties of Doped Lanthanum Chromites as New Anode Materials for Solid Oxide Fuel Cells. *J. Am. Ceram. Soc.* **2004**, *84* (10), 2289–2295. <https://doi.org/10.1111/j.1151-2916.2001.tb01004.x>.
- (48) Rohnke, M.; Falk, M.; Huber, A.-K.; Janek, J. Combining High Temperature Electrochemistry and Time of Flight Secondary Ion Mass Spectrometry: Quasi in Situ Study of Lanthanum Strontium Chromate Manganate Electrodes. *J. Power Sources* **2013**, *221*, 97–107. <https://doi.org/10.1016/j.jpowsour.2012.07.139>.
- (49) Tao, S.; Irvine, J. T. S. Synthesis and Characterization of (La<sub>0.75</sub>Sr<sub>0.25</sub>)Cr<sub>0.5</sub>Mn<sub>0.5</sub>O<sub>3-δ</sub>, a Redox-Stable, Efficient Perovskite Anode for SOFCs. *J. Electrochem. Soc.* **2004**, *151* (2), A252. <https://doi.org/10.1149/1.1639161>.
- (50) Zha, S.; Tsang, P.; Cheng, Z.; Liu, M. Electrical Properties and Sulfur Tolerance of La<sub>0.75</sub>Sr<sub>0.25</sub>Cr<sub>1-x</sub>Mn<sub>x</sub>O<sub>3</sub> under Anodic Conditions. *J. Solid State Chem.* **2005**, *178* (6), 1844–1850. <https://doi.org/10.1016/j.jssc.2005.03.027>.
- (51) Raffaele, R.; Anderson, H. U.; Sparlin, D. M.; Parris, P. E. Transport Anomalies in the High-Temperature Hopping Conductivity and Thermopower of Sr-Doped La(Cr,Mn)O<sub>3</sub>. *Phys. Rev. B* **1991**, *43* (10), 7991–7999. <https://doi.org/10.1103/physrevb.43.7991>.

- (52) Tao, S.; Irvine, J. T. S. Phase Transition in Perovskite Oxide  $\text{La}_{0.75}\text{Sr}_{0.25}\text{Cr}_{0.5}\text{Mn}_{0.5}\text{O}_{3-\delta}$  Observed by in Situ High-Temperature Neutron Powder Diffraction. *Chem. Mater.* **2006**, *18* (23), 5453–5460. <https://doi.org/10.1021/cm061413n>.
- (53) Raj, E.; Kilner, J.; Irvine, J. Oxygen Diffusion and Surface Exchange Studies on  $(\text{La}_{0.75}\text{Sr}_{0.25})_{0.95}\text{Cr}_{0.5}\text{Mn}_{0.5}\text{O}_{3-\delta}$ . *Solid State Ion.* **2006**, *177* (19–25), 1747–1752. <https://doi.org/10.1016/j.ssi.2006.04.011>.
- (54) Kharton, V. V.; Tsipis, E. V.; Marozau, I. P.; Viskup, A. P.; Frade, J. R.; Irvine, J. T. S. Mixed Conductivity and Electrochemical Behavior of  $(\text{La}_{0.75}\text{Sr}_{0.25})_{0.95}\text{Cr}_{0.5}\text{Mn}_{0.5}\text{O}_{3-\delta}$ . *Solid State Ion.* **2007**, *178* (1–2), 101–113. <https://doi.org/10.1016/j.ssi.2006.11.012>.
- (55) Zhang, S.; Wan, Y.; Xu, Z.; Xue, S.; Zhang, L.; Zhang, B.; Xia, C. Bismuth Doped  $\text{La}_{0.75}\text{Sr}_{0.25}\text{Cr}_{0.5}\text{Mn}_{0.5}\text{O}_{3-\delta}$  Perovskite as a Novel Redox-Stable Efficient Anode for Solid Oxide Fuel Cells. *J. Mater. Chem. A* **2020**, *8* (23), 11553–11563. <https://doi.org/10.1039/D0TA03328F>.
- (56) Jardiel, T.; Caldes, M. T.; Moser, F.; Hamon, J.; Gauthier, G.; Joubert, O. New SOFC Electrode Materials: The Ni-Substituted LSCM-Based Compounds  $(\text{La}_{0.75}\text{Sr}_{0.25})(\text{Cr}_{0.5}\text{Mn}_{0.5-x}\text{Ni}_x)\text{O}_{3-\delta}$  and  $(\text{La}_{0.75}\text{Sr}_{0.25})(\text{Cr}_{0.5-x}\text{Ni}_x\text{Mn}_{0.5})\text{O}_{3-\delta}$ . *Solid State Ion.* **2010**, *181* (19–20), 894–901. <https://doi.org/10.1016/j.ssi.2010.05.012>.
- (57) Lay, E.; Benamira, M.; Pirovano, C.; Gauthier, G.; Dessemond, L. Effect of Ce-Doping on the Electrical and Electrocatalytical Behavior of La/Sr Chromo-Manganite Perovskite as New SOFC Anode. *Fuel Cells* **2012**, *12* (2), 265–274. <https://doi.org/10.1002/fuce.201100070>.
- (58) Ruiz-Morales, J. C.; Canales-Vázquez, J.; Peña-Martínez, J.; López, D. M.; Núñez, P. On the Simultaneous Use of  $\text{La}_{0.75}\text{Sr}_{0.25}\text{Cr}_{0.5}\text{Mn}_{0.5}\text{O}_{3-\delta}$  as Both Anode and Cathode Material with Improved Microstructure in Solid Oxide Fuel Cells. *Electrochimica Acta* **2006**, *52* (1), 278–284. <https://doi.org/10.1016/j.electacta.2006.05.006>.
- (59) Lay, E.; Dessemond, L.; Gauthier, G. H. Synthesis and Characterization of  $\text{Ce}_x\text{Sr}_{1-x}\text{Cr}_{0.5}\text{Mn}_{0.5}\text{O}_{3-\delta}$  Perovskites as Anode Materials for Solid Oxide Fuel Cells (SOFC). *Electrochimica Acta* **2016**, *216*, 420–428. <https://doi.org/10.1016/j.electacta.2016.09.044>.
- (60) Fowler, D. E.; Haag, J. M.; Boland, C.; Bierschenk, D. M.; Barnett, S. A.; Poeppelmeier, K. R. Stable, Low Polarization Resistance Solid Oxide Fuel Cell Anodes:  $\text{La}_{1-x}\text{Sr}_x\text{Cr}_{1-x}\text{Fe}_x\text{O}_{3-\delta}$  ( $x = 0.2-0.67$ ). *Chem. Mater.* **2014**, *26* (10), 3113–3120. <https://doi.org/10.1021/cm500423n>.
- (61) Minh, N. Q. Ceramic Fuel Cells. *J. Am. Ceram. Soc.* **1993**, *76* (3), 563–588. <https://doi.org/10.1111/j.1151-2916.1993.tb03645.x>.
- (62) Ivers-Tiffée, E.; Weber, A.; Herbstritt, D. Materials and Technologies for SOFC-Components. *J. Eur. Ceram. Soc.* **2001**, *21* (10–11), 1805–1811. [https://doi.org/10.1016/S0955-2219\(01\)00120-0](https://doi.org/10.1016/S0955-2219(01)00120-0).
- (63) Wincewicz, K.; Cooper, J. Taxonomies of SOFC Material and Manufacturing Alternatives. *J. Power Sources* **2005**, *140* (2), 280–296. <https://doi.org/10.1016/j.jpowsour.2004.08.032>.
- (64) Zha, S.; Xia, C.; Meng, G. Effect of Gd (Sm) Doping on Properties of Ceria Electrolyte for Solid Oxide Fuel Cells. *J. Power Sources* **2003**, *115* (1), 44–48. [https://doi.org/10.1016/S0378-7753\(02\)00625-0](https://doi.org/10.1016/S0378-7753(02)00625-0).

- (65) Ishihara, T.; Shibayama, T.; Nishiguchi, H.; Takita, Y. Oxide Ion Conductivity in  $\text{La}_{0.8}\text{Sr}_{0.2}\text{Ga}_{0.8}\text{Mg}_{0.2-x}\text{Ni}_x\text{O}_3$  Perovskite Oxide and Application for the Electrolyte of Solid Oxide Fuel Cells. *J. Mater. Sci.* **2001**, *36*, 1125–1131. <https://doi.org/10.1023/A:1004821607054>.
- (66) Abraham, F.; Boivin, J.; Mairesse, G.; Nowogrocki, G. The Bimevox Series: A New Family of High Performances Oxide Ion Conductors. *Solid State Ion.* **1990**, *40–41*, 934–937. [https://doi.org/10.1016/0167-2738\(90\)90157-M](https://doi.org/10.1016/0167-2738(90)90157-M).
- (67) Steil, M.; Ratajczak, F.; Capoen, E.; Pirovano, C.; Vannier, R.; Mairesse, G. Thermal Stability and Preparation of Dense Membrane Ceramics of BIMEVOX. *Solid State Ion.* **2005**, *176* (29–30), 2305–2312. <https://doi.org/10.1016/j.ssi.2005.06.017>.
- (68) Ralph, J. M.; Schoeler, A. C.; Krumpelt, M. Materials for Lower Temperature Solid Oxide Fuel Cells. *J. Mater. Sci.* **2001**, *36* (5), 1161–1172. <https://doi.org/10.1023/A:1004881825710>.
- (69) Mahato, N.; Banerjee, A.; Gupta, A.; Omar, S.; Balani, K. Progress in Material Selection for Solid Oxide Fuel Cell Technology: A Review. *Prog. Mater. Sci.* **2015**, *72*, 141–337. <https://doi.org/10.1016/j.pmatsci.2015.01.001>.
- (70) Zarabi Golkhatmi, S.; Asghar, M. I.; Lund, P. D. A Review on Solid Oxide Fuel Cell Durability: Latest Progress, Mechanisms, and Study Tools. *Renew. Sustain. Energy Rev.* **2022**, *161*, 112339. <https://doi.org/10.1016/j.rser.2022.112339>.
- (71) De Vero, J. C.; Bagarinao, K. D.-; Ishiyama, T.; Kishimoto, H.; Yamaji, K.; Horita, T.; Yokokawa, H. Effect of  $\text{SrZrO}_3$  Formation at LSCF-Cathode/GDC-Interlayer Interfaces on the Electrochemical Properties of Solid Oxide Fuel Cells. *ECS Trans.* **2017**, *75* (42), 75–81. <https://doi.org/10.1149/07542.0075ecst>.
- (72) Jiang, S. P.; Zhen, Y. Mechanism of Cr Deposition and Its Application in the Development of Cr-Tolerant Cathodes of Solid Oxide Fuel Cells. *Solid State Ion.* **2008**, *179* (27–32), 1459–1464. <https://doi.org/10.1016/j.ssi.2008.01.006>.
- (73) Benson, S. J.; Waller, D.; Kilner, J. A. Degradation of  $\text{La}_{0.6}\text{Sr}_{0.4}\text{Fe}_{0.8}\text{Co}_{0.2}\text{O}_{3-\delta}$  in Carbon Dioxide and Water Atmospheres. *J. Electrochem. Soc.* **1999**, *146*, 1305. <https://doi.org/10.1149/1.1391762>.
- (74) Kubicek, M.; Limbeck, A.; Frömling, T.; Hutter, H.; Fleig, J. Relationship between Cation Segregation and the Electrochemical Oxygen Reduction Kinetics of  $\text{La}_{0.6}\text{Sr}_{0.4}\text{CoO}_{3-\delta}$  Thin Film Electrodes. *J. Electrochem. Soc.* **2011**, *158* (6), B727–B734. <https://doi.org/10.1149/1.3581114>.
- (75) Oh, D.; Gostovic, D.; Wachsman, E. D. Mechanism of  $\text{La}_{0.6}\text{Sr}_{0.4}\text{Co}_{0.2}\text{Fe}_{0.8}\text{O}_3$  Cathode Degradation. *J. Mater. Res.* **2012**, *27* (15), 1992–1999. <https://doi.org/10.1557/jmr.2012.222>.
- (76) Niania, M.; Podor, R.; Britton, T. B.; Li, C.; Cooper, S. J.; Svetkov, N.; Skinner, S.; Kilner, J. In Situ Study of Strontium Segregation in  $\text{La}_{0.6}\text{Sr}_{0.4}\text{Co}_{0.2}\text{Fe}_{0.8}\text{O}_{3-\delta}$  in Ambient Atmospheres Using High-Temperature Environmental Scanning Electron Microscopy. *J. Mater. Chem. A* **2018**, *6* (29), 14120–14135. <https://doi.org/10.1039/C8TA01341A>.
- (77) Dulli, H.; Dowben, P. A.; Liou, S.-H.; Plummer, E. W. Surface Segregation and Restructuring of Colossal-Magnetoresistant Manganese Perovskites  $\text{La}_{0.65}\text{Sr}_{0.35}\text{MnO}_3$ . *Phys. Rev. B* **2000**, *62* (22), R14629–R14632. <https://doi.org/10.1103/PhysRevB.62.R14629>.
- (78) Huber, A.-K.; Falk, M.; Rohnke, M.; Luerssen, B.; Amati, M.; Gregoratti, L.; Hesse, D.; Janek, J. In Situ Study of Activation and De-Activation of LSM Fuel Cell Cathodes –

- Electrochemistry and Surface Analysis of Thin-Film Electrodes. *J. Catal.* **2012**, *294*, 79–88. <https://doi.org/10.1016/j.jcat.2012.07.010>.
- (79) Sha, Z.; Cali, E.; Shen, Z.; Ware, E.; Kerherve, G.; Skinner, S. J. Significantly Enhanced Oxygen Transport Properties in Mixed Conducting Perovskite Oxides under Humid Reducing Environments. *Chem. Mater.* **2021**, *33* (21), 8469–8476. <https://doi.org/10.1021/acs.chemmater.1c02909>.
- (80) Sha, Z.; Shen, Z.; Cali, E.; Kilner, J. A.; Skinner, S. J. Understanding Surface Chemical Processes in Perovskite Oxide Electrodes. *J. Mater. Chem. A* **2023**, *11*, 5645–5659. <https://doi.org/10.1039/D3TA00070B>.
- (81) Kubicek, M.; Rupp, G. M.; Huber, S.; Penn, A.; Opitz, A. K.; Bernardi, J.; Stöger-Pollach, M.; Hutter, H.; Fleig, J. Cation Diffusion in  $\text{La}_{0.6}\text{Sr}_{0.4}\text{CoO}_{3-\delta}$  below 800 °C and Its Relevance for Sr Segregation. *Phys. Chem. Chem. Phys.* **2014**, *16* (6), 2715. <https://doi.org/10.1039/c3cp51906f>.
- (82) Kim, D.; Hunt, A.; Waluyo, I.; Yildiz, B. Cation Deficiency Enables Reversal of Dopant Segregation at Perovskite Oxide Surfaces under Anodic Potential. *J. Mater. Chem. A* **2023**, *11* (13), 7299–7313. <https://doi.org/10.1039/D2TA09118F>.
- (83) Tripković, Đ.; Küngas, R.; Mogensen, M. B.; Hendriksen, P. V. Surface Recrystallization – an Underestimated Phenomenon Affecting Oxygen Exchange Activity. *J. Mater. Chem. A* **2019**, *7* (19), 11782–11791. <https://doi.org/10.1039/C9TA02607J>.
- (84) Tripković, Đ.; Wang, J.; Küngas, R.; Mogensen, M. B.; Yildiz, B.; Hendriksen, P. V. Thermally Controlled Activation and Passivation of Surface Chemistry and Oxygen-Exchange Kinetics on a Perovskite Oxide. *Chem. Mater.* **2022**, *34* (4), 1722–1736. <https://doi.org/10.1021/acs.chemmater.1c03901>.
- (85) Riedl, C.; Siebenhofer, M.; Nenning, A.; Schmid, A.; Weiss, M.; Rameshan, C.; Limbeck, A.; Kubicek, M.; Opitz, A. K.; Fleig, J. *In Situ* Techniques Reveal the True Capabilities of SOFC Cathode Materials and Their Sudden Degradation Due to Omnipresent Sulfur Trace Impurities. *J. Mater. Chem. A* **2022**, *10* (28), 14838–14848. <https://doi.org/10.1039/D2TA03335F>.
- (86) Siebenhofer, M.; Haselmann, U.; Nenning, A.; Friedbacher, G.; Ewald Bumberger, A.; Wurster, S.; Artner, W.; Hutter, H.; Zhang, Z.; Fleig, J.; Kubicek, M. Surface Chemistry and Degradation Processes of Dense  $\text{La}_{0.6}\text{Sr}_{0.4}\text{CoO}_{3-\delta}$  Thin Film Electrodes. *J. Electrochem. Soc.* **2023**, *170* (1), 014501. <https://doi.org/10.1149/1945-7111/acada8>.
- (87) Feng, Z.; Yacoby, Y.; Gadre, M. J.; Lee, Y.-L.; Hong, W. T.; Zhou, H.; Biegalski, M. D.; Christen, H. M.; Adler, S. B.; Morgan, D.; Shao-Horn, Y. Anomalous Interface and Surface Strontium Segregation in  $(\text{La}_{1-y}\text{Sr}_y)_2\text{CoO}_{4\pm\delta}/\text{La}_{1-x}\text{Sr}_x\text{CoO}_{3-\delta}$  Heterostructured Thin Films. *J. Phys. Chem. Lett.* **2014**, *5* (6), 1027–1034. <https://doi.org/10.1021/jz500293d>.
- (88) la O', G. J.; Savinell, R. F.; Shao-Horn, Y. Activity Enhancement of Dense Strontium-Doped Lanthanum Manganite Thin Films under Cathodic Polarization: A Combined AES and XPS Study. *J. Electrochem. Soc.* **2009**, *156* (6), B771–B781. <https://doi.org/10.1149/1.3116228>.
- (89) Baharuddin, N. A.; Abdul Rahman, N. F.; Abd. Rahman, H.; Somalu, M. R.; Azmi, M. A.; Raharjo, J. Fabrication of High-quality Electrode Films for Solid Oxide Fuel Cell by



- Screen Printing: A Review on Important Processing Parameters. *Int. J. Energy Res.* **2020**, *44* (11), 8296–8313. <https://doi.org/10.1002/er.5518>.
- (90) Beckel, D.; Bieberle-Hütter, A.; Harvey, A.; Infortuna, A.; Muecke, U. P.; Prestat, M.; Rupp, J. L. M.; Gauckler, L. J. Thin Films for Micro Solid Oxide Fuel Cells. *J. Power Sources* **2007**, *173* (1), 325–345. <https://doi.org/10.1016/j.jpowsour.2007.04.070>.
- (91) Lee, Y. H.; Chang, I.; Cho, G. Y.; Park, J.; Yu, W.; Tanveer, W. H.; Cha, S. W. Thin Film Solid Oxide Fuel Cells Operating Below 600°C: A Review. *Int. J. Precis. Eng. Manuf.-Green Technol.* **2018**, *5* (3), 441–453. <https://doi.org/10.1007/s40684-018-0047-0>.
- (92) Wu, X.; Jiang, J.; Zhao, W.; Li, X.; Li, J. Two-Dimensional Temperature Distribution Estimation for a Cross-Flow Planar Solid Oxide Fuel Cell Stack. *Int. J. Hydrog. Energy* **2020**, *45* (3), 2257–2278. <https://doi.org/10.1016/j.ijhydene.2019.11.091>.
- (93) Gómez, S. Y.; Hotza, D. Current Developments in Reversible Solid Oxide Fuel Cells. *Renew. Sustain. Energy Rev.* **2016**, *61*, 155–174. <https://doi.org/10.1016/j.rser.2016.03.005>.
- (94) Mogensen, M. B. Materials for Reversible Solid Oxide Cells. *Curr. Opin. Electrochem.* **2020**, *21*, 265–273. <https://doi.org/10.1016/j.coelec.2020.03.014>.
- (95) Laurencin, J.; Hubert, M.; Sanchez, D. F.; Pylypko, S.; Morales, M.; Morata, A.; Morel, B.; Montinaro, D.; Lefebvre-Joud, F.; Siebert, E. Degradation Mechanism of  $\text{La}_{0.6}\text{Sr}_{0.4}\text{Co}_{0.2}\text{Fe}_{0.8}\text{O}_{3-\delta}$  /  $\text{Gd}_{0.1}\text{Ce}_{0.9}\text{O}_{2-\delta}$  Composite Electrode Operated under Solid Oxide Electrolysis and Fuel Cell Conditions. *Electrochimica Acta* **2017**, *241*, 459–476. <https://doi.org/10.1016/j.electacta.2017.05.011>.
- (96) Zamudio-García, J.; Caizán-Juanarena, L.; Porras-Vázquez, J. M.; Losilla, E. R.; Marrero-López, D. A Review on Recent Advances and Trends in Symmetrical Electrodes for Solid Oxide Cells. *J. Power Sources* **2022**, *520*, 230852. <https://doi.org/10.1016/j.jpowsour.2021.230852>.
- (97) Gupta, S.; Zhong, Y.; Mahapatra, M.; Singh, P. Processing and Electrochemical Performance of Manganese-Doped Lanthanum-Strontium Chromite in Oxidizing and Reducing Atmospheres. *Int. J. Hydrog. Energy* **2015**, *40* (39), 13479–13489. <https://doi.org/10.1016/j.ijhydene.2015.07.153>.
- (98) Zamudio-García, J.; Porras-Vázquez, J. M.; Losilla, E. R.; Marrero-López, D. Efficient Symmetrical Electrodes Based on  $\text{LaCrO}_3$  via Microstructural Engineering. *J. Eur. Ceram. Soc.* **2021**, *42* (1), 181–192. <https://doi.org/10.1016/j.jeurceramsoc.2021.09.059>.
- (99) Yoon, J.; Cho, S.; Kim, J.-H.; Lee, J.; Bi, Z.; Serquis, A.; Zhang, X.; Manthiram, A.; Wang, H. Vertically Aligned Nanocomposite Thin Films as a Cathode/Electrolyte Interface Layer for Thin-Film Solid Oxide Fuel Cells. *Adv. Funct. Mater.* **2009**, *19* (24), 3868–3873. <https://doi.org/10.1002/adfm.200901338>.
- (100) Morales, M.; Pesce, A.; Slodczyk, A.; Torrell, M.; Piccardo, P.; Montinaro, D.; Tarancón, A.; Morata, A. Enhanced Performance of Gadolinia-Doped Ceria Diffusion Barrier Layers Fabricated by Pulsed Laser Deposition for Large-Area Solid Oxide Fuel Cells. *ACS Appl. Energy Mater.* **2018**, *1* (5), 1955–1964. <https://doi.org/10.1021/acsaem.8b00039>.
- (101) Garbayo, I.; Pla, D.; Morata, A.; Fonseca, L.; Sabaté, N.; Tarancón, A. Full Ceramic Micro Solid Oxide Fuel Cells: Towards More Reliable MEMS Power Generators

- Operating at High Temperatures. *Energy Environ. Sci.* **2014**, 7 (11), 3617–3629. <https://doi.org/10.1039/c4ee00748d>.
- (102) Huang, H.; Nakamura, M.; Su, P.; Fasching, R.; Saito, Y.; Prinz, F. B. High-Performance Ultrathin Solid Oxide Fuel Cells for Low-Temperature Operation. *J. Electrochem. Soc.* **2007**, 154 (1), B20. <https://doi.org/10.1149/1.2372592>.
- (103) Evans, A.; Bieberle-Hütter, A.; Rupp, J. L. M.; Gauckler, L. J. Review on Microfabricated Micro-Solid Oxide Fuel Cell Membranes. *J. Power Sources* **2009**, 194 (1), 119–129. <https://doi.org/10.1016/j.jpowsour.2009.03.048>.
- (104) Navickas, E.; Huber, T. M.; Chen, Y.; Hetaba, W.; Holzlechner, G.; Rupp, G.; Stöger-Pollach, M.; Friedbacher, G.; Hutter, H.; Yildiz, B.; Fleig, J. Fast Oxygen Exchange and Diffusion Kinetics of Grain Boundaries in Sr-Doped LaMnO<sub>3</sub> Thin Films. *Phys. Chem. Chem. Phys.* **2015**, 17 (12), 7659–7669. <https://doi.org/10.1039/C4CP05421K>.
- (105) Chiabrera, F.; Garbayo, I.; Pla, D.; Burriel, M.; Wilhelm, F.; Rogalev, A.; Núñez, M.; Morata, A.; Tarancón, A. Unraveling Bulk and Grain Boundary Electrical Properties in La<sub>0.8</sub>Sr<sub>0.2</sub>Mn<sub>1-y</sub>O<sub>3±δ</sub> Thin Films. *APL Mater.* **2019**, 7 (1), 013205. <https://doi.org/10.1063/1.5054576>.
- (106) Rupp, G. M.; Téllez, H.; Druce, J.; Limbeck, A.; Ishihara, T.; Kilner, J.; Fleig, J. Surface Chemistry of La<sub>0.6</sub>Sr<sub>0.4</sub>CoO<sub>3-δ</sub> Thin Films and Its Impact on the Oxygen Surface Exchange Resistance. *J. Mater. Chem. A* **2015**, 3 (45), 22759–22769. <https://doi.org/10.1039/C5TA05279C>.
- (107) Zhang, Y.; Wen, Y.; Huang, K.; Nicholas, J. D. Atomic Layer Deposited Zirconia Overcoats as On-Board Strontium Getters for Improved Solid Oxide Fuel Cell Nanocomposite Cathode Durability. *ACS Appl. Energy Mater.* **2020**, 3 (4), 4057–4067. <https://doi.org/10.1021/acsaem.0c00558>.
- (108) Kubicek, M.; Cai, Z.; Ma, W.; Yildiz, B.; Hutter, H.; Fleig, J. Tensile Lattice Strain Accelerates Oxygen Surface Exchange and Diffusion in La<sub>1-x</sub>Sr<sub>x</sub>CoO<sub>3-δ</sub> Thin Films. *ACS Nano* **2013**, 7 (4), 3276–3286. <https://doi.org/10.1021/nn305987x>.
- (109) Baiutti, F.; Chiabrera, F.; Diercks, D.; Cavallaro, A.; Yedra, L.; López-Conesa, L.; Estradé, S.; Peiró, F.; Morata, A.; Aguadero, A.; Tarancón, A. Direct Measurement of Oxygen Mass Transport at the Nanoscale. *Adv. Mater.* **2021**, 33 (48), 2105622. <https://doi.org/10.1002/adma.202105622>.
- (110) Shim, J. H.; Han, G. D.; Choi, H. J.; Kim, Y.; Xu, S.; An, J.; Kim, Y. B.; Graf, T.; Schladt, T. D.; Gür, T. M.; Prinz, F. B. Atomic Layer Deposition for Surface Engineering of Solid Oxide Fuel Cell Electrodes. *Int. J. Precis. Eng. Manuf.-Green Technol.* **2019**, 6 (3), 629–646. <https://doi.org/10.1007/s40684-019-00092-7>.
- (111) dos Santos-Gómez, L.; Sanna, S.; Norby, P.; Pryds, N.; Losilla, E. R.; Marrero-López, D.; Esposito, V. Electrochemical Stability of (La,Sr)CoO<sub>3-δ</sub> in (La,Sr)CoO<sub>3-δ</sub>/(Ce,Gd)O<sub>2-δ</sub> Heterostructures. *Nanoscale* **2019**, 11 (6), 2916–2924. <https://doi.org/10.1039/C8NR08528E>.
- (112) Develos-Bagarinao, K.; De Vero, J.; Kishimoto, H.; Ishiyama, T.; Yamaji, K.; Horita, T.; Yokokawa, H. Multilayered LSC and GDC: An Approach for Designing Cathode Materials with Superior Oxygen Exchange Properties for Solid Oxide Fuel Cells. *Nano Energy* **2018**, 52, 369–380. <https://doi.org/10.1016/j.nanoen.2018.08.014>.

- (113) Ma, W.; Kim, J. J.; Tsvetkov, N.; Daio, T.; Kuru, Y.; Cai, Z.; Chen, Y.; Sasaki, K.; Tuller, H. L.; Yildiz, B. Vertically Aligned Nanocomposite  $\text{La}_{0.8}\text{Sr}_{0.2}\text{CoO}_3/(\text{La}_{0.5}\text{Sr}_{0.5})_2\text{CoO}_4$  Cathodes – Electronic Structure, Surface Chemistry and Oxygen Reduction Kinetics. *J. Mater. Chem. A* **2015**, *3* (1), 207–219. <https://doi.org/10.1039/C4TA04993D>.
- (114) Lee, S.; MacManus-Driscoll, J. L. Research Update: Fast and Tunable Nanoionics in Vertically Aligned Nanostructured Films. *APL Mater.* **2017**, *5* (4), 042304. <https://doi.org/10.1063/1.4978550>.
- (115) MacManus-Driscoll, J. L.; Suwardi, A.; Wang, H. Composite Epitaxial Thin Films: A New Platform for Tuning, Probing, and Exploiting Mesoscale Oxides. *MRS Bull.* **2015**, *40* (11), 933–942. <https://doi.org/10.1557/mrs.2015.258>.
- (116) Chen, A.; Su, Q.; Han, H.; Enriquez, E.; Jia, Q. Metal Oxide Nanocomposites: A Perspective from Strain, Defect, and Interface. *Adv. Mater.* **2019**, *31* (4), 1803241. <https://doi.org/10.1002/adma.201803241>.
- (117) Su, Q.; Yoon, D.; Chen, A.; Khatkhatay, F.; Manthiram, A.; Wang, H. Vertically Aligned Nanocomposite Electrolytes with Superior Out-of-Plane Ionic Conductivity for Solid Oxide Fuel Cells. *J. Power Sources* **2013**, *242*, 455–463. <https://doi.org/10.1016/j.jpowsour.2013.05.137>.
- (118) Develos-Bagarinao, K.; Ishiyama, T.; Kishimoto, H.; Shimada, H.; Yamaji, K. Nanoengineering of Cathode Layers for Solid Oxide Fuel Cells to Achieve Superior Power Densities. *Nat. Commun.* **2021**, *12* (1), 3979. <https://doi.org/10.1038/s41467-021-24255-w>.
- (119) Chueh, W. C.; Haile, S. M. Electrochemical Studies of Capacitance in Cerium Oxide Thin Films and Its Relationship to Anionic and Electronic Defect Densities. *Phys. Chem. Chem. Phys.* **2009**, *11* (37), 8144–8148. <https://doi.org/10.1039/b910903j>.
- (120) Burnat, D.; Nasdaurk, G.; Holzer, L.; Kopecki, M.; Heel, A. Lanthanum Doped Strontium Titanate - Ceria Anodes: Deconvolution of Impedance Spectra and Relationship with Composition and Microstructure. *J. Power Sources* **2018**, *385*, 62–75. <https://doi.org/10.1016/j.jpowsour.2018.03.024>.
- (121) Park, J. H.; Lee, J.-H.; Yoon, K. J.; Kim, H.; Ji, H.-I.; Yang, S.; Park, S.; Han, S. M.; Son, J.-W. A Nanoarchitected Cermet Composite with Extremely Low Ni Content for Stable High-Performance Solid Oxide Fuel Cells. *Acta Mater.* **2021**, *206*, 116580. <https://doi.org/10.1016/j.actamat.2020.116580>.
- (122) Rath, M. K.; Choi, B.-H.; Lee, K.-T. Properties and Electrochemical Performance of  $\text{La}_{0.75}\text{Sr}_{0.25}\text{Cr}_{0.5}\text{Mn}_{0.5}\text{O}_{3-\delta}$ - $\text{La}_{0.2}\text{Ce}_{0.8}\text{O}_{2-\delta}$  Composite Anodes for Solid Oxide Fuel Cells. *J. Power Sources* **2012**, *213*, 55–62. <https://doi.org/10.1016/j.jpowsour.2012.03.105>.
- (123) He, S.; Chen, H.; Li, R.; Ge, L.; Guo, L. Effect of  $\text{Ce}_{0.8}\text{Sm}_{0.2}\text{O}_{1.9}$  Interlayer on the Electrochemical Performance of  $\text{La}_{0.75}\text{Sr}_{0.25}\text{Cr}_{0.5}\text{Mn}_{0.5}\text{O}_{3-\delta}$ - $\text{Ce}_{0.8}\text{Sm}_{0.2}\text{O}_{1.9}$  Composite Anodes for Intermediate-Temperature Solid Oxide Fuel Cells. *J. Power Sources* **2014**, *253*, 187–192. <https://doi.org/10.1016/j.jpowsour.2013.12.071>.
- (124) Noh, H.-S.; Son, J.-W.; Lee, H.; Song, H.-S.; Lee, H.-W.; Lee, J.-H. Low Temperature Performance Improvement of SOFC with Thin Film Electrolyte and Electrodes Fabricated by Pulsed Laser Deposition. *J. Electrochem. Soc.* **2009**, *156* (12), B1484. <https://doi.org/10.1149/1.3243859>.

- (125) Evans, A.; Martynczuk, J.; Stender, D.; Schneider, C. W.; Lippert, T.; Prestat, M. Low-Temperature Micro-Solid Oxide Fuel Cells with Partially Amorphous  $\text{La}_{0.6}\text{Sr}_{0.4}\text{CoO}_{3-\delta}$  Cathodes. *Adv. Energy Mater.* **2015**, *5* (1), 1400747. <https://doi.org/10.1002/aenm.201400747>.
- (126) Wells, M. P.; Lovett, A. J.; Chalklen, T.; Baiutti, F.; Tarancón, A.; Wang, X.; Ding, J.; Wang, H.; Kar-Narayan, S.; Acosta, M.; MacManus-Driscoll, J. L. Route to High-Performance Micro-Solid Oxide Fuel Cells on Metallic Substrates. *ACS Appl. Mater. Interfaces* **2021**, *13* (3), 4117–4125. <https://doi.org/10.1021/acsami.0c15368>.
- (127) Bianchini, M. Integration of Ceramic Thin Films in Silicon Technology for Energy Conversion and Oxygen Sensing, Universitat Autònoma de Barcelona, 2022.
- (128) Garbayo, I.; Dezanneau, G.; Bogicevic, C.; Santiso, J.; Gràcia, I.; Sabaté, N.; Tarancón, A. Pinhole-Free YSZ Self-Supported Membranes for Micro Solid Oxide Fuel Cell Applications. *Solid State Ion.* **2012**, *216*, 64–68. <https://doi.org/10.1016/j.ssi.2011.09.011>.
- (129) Li, Y.; Wang, S.; Su, P.-C. Proton-Conducting Micro-Solid Oxide Fuel Cells with Improved Cathode Reactions by a Nanoscale Thin Film Gadolinium-Doped Ceria Interlayer. *Sci. Rep.* **2016**, *6* (1), 22369. <https://doi.org/10.1038/srep22369>.
- (130) Baek, J. D.; Liu, K.-Y.; Su, P.-C. A Functional Micro-Solid Oxide Fuel Cell with a 10 Nm-Thick Freestanding Electrolyte. *J. Mater. Chem. A* **2017**, *5* (35), 18414–18419. <https://doi.org/10.1039/C7TA05245F>.
- (131) Lai, B.-K.; Kerman, K.; Ramanathan, S. Nanostructured  $\text{La}_{0.6}\text{Sr}_{0.4}\text{Co}_{0.8}\text{Fe}_{0.2}\text{O}_3/\text{Y}_{0.08}\text{Zr}_{0.92}\text{O}_{1.96}/\text{La}_{0.6}\text{Sr}_{0.4}\text{Co}_{0.8}\text{Fe}_{0.2}\text{O}_3$  (LSCF/YSZ/LSCF) Symmetric Thin Film Solid Oxide Fuel Cells. *J. Power Sources* **2011**, *196* (4), 1826–1832. <https://doi.org/10.1016/j.jpowsour.2010.09.066>.
- (132) Liu, R.; Li, X.; Lam, K. S. Combinatorial Chemistry in Drug Discovery. *Curr. Opin. Chem. Biol.* **2017**, *38*, 117–126. <https://doi.org/10.1016/j.cbpa.2017.03.017>.
- (133) Sun, X.; Vilar, S.; Tatonetti, N. P. High-Throughput Methods for Combinatorial Drug Discovery. *Sci. Transl. Med.* **2013**, *5* (205), 205rv1. <https://doi.org/10.1126/scitranslmed.3006667>.
- (134) Fonoll-Rubio, R.; Becerril-Romero, I.; Vidal-Fuentes, P.; Grau-Luque, E.; Atlan, F.; Perez-Rodriguez, A.; Izquierdo-Roca, V.; Guc, M. Combinatorial Analysis Methodologies for Accelerated Research: The Case of Chalcogenide Thin-Film Photovoltaic Technologies. *Sol. RRL* **2022**, *6* (9), 2200235. <https://doi.org/10.1002/solr.202200235>.
- (135) Muster, T. H.; Trinchi, A.; Markley, T. A.; Lau, D.; Martin, P.; Bradbury, A.; Bendavid, A.; Dligatch, S. A Review of High Throughput and Combinatorial Electrochemistry. *Electrochimica Acta* **2011**, *56* (27), 9679–9699. <https://doi.org/10.1016/j.electacta.2011.09.003>.
- (136) Xu, X.; Valavanis, D.; Ciocci, P.; Confederat, S.; Marcuccio, F.; Lemineur, J.-F.; Actis, P.; Kanoufi, F.; Unwin, P. R. The New Era of High-Throughput Nanoelectrochemistry. *Anal. Chem.* **2023**, *95* (1), 319–356. <https://doi.org/10.1021/acs.analchem.2c05105>.
- (137) Alberi, K.; Nardelli, M. B.; Zakutayev, A.; Mitas, L.; Curtarolo, S.; Jain, A.; Fornari, M.; Marzari, N.; Takeuchi, I.; Green, M. L.; Kanatzidis, M.; Toney, M. F.; Butenko, S.; Meredig, B.; Lany, S.; Kattner, U.; Davydov, A.; Toberer, E. S.; Stevanovic, V.; Walsh, A.;

- Park, N.-G.; Aspuru-Guzik, A.; Tabor, D. P.; Nelson, J.; Murphy, J.; Setlur, A.; Gregoire, J.; Li, H.; Xiao, R.; Ludwig, A.; Martin, L. W.; Rappe, A. M.; Wei, S.-H.; Perkins, J. The 2019 Materials by Design Roadmap. *J. Phys. Appl. Phys.* **2019**, *52* (1), 013001. <https://doi.org/10.1088/1361-6463/aad926>.
- (138) Saranya, A. M.; Morata, A.; Pla, D.; Burriel, M.; Chiabrera, F.; Garbayo, I.; Hornés, A.; Kilner, J. A.; Tarancón, A. Unveiling the Outstanding Oxygen Mass Transport Properties of Mn-Rich Perovskites in Grain Boundary-Dominated  $\text{La}_{0.8}\text{Sr}_{0.2}(\text{Mn}_{1-x}\text{Co}_x)_{0.85}\text{O}_{3\pm\delta}$  Nanostructures. *Chem. Mater.* **2018**, *30* (16), 5621–5629. <https://doi.org/10.1021/acs.chemmater.8b01771>.
- (139) Chiabrera, F.; Garbayo, I.; López-Conesa, L.; Martín, G.; Ruiz-Caridad, A.; Walls, M.; Ruiz-González, L.; Kordatos, A.; Núñez, M.; Morata, A.; Estradé, S.; Chronos, A.; Peiró, F.; Tarancón, A. Engineering Transport in Manganites by Tuning Local Nonstoichiometry in Grain Boundaries. *Adv. Mater.* **2019**, *31* (4), 1805360. <https://doi.org/10.1002/adma.201805360>.
- (140) Chiabrera, F. M.; Baiutti, F.; Börgers, J. M.; Harrington, G. F.; Yedra, L.; Liedke, M. O.; Kler, J.; Nandi, P.; Sirvent, J. de D.; Santiso, J.; López-Haro, M.; Calvino, J. J.; Estradé, S.; Butterling, M.; Wagner, A.; Peiró, F.; De Souza, R. A.; Tarancón, A. The Impact of Mn Nonstoichiometry on the Oxygen Mass Transport Properties of  $\text{La}_{0.8}\text{Sr}_{0.2}\text{Mn}_y\text{O}_{3\pm\delta}$  Thin Films. *J. Phys. Energy* **2022**, *4* (4), 044011. <https://doi.org/10.1088/2515-7655/ac98df>.
- (141) Papac, M. C.; Talley, K. R.; O'Hayre, R.; Zakutayev, A. Instrument for Spatially Resolved, Temperature-Dependent Electrochemical Impedance Spectroscopy of Thin Films under Locally Controlled Atmosphere. *Rev. Sci. Instrum.* **2021**, *92* (6), 065105. <https://doi.org/10.1063/5.0024875>.
- (142) Papac, M. C.; Huang, J.; Zakutayev, A.; O'Hayre, R. Combinatorial Impedance Spectroscopy with Bayesian Analysis for Triple Ionic-Electronic Conducting Perovskites. *J. Mater. Chem. A* **2023**, *11* (10), 5267–5278. <https://doi.org/10.1039/D2TA01736A>.
- (143) Huang, J.; Papac, M.; O'Hayre, R. Towards Robust Autonomous Impedance Spectroscopy Analysis: A Calibrated Hierarchical Bayesian Approach for Electrochemical Impedance Spectroscopy (EIS) Inversion. *Electrochimica Acta* **2021**, *367*, 137493. <https://doi.org/10.1016/j.electacta.2020.137493>.
- (144) Greeley, J. Theoretical Heterogeneous Catalysis: Scaling Relationships and Computational Catalyst Design. *Annu. Rev. Chem. Biomol. Eng.* **2016**, *7* (1), 605–635. <https://doi.org/10.1146/annurev-chembioeng-080615-034413>.
- (145) Lee, Y.-L.; Kleis, J.; Rossmeisl, J.; Shao-Horn, Y.; Morgan, D. Prediction of Solid Oxide Fuel Cell Cathode Activity with First-Principles Descriptors. *Energy Environ. Sci.* **2011**, *4* (10), 3966. <https://doi.org/10.1039/c1ee02032c>.
- (146) Giordano, L.; Akkiraju, K.; Jacobs, R.; Vivona, D.; Morgan, D.; Shao-Horn, Y. Electronic Structure-Based Descriptors for Oxide Properties and Functions. *Acc. Chem. Res.* **2022**, *55* (3), 298–308. <https://doi.org/10.1021/acs.accounts.1c00509>.
- (147) Butler, K. T.; Davies, D. W.; Cartwright, H.; Isayev, O.; Walsh, A. Machine Learning for Molecular and Materials Science. *Nature* **2018**, *559* (7715), 547–555. <https://doi.org/10.1038/s41586-018-0337-2>.

- (148) Barrett, D. H.; Haruna, A. Artificial Intelligence and Machine Learning for Targeted Energy Storage Solutions. *Curr. Opin. Electrochem.* **2020**, *21*, 160–166. <https://doi.org/10.1016/j.coelec.2020.02.002>.
- (149) Gu, G. H.; Noh, J.; Kim, I.; Jung, Y. Machine Learning for Renewable Energy Materials. *J. Mater. Chem. A* **2019**, *7* (29), 17096–17117. <https://doi.org/10.1039/C9TA02356A>.
- (150) Yang, K.; Liu, J.; Wang, Y.; Shi, X.; Wang, J.; Lu, Q.; Ciucci, F.; Yang, Z. Machine-Learning-Assisted Prediction of Long-Term Performance Degradation on Solid Oxide Fuel Cell Cathodes Induced by Chromium Poisoning. *J. Mater. Chem. A* **2022**, *10* (44), 23683–23690. <https://doi.org/10.1039/D2TA03944C>.



## 2. *Experimental Methods*



2.1 Introduction.....	43
2.2 Fabrication and processing.....	43
2.2.1 Deposition of thin films by physical methods.....	43
2.2.2 Combinatorial deposition of material libraries .....	45
2.2.3 Si-based devices: micro- and nanofabrication.....	48
2.3 Morphological and structural characterization techniques .....	50
2.3.1 Scanning Electron Microscopy .....	50
2.3.2 Transmission Electron Microscopy .....	51
2.3.3 X-Ray Diffraction.....	51
2.3.4 Atomic Force Microscopy .....	52
2.3.5 Spectroscopic Ellipsometry.....	53
2.4 Advanced characterization techniques.....	55
2.4.1 Low Energy Ion Scattering .....	55
2.4.2 X-Ray Photoelectron Spectroscopy .....	57
2.4.3 Tip Enhanced Raman Spectroscopy.....	58
2.4.4 Positron Annihilation Spectroscopy .....	59
2.4.4.1 Doppler Broadening Variable Energy Positron Annihilation Spectroscopy.....	60
2.4.4.2 Variable Energy Positron Annihilation Lifetime Spectroscopy .....	62
2.5 Functional characterization .....	63
2.5.1 In-plane conductivity measurements .....	63
2.5.2 Electrochemical Impedance Spectroscopy.....	64
2.5.2.1 Electrochemical characterization of thin film electrodes .....	64
2.5.2.2 Electrochemical characterization of thin film electrodes during thermal ageing in oxidizing conditions .....	69
2.5.3 Electrochemical characterization in full device architectures .....	69
2.5.3.1 Conceptualization of the measurement setup .....	69
2.5.3.2 Electrical characterization .....	72
2.6 Characterization tools for studying material libraries .....	72
2.6.1 High throughput X-Ray Fluorescence .....	72
2.6.2 High throughput X-Ray Diffraction.....	73
2.6.3 High throughput Spectroscopic Ellipsometry.....	74

2.6.4 Raman Spectroscopy .....	74
2.6.5 Electrochemical test station.....	75
2.6.6 Isotope Exchange Depth Profiling coupled with Secondary Ion Mass Spectrometry .....	79
References.....	83



## 2.1 Introduction

The goal of this chapter is to describe the experimental methodologies employed in the development of the work presented in this thesis. In Section 2.2 Pulsed Laser Deposition (PLD) is introduced as the main fabrication technique employed in this work. Section 2.3 describes the main characterization techniques utilized for studying the microstructural, crystallographic and chemical nature of the thin films under analysis. Surface analysis methods are described in Section 2.4. Section 2.5 is focused on describing the functional characterization techniques employed for studying the electrochemical activity of the materials under study and the performance of the devices tested during the thesis. Finally, Section 2.6 shows the collection of experimental techniques employed for the characterization of combinatorial libraries of materials following high throughput methodologies.

## 2.2 Fabrication and processing

### 2.2.1 Deposition of thin films by physical methods

The thin films studied in the present thesis have been deposited by PLD. PLD is a type of physical vapor deposition (PVD) technique in which the material to be deposited is ejected from a target material through high energy laser ablation. The interaction of the laser with the target results in plasma generation formed by the atoms ejected from the target material and the background gas. The plasma is generally referred as the PLD plume and is projected onto the sample substrate. The material atoms and molecules reaching the substrate rearrange to give form to the thin film deposited. The final microstructure and chemical nature of film depend on the conditions of the deposition. Some of the most critical parameters determining the result of a PLD deposition are listed in the following: substrate temperature, background gas species (e.g. O<sub>2</sub> or Ar) and partial pressure, laser fluency, pulse frequency, time of deposition, target-to-substrate distance and target material. Complex oxides might result in the deposition of secondary phases if the conditions are not properly controlled. Figure 2-1a shows a schematic of a PLD equipment with the most characteristic elements that are found in these systems.

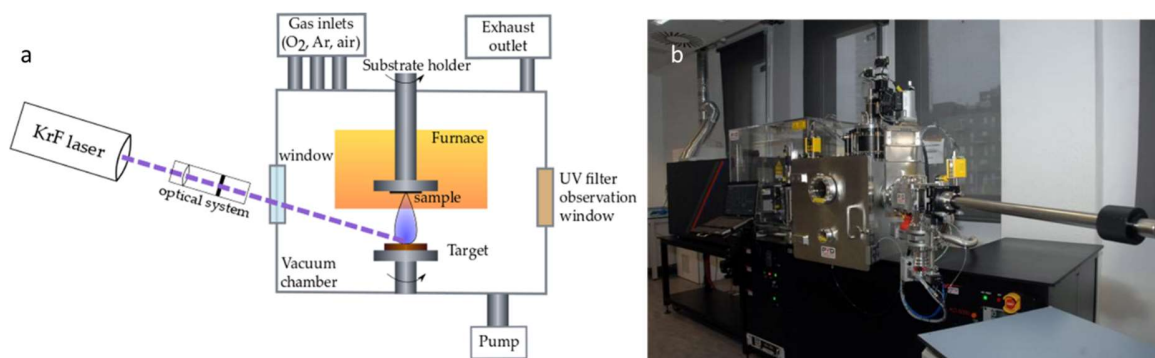


Figure 2-1. Schematic representation of PLD reproduced with permission from IOP Publishing<sup>1</sup> (a) and photograph of the large area PLD equipment utilised.

In this thesis a large area pulsed laser deposition equipment (LA-PLD) model 5000 from PVD Products (see Figure 2-1b) located at IREC has been used for the fabrication of thin films deposited on top of single crystal substrates, either in chip or in wafer form. A brief description of the targets employed for the depositions made during the development of this thesis are described in the following:

- For the work presented in Chapter 3, home-made targets were obtained by mixing commercial powders of  $\text{La}_{0.75}\text{Sr}_{0.25}\text{Cr}_{0.5}\text{Mn}_{0.5}\text{O}_3$  (LSCrMn) and  $\text{Ce}_{0.8}\text{Sm}_{0.2}\text{O}_2$  (SDC) (1:1 wt. % - Kceracell) via ball milling in ethanol solution. The dried powder mix was uniaxially pressed (7 MPa, 30 s) to form a pellet (diameter  $\approx$  1 inch). Sintering was carried out at 1300 °C for 4 hours (heating and cooling ramps  $\approx$  5 °C/min). These targets were employed for the fabrication of LSCrMn and LSCrMn-SDC films studied. Additionally, commercial targets of SDC,  $\text{Ce}_{0.8}\text{Gd}_{0.2}\text{O}_2$  (CGO) and  $\text{NiO}:\text{Ce}_{0.9}\text{Gd}_{0.1}\text{O}_2$  (NiCGO) –3.5 vol% of NiO– have been employed for the deposition of the ceria-based electrodes studied.
- For the work presented in Chapter 4, commercial targets of  $\text{La}_{0.8}\text{Sr}_{0.2}\text{CoO}_3$  (LSC),  $\text{La}_{0.8}\text{Sr}_{0.2}\text{FeO}_3$  (LSF),  $\text{La}_{0.8}\text{Sr}_{0.2}\text{MnO}_3$  (LSM) and CGO have been employed for the deposition of the thin films.
- For the work presented in Chapter 5, commercial targets of  $\text{La}_{0.8}\text{Sr}_{0.2}\text{CoO}_3$  (LSC82),  $\text{La}_{0.6}\text{Sr}_{0.4}\text{CoO}_3$  (LSC64),  $\text{La}_{0.9}\text{Sr}_{0.1}\text{CrO}_3$  (LSCr), CGO, SDC and  $(\text{ZrO}_2)_{0.97}(\text{Y}_2\text{O}_3)_{0.03}$  (3YSZ) have been employed for the deposition of the materials employed in the solid oxide cell (SOC) and micro solid oxide fuel cell ( $\mu$ SOFC) devices fabricated.

During the development of this thesis, the conditions set for PLD deposition have been varied depending on the motivation of each research line. Nevertheless, some generalized conditions were defined. Given that all of the materials studied in this work have been oxides, oxygen was employed as the background gas for every deposition made. The partial pressure was set to 5 mTorr for depositing dense thin films, while higher partial pressures in the 150-200 mTorr range were employed for the deposition of porous materials. Similarly, dense electrodes were always deposited in the 700-800 °C temperature range, while lower

temperatures were set for materials with higher porosity. All porous materials and single dense films were ablated at a frequency of 10 Hz, while the dense nanocomposites studied were deposited at 2 Hz and with no rotation of the substrate. The laser fluency employed was always in the range of 0.5-1 J·cm<sup>-2</sup>.

### 2.2.2 Combinatorial deposition of material libraries

Thin film material libraries have been fabricated by combinatorial PLD. This deposition technique has been previously utilized in the group for the study of the binary system La<sub>0.8</sub>Sr<sub>0.2</sub>Mn<sub>x</sub>Co<sub>1-x</sub>O<sub>3</sub><sup>2</sup> (LSMC) and for investigating LSM cathodes with variation in the nominal stoichiometry of the Mn site<sup>3,4</sup>. In the present work, further advances in the technique have been achieved, with the goal to extend its application to the study of more complex geometries based in ternary material libraries. The main principle behind the technique consists in the alternated deposition of ultrathin layers of two (or more) materials for a number of cycles. The multilayered structure undergoes cationic intermixing in-situ due to the high processing temperature, resulting in the formation of a single phase film. The composition of the layer deposited presents a gradient derived from the partial overlap in-plane between the plume positions and can be tuned depending on the relative position, shape of the plumes and amount of single material deposited for each cycle. In this thesis, combinatorial PLD has been employed for the fabrication of a La<sub>0.8</sub>Sr<sub>0.2</sub>Mn<sub>x</sub>Co<sub>y</sub>Fe<sub>1-x-y</sub>O<sub>3</sub> (LSMCF) perovskite film obtained by sequential ablation of targets of LSC, LSF and LSM, as depicted in Figure 2-2.

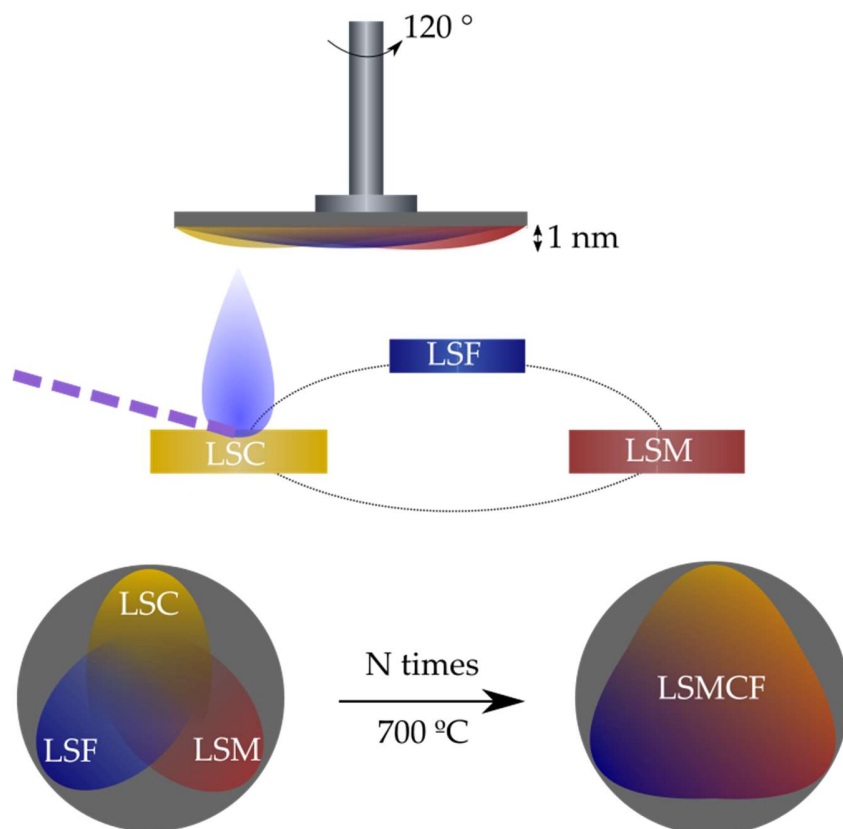


Figure 2-2. Schematic representation of the deposition process of a combinatorial thin film of LSMCF.

The total number of pulses applied to each target in a single cycle were adjusted to deposit an approximate layer of 1 nm of thickness in the maximum position of the PLD plume, for each parent material. The radial separation between the maximum of each plume on the wafer substrate was  $120^\circ$ . The final thickness of the film was controlled by adjusting the number of cycles of the deposition. For that, the plume of each parent compound had to be studied preliminarily. Figure 2-3a-c shows the deposition of each plume of LSM, LSF and LSC, respectively.



Figure 2-3. Deposition of ceramic perovskites on Si (100) wafers: LSM, LSF, and LSC, respectively (a-c).

For the development of the work presented in Chapter 4, combinatorial LSMCF films were deposited into different substrates. The wafers employed had the following characteristics: 3" yttria-stabilized zirconia (YSZ) with composition  $(\text{ZrO}_2)_{0.92}(\text{Y}_2\text{O}_3)_{0.08}$  (8YSZ) (100), 10 cm diameter Si (100) and 3" Si (100) single crystal substrates. In the case of the depositions on YSZ, a large area buffer interlayer of CGO was deposited, in order to avoid undesired reactions at the interface. The large area CGO layer deposition differed to single plume depositions in two particular aspects. First, in order to maximize the thickness homogeneity the substrate was rotated at 10 rpm and secondly, the position of the laser spot on the target was rastered. This procedure maximized the coverage of the plume along the wafer. Figure 2-4a shows an example of this large area CGO layers deposited on Si. Once the parameters were optimized and set the successful deposition of LSMCF combinatorial films like the one shown in Figure 2-4b was achieved.

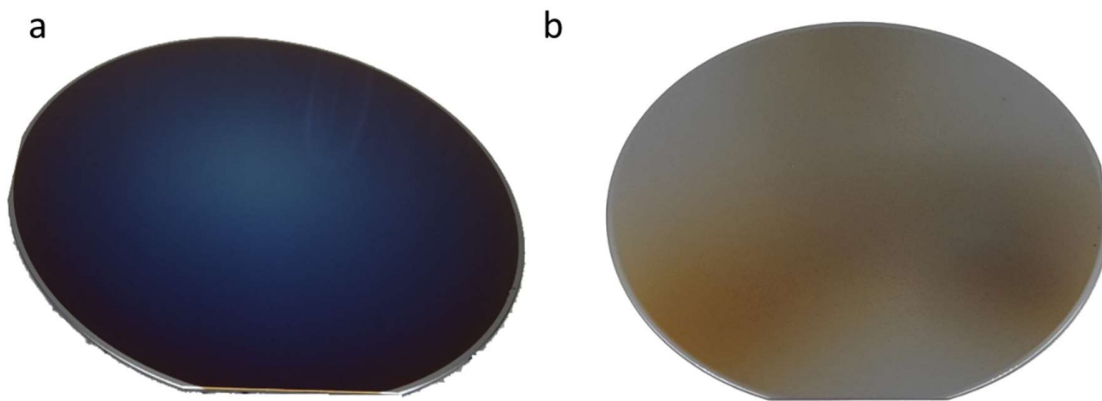


Figure 2-4. Deposition of a large area CGO film (a) and LSMCF combinatorial layer (b) on Si (100) substrates.

Some of the characterization techniques and analyses planned for the LSMCF combinatorial system required of some post post-processing of the films. This is the case of the films deposited on top of YSZ single crystal substrates. In order to be able to electrically contact individual areas of the film (see Section 2.6.5) and avoid influence of surrounding areas with different stoichiometry, the film was scribed with a custom made diamond cutter coupled to an automated robocasting equipment (see Figure 2-5a). Additionally, for the studies on the evolution on degradation of LSMCF combinatorial films presented in Chapter 4, it was required to analyze the films on a chip level. To do so, a DISCO DAD322 automatic dicing saw machine was employed to cut the wafer in  $10 \times 10 \text{ mm}^2$  samples, as it can be observed in Figure 2-5b.



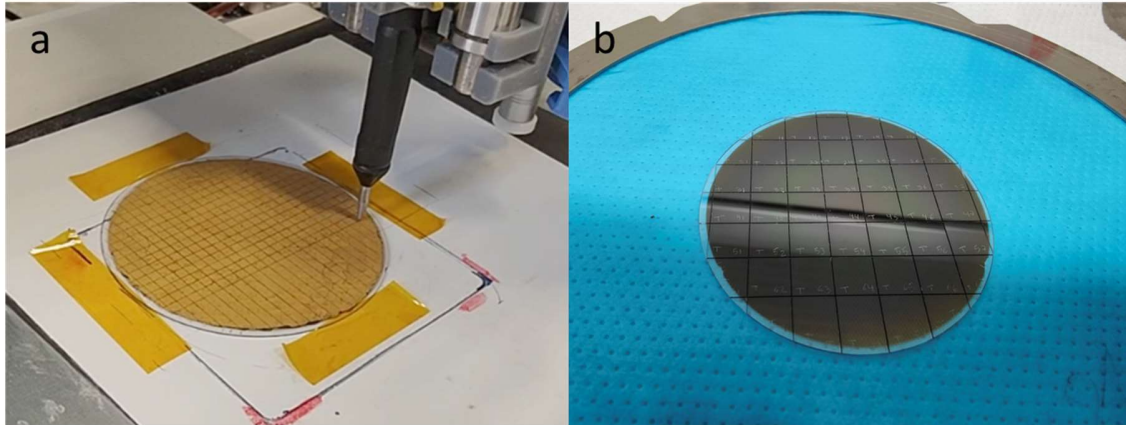


Figure 2-5. Photographs of post-processed combinatorial wafers deposited on YSZ single crystal substrates after different methods: automated scribing procedure (a) and wafer cut in individual chips with a dicing saw.

### 2.2.3 Si-based devices: micro- and nanofabrication

Part of the work carried out in this thesis has focused on the fabrication of SOC devices integrated with silicon technologies. Fabrication of the functional microdevice has been carried out at the IMB-CNM clean room facilities. Figure 2-6 shows a schematic of the different microfabrication processes involved in the fabrication of the  $\mu$ SOFCs studied in this thesis. The substrate selected was a 10 cm Si (100) single crystal wafer. First, a 100 nm  $\text{SiO}_2$  layer followed by a 300 nm  $\text{Si}_3\text{N}_4$  layer was fabricated by Plasma Laser Chemical Vapor Deposition (PLCVD) on both sides of the wafer.

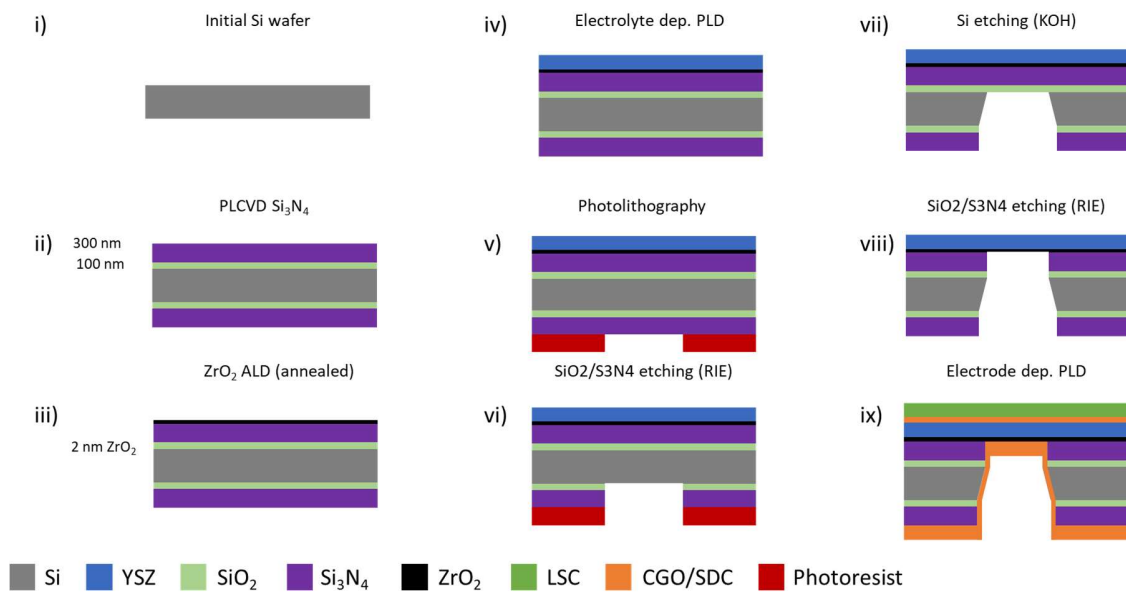


Figure 2-6. Schematic of the processes involved in the fabrication of the  $\mu$ SOFC.

In order to prevent pinhole formation during the fabrication of the ceramic layers, a 20 nm layer of  $ZrO_2$  was deposited next by Atomic Layer Deposition (ALD). Next, the electrolyte layer of 3YSZ was deposited by PLD (see Figure 2-7a-b). Once the electrolyte was deposited, a photoresist was patterned by photolithography (Karl Süss MA6) in the back side with the membranes design (i.e. squared patterns with a side length of 200 to 800  $\mu m$ ). In the regions with the remaining exposed area, the  $Si_3N_4/SiO_2$  bilayer was etched by reactive ion etching (RIE). Subsequently, Si was anisotropically removed by KOH wet etching with a 40% solution at 80 °C. An additional RIE step allowed to release the ceramic layers of the membrane from the substrate. Prior to the deposition of the electrode layers, the wafer was cut into individual chip samples. For that, a micro-resist was applied on top of the wafer, in order to add mechanical stability to the membranes. The micro-resist was spin coated on the wafer, and then cured in a hot plate at 175 °C for 30 min. The wafer was then cut with the DISCO dicing saw machine previously mentioned. Finally, the wafer was placed in a solution with acetone in order to remove the photoresist and free the chips from the blue tape employed to cut the wafer. Figure 2-7c-d show the state of the wafer after the cut and the placement of the chips in the organic solution, respectively. Finally, the chips were rinsed in isopropanol and water solutions sequentially in order to remove any remaining organic residue.

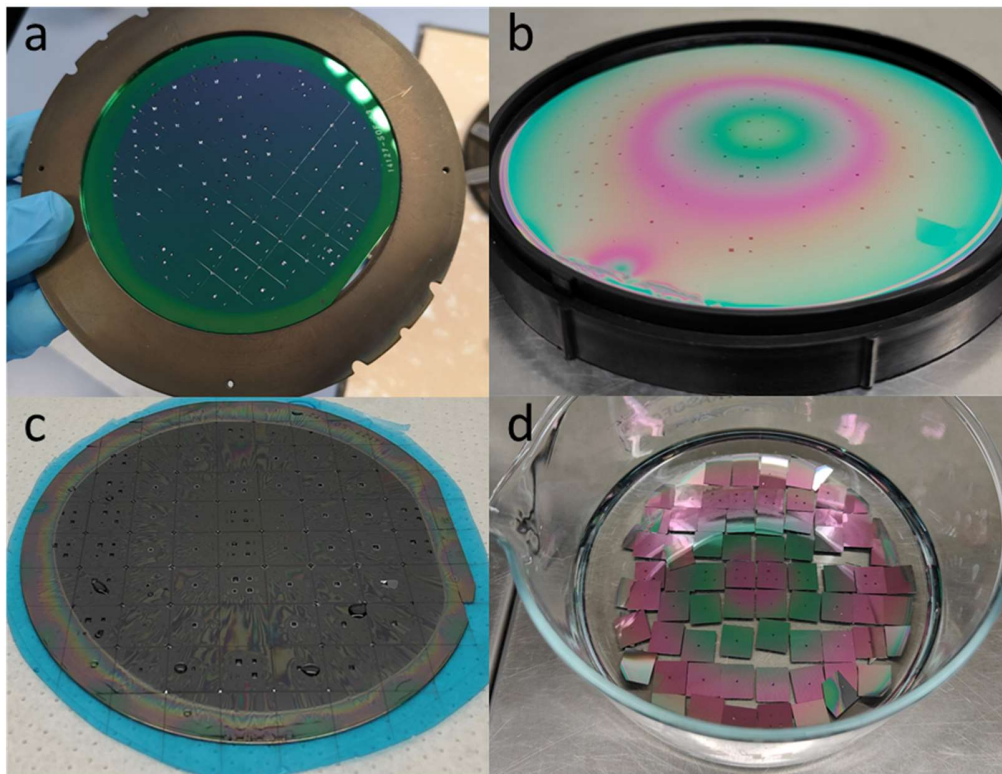
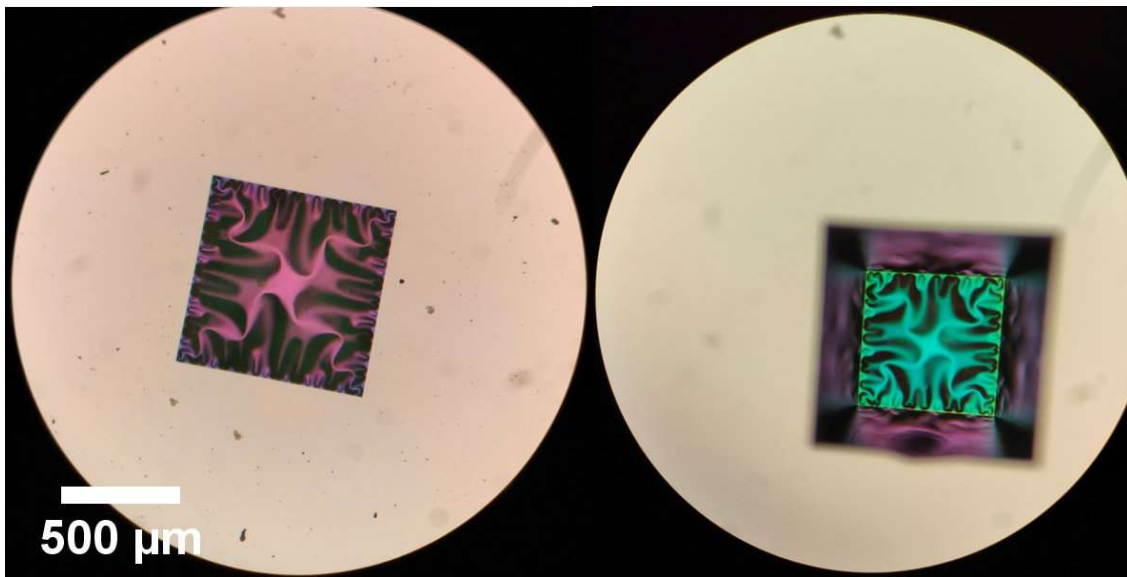


Figure 2-7. Different steps of the fabrication of  $\mu SOFCs$ : Pictures of the wafer placed in the PLD sample holder (backside shown) before the deposition of the 3YSZ electrolyte (a), top-side after the

*deposition (b), right after cutting the wafer into individual chips (c) and chip membranes being separated immersed in acetone solution (d).*

The structural state of the membranes after the whole microfabrication and cut processes were checked by optical microscopy, as shown in Figure 2-8. As it can be observed, completely released membranes were successfully fabricated with the procedure employed. It should be noted that the optimization of the microfabrication process had been investigated previously in the group<sup>5-7</sup> and that minor adjustments related to the etching exposure time were needed for the proper release of the ceramic membranes studied in this thesis.



*Figure 2-8. Optical micrographs of individual membranes fabricate from the top (left) and bottom (right) of the silicon chip.*

## 2.3 Morphological and structural characterization techniques

### 2.3.1 Scanning Electron Microscopy

Electron microscopies, and in particular scanning electron microscopy (SEM) have become an indispensable tool to be employed in materials science. The technique is based on the interaction of the electron beam with the sample, and the detection of the not transmitted electrons (i.e. secondary or backscattered electrons). This allows to obtain an image of the surface of the area analyzed. Depending on the experimental parameters selected and the detectors employed the image can vary from a topographical view showing the surface morphology to a more planar projection-like visualization of the surface, offering different information on the sample. Commonly, SEM equipments are provided with an Energy-dispersive X-Ray spectroscopy detector (EDS,EDX). This detector analyzes the X-ray emitted from the interaction of the electron beam with the sample, offering compositional

information on the specimen under study. In this thesis, a Carl ZEISS Auriga scanning electron microscope located at IREC and equipped with an EDX detector has been employed for analyzing the thin films surface morphologies. The EDX detector has been utilized for obtaining semi-quantitative information on the relative composition of samples regions. SEM characterization has also been utilized for evaluating the differences in the microstructure with changes in the parameters set for PLD deposition. Additionally, SEM has been employed for analyzing the structure of the  $\mu$ SOFCs fabricated in this thesis and their post-mortem analysis after the operation tests.

### 2.3.2 Transmission Electron Microscopy\*

Transmission Electron Microscopy (TEM), similarly to the aforementioned SEM, is a type of characterization technique based on the interaction of an electron beam with the sample. In this case, the signal collected consists in the electrons that have been transmitted through the sample. In this thesis, TEM and high resolution TEM (HRTEM) images were recorded for the study of LSCrMn-SDC based heterostructures. The equipment employed was a JEOL JEM 2010 LaB6 microscope operating at 200 kV with a 0.19 nm point-to-point resolution. EDX mapping was performed by STEM with a JEOL 2100F FEG microscope operating at 200 kV with a 0.2 nm resolution in the scanning mode and equipped with a JEOL SDD Centurio detector with a large solid angle of up to 0.98 sr. Local structural properties were investigated by automated crystal phase and orientation mapping (ACOM) with a precession system (ASTAR) implemented in the JEOL 2100F FEG microscope. Crystal phase and orientation maps were obtained by the precession of the primary electron beam around the microscope's optical axis at an angle of  $1.2^\circ$  while collecting the electron diffraction patterns at a rate of 100 frames/s. In this technique, the incident electron beam was a few nanometers in size and was processed to reduce the dynamical effects and to enhance the indexing quality. The electron beam was simultaneously scanned over the area of interest to record an electron diffraction pattern at each location. The experimental electron diffraction patterns were compared with the complete set of theoretical diffraction patterns, which were computed for every expected crystalline phase and for a large number of orientations. The best match between the experimental and theoretical electron diffraction patterns permitted the identification of both the crystalline phase and orientation with high precision.

### 2.3.3 X-Ray Diffraction

X-ray diffraction (XRD) is a characterization technique that allows to obtain information on the crystallographic structure of the materials studied. The basic principles of XRD are based on the scattering effect of X-ray radiation when it interacts with the atomic layers of the

---

\* The TEM characterization was carried out with the collaboration of Dr. Mónica Burriel and Ing. Laetitia Rapenne at Univ. Grenoble Alpes, CNRS, Grenoble INP, LMGP.

sample. The positive interferences between the waves scattered give rise to the diffraction reflection peaks characteristic of crystalline materials. In this thesis, crystallographic information was retrieved by a Bruker D8 Advanced diffractometer equipped with Cu K $\alpha$  radiation source. The measurements were carried out in the  $\theta$ - $2\theta$  configuration, as it is represented in Figure 2-9. In this configuration, only the diffraction signal coming from the atomic planes parallel to the surface are collected. The reflections observed follow Bragg's law –see equation (2-1)–, which relates the angle of the diffracted X-rays with the distance between the atomic planes responsible of the diffraction.

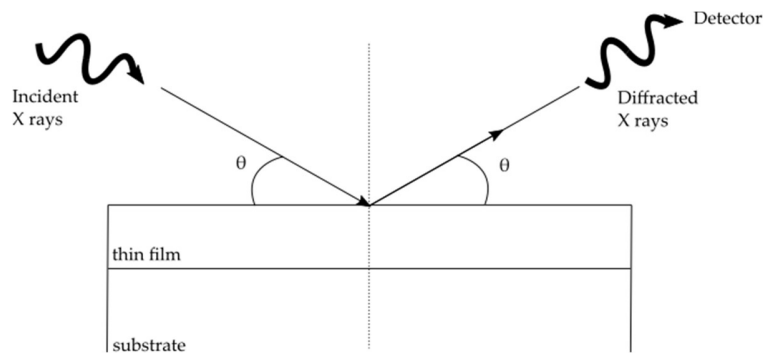


Figure 2-9. Schematic of the configuration  $\theta$ - $2\theta$  employed for XRD characterization.

$$2d \sin \theta = \lambda \quad (2-1)$$

In this thesis, XRD characterization measurements have been carried out in order to obtain information of the crystalline nature of the thin film materials studied. The main objective has been to detect the presence of perovskite and fluorite phases, and the presence or absence of secondary phase. Additional information on the evolution of the crystallinity of the films on thermal annealing and degradation has also been explored. It should be noted that for the study of combinatorial libraries of materials discussed in Chapter 4, the experimental description of the XRD measurements and analysis performed is described later in the text, in Section 2.6.2 of the present chapter.

#### 2.3.4 Atomic Force Microscopy

Atomic Force Microscopy (AFM) is a characterization technique that allows to visualize the surface microstructure of thin films and related micro/nanostructures. The working principle behind the technique is based on the interaction between a tip employed to probe the surface and the material atoms. This interaction result in the appearance of either attractive or repulsive forces tip-sample, depending on the specifics of the operation and the working distance. Some of the forces that can be present are quantum mechanical interactions, coulombic forces and polarization induced (Van der Waals) forces. Characterization by AFM is particularly useful when analyzing non-conductive samples as it is not based on electronic conduction, as opposed to electronic microscopies. Additionally,

it is of interest for quantifying materials properties such as surface roughness and grain size. In this thesis, topographical microstructural characterization was performed in tapping mode using an XE 100 model atomic force microscope provided by Park System Corp. and located at IREC facilities. AFM has been employed for comparing the surface microstructure of LSCrMn-SDC heterostructures and ceria-based thin films (see Chapter 3) as well as for studying the evolution on thermal degradation of the surface of LSMCF based oxygen electrodes (see Chapter 4).

### 2.3.5 Spectroscopic Ellipsometry

Spectroscopic ellipsometry (SE) is a non-destructive characterization technique employed for the analysis of the optical response of the material under study. The technique allows to extract the optical properties of the material (i.e. the refraction index and the extinction coefficient, and related parameters), as well as obtain information on features that may influence the optical response, such as the thickness of the material, the porosity, or the roughness. The basic principles of ellipsometry are depicted in Figure 2-10a. In ellipsometry measurements, an incident light source reaches the sample at a given angle and linearly polarized. As a result of the interaction with the sample under study, the light reflected is elliptically polarized. The reflected light then passes through a modulator and an analyzer, recovering the linear polarization, which then passes to the detector. Ellipsometry analyzes the changes in the polarization of the light by measuring the phase shift ( $\Delta$ ) and the ratio of amplitude change ( $\Psi$ ) of the incident optical wave. In particular, the complex reflectance ratio ( $\rho$ ) can be defined from the elliptical components  $r_p$  and  $r_s$  can be calculated from the measured values of  $\Delta$  and  $\Psi$  through equation (2-2).

$$\rho = \frac{r_p}{r_s} = \tan(\Psi) e^{i\Delta} \quad (2-2)$$

From these measurements, a mathematical model can be applied in order to fit the optical properties of the material. In the case of a semi-infinite model, the following relation between the dielectric constant and the complex reflectance can be employed:

$$\bar{\epsilon} = \bar{\epsilon}_a \sin^2 \varphi \left[ 1 + \tan^2 \varphi \left( \frac{1 - \rho}{1 + \rho} \right)^2 \right] \quad (2-3)$$

In order to fit the measurement retrieved by ellipsometry, a series of Lorentzian oscillators were employed, as it is known to be a proper model to fit perovskite semiconductors<sup>8-10</sup>. The dielectric constant of the material is modeled with equation (2-4).

$$\bar{\epsilon} = \epsilon_0 + \sum_{j=1}^n \frac{f_j \omega_{o,j}^2}{\omega_{o,j}^2 - \omega^2 + i\gamma_j \omega} \quad (2-4)$$

Where  $\epsilon_0$  is the high frequency dielectric constant,  $f$  is the amplitude of the oscillator,  $\omega_0$  is the resonance frequency,  $\gamma$  is the broadening of the oscillator and  $\omega$  is the angular frequency.

Figure 2-10b shows an example of the acquisition spectra obtained by ellipsometry, and the fit result. Figure 2-10c shows an example of the modeled spectra of the imaginary component of the dielectric constant, with the contribution of each of the oscillators fitted.

In this thesis, spectroscopic ellipsometry has been utilized for measuring the thickness of the thin films fabricated by PLD and for studying the optical absorption coefficient of perovskite materials. The equipment employed was an ellipsometer UVISSEL from Horiba scientific and the experimental parameters set were photon energy range of 0.6 to 5.0 eV with a step of 0.05 eV. The angle of incident light beam was 70°. The ellipsometry data were modeled and fitted using DeltaPsi2 software from Horiba scientific. Ellipsometry has also been utilized for the calibration of the thickness of combinatorial libraries of perovskite materials and for the study of their optical properties, as it is further explained in Section 2.6.3.

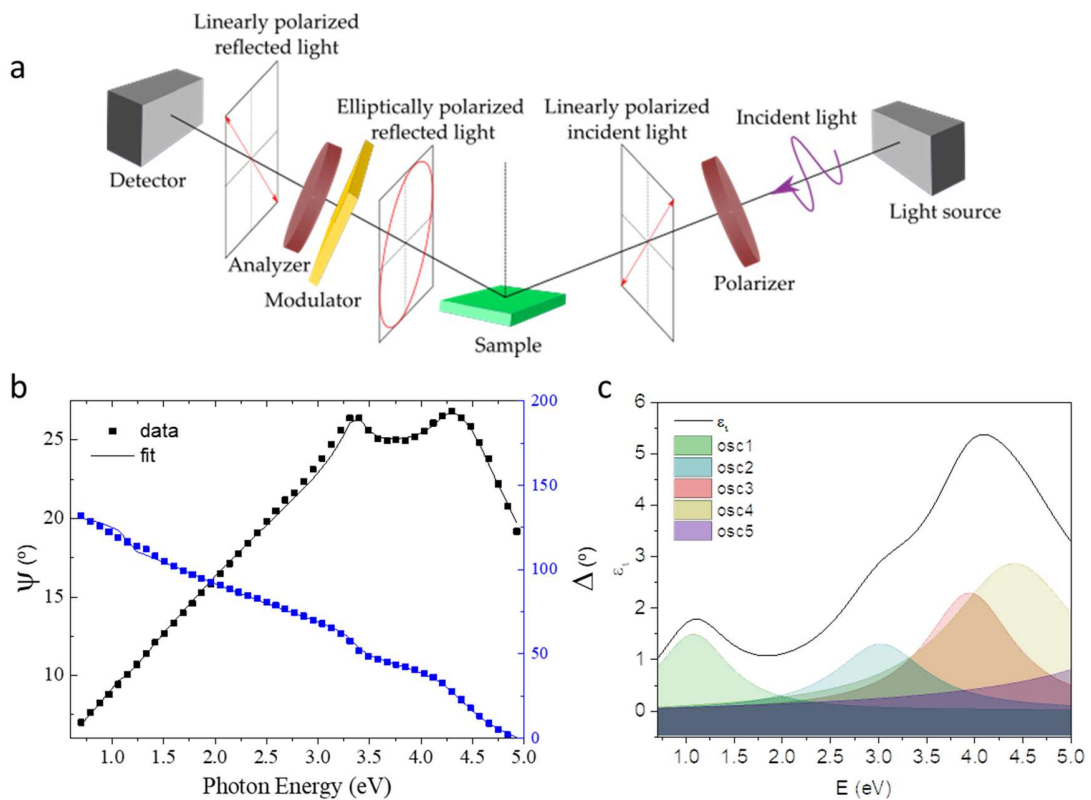


Figure 2-10. Schematic illustration of the fundamental principles of ellipsometry (a). Raw data obtained by ellipsometry and fit result (b). Imaginary value of the dielectric constant obtained as a function of energy with the contribution of each oscillator employed in the fit (c).

## 2.4 Advanced characterization techniques

The study of thin film materials often requires the use of more sophisticated analysis techniques aimed at the characterization of specific features. This is even more critical when the goal is to study the properties and evolution of a thin film material (or materials) derived from carrying out a particular process (e.g. post-fabrication treatments, electrochemical operation or induced degradation). These processes might induce changes on a local level in the form of structural evolution, changes in surface composition, cationic restructuring, defect formation, among other phenomena. In this thesis, several advanced characterization techniques have been employed in order to characterize the structural and compositional changes induced by thermal degradation on LSMCF thin film at the surface, subsurface and bulk levels (see Chapter 4), as illustrated in Figure 2-11.

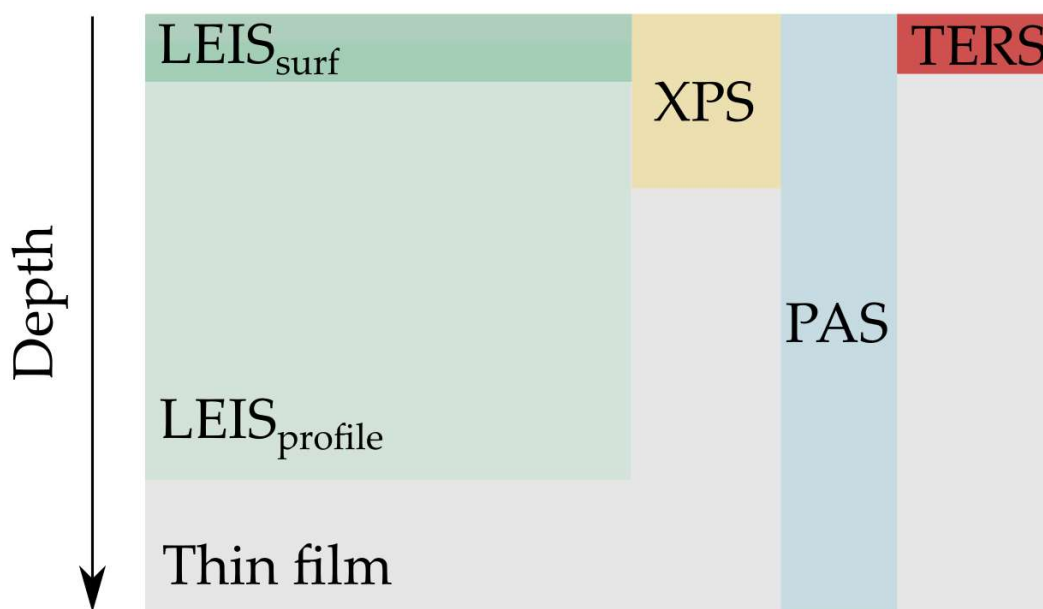


Figure 2-11. Schematic illustration of the advanced characterization techniques employed in this thesis and their analysis length scale.

### 2.4.1 Low Energy Ion Scattering<sup>†</sup>

Low Energy Ion Scattering (LEIS) is an analytical characterization technique based on the interaction of a noble gas (typically He<sup>+</sup>, Ne<sup>+</sup> and Ar<sup>+</sup>) with the material subject of the analysis<sup>11</sup>. In LEIS, the collision of the beam ions with the surface of the sample results in backscattering of the incident atoms (see Figure 2-12). Contrary to other beam techniques like Time of Flight (ToF)-Secondary Ion Mass Spectrometry (SIMS) that need to sputter the

<sup>†</sup> LEIS analysis was performed at Imperial College London, Department of Materials, Surface Analysis Facility, with the support of Dr. Sarah Fearn and Dr. Zijie Sha.



sample (see Section 2.6.6), the low energy utilized in LEIS (normally in the 0.5-10 keV energy range) allows to operate in the so called “static” regime, avoiding sputtering of the sample.

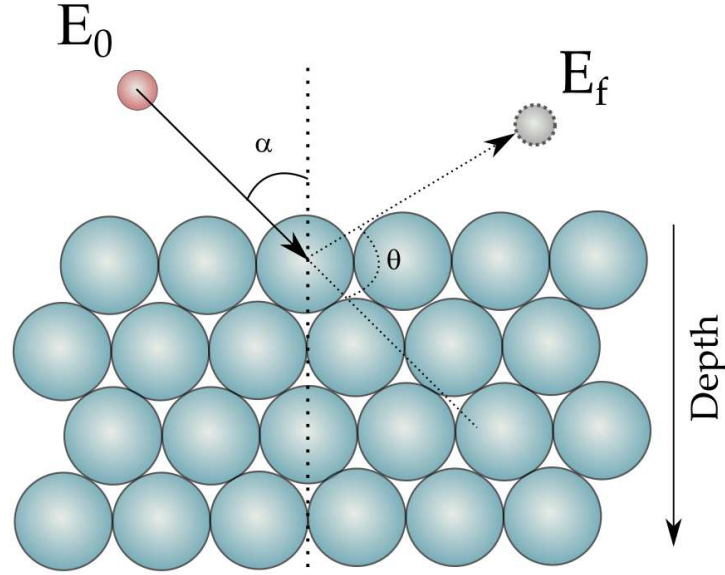


Figure 2-12. Schematic illustration of particle interaction during LEIS analysis. Adapted from Ref.<sup>11</sup> with permission of Elsevier.

In this regime, the backscattered ions are the result of (almost exclusively) elastic collisions with the atoms in the sample surface. In these types of collisions, the incident ion with energy  $E_0$  interacts with the atoms at the surface with an angle  $\alpha$  and is scattered with an angle  $\theta$  and energy  $E_f$ . The relation between  $E_f$  and  $E_0$  is the so called kinematic factor ( $K$ ) and is given by the expression in equation (2-5), where  $m_1$  is the mass of the incident ion and  $m_2$  the mass of the target atom. The detection and analysis of the scattered ions with energy  $E_f$  can then be employed for the quantification of the atomic composition of the surface down to the outermost level (i.e. to monolayer resolution).

$$E_f = K \cdot E_0 = \left( \frac{\cos \theta \pm \sqrt{\left(\frac{m_2}{m_1}\right)^2 - \sin^2 \theta}}{1 + \frac{m_2}{m_1}} \right)^2 \cdot E_0 \quad (2-5)$$

For multicomponent materials with more than one type of element the masses are retrieved following the same process, resulting in the formation of an energy spectra. The atomic surface concentration ( $N_i$ ) of a particular atom is then given by equation (2-6):

$$S_i = \frac{I_p}{e} \cdot t \cdot \xi \cdot R \cdot \eta_i \cdot N_i \quad (2-6)$$

For which  $S_i$  is the yield of ions backscattered from the surface,  $I_p$  is the primary ion beam current,  $e$  the elementary charge,  $t$  is the acquisition time,  $\xi$  is an instrumental factor (covering detector solid angle, efficiency and analyzer transmission),  $R$  is a factor related to

surface roughness and shielding by neighbor atoms and  $\eta_i$  the elemental sensitivity factor. Although quantification of absolute atomic concentration values is in principle possible, in reality quantification is difficult to obtain due to uncertainties in the elemental sensitivity, and is generally achieved by calibration against reference samples. Additionally, LEIS can be coupled with a sputtering beam, in order to reconstruct elemental depth profiles. In these cases, the appearance of preferential sputtering of lighter elements might result in alteration of the nominal stoichiometry of the material under study. The work from Niania et al. offers an interesting analysis on this effect, particularly relevant in the first stages of the ablation (resulting in subsurface off-stoichiometry), when the sputtering process has not reached equilibrium<sup>12</sup>. In order to account for this phenomenon, employment of correction factors are needed for obtaining quantitative analyses.

In this thesis, a Qtac100 LEIS instrument (IONTOF GmbH, Münster, Germany) operated with normal incidence was employed for analyzing the surface and subsurface of LSMCF combinatorial films under study in Chapter 4. Two beams of He<sup>+</sup> (3 keV) and Ne<sup>+</sup> (5 keV) were employed as primary beam sources. A beam of 1keV Ar<sup>+</sup> incident at 45° was applied to sputter the film surface and carry out depth analyses on the samples. The LEIS depth profile was obtained by alternating analyses with the Ne<sup>+</sup> primary beam and sputtering with the Ar<sup>+</sup> for 10 s. The scanning area was 1000 x 1000  $\mu\text{m}^2$  while the sputtering area was 1300 x 1300  $\mu\text{m}^2$ . Each cation signal was calculated by integrating the corresponding peak in the LEIS spectra. The Mn, Fe and Co signals were integrated altogether and referred to as the B-cation signal due to the overlap between the peaks. For the calculation of the thickness sputtered, the Ar<sup>+</sup> ion dose was translated to depth units by considering that approximately 10<sup>5</sup> ions/cm<sup>2</sup> result in the sputtering of a monolayer. The Sr/Sr+La profiles obtained were then integrated over two regions of interest, the surface and the subsurface of the film, to study the rearrangement of Sr from the pristine state to after thermal annealing.

#### 2.4.2 X-Ray Photoelectron Spectroscopy<sup>†</sup>

X-Ray Photoelectron Spectroscopy (XPS) is an analytical technique that provides semi/quantitative information on the composition and chemical state of the materials analyzed. Despite retrieving quantitative information on the sample is possible, depending on the system under study it may not be a simple process. Factors related to the information depth of the analysis, background subtraction, complexity of the material composition in terms of peak overlap, presence of layered structures at the surface level may be some examples that may increase the uncertainty of the analysis. The technique is based on irradiating X-Ray energy to the material of analysis, resulting in the emission of a photoelectron from a core level. The energy of the incident X-ray and the measurement of the kinetic energy (KE) of the photoelectron emitted allow the quantification of the binding

---

<sup>†</sup> XPS measurements were carried out at Imperial College London, Department of Materials, Advanced Photoelectron Spectroscopy Laboratory Facility.

energy (BE) of the ejected photoelectron, as shown in equation (2-7), where  $\Phi_{spec}$  is the spectrometer work function, a constant value.

$$h\nu = BE + KE + \Phi_{spec} \quad (2-7)$$

In this thesis, XPS was performed with the goal to analyze the changes in the surface chemical environment of LSMCF perovskites after thermal degradation. The equipment employed consisted in a high-throughput X-ray photoelectron spectrometer (K-Alpha+, Thermo Fisher Scientific, US) with a monochromated Al  $K_{\alpha}$  radiation source ( $h\nu = 1486.6$  eV) operating at  $2 \times 10^{-9}$  mbar base pressure. The X-ray source used a 6 mA emission current and 12 kV anode bias, giving a X-ray spot size of up to  $400 \mu\text{m}^2$ . Survey and core-level spectra were obtained with pass energies of 200 and 20 eV, respectively. The average penetration depth considered for these conditions is 10 nm. XPS spectra for C 1s, O 1s, Mn 3d, Co 3d, Fe 3d, La 3d and Sr 3d were measured to properly evaluate the surface chemical environment. All the spectra obtained were fitted with the Avantage software. The binding energies observed were corrected by considering the C 1s peak position at a reference value of 284.8 eV characteristic of surface hydrocarbons. The obtained spectra were processed by subtraction of a Shirley-type background, while the peaks were fitted using a Gaussian-Lorentzian line shape. The Sr 3d spectra was fitted by differentiating three different Sr species: Sr present in the lattice of the perovskite film ( $\text{Sr}_{latt}$ ), Sr present in the surface forming carbonates and other compounds of similar binding energy ( $\text{Sr}_{mix}$ ) and Sr present in the form of sulfates ( $\text{Sr}_{sulfates}$ ). This was done by attributing a peak (and their corresponding doublets) at each one of the selected species. The BE range was restricted for each one of the  $3d_{5/2}$  contributions, specifically 131.70-132.30 eV for  $\text{Sr}_{latt}$ , 132.70-133.30 eV for  $\text{Sr}_{mix}$  and 133.70-134.30 eV for  $\text{Sr}_{sulfates}$ . The distance of between the  $3d_{5/2}$  and  $3d_{3/2}$  peak doublets was set to a difference in BE of  $+1.80 (\pm 0.1)$  eV with respect to  $3d_{5/2}$ .

### 2.4.3 Tip Enhanced Raman Spectroscopy

Tip Enhanced Raman Spectroscopy (TERS) is a characterization tool that combines the possibilities offered by scanning probe microscopy technologies with the analysis and information retrieved with Raman Spectroscopy<sup>13</sup> –see section 2.6.4 for more details on Raman analysis in this thesis–. One aspect that makes TERS a particularly interesting technique is that allows to couple the Raman signal with the area scanned. In TERS, the metallic tip (generally made of gold or silver) is employed to amplify the incident light in the area surrounding the tip apex, as a result of plasmon generation. This effect results in an enhancement of the Raman sensitivity factor by several orders of magnitude and makes possible to observe vibrational modes that may not be generally detected with regular Raman analysis. In this thesis, the use of TERS has been explored as a possible technique to directly visualize the chemical nature of segregated species in thermally degraded LSMCF perovskites (see Appendix 1). The measurements were performed on a Xplora Nano from HORIBA, using a 638 nm laser (38.6 mW of power at laser exit and 31.9 mW at sample) and

Au-coated OMNI TERS tips. Maps were acquired with a 10 nm px<sup>-1</sup> resolution to build 500×500 nm<sup>2</sup> maps, plotted using a 1.8 px weight average. Acquisition times of 10 s per spectra and a 1200 g.mm<sup>-1</sup> grating were employed.

#### 2.4.4 Positron Annihilation Spectroscopy<sup>§</sup>

Positron Annihilation Spectroscopy (PAS) is an experimental technique that is gaining interest in materials science. The technique allows to characterize the presence of lattice defects in solid materials<sup>15</sup>. Interestingly, defects of the order of ≈0.1-10 nm can be characterized (e.g. from ionic vacancy defects to free open volume defects in the material) with analysis length ranging from the nanometer scale up to millimeters. Additionally, it presents the advantage of being a non-destructive technique, contrary to other techniques like ToF-SIMS or TEM. The fundamental principles of the technique are based on the interaction of an incident beam of positrons into the sample and their annihilation result of the interaction with the material electrons, as depicted in Figure 2-13. Positrons implanted in the material thermalize (i.e. slow down) at a given penetration depth in scale of picoseconds<sup>16,17</sup>. In the general case of metals, the positrons diffuse through the crystal lattice through the interstitial region between the atoms, as a result of the Coulomb repulsion from the positive atom cores. The presence of vacancy-like defects in the lattice derives in a lowering of the repulsion forces sensed by positrons (i.e. due to the absence of the positive ion core), acting as potential wells and leading to a localized positron state. This phenomenon is generally referred as positron trapping. As a result of the positive charge of positrons, trapping is favoured in negatively charged vacancies and can also be detected in neutral vacancies. Trapping in positively-charged defects cannot be detected within the lifetime of positrons. As vacancy defects present lower electron density, the positrons take longer to annihilate, reaching lifetime values of hundreds of picoseconds. The annihilation process provokes the release of gamma radiation in conditions of energy and momentum conservation. This results in the emission of two photons of approximately 511 keV emitted in opposite directions.

---

<sup>§</sup> PAS analyses were conducted at the Mono-energetic Positron Source beamline at HZDR, Germany<sup>14</sup>. The experiments and data analysis were performed with collaboration of Dr. Maciej Oskar Liedke.

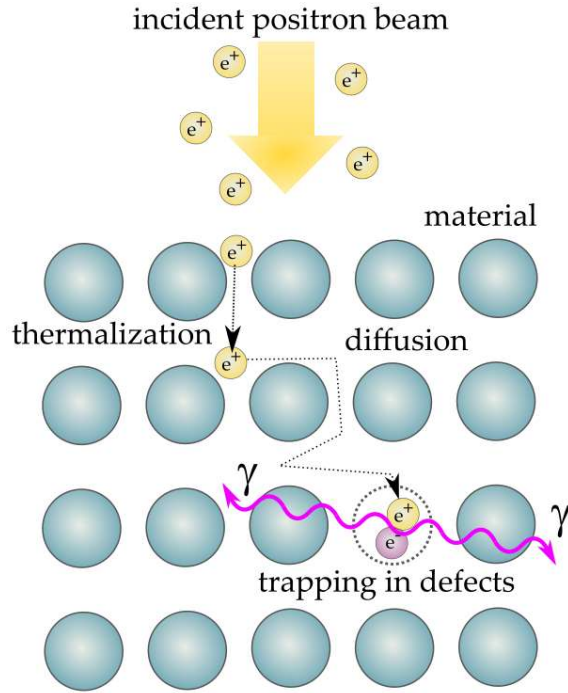


Figure 2-13. Schematic of the working principle of PAS analysis.

The annihilation process is characterized by a specific lifetime constant ( $\tau$ ). As it has been mentioned, the differences in the electronic density present in crystal defects lead to longer lifetimes than in the defect-free state. Therefore, the positron lifetime is generally proportional to the defect size, i.e. the larger the open volume, the lower the probability positron-electron interaction and the longer it takes for positrons to be annihilated with electrons<sup>15,18</sup>. It is worth mentioning that by employing variable energy (VE) positron beams the penetration depth of the incident positrons can be easily tuned, allowing to extend the analysis into depth profile information.

In this thesis, variable energy positron annihilation lifetime spectroscopy (VEPALS) and Doppler broadening variable energy positron annihilation spectroscopy (DB-VEPAS) have been utilized for characterizing the defect nature of perovskite thin films and their evolution upon thermal degradation. Several works have employed PALS for the characterization of cationic defects present in perovskites such as LSM and SrTiO<sub>3</sub><sup>4,19-22</sup>, hence validating the viability of the experiments.

#### 2.4.4.1 Doppler Broadening Variable Energy Positron Annihilation Spectroscopy

DB-VEPAS are measurements in which positrons are accelerated and monoenergetically implanted into the sample, allowing to obtain a depth profile analysis (in this case, in the 0.05 - 35 keV energy range). A mean positron implantation depth can be estimated by using a simple expression depending on the material density<sup>19</sup> (see equation (2-8), where  $E_p$  is the

implantation energy in keV,  $\rho$  is given in  $\text{g/cm}^3$  and the resulting  $\langle z \rangle$  is given in nm). This value cannot be treated as an absolute measure as it does not account for positron diffusion, despite it is a reasonable approximation of the material depth. The best estimation is given for materials with large defect concentration, hence low positron diffusion length.

$$\langle z \rangle = \frac{36}{\rho} E_p^{1.62} \quad (2-8)$$

Annihilation of positrons in vacancy-like defects emits usually two anti-collinear 511 keV gamma photons, which are measured with two high-purity Ge detectors (energy resolution of  $1.09 \pm 0.01$  keV at 511 keV). Since thermalized positrons have very small momentum compared to electrons, a broadening of the 511 keV line is present in the annihilation spectra, mostly due to the momentum of the annihilated electrons. This broadening is characterized by two distinct parameters (S and W) defined as a fraction of the annihilation line in the central ( $511 \pm 0.93$  keV) and outer regions ( $508.33 \pm 0.35$  keV and  $513.67 \pm 0.35$  keV), respectively. Figure 2-14 shows a schematic visualization of the broadening of the annihilation spectra and the corresponding calculation of the S and W parameters. The S-parameter corresponds to a fraction of positrons annihilating with low momentum valence electrons and is related to vacancy type defects and their concentration. The W-parameter approximates overlap of positron wavefunction with high momentum core electrons –i.e. electrons most responsible of the broadening–<sup>20</sup>. Plotting calculated S as a function of positron implantation energy provides depth dependent information on the defect content, whereas S-W plots are normally employed to examine atomic surrounding of the defect site and its size (type)<sup>21</sup>. This is due to the nature of the electrons involved in the calculation of S and W parameters. Since positron trapping leads to a higher probability of annihilation with low momentum, valence electrons and S is directly related to these electrons, an increase in the S parameter is a direct reflection of increase of vacancy-like defects. On the other hand, as W is related to core shell electrons, its signal is related to the chemical nature of the atoms surrounding the vacancy defect. In this thesis, DB-VEPAS analyses have been conducted at the apparatus for in-situ defect analysis (AIDA)<sup>22</sup> of the slow positron beamline (SPONSOR)<sup>23</sup> located at HZDR.

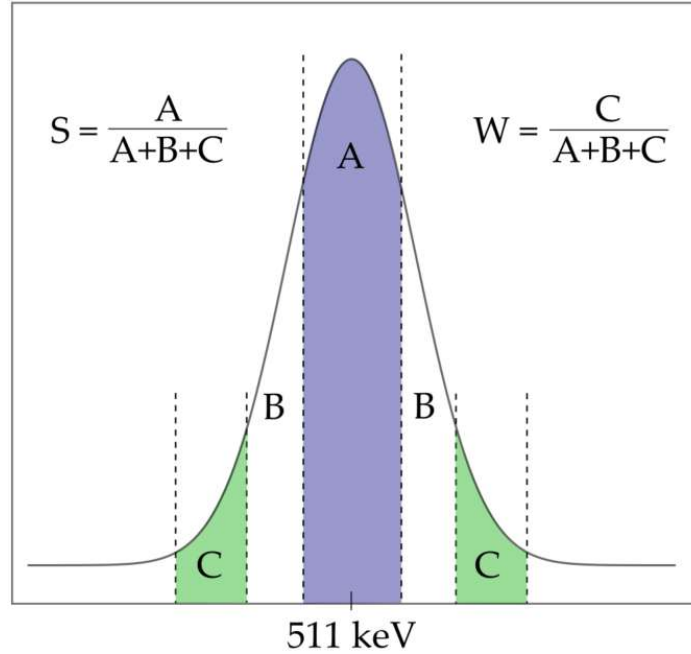


Figure 2-14. Schematic representation of the definition of the parameters  $S$  and  $W$  from the annihilation spectra.

#### 2.4.4.2 Variable Energy Positron Annihilation Lifetime Spectroscopy

In VEPALS analyses, the lifetime of the positrons interacting with the sample is measured. The lifetime experiment is performed by detecting the photons emitted as a result of annihilation with two scintillator detectors in combination with a photomultiplier tubes. Each of the detectors is optimized for one of the two photos involved in the analysis, i.e. a photon serving as start signal and another as the stop signal<sup>15</sup>. The resolution function required for analyzing the resulting lifetime spectrum uses two Gaussian functions with distinct intensities depending on the positron implantation energy, and appropriate relative shifts. Typical lifetime spectrum  $N(t)$  is described by equation (2-9), where  $\tau_i$  and  $I_i$  are the positron lifetime and intensity of the corresponding component, respectively.

$$N(t) = \sum_i \frac{1}{\tau_i} I_i e^{-\frac{t}{\tau_i}} \quad (2-9)$$

In this thesis, VEPALS measurements were conducted on  $\approx 80$ -100 nm LSMCF samples using a digital lifetime  $\text{CrBr}_3$  scintillator detector [51 mm diameter (2") and 25.4 mm length (1")] coupled to a Hamamatsu R13089-100 PMT with a  $\mu$ -metal shield and housed inside a solid Au casing. A homemade software employing a SPDevices ADQ14DC-2X with 14 bit vertical resolution and 2GS/s horizontal resolution<sup>24</sup> and with a time resolution function down to about 0.240 ns was employed. All spectra contained at least  $10^7$  counts. All the spectra were deconvoluted using a non-linear least-squares fitting method using the fitting software

package PALSfit<sup>25</sup> into 3 discrete lifetime components, which directly evidence localized annihilation of two different defect types ( $\tau_1$  and  $\tau_2$ ). The third component  $\tau_3$  is residual and reflects small ( $I_3 \ll 1\%$ ) spectra distortions related to the beamline. The corresponding relative intensities reflect to a large extent the concentration of each defect type as long as the size of compared defects is in the similar range.

## 2.5 Functional characterization

### 2.5.1 In-plane conductivity measurements

The conductivity of the materials studied in Chapter 3 was investigated in order to evaluate their performance as electrode materials for SOCs. DC conductivity measurements under both reducing and oxidizing atmospheres were performed in a four-probe heating station (Linkam instruments THMS600) using the Van der Pauw configuration<sup>26</sup>, as depicted in Figure 2-15. In the configuration set, the current is applied between the contacts A and B ( $I_{AB}$ ), while the voltage is measured with the C and D probes ( $V_{CD}$ ). The resistance  $R_0$  can be calculated then as the ratio  $V_{CD}/I_{AB}$ . Additionally,  $R_v$  can be defined as the resistance value calculated from the ratio  $V_{CB}/I_{AD}$ , i.e. the resistance calculated changing the polarity and the contacts side. The sheet resistance ( $R_s$ ) can be then obtained by the Van der Pauw method with the following expression:

$$e^{-\frac{\pi R_v}{R_s}} + e^{-\frac{\pi R_0}{R_s}} = 1 \quad (2-10)$$

The solution for this expression is not trivial, but it can be simplified by introducing the average of  $R_0$  and  $R_v$ , and introduce a correction factor  $f$  that depends on the  $R_v/R_0$  ratio (details on the calculation of the correction can be checked in Ref.<sup>27</sup>). Finally, multiplying  $R_s$  by the thin film thickness ( $d$ ) results in the calculation of the resistivity ( $\rho$ ) as stated in equation (2-11).

$$\rho = R_s d = \frac{\pi d}{\ln 2} \frac{(R_0 + R_v)}{2} f\left(\frac{R_v}{R_0}\right) \quad (2-11)$$

For the samples measured in this thesis, silver paste (Sigma-Aldrich) was brushed locally for improving the electrical contact between the film and the probes. The DC measurements were carried out with a Keithley 2400 sourcemeter, applying current values in the 0.1-10  $\mu\text{A}$  range. The reducing atmosphere set was 5%  $\text{H}_2$  in Ar with a flow of 100 mL/min. The oxidizing atmosphere set was synthetic air at 100 mL/min. The temperature range was restricted up to 350 °C to avoid any parasitic current from the substrate.



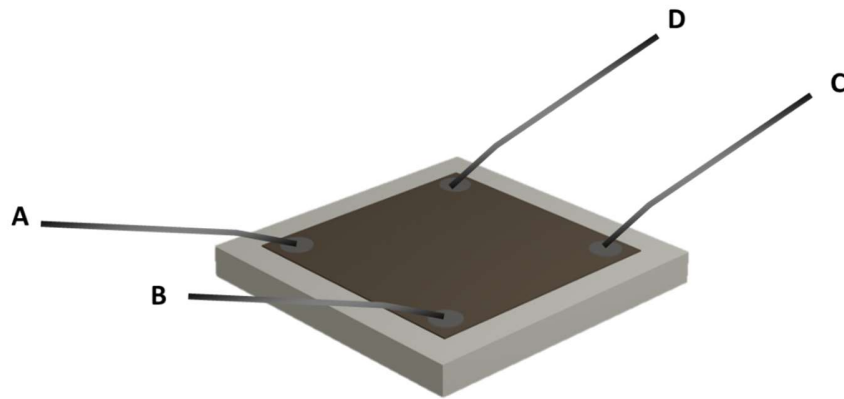


Figure 2-15. Schematic of the contacts made on the contacts made for the in-plane conductivity measurements carried out in the Van der Pauw configuration.

## 2.5.2 Electrochemical Impedance Spectroscopy

### 2.5.2.1 Electrochemical characterization of thin film electrodes

For the characterization of the electrochemical properties of the thin films studied in this thesis, Electrochemical Impedance Spectroscopy (EIS) was employed. EIS is a characterization technique employed in a large variety of electrochemical systems, such as SOCs<sup>28</sup>, solid state batteries<sup>29</sup> or biosensors<sup>30</sup>. EIS consists in the excitation of the sample or device under study with an AC voltage (see equation (2-12)) in a given frequency range, resulting in the perturbation of the equilibrium state of the system.

$$V(t) = V_0 e^{i\omega t} \quad (2-12)$$

Where  $V_0$  is the voltage amplitude,  $\omega$  is the angular frequency and  $t$  is the time. The system response to the AC voltage will give rise to a sinusoidal current, characterized by the same frequency but shifted in phase, as seen in equation (2-13):

$$I(t) = I_0 e^{i(\omega t + \theta)} \quad (2-13)$$

The impedance of the system can be calculated then similarly to the case of an ohmic resistance, i.e. by the ratio between the excitation voltage and the current:

$$Z(t) = \frac{V_0}{I_0} \frac{e^{i\omega t}}{e^{i(\omega t + \theta)}} = |Z| e^{-i\theta} \quad (2-14)$$

The screening along the frequency scale typically goes from high frequencies (of the order of 1 MHz) to low frequencies (up to 10-100 mHz). The analysis of the response in these regions allows to obtain information on the electrochemical processes that are involved in the system, i.e. the phenomena that are limiting the current of the electrochemical system. Each electrochemical phenomena is characterized by a particular characteristic frequency or relaxation time, related to the time involved in reaching the equilibrium state after the

application of the perturbation signal. Hence, screening the system in frequency allows to differentiate electrochemical processes that take place in different time scales allowing to distinguish the charge transport phenomena present in the electrochemical cell. One important aspect to keep into account when characterizing by EIS is to not excite the cell with a voltage signal that goes beyond the linearity of the system studied. For this reason, as many electrochemical systems present a nonlinear response on the voltage applied, the AC amplitude is typically kept to values in the order of 50-100 mV, for which the linearity is maintained. By measuring the impedance of the system studied, one can plot the real and imaginary components of the impedance in a x-y representation, forming the so called Nyquist plots. For more details of the fundamental principles of EIS and their application in electrochemical system the reader can refer to dedicated books<sup>31</sup> and paper reviews<sup>32</sup>. Most of the EIS spectra measured for the work discussed in this thesis has been analyzed by equivalent circuit modeling. This analysis allows to simulate the impedance response of electrical circuits and fit the parameters so the simulated impedance is adjusted to the experimental data obtained. Figure 2-16 shows the equivalent circuits employed for fitting the EIS results obtained in this thesis. The circuit in Figure 2-16a consists in a simple circuit with two ZARC elements (i.e. a resistor R in parallel to a constant phase element (CPE)). The CPE element is normally included in equivalent circuit modelling to replace a capacitor. This is done in order to account for the non-homogeneities present in real electrochemical systems, which differ from ideal capacitive behavior. It is characterized by presenting a capacitive parameter  $Q$  and the dispersion parameter  $n$ . The impedance of a ZARC element is then given by equation (2-15). It should be noted that when the parameter  $n = 1$ , the CPE behaves as an ideal capacitor.

$$Z_{CPE} = \frac{1}{Q(i\omega)^n} \quad (2-15)$$

The circuit in Figure 2-16a is generally employed when two arc-shape contributions, one located in the high frequency (HF) range and the second in the low frequency (LF) part, are found in the Nyquist representation. The circuit presented in Figure 2-16b is a Jamnik-Maier-like circuit<sup>33,34</sup> that allows to model the impedance response of materials that are colimited by both ionic diffusion transport through the electrode ( $R_{ion}$ ) and the surface reaction ( $R_{surf}$ ,  $CPE_{surf}$ ), e.g. as it is the case when modelling LSM impedance<sup>35,36</sup>. The circuit also includes chemical capacitance elements ( $C_{chem}$ ), which is related to the chemical energy stored through changes in the material stoichiometry. Interfacial elements ( $R_i$ ,  $C_e$ ) are also included in the circuit in order to account for the charge-transport process in the electrolyte-electrode interface, as well as for the blockage of electrons into the electrolyte. Finally, the circuit showed in Figure 2-16c shows a simplified version of the circuit in Figure 2-16b for the case in which the ionic contribution is not limiting and the chemical capacitance surpasses the surface constant phase element, i.e.  $R_{ion} \approx 0$  and  $CPE_{surf} \ll C_{chem}$ . The capacitive elements were then replaced by general constant phase elements. Please refer to Ref.<sup>37</sup> for a

more detailed explanation on the simplification process. Although the similarities of the circuits in Figure 2-16a and c are evident in terms of system applicability (i.e. two arc-like contributions in the HF and LF regions), when discussing constant phase elements and related capacitances for the MIEC materials studied in Chapter 3, the circuit in Figure 2-16c is more representative of the system modelled and hence, is formally more correct. All of the circuits also include a series resistor element ( $R_{\text{series}}$ ) representative of the ohmic resistance of the electrolyte substrate, and an inductance element (L) in order to model the possible inductive behavior coming from the wiring of the setup. In this thesis, EIS measurements have been carried out in order to study the electrochemical performance of SOC thin film electrodes under both reducing and oxidizing conditions, as well as for SOC full cell characterization. In the case of full cell measurements, the general circuit shown in Figure 2-16a was employed, in order to fit the resistance components of the impedance recorded corresponding to each electrode, as well as the electrolyte. Two configurations were employed when studying the thin films by EIS, symmetric and asymmetric configurations. In the first, the material under study was deposited in both sides of YSZ single crystal substrates, while in the latter a low impedance counter electrode was applied in the back side of the substrates. The symmetric configuration was employed to study the materials discussed in Chapter 3, mainly characterized under hydrogen atmosphere, for which the use of a low impedance counter electrode was not optimized. The asymmetric configuration was employed for fitting the spectra studied in Chapter 4, which was recorded in oxidizing atmosphere (i.e. for the study of oxygen electrode materials). In this case, a low impedance counter electrode made of porous Ag allowed for the study of a single film of the materials under study. This prevented the need to fabricate symmetrical samples, simplifying the fabrication process, and facilitated the study of the combinatorial films studied.

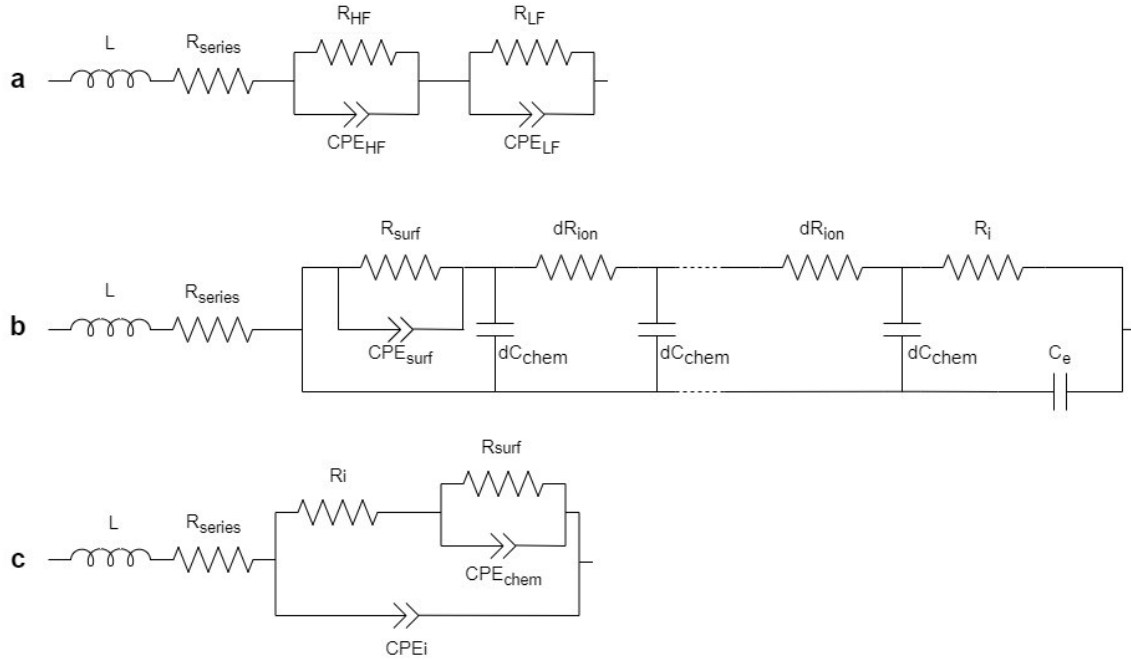


Figure 2-16. Equivalent circuits employed for fitting the impedance spectra measured in the thesis: circuit with two ZARC elements (a), generalized Jammik-Maier circuit (b) and simplified version derived from circuit b for cases not limited by ionic transport (c).

The analysis of EIS spectra is not constricted to modelling through equivalent circuit methods. Another type of analysis that is gaining popularity, in particular for analyzing SOFC impedances, is the Distribution of Relaxation Times (DRT)<sup>38</sup>. This analysis is based on the use of a mathematical approach that transforms the impedance spectra from the frequency domain to the time domain, based on the relaxation time parameter ( $\tau$ ), defined in equation (2-16).

$$\tau = (RQ)^{\frac{1}{n}} \quad (2-16)$$

This transformation results in treating the impedance data as a series of ZARC elements, each with its corresponding time constant  $\tau_i$ . The data is then represented as the value of the transformation function  $G(\tau)$  as a function of  $\tau$ , ideally presenting a peak for each representative transport phenomenon.  $G(\tau)$  is a normalized function that satisfies the condition in equation (2-17):

$$\int_{-\infty}^{\infty} G(\tau) d \ln \tau = 1 \quad (2-17)$$

In this thesis, DRT data has been employed for studying the LSCrMn-SDC based dense electrodes discussed in Chapter 3, in order to gain knowledge on the different mechanisms governing their electrochemical performance under reducing and oxidizing atmospheres.

The EIS characterization of the thin films studied in this thesis was performed with a Novocontrol impedance spectrometer, in the frequency range of 1 MHz – 0.1 Hz, open circuit potential, an AC amplitude of 50 mV for a total of 150 points. For the characterization of reversible electrodes discussed in Chapter 3, the measurements were performed in symmetric configuration with the films deposited on both sides of the CGO/YSZ substrates. For the characterization of the parent material-based oxygen electrodes discussed in Chapter 4, the configuration employed was asymmetric, with silver paste (Sigma-Aldrich) brushed in the backside of the substrates acting as the counter electrode. In all the cases, porous gold paste (Fuel Cell Materials) was brushed on top of the films to minimize any possible current percolation losses. The atmosphere set for the characterization in reducing conditions was 100 mL/min pure H<sub>2</sub> passing through a bubbler, while the measurements in an oxidizing atmosphere were performed using 100 mL/min synthetic air. The measurements were carried out in a ProboStat station (NorECs) placed in a vertical furnace, as it can be observed in Figure 2-17.

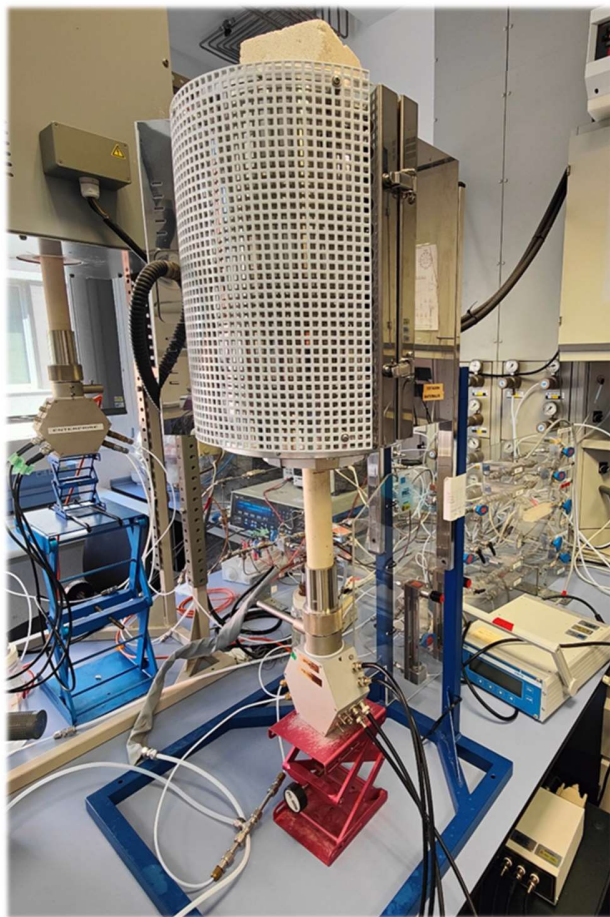


*Figure 2-17. ProboStat placed in a vertical furnace for the electrochemical characterization of thin film electrodes.*

### 2.5.2.2 Electrochemical characterization of thin film electrodes during thermal ageing in oxidizing conditions

The evolution of the electrochemical performance of the thin film electrodes studied in the present thesis was evaluated by tracking the changes in the impedance during thermal aging. The experiments have been carried out in the 700-800 °C range in similar conditions than for regular electrochemical characterization, i.e. AC amplitude of 50 mV, open circuit voltage in atmosphere of synthetic air flowing at 100 mL/min. The impedance spectra was measured with a time step of 30 min in between measurements. The potentiostats employed have been either a PARSTAT 2273 or a Novocontrol impedance. The cells were mounted in asymmetric configuration with the functional film deposited on one side of the CGO/YSZ substrate. Silver paste (Sigma-Aldrich) was brushed on the opposite side to act as a low-impedance electrode.

### 2.5.3 Electrochemical characterization in full device architectures

#### 2.5.3.1 Conceptualization of the measurement setup

Full devices were measured in ProboStat stations with customized holders and setups in order to optimize and explore the limitations when characterizing the performance of thin film SOCs and  $\mu$ SOCs. Different 3D printed alumina and YSZ holders were designed and printed (see Figure 2-18) in order to accommodate the dimension of the samples to be tested, either fabricated on YSZ or Si (100) single crystal substrates. Different geometrical designs were tested with the aim to improve aspects regarding sealing of the samples and placement of the current collectors. The holders were fabricated with a CERAMAKER 3D printed from 3DCERAM. Details on the equipment can be found in the work of Pesce et al.<sup>39</sup>.

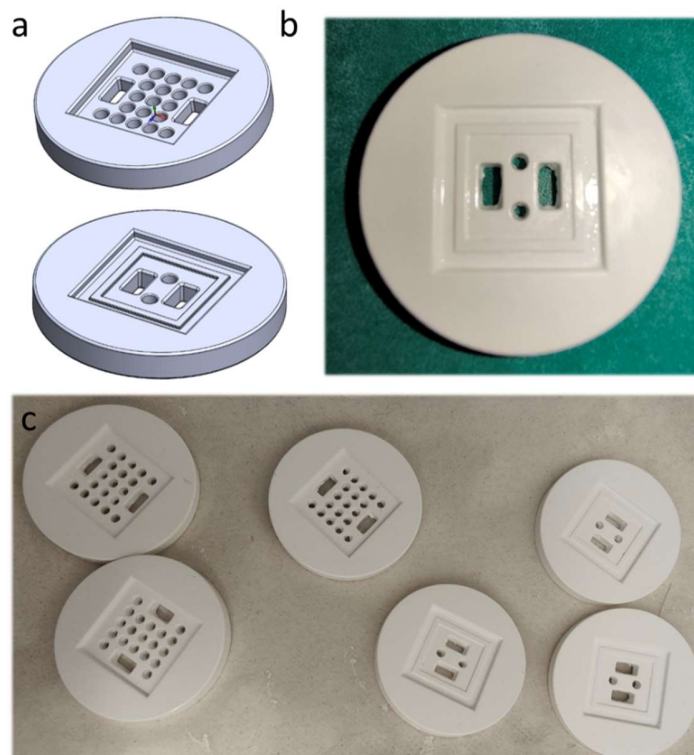


*Figure 2-18. 3D designs of sample holders for device characterization (a). Picture of a holder right after the printing process (b). Photograph of different holders after a curing treatment and ready to be used.*

A schematic of the setup employed for the characterization of thin film SOCs and  $\mu$ SOFCs is shown in Figure 2-19a. The 3D printed holder allowed for the accommodation of the squared samples (either the YSZ single crystal supported cells or the ceramic membranes supported on silicon) into the alumina tubes. Before mounting the sample, a metallic grid (gold or platinum) was placed on the holder in order to facilitate the collection of current to the electrical wires located in the inner tube (a platinum wire was passed through the holder holes in order to contact the grid). Platinum paste was brushed on the surface of the holder in order to improve the electrical connection. Then the sample was placed into the holder and the top current collector was placed, along with some gold paste (Fuel Cell Materials), again for improving current percolation. Once the cell was assembled, a ceramic paste was applied to seal the cell. Two formulations from Aremco were employed and tested, references 552 (alumina based) and 885 (zirconia based).

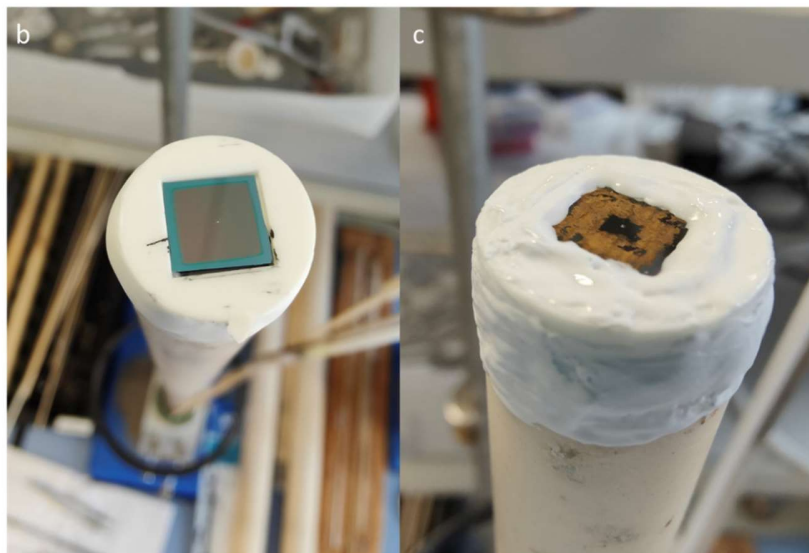
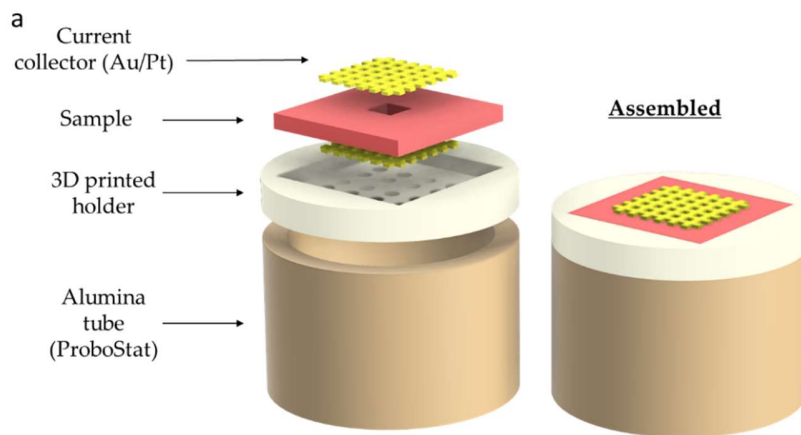


Figure 2-19. Schematic of the experimental setup employed for the electrochemical characterization of SOCs (a). Photographs of a  $\mu$ SOFC placed in the ProboStat setup before (b) and after applying the ceramic paste for sealing the cell (c).

Actual setup photographs of the sample cells mounted in the ProboStat station are shown in Figure 2-19b. The application of the ceramic paste was made along the joint between the sample and the holder (see Figure 2-19c), and left to dry before placing the cell into the furnace. For curing the sealant the sample was heated up in synthetic air atmosphere to 90 °C at a slope of 1 °C/min, dwelled for 2 h, then heated up to 260 °C at the same rate and dwelled for another 2 h. Aremco 885 ceramic paste required an additional dwell of 2 h at 370 °C, according to the specifics of the product. The sample was then ramped up at the same rate of 1 °C/min to the chosen minimum temperature of operation for the electrochemical characterization.



### 2.5.3.2 Electrical characterization

The SOCs and  $\mu$ SOFCs measured in this thesis were characterized with a PARSTAT 2273 potentiostat. Voltage-current curves, galvanostatic operation and EIS measurements were performed under different conditions of atmosphere (i.e. in SOFC and SOEC modes) and temperature. For measurements in electrolysis mode (SOEC), a mixed atmosphere of 50 % H<sub>2</sub>O:H<sub>2</sub> was set, while for fuel cell SOFC characterization the mixture was set to 3 % H<sub>2</sub>O:H<sub>2</sub>. The oxygen chamber was flown with synthetic air in all cases. Gas flows were adjusted to maximize the OCV of the cells. Additionally, OCV measurements were employed to evaluate the presence of gas leakages in the cell. Galvanostatic measurements were performed for characterizing the performance of the cells in the range of 0.3-3 mA. EIS was measured in the frequency range of 1 MHz – 100 mHz, 50 mV of amplitude, open circuit potential, 0.6 V of DC bias (SOFC), 1.2 V of bias (SOEC) and for a total of 150 points.

## 2.6 Characterization tools for studying material libraries

Part of the work developed in this thesis has been devoted to the study of combinatorial libraries of materials by employing high-throughput methods. In the next sections a description on the equipment and experimental setups utilized is given.

### 2.6.1 High throughput X-Ray Fluorescence\*\*

X-ray fluorescence (XRF) is an analytical technique that allows to retrieve compositional information on the sample measured. The working principle is based on the emission of fluorescence X-rays from the test material as a result of the interaction with a high energy primary X-Ray source. More specifically, the incident X-Rays provoke the ejection of an electron from the inner orbital shell of the material atoms. This results in the formation of an electron hole in the electron structure of the atom, a highly unstable state. This hole is then filled with an electron from the outer orbital levels of the atom. The lowering of the outer electron to a lower energy level results in the emission of the fluorescence X-Rays. The analysis of the energy released allows for the identification of the atoms present in the material, hence retrieving its composition.

In this thesis, XY-resolved XRF elemental characterization was carried out using primary beam energy of 12 keV and an incident angle of 10° between the source beam and the sample surface. The beam size was a square with sides of 0.3 mm, but due to the incident angle, the projected area onto the sample surface increased to 1.25 mm in the vertical direction. The fluorescence signal was collected with a 4-element silicon drift detector placed at a distance

---

\*\* High throughput XRF measurements were performed at SOLEIL Synchrotron, DIFFABS beamline. Data analysis was performed by Dr. Giulio Cordaro at Université Paris-Saclay, CentraleSupélec, CNRS, Laboratoire SPMS.

of 50 cm. The acquisition was performed within a square mesh coordinate system with sides of 110 mm and lateral steps of 1 mm in horizontal and vertical directions. Each XRF spectrum was collected with an integration time of 0.2 s, and the entire map acquisition took approximately 40 minutes. A total of 12100 XRF patterns were obtained, with almost 5000 focused on the sample. To enhance the signal/noise ratio of the XRF data, binning with 3 mm intervals was applied, resulting in about 500 patterns to study. A Matlab code was developed to analyze each XRF spectrum and calculate the elemental ratio between Mn, Fe, and Co. Figure 2-20 shows pictures of the setup employed for the measurement.

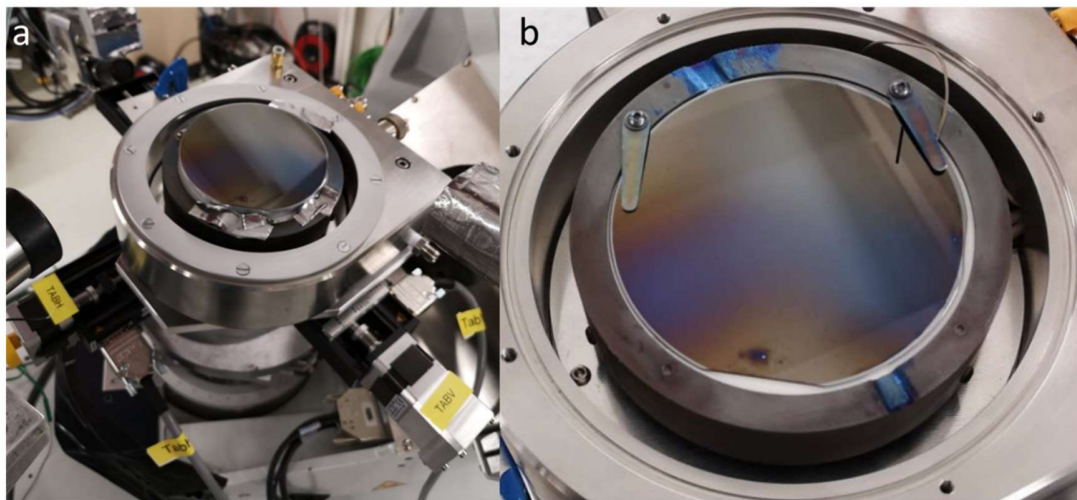


Figure 2-20. Measurement stage at DiffAbs beamline at SOLEIL synchrotron for XRF mapping of combinatorial wafers.

### 2.6.2 High throughput X-Ray Diffraction<sup>††</sup>

In-plane (XY) resolved structural characterization was performed using a Panalytical X'pert MRD X-ray diffractometer in the  $\omega$ - $2\theta$  Bragg-Brentano configuration. The instrument was equipped with a copper X-ray tube in line focus mode and a PIXcel3D detector in scanning line mode, with an active length of  $2.511^\circ 2\theta$ . The incident beam was modulated through  $1/8^\circ$  divergence, 4 mm vertical, and 0.02 rad Soller slits, leading to a spot size of approximately 2 mm<sup>2</sup>. Data acquisition was carried out within a square mesh coordinate system with sides of 90 mm and lateral steps of 5 mm in horizontal and vertical directions, resulting in a total of 289 diffractograms. Each XRD pattern was collected with a  $1.1^\circ$  tilt angle ( $\omega$ ) to reduce the intensity of the YSZ (200) and (400) reflections over the 20-80°  $2\theta$  range with  $0.02^\circ$  step and 140 s/step. The acquisition of each diffractogram took approximately 30 minutes, resulting in a total measurement time of about 142 hours.

---

<sup>††</sup> High throughput XRD measurements were performed and analyzed at Université Paris-Saclay, CentraleSupélec, CNRS, Laboratoire SPMS with the collaboration of Dr. Guilhem Dezanneau and Dr. Giulio Cordaro.

A custom Matlab code was developed to analyze the large number of diffractograms efficiently and obtain a sample map with the lattice parameters of LSMCF. The code identifies the presence of LSMCF and CGO peaks in each XRD pattern. All the identified peaks are fitted using a function composed of two pseudo-Voigt profiles, simulating the  $K_{\alpha 1}$  (1.5405929 Å) and  $K_{\alpha 2}$  (1.5444274 Å) Cu lines. The angular position in  $^{\circ}2\theta$  is calculated for each peak and used in a minimization routine to determine the sample displacement and the lattice parameter of the LSMCF deposition.

### 2.6.3 High throughput Spectroscopic Ellipsometry

The optical properties of the combinatorial films have been measured by spectroscopic ellipsometry, following the same principles explained in Section 2.3.5 of this chapter, with slight variations on the setup. A multiwavelength light source of the equipment was utilized instead of the monochromator source, as it allowed for the fast acquisition of ellipsometric spectra in the 1.5-5 eV energy range. An automatized XY stage was then employed for mapping the sample wafers. Figure 2-21a shows the setup with the wafer placed in the center of XY stage. For the mapping, cartesian grids presenting up to 300 points of measurement were defined (see Figure 2-21b). A batch processing functionality from the DeltaPsi2 analysis software from Horiba was employed to model and fit the maps obtained.

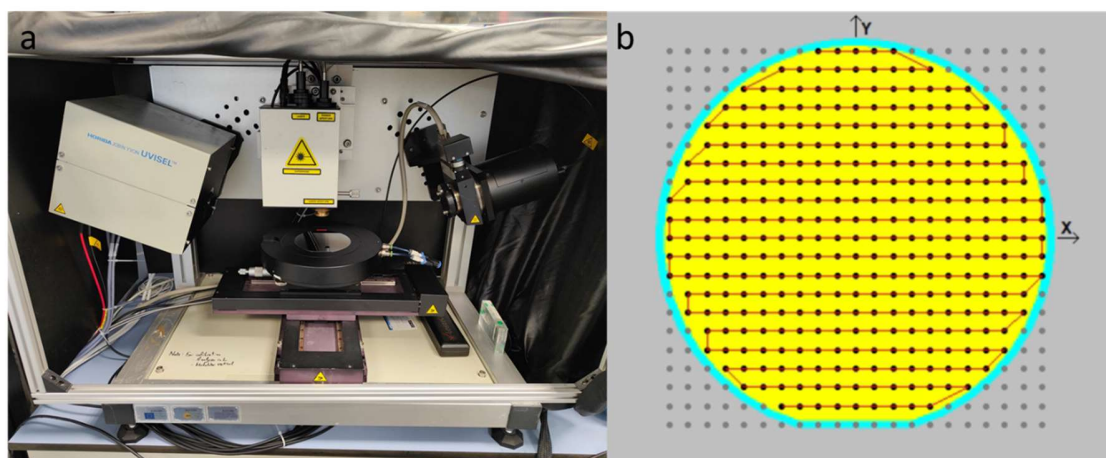


Figure 2-21. Picture of the setup with a combinatorial wafer placed to be measured by high throughput ellipsometry (a). Cartesian grid designed for mapping the sample.

### 2.6.4 Raman Spectroscopy

Raman Spectroscopy is a characterization technique based on the interaction of light with the sample, giving rise to Raman scattering. This is a type of inelastic scattering in which the incident light excites vibrational modes of the atomic bonds of the sample. The resulting interaction (reflected light) allows to retrieve information on the chemical nature present in the material, making it possible to obtain compositional and structural details. In this thesis,

Raman spectroscopy has been employed for characterizing the vibrational modes present in LSMCF combinatorial films, and their evolution with the changes in composition. Raman spectroscopy mappings were measured on a Xplora Nano equipment from HORIBA, as depicted in Figure 2-22a-b. The measurements were carried out with a x100 objective, grating of 1800 (450 – 850nm range), using a 638 nm laser LSMCF with a power filter of 25 %, slit of 200  $\mu\text{m}$  and hole of 500  $\mu\text{m}$ . The acquisition parameters were set to an acquisition time of 2-5 s with 15-30 accumulations. LSMCF combinatorial films deposited on Si (100) wafers were measured with a spacing of 7 mm between points. In order to adapt the equipment so the wafer could be measured systematically with the spacing selected, a holder was designed and 3D printed (see Figure 2-22c). For the analysis and evaluation of the spectra obtained, the Raman shift at the maximum of the peak present in the 550 – 700  $\text{cm}^{-1}$  range was evaluated.

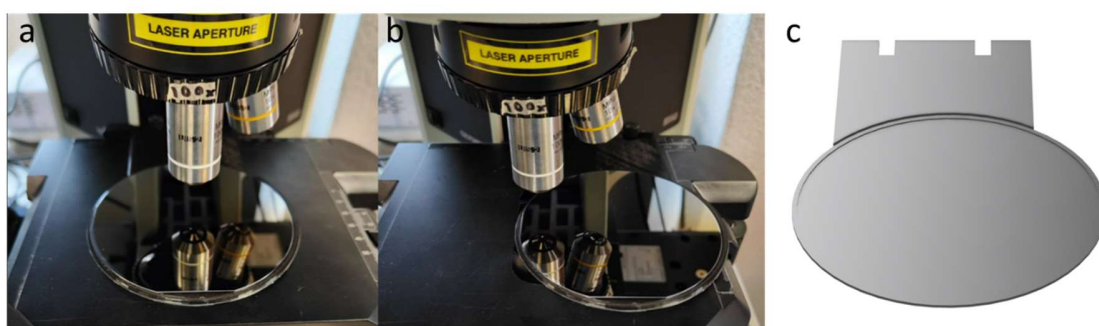


Figure 2-22. Experimental setup for the Raman Spectroscopy map. Optical photographs at different positions of the wafer (a-b) and 3D printing design of a custom made wafer holder.

### 2.6.5 Electrochemical test station

The electrochemical performance of the combinatorial LSMCF electrodes investigated in this thesis has been evaluated by customizing a commercial electrochemical test station with automated mapping capabilities. A large-size high temperature probe station (MicroXact CPS-HT) was employed to carry out the measurements. The station incorporates a hot stage made of metallic silver, capable of reaching temperatures up to 800  $^{\circ}\text{C}$  and up to 5-probe arms to contact the stage. The chamber was sealed during the measurements and synthetic air was passed through at a flow of 500 mL/min. For measuring the LSMCF samples two probes were utilized, i.e. a gold plated tip for contacting the top film, and a platinum wire contacting the back side of the wafer, as it is shown in the schematic of Figure 2-23. A low impedance silver paste electrode (Sigma-Aldrich) was brushed on the back of the combinatorial wafer, while a top layer of gold paste (Fuel Cell Materials) was applied to improve the electrical contact with the film. Then, the combinatorial sample was scribed prior to the experiment with an automatized diamond cutter in a 3x3  $\text{mm}^2$  square size pattern in order to measure specific LSMCF representative compositions.

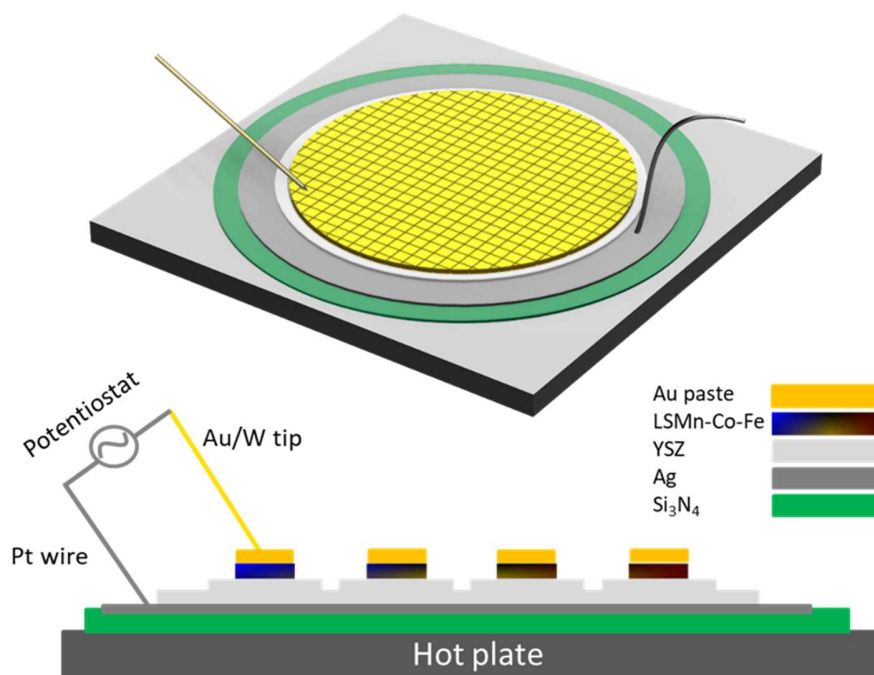


Figure 2-23. Schematic of the setup utilized for mapping the electrochemical performance of the combinatorial film (a).

The experimental setup incorporated a stainless steel metallic ring, clamp and alumina felt insulators to improve the homogeneity of the thermal distribution along the sample (see Figure 2-24a). Additionally, the effectiveness of the setup on the thermal distribution was checked with a FLIR E6-XT infrared thermal camera, with the chamber open and a set point temperature of 200 °C (Figure 2-24b). It can be observed that the metallic ring facilitates the thermal contact with the stage, while the temperature at the central part of the wafer is lower. The measurement performed allowed to map the LSMCF wafer at several temperatures in the 675-750 °C range. The time dedicated for the mapping at each temperature was critical in order to avoid possible drifts in the performance measured as a consequence of film degradation. With that aim, the conditions for the experiment and the selection of the points to be measured was carefully selected. EIS measurements were performed with a Novocontrol impedance spectrometer in the 1 MHz – 0.5 Hz frequency range, open circuit potential and 50 mV of amplitude. A total of 50 frequency points was measured per impedance spectra. In order to avoid drift effects in the impedance measured the sample was held for 15 min after reaching the temperature set. Additionally, several impedance spectra was measured at each point selected in order to confirm the absence of the thermal drift due to the contact with the gold probe.

The impedance spectra was fit with a modified Jamnik-Maier equivalent circuit (see Figure 2-16b) model in order to obtain a high quality fit for all the compositions measured. Two

main parameters extracted from the fitting were employed for the subsequent analysis, the series resistance, and the polarization resistance.

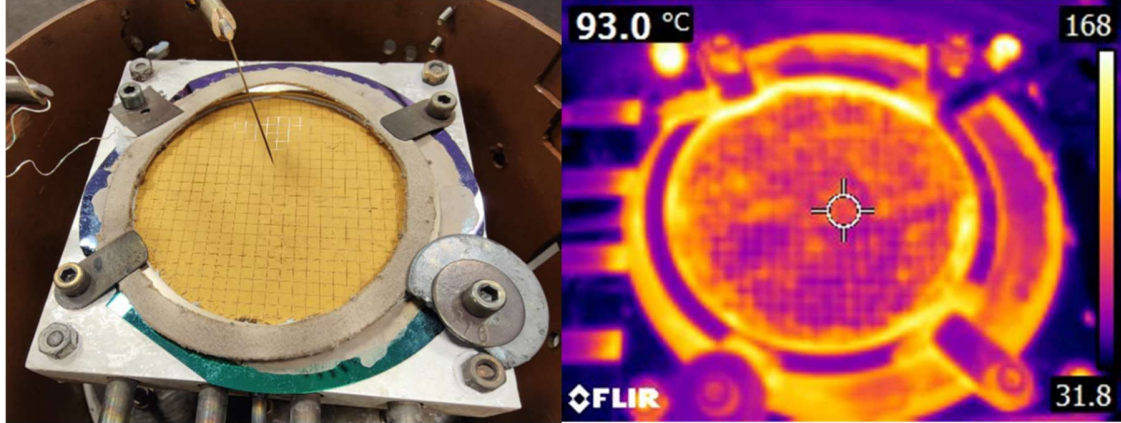


Figure 2-24. Picture of the setup employed for the electrochemical impedance mapping measurement (a). Thermal image obtained with a temperature set at 200 °C (b).

The series resistance was employed to obtain the temperature distribution along the wafer, through the Arrhenius-like behaviour of the ionic resistance of the YSZ substrate (see equation (2-18)). Where  $\sigma$  is the conductivity,  $k_b$  is the Boltzmann constant,  $E_a$  is the activation energy and  $\sigma_0$  is the pre-exponential factor.

$$\sigma(T) = \frac{\sigma_0}{T} e^{-\frac{E_a}{k_b T}} \quad (2-18)$$

With this aim, EIS measurements were performed to a reference YSZ chip sample with Ag-paste electrodes in a ProboStat setup (see Figure 2-17). The values of the series resistance obtained through the measurements were linearly fitted to equation (2-19) in order to obtain the dependence of the ionic resistance of the substrate with temperature. Please note that equation (2-18) derives in equation (2-19) by taking the natural logarithm and changing from conductivity magnitude to area specific resistance (ASR) –done to obtain a more direct expression to employ with the values obtained from the impedance–. The resulting linear equation was then employed during analysis of the EIS mapping experiments in order to calculate the real temperature at the wafer.

$$\ln \frac{T}{ASR} = \ln \frac{1}{ASR_0} - \frac{E_a}{k_b T} \quad (2-19)$$

Once the calculated temperature distribution was mapped along the wafer at each temperature set, a linear fit was obtained ( $T_{\text{real}}$  vs  $T_{\text{set}}$ ) in order to correct for artefacts coming from parasitic resistances in the setup. An example of this analysis is shown in Figure 2-25, which shows the calculated  $T_{\text{real}}$  values for six points of the analysis at different set temperatures. It can be observed that the linear fits fall quite closely to the majority of the corresponding data points, with a couple of exceptions. The linear fits were then employed

for quantifying the real temperature at each position of the wafer, preventing the presence of local points outside the observed trend that may lead to induced errors in the analysis.

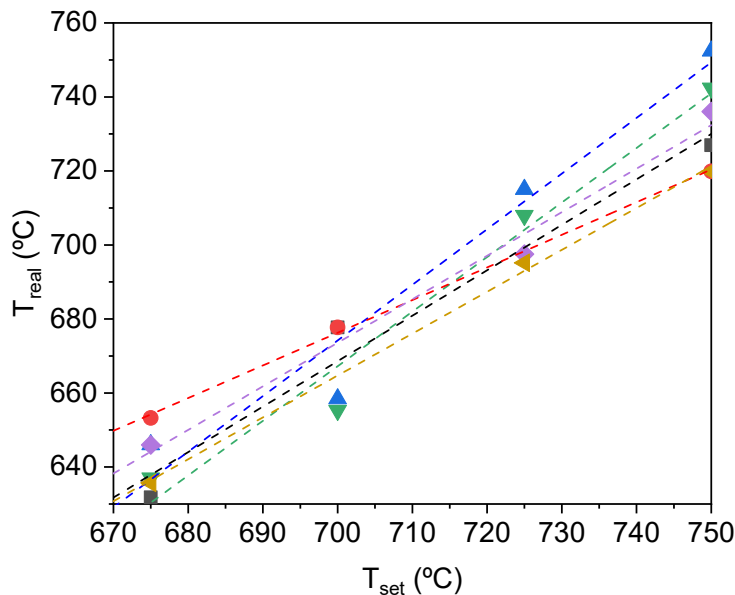


Figure 2-25. Plot showing the  $T_{real}$  vs  $T_{set}$  relation obtained for the analysis for an example collection of six points. The dashed lines correspond to linear fits of the scattered data.

The plots presented in Figure 2-26 show the calculated distribution of temperatures for all of the experiments performed. The maps show a temperature distribution similar to the thermal image obtained prior to the experiment, with the presence of points with higher temperature along the edges and colder spots in the central regions.

With this analysis, an Arrhenius fitting was calculated for the LSMCF combinatorial film. The pre-exponential factor and activation energy were extracted from the fitting, which allowed to calculate the equivalent ASR at a given temperature (see equation (2-19)). This analysis allowed to make a proper comparison of the ASR in the combinatorial wafer irrespectively of the differences in thermal distribution present in the setup. Reference samples of LSM, LSC and LSF were measured as described in Section 2.5.2.1 in order to give reference values of the electrochemical performance of each parent material and make a thorough comparison with the measurements done on the LSMCF combinatorial wafer.

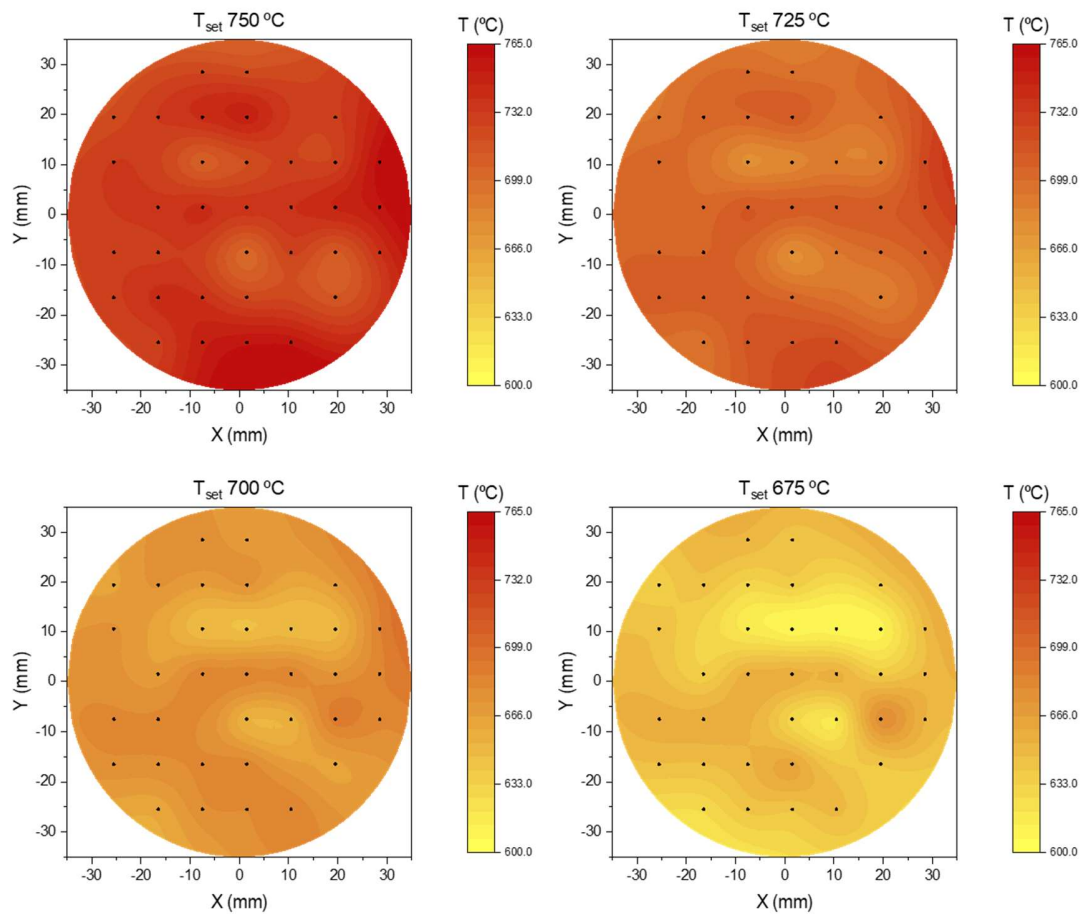


Figure 2-26. Distribution of the real temperature calculated and utilized in the Arrhenius analysis for each temperature set in the range 750-675 °C.

### 2.6.6 High Throughput Isotope Exchange Depth Profiling coupled with Secondary Ion Mass Spectrometry<sup>††</sup>

The oxygen mass transport properties of the LSMCF combinatorial wafer was explored by Isotope Exchange Depth Profiling (IEDP) coupled with ToF-SIMS<sup>40,41</sup>. This analytical technique allows to measure the oxygen kinetic parameters (i.e. the oxygen surface exchange coefficient ( $k^*$ ) and the oxygen diffusion coefficient ( $D^*$ )) of the material studied after carrying out an exchange treatment with isotopic oxygen ( $^{18}\text{O}$ ). This is done by sputtering the exchange sample and analyzing the composition in depth with ToF-SIMS. The amount of  $^{18}\text{O}$  detected in the film is employed then to determine the material activity with respect to oxygen incorporation.

<sup>††</sup> High throughput IEDP-SIMS was performed at Imperial College London, Department of Materials, Surface Analysis Facility, with the collaboration of Dr. Sarah Fearn and Dr. Andrea Cavallaro.



Depending on the kinetic properties of the material, as well as the conditions for the exchange, different oxygen profiles are measured. In general, most exchange treatments are designed so that the diffusion fronts of  $^{18}\text{O}$  do not penetrate the whole active material and that different fronts do not compete between each other (e.g. from lateral diffusion), in order to be able to extract the mass transport parameters. For bulk materials this is generally under control thanks to the dimension of the sample, contrary to the case of thin films. If these conditions are ensured, and with the absence of additional features influencing the kinetics, equation (2-20) can be employed for fitting the  $k^*$  and  $D^*$  of the material. This expression consists in the Crank's solution to plane diffusion on a semi-infinite media<sup>42</sup>.

$$f(^{18}\text{O}) = c_{bg} + (c_g - c_{bg}) * \left( \operatorname{erfc}\left(\frac{z}{2\sqrt{D^*t}}\right) - (\exp(hz + h^2D^*t) * \operatorname{erfc}\left(\frac{z}{2\sqrt{D^*t}} + \frac{\sqrt{D^*t}}{h}\right)) \right) \quad (2-20)$$

Where  $f(^{18}\text{O})$  is the fraction of  $^{18}\text{O}$  vs total oxygen measured,  $z$  is the penetration depth value,  $c_{bg}$  is the natural isotope background (0.2 %),  $c_g$  is the concentration of the enriched  $^{18}\text{O}$  gas employed in the treatment,  $t$  is the exchange time and parameter  $h$  is the  $D^*/k^*$  ratio. Nonetheless, there are phenomena that may result in deviation of the  $^{18}\text{O}$  fraction from an ideal transport model. Materials presenting open cavities, segregated impurities or an enhanced (or blocked) transport activity through grain boundaries are examples of these phenomena. In those conditions, calculating the mass transport properties through equation (2-20) might be an insufficient approach and a more complete calculation would be needed<sup>43</sup>. Additionally, if the oxygen transport activity of the material analysed is high, a planar or semi-planar profile might be obtained, characteristic of an exchange not limited by oxygen diffusion and only by the surface exchange coefficient. In these cases, the exchange coefficient can be estimated by solving the corresponding differential equation for constant flux transport, resulting in the expression in equation (2-21), where  $L$  is the layer thickness. The diffusivity cannot not be estimated in this regime.

$$k^* = -\frac{L}{t} \ln\left(1 - \frac{c - c_{bg}}{c_g - c_{bg}}\right) \quad (2-21)$$

In this thesis, IEDP-SIMS was employed for studying the oxygen kinetics of LSMCF combinatorial libraries. A combinatorial LSMCF film grown directly on a 3" diameter Si (100) substrate was selected for the analysis. The sample was enclosed in a quartz tube and pumped down to  $10^{-7}$  mbar. A first annealing at 400 °C in 200 mbar of pure oxygen (99.999 %) with  $^{18}\text{O}_2$  in the normal isotopic abundance was performed. After the first annealing, the tube was pumped down and re-filled with a ~90 %  $^{18}\text{O}_2$  enriched gas (200 mbar). The sample was quenched to room temperature once the exchange was completed. The conditions selected for the isotope exchange were 400 °C and 30 min. The  $^{18}\text{O}$  diffusion profile signal was recorded using a TOF-SIMS 5 instrument (IONTOF GmbH, Munster, Germany). The map was carried out by scanning the sample with a spacing of 3 mm in between the points measured. Figure 2-27 shows a picture of the sample after measuring two pieces of the

wafer. The numbers and arrows on the figure indicate the direction in which the measurements were done. A total of 480 points were measured by the end of the experiment.

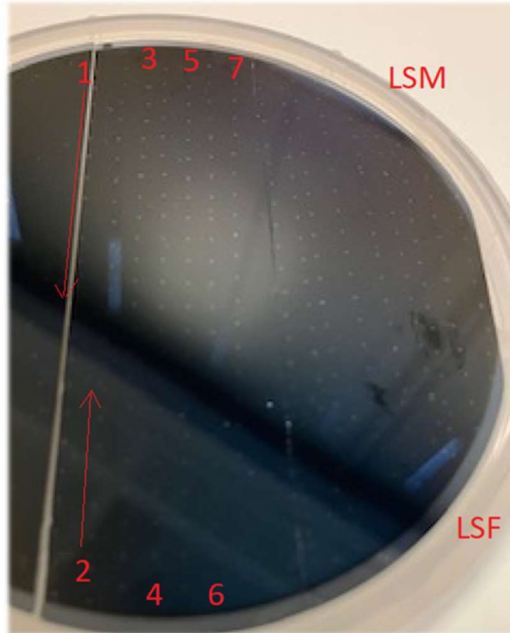


Figure 2-27. Photograph of a LSMCF wafer after IEDP-SIMS measurements. Numbers indicate the column and direction of the scan performed in the central piece.

In order to properly evaluate the profiles obtained, the depth axis had to be translated from sputter time units (i.e. the parameter measured during the analysis) to actual depth units. To do so, the thickness of the sample was previously measured by ellipsometry (see Figure 2-28a). Then, the appearance of the silicon signal (the Si<sup>-</sup> ion, specifically) was utilized as a reference for when the film was completely sputtered. Figure 2-28b shows the profile of several of the points measured, while Figure 2-28c shows the map of the sputtering time obtained for the whole wafer. Finally, the sputtering rate was calculated by dividing the time obtained with the values of the thickness measured initially. In order to calculate the sputtering rate for every point measured, an approximation was made by selecting the thickness values measured that was closest in terms of XY coordinates. Two approaches were employed for analysing the profile obtained. For the regions in which the <sup>18</sup>O fraction showed saturation (i.e., a planar or close to planar profile), the film was considered to be only limited by the oxygen surface exchange coefficient (*k*<sup>\*</sup>). In this case, a lower limit value of the oxygen diffusivity (*D*<sup>\*</sup><sub>min</sub> << *D*<sup>\*</sup><sub>real</sub>) was extracted given the relation in equation (2-22). For the calculus of *D*<sup>\*</sup><sub>min</sub> the relation was set as equal, leading to an underestimate value of *D*<sup>\*</sup>.

$$\frac{D^*}{k^*} \gg L \quad (2-22)$$

On the other hand, for the profiles that showed a decay in the  $^{18}\text{O}$  fraction approaching the natural  $^{18}\text{O}$  background concentration of 0.2 % in the film-substrate interface, the semi-infinite solution of oxygen diffusion was employed to obtain both  $D^*$  and  $k^*$  (see equation (2-20)). A reference value of 0.8 % of  $^{18}\text{O}$  fraction in the film-substrate interface was set to differentiate between the two models.

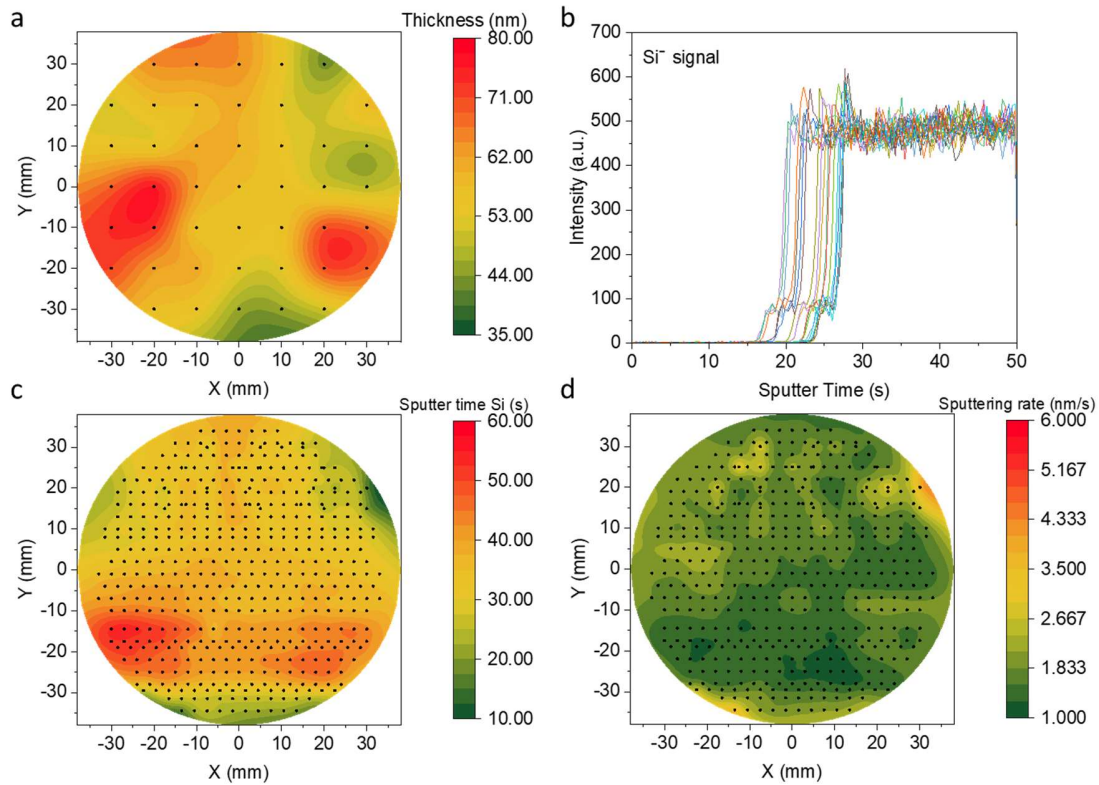


Figure 2-28. Analysis carried out for the processing of the IEDP-SIMS profiles obtained. Thickness measurement of the combinatorial film (a). Selection of SIMS profiles corresponding to the Si<sup>-</sup> signal (b). Sputter time characteristic of the appearance of the Si signal in the SIMS profile for all the points measured (c). Sputtering rate calculated from the film thickness and the sputter time of the Si signal (d).

## References

- (1) Sirvent, J. de D.; Buzi, F.; Baiutti, F.; Tarancón, A. Advances in Nanoengineered Air Electrodes: Towards High-Performance Solid Oxide Cells. In *Nanoengineered Materials for Solid Oxide Cells*; Develos-Bagarinao, K., Ed.; IOP Publishing, 2023; pp 1-1-1–35. <https://doi.org/10.1088/978-0-7503-4064-9ch1>.
- (2) Saranya, A. M.; Morata, A.; Pla, D.; Burriel, M.; Chiabrera, F.; Garbayo, I.; Hornés, A.; Kilner, J. A.; Tarancón, A. Unveiling the Outstanding Oxygen Mass Transport Properties of Mn-Rich Perovskites in Grain Boundary-Dominated  $\text{La}_{0.8}\text{Sr}_{0.2}(\text{Mn}_{1-x}\text{Co}_x)_{0.85}\text{O}_{3\pm\delta}$  Nanostructures. *Chem. Mater.* **2018**, *30* (16), 5621–5629. <https://doi.org/10.1021/acs.chemmater.8b01771>.
- (3) Chiabrera, F.; Garbayo, I.; López-Conesa, L.; Martín, G.; Ruiz-Caridad, A.; Walls, M.; Ruiz-González, L.; Kordatos, A.; Núñez, M.; Morata, A.; Estradé, S.; Chronos, A.; Peiró, F.; Tarancón, A. Engineering Transport in Manganites by Tuning Local Nonstoichiometry in Grain Boundaries. *Adv. Mater.* **2019**, *31* (4), 1805360. <https://doi.org/10.1002/adma.201805360>.
- (4) Chiabrera, F. M.; Baiutti, F.; Börgers, J. M.; Harrington, G. F.; Yedra, L.; Liedke, M. O.; Kler, J.; Nandi, P.; Sirvent, J. de D.; Santiso, J.; López-Haro, M.; Calvino, J. J.; Estradé, S.; Butterling, M.; Wagner, A.; Peiró, F.; De Souza, R. A.; Tarancón, A. The Impact of Mn Nonstoichiometry on the Oxygen Mass Transport Properties of  $\text{La}_{0.8}\text{Sr}_{0.2}\text{Mn}_y\text{O}_{3\pm\delta}$  Thin Films. *J. Phys. Energy* **2022**, *4* (4), 044011. <https://doi.org/10.1088/2515-7655/ac98df>.
- (5) Bianchini, M. Integration of Ceramic Thin Films in Silicon Technology for Energy Conversion and Oxygen Sensing, Universitat Autònoma de Barcelona, 2022.
- (6) Garbayo, I.; Pla, D.; Morata, A.; Fonseca, L.; Sabaté, N.; Tarancón, A. Full Ceramic Micro Solid Oxide Fuel Cells: Towards More Reliable MEMS Power Generators Operating at High Temperatures. *Energy Environ. Sci.* **2014**, *7* (11), 3617–3629. <https://doi.org/10.1039/c4ee00748d>.
- (7) Garbayo, I.; Esposito, V.; Sanna, S.; Morata, A.; Pla, D.; Fonseca, L.; Sabaté, N.; Tarancón, A. Porous  $\text{La}_{0.6}\text{Sr}_{0.4}\text{CoO}_{3-\delta}$  Thin Film Cathodes for Large Area Micro Solid Oxide Fuel Cell Power Generators. *J. Power Sources* **2014**, *248*, 1042–1049. <https://doi.org/10.1016/j.jpowsour.2013.10.038>.
- (8) Scafetta, M. D.; Xie, Y. J.; Torres, M.; Spanier, J. E.; May, S. J. Optical Absorption in Epitaxial  $\text{La}_{1-x}\text{Sr}_x\text{FeO}_3$  Thin Films. *Appl. Phys. Lett.* **2013**, *102* (8), 081904. <https://doi.org/10.1063/1.4794145>.
- (9) Mildner, S.; Hoffmann, J.; Blöchl, P. E.; Techert, S.; Jooss, C. Temperature- and Doping-Dependent Optical Absorption in the Small-Polaron System  $\text{Pr}_{1-x}\text{Ca}_x\text{MnO}_3$ . *Phys. Rev. B - Condens. Matter Mater. Phys.* **2015**, *92* (3), 035145. <https://doi.org/10.1103/PhysRevB.92.035145>.
- (10) Nomerovannaya, L. V.; Makhnev, A. A.; Romyantsev, A. Y. Evolution of the Optical Properties of Single-Crystal  $\text{La}_{1-x}\text{Sr}_x\text{MnO}_3$ . *Phys. Solid State* **1999**, *41* (8), 1322–1326. <https://doi.org/10.1134/1.1130991>.

- (11) Brongersma, H.; Draxler, M.; Deridder, M.; Bauer, P. Surface Composition Analysis by Low-Energy Ion Scattering. *Surf. Sci. Rep.* **2007**, *62* (3), 63–109. <https://doi.org/10.1016/j.surfrep.2006.12.002>.
- (12) Niania, M.; Sharpe, M.; Webb, R.; Kilner, J. A. The Surface of Complex Oxides; Ion Beam Based Analysis of Energy Materials. *Nucl. Instrum. Methods Phys. Res. Sect. B Beam Interact. Mater. At.* **2020**, *480*, 27–32. <https://doi.org/10.1016/j.nimb.2020.07.022>.
- (13) Verma, P. Tip-Enhanced Raman Spectroscopy: Technique and Recent Advances. *Chem. Rev.* **2017**, *117* (9), 6447–6466. <https://doi.org/10.1021/acs.chemrev.6b00821>.
- (14) Wagner, A.; Butterling, M.; Liedke, M. O.; Potzger, K.; Krause-Rehberg, R. Positron Annihilation Lifetime and Doppler Broadening Spectroscopy at the ELBE Facility; Newport News, VA, USA, 2018; p 040003. <https://doi.org/10.1063/1.5040215>.
- (15) Tuomisto, F.; Makkonen, I. Defect Identification in Semiconductors with Positron Annihilation: Experiment and Theory. *Rev. Mod. Phys.* **2013**, *85* (4), 1583–1631. <https://doi.org/10.1103/RevModPhys.85.1583>.
- (16) Jensen, K. O.; Walker, A. B. Positron Thermalization and Non-Thermal Trapping in Metals. *J. Phys. Condens. Matter* **1990**, *2* (49), 9757–9775. <https://doi.org/10.1088/0953-8984/2/49/004>.
- (17) Jorch, H. H.; Lynn, K. G.; McMullen, T. Positron Diffusion in Germanium. *Phys. Rev. B* **1984**, *30* (1), 93–105. <https://doi.org/10.1103/PhysRevB.30.93>.
- (18) Krause-Rehberg, R.; Leipner, H. S. *Positron Annihilation in Semiconductors: Defect Studies*; Springer series in solid-state sciences; Springer: Berlin; New York, 1999.
- (19) Dryzek, J.; Horodek, P. GEANT4 Simulation of Slow Positron Beam Implantation Profiles. *Nucl. Instrum. Methods Phys. Res. Sect. B Beam Interact. Mater. At.* **2008**, *266* (18), 4000–4009. <https://doi.org/10.1016/j.nimb.2008.06.033>.
- (20) Selim, F. A. Positron Annihilation Spectroscopy of Defects in Nuclear and Irradiated Materials- a Review. *Mater. Charact.* **2021**, *174*, 110952. <https://doi.org/10.1016/j.matchar.2021.110952>.
- (21) Clement, M.; de Nijs, J. M. M.; Balk, P.; Schut, H.; van Veen, A. Analysis of Positron Beam Data by the Combined Use of the Shape- and Wing-Parameters. *J. Appl. Phys.* **1996**, *79* (12), 9029–9036. <https://doi.org/10.1063/1.362635>.
- (22) Liedke, M. O.; Anwand, W.; Bali, R.; Cornelius, S.; Butterling, M.; Trinh, T. T.; Wagner, A.; Salamon, S.; Walecki, D.; Smekhova, A.; Wende, H.; Potzger, K. Open Volume Defects and Magnetic Phase Transition in Fe<sub>60</sub>Al<sub>40</sub> Transition Metal Aluminide. *J. Appl. Phys.* **2015**, *117* (16), 163908. <https://doi.org/10.1063/1.4919014>.
- (23) Anwand, W.; Brauer, G.; Butterling, M.; Kissener, H. R.; Wagner, A. Design and Construction of a Slow Positron Beam for Solid and Surface Investigations. *Defect Diffus. Forum* **2012**, *331*, 25–40. <https://doi.org/10.4028/www.scientific.net/DDF.331.25>.
- (24) Hirschmann, E.; Butterling, M.; Hernandez Acosta, U.; Liedke, M. O.; Attallah, A. G.; Petring, P.; Görler, M.; Krause-Rehberg, R.; Wagner, A. A New System for Real-Time Data Acquisition and Pulse Parameterization for Digital Positron Annihilation Lifetime Spectrometers with High Repetition Rates. *J. Instrum.* **2021**, *16* (08), P08001. <https://doi.org/10.1088/1748-0221/16/08/P08001>.

- (25) Olsen, J. V.; Kirkegaard, P.; Pedersen, N. J.; Eldrup, M. PALSfit: A New Program for the Evaluation of Positron Lifetime Spectra. *Phys. Status Solidi C* **2007**, *4* (10), 4004–4006. <https://doi.org/10.1002/pssc.200675868>.
- (26) van der Pauw, L. J. A Method of Measuring Specific Resistivity and Hall Effect of Discs of Arbitrary Shape. *Philips Res. Rep.* **1958**, *13* (1).
- (27) Chan, W. K. On the Calculation of the Geometric Factor in a van Der Pauw Sheet Resistance Measurement. *Rev. Sci. Instrum.* **2000**, *71* (10), 3964–3965. <https://doi.org/10.1063/1.1290496>.
- (28) Nielsen, J.; Hjelm, J. Impedance of SOFC Electrodes: A Review and a Comprehensive Case Study on the Impedance of LSM:YSZ Cathodes. *Electrochimica Acta* **2014**, *115*, 31–45. <https://doi.org/10.1016/j.electacta.2013.10.053>.
- (29) Vadhva, P.; Hu, J.; Johnson, M.; Stocker, R.; Braglia, M.; Brett, D.; Rettie, A. Electrochemical Impedance Spectroscopy for All-Solid-State Batteries: Theory, Methods and Future Outlook. *ChemElectroChem* **2021**, *8* (11), 1930–1947. <https://doi.org/10.1002/celec.202100108>.
- (30) Prodromidis, M. I. Impedimetric Immunosensors—A Review. *Electrochimica Acta* **2010**, *55* (14), 4227–4233. <https://doi.org/10.1016/j.electacta.2009.01.081>.
- (31) Lasia, A. *Electrochemical Impedance Spectroscopy and Its Applications*; Springer New York: New York, NY, 2014. <https://doi.org/10.1007/978-1-4614-8933-7>.
- (32) Lazanas, A. Ch.; Prodromidis, M. I. Electrochemical Impedance Spectroscopy—A Tutorial. *ACS Meas. Sci. Au* **2023**, *3* (3), 162–193. <https://doi.org/10.1021/acsmesuresciau.2c00070>.
- (33) Jamnik, J.; Maier, J. Generalised Equivalent Circuits for Mass and Charge Transport: Chemical Capacitance and Its Implications. *Phys. Chem. Chem. Phys.* **2001**, *3* (9), 1668–1678. <https://doi.org/10.1039/b100180i>.
- (34) Jamnik, J. Impedance Spectroscopy of Mixed Conductors with Semi-Blocking Boundaries. *Solid State Ion.* **2003**, *157* (1–4), 19–28. [https://doi.org/10.1016/S0167-2738\(02\)00183-2](https://doi.org/10.1016/S0167-2738(02)00183-2).
- (35) Usiskin, R. E.; Maruyama, S.; Kucharczyk, C. J.; Takeuchi, I.; Haile, S. M. Probing the Reaction Pathway in  $(\text{La}_{0.8}\text{Sr}_{0.2})_{0.95}\text{MnO}_{3+\delta}$  Using Libraries of Thin Film Microelectrodes. *J. Mater. Chem. A* **2015**, *3* (38), 19330–19345. <https://doi.org/10.1039/c5ta02428e>.
- (36) Chiabrera, F.; Morata, A.; Pacios, M.; Tarancón, A. Insights into the Enhancement of Oxygen Mass Transport Properties of Strontium-Doped Lanthanum Manganite Interface-Dominated Thin Films. *Solid State Ion.* **2017**, *299*, 70–77. <https://doi.org/10.1016/j.ssi.2016.08.009>.
- (37) Baumann, F. S.; Fleig, J.; Habermeier, H.-U.; Maier, J. Impedance Spectroscopic Study on Well-Defined  $(\text{La,Sr})(\text{Co,Fe})\text{O}_{3-\delta}$  Model Electrodes. *Solid State Ion.* **2006**, *177* (11–12), 1071–1081. <https://doi.org/10.1016/j.ssi.2006.02.045>.
- (38) Boukamp, B. A.; Rolle, A. Use of a Distribution Function of Relaxation Times (DFRT) in Impedance Analysis of SOFC Electrodes. *Solid State Ion.* **2018**, *314* (September 2017), 103–111. <https://doi.org/10.1016/j.ssi.2017.11.021>.

- (39)Pesce, A.; Hornés, A.; Núñez, M.; Morata, A.; Torrell, M.; Tarancón, A. 3D Printing the next Generation of Enhanced Solid Oxide Fuel and Electrolysis Cells. *J. Mater. Chem. A* **2020**, *8* (33), 16926–16932. <https://doi.org/10.1039/D0TA02803G>.
- (40)De Souza, R. A.; Zehnpfenning, J.; Martin, M.; Maier, J. Determining Oxygen Isotope Profiles in Oxides with Time-of-Flight SIMS. *Solid State Ion.* **2005**, *176* (15–16), 1465–1471. <https://doi.org/10.1016/j.ssi.2005.03.012>.
- (41)Kilner, J. A.; Skinner, S. J.; Brongersma, H. H. The Isotope Exchange Depth Profiling (IEDP) Technique Using SIMS and LEIS. *J. Solid State Electrochem.* **2011**, *15* (5), 861–876. <https://doi.org/10.1007/s10008-010-1289-0>.
- (42)Crank, J. *The Mathematics of Diffusion*, 2nd ed.; Clarendon Press: Oxford, 1975.
- (43)Thoreton, V.; Niania, M.; Druce, J.; Tellez, H.; Kilner, J. Oxygen Diffusion in Ceramic Mixed Conducting  $\text{La}_{0.6}\text{Sr}_{0.4}\text{Co}_{0.2}\text{Fe}_{0.8}\text{O}_{3-\delta}$ : The Role of Grain and Twin Boundaries. *J. Electrochem. Soc.* **2022**, *169*, 044513. <https://doi.org/10.1149/1945-7111/ac6396>.

3. *Thin film nanostructures for symmetrical and fuel electrodes in solid oxide cells*



3.1 Motivation .....	89
3.2 Ceria-based state-of-the-art all-ceramic hydrogen electrode.....	92
3.3 NiCGO thin films for hydrogen electrode application in thin film SOCs .....	94
3.3.1 Microstructural characterization of the NiCGO thin film hydrogen electrodes.....	94
3.3.2 Electrochemical performance of the NiCGO thin film hydrogen electrodes.....	96
3.4 Functional layers based on LSCrMn-SDC heterostructures .....	99
3.4.1 Development of dense LSCrMn-SDC functional layers for hydrogen and symmetric electrodes.....	99
3.4.1.1 Microstructural characterization of the thin film heterostructures.....	99
3.4.1.2 Measurement of the sheet conductivity under reducing and oxidizing conditions.....	105
3.4.1.3 Electrochemical performance of the heterostructures.....	107
3.4.1.4 Evolution of the electrochemical performance of the LSCrMn-SDC nanocomposite on thermal degradation.....	113
3.4.2 Optimization of LSCrMn-SDC thin film microstructure for anode application.....	114
3.4.2.1 Structural characterization of microstructure-variant LSCrMn-SDC thin films .....	115
3.4.2.2 Electrochemical performance of microstructure-variant LSCrMn-SDC heterostructures on hydrogen oxidation .....	118
3.5 Conclusions .....	123
References.....	125

### 3.1 Motivation\*

This chapter is dedicated to the study of thin film based heterostructures and nanocomposites as potential candidates to be applied as symmetric and fuel electrodes for high-temperature applications. As discussed in Chapter 1, hydrogen electrodes in solid oxide cells (SOCs) generally consist in porous metals<sup>2</sup> and ceramic-metal composites (cermets)<sup>3-5</sup>. Oxide materials suppose a promising alternative to overcome the limitations of the state-of-the-art electrodes, mainly in terms of structural stability, sulphur poisoning<sup>6</sup> and poor current collection of porous phases. The most widely known all-ceramic materials employed as hydrogen electrodes in SOC are based in lanthanum chromites and doped-ceria. More specifically, the use of  $\text{La}_{0.75}\text{Sr}_{0.25}\text{Cr}_{0.5}\text{Mn}_{0.5}\text{O}_3$  (LSCrMn) has been extensively studied in the literature<sup>7-10</sup>, mainly due to its mixed ionic-electronic conduction behavior and its stability in reducing conditions<sup>11</sup>. In the case of ceria, it presents excellent catalytic activity for the hydrogen oxidation reaction (HOR), as reported in a large number of publications<sup>12-15</sup>. Nonetheless, doped-ceria materials are characterized by limited electronic conductivity<sup>16,17</sup>, which may lead to additional overpotential losses. In order to overcome these limitations, this chapter investigates the suitability of applying these materials through nanostructuring approaches, resulting in electrochemically active functional layers and electrodes for hydrogen oxidation. Several strategies have been explored with this purpose: i) making use of a novel cermet with low metal content, ii) fabricating dual-phase thin film nanostructures and iii) optimizing the microstructure of the nanostructures through changes in pulsed laser deposition (PLD) fabrication conditions.

Section 3.2 introduces a porous  $\text{Ce}_{0.8}\text{Sm}_{0.2}\text{O}_2$  (SDC) layer deposited by PLD and previously optimized by our group. This material is taken as the all-ceramic hydrogen electrode of reference in this chapter. Even though the material presents high electrochemical activity for hydrogen oxidation, it shows important limitations for the application aimed in this thesis. The porous microstructure makes it incompatible for device integration beyond 1-cell architectures. Additionally, the SDC material shows poor electronic conductivity, intensified by the presence of a porous microstructure, which also limits its implementation in real device systems. For this reason, novel materials aimed at overcoming these limitations are explored in this chapter.

The use of novel formulations of  $\text{Ni-Ce}_{0.9}\text{Gd}_{0.1}\text{O}_2$  (NiCGO) nanocomposites with low Ni content and the optimization of electrode microstructure are discussed in Section 3.3. A

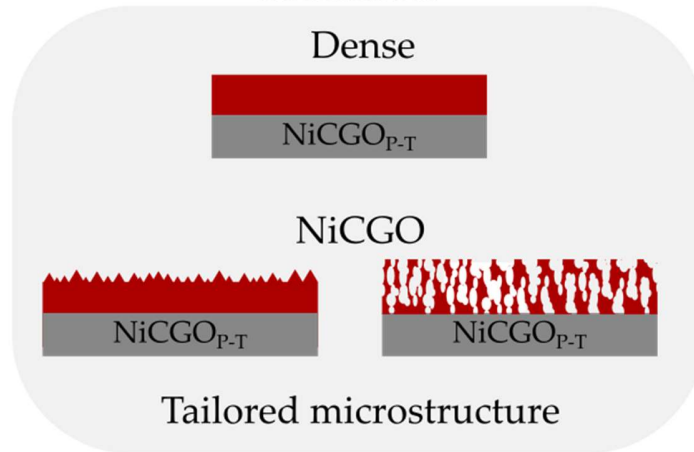
---

\* Part of the work presented on this chapter is adapted from Sirvent, J. de D.; Carmona, A.; Rapenne, L.; Chiabrera, F.; Morata, A.; Burriel, M.; Baiutti, F.; Tarancón, A. Nanostructured  $\text{La}_{0.75}\text{Sr}_{0.25}\text{Cr}_{0.5}\text{Mn}_{0.5}\text{O}_3$ - $\text{Ce}_{0.8}\text{Sm}_{0.2}\text{O}_2$  Heterointerfaces as All-Ceramic Functional Layers for Solid Oxide Fuel Cell Applications. *ACS Appl. Mater. Interfaces* **2022**, *14* (37), 42178–42187. <https://doi.org/10.1021/acsami.2c14044>, under Creative Commons Attribution 4.0 International Public License<sup>1</sup>.

recent publication reported the promising activity of NiCGO electrodes with surprisingly low content of Ni<sup>18</sup>. The work carried out in this section explores the possibilities that this formulation offers on the HOR when implementing changes in the film microstructure. Different dense-to-porous microstructured thin films were fabricated and studied by means of impedance spectroscopy. In Section 3.4.1 of this chapter, the fundamental electrochemical properties of thin-film heterostructures having potential application as hydrogen and symmetric electrode functional layers are investigated, namely: an intermixed LSCrMn-SDC nanocomposite, and a bilayer with a thin layer of SDC deposited on top of the LSCrMn film. Electrochemical impedance spectroscopy (EIS) and conductivity measurements are employed in order to analyse the enhancement derived from heterostructuring under both oxidizing and reducing conditions. The nanocomposite performance evolution on thermal degradation after a period of 400 h is also studied. Section 3.4.2 is focused on the optimization of the microstructure of the LSCrMn-SDC heterostructures explored in Section 3.4.1 for enhancing the activity as hydrogen electrodes. Pursuing this goal, different fabrication conditions are explored by i) reducing the temperature and ii) increasing the oxygen partial pressure during the PLD deposition. The resulting films were studied by means of structural characterization techniques and impedance spectroscopy. The evolution of the microstructure observed after the electrochemical analysis is also discussed. Given the large amount of samples studied in this chapter, Figure 3-1 shows a schematic of the main features of the thin films studied in terms of microstructure and composition, and classified by section.

## Nanostructured thin film electrodes

### Section 3.3



### Section 3.4

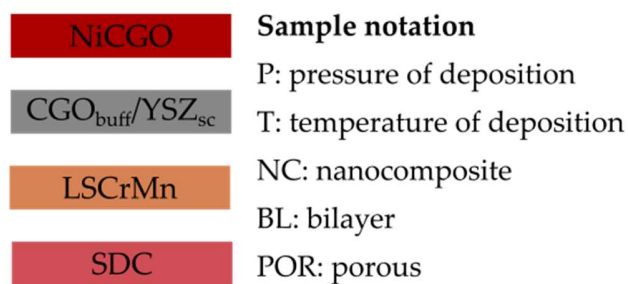
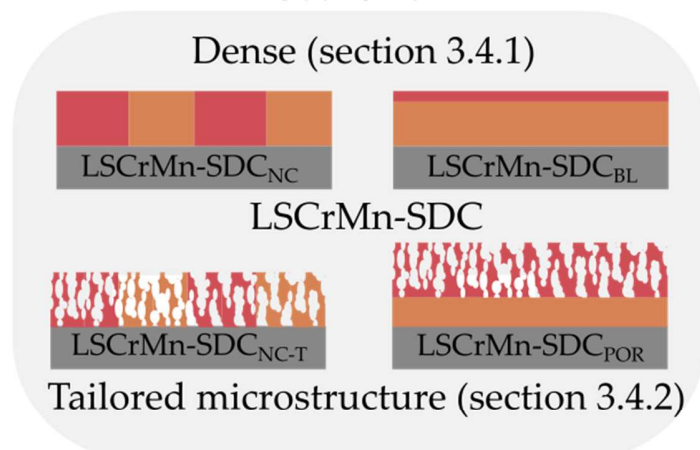


Figure 3-1. Schematic of the nanostructured thin film materials studied in the chapter specified for each section.

### 3.2 Ceria-based state-of-the-art all-ceramic hydrogen electrode

As previously mentioned, porous SDC was considered as the state-of-the-art all-ceramic hydrogen electrode in this work. This material was fabricated by PLD on yttria-stabilized zirconia (YSZ) substrates following an approach based on previous experience in the group<sup>19</sup>. The parameters for the deposition were set with the aim of obtaining highly porous layers, as described in Chapter 2 (section 2.2.1). In particular, the oxygen partial pressure in the PLD chamber was fixed to 200 mTorr, and the deposition temperature was set to 100 °C. Applying these conditions to the deposition allows to fabricate layers with increased roughness and exposed area, as generally results in the generation of a larger number of nucleation sites<sup>20</sup>. In this section, a general description of the structural, microstructural and electrochemical properties of the state-of-the-art porous SDC electrode is given.

Figure 3-2a shows a micrograph obtained by scanning electron microscopy (SEM) of the porous SDC layer obtained under the conditions described. The microstructure presents a homogeneous distribution of globular grains with slight spatial separation in between them. In order to improve the crystallinity of the layer and to increase its porosity, the sample was thermally treated at 800 °C for 1 h in a furnace under ambient air. The final microstructure obtained with the post-deposition thermal treatment can be visualized in Figure 3-2b. One can observe that the microstructure evolves into a more open structure, resulting in an increase of the solid/gas interface area of the material. Figure 3-2c shows a cross section of the film after the thermal treatment. Note that a platinum layer is placed on top of the layer in order to perform electrochemical characterization. Despite the evolved microstructure observed in the top-view micrograph, the layer maintains ordered vertical growth and homogenous distribution along the film. Additionally, Figure 3-2d shows the X-Ray Diffraction (XRD) patterns obtained for the porous SDC layers both before and after the annealing performed. In both cases, the diffraction signal observed indicates the presence of crystallographic phases. In particular, the SDC grows with orientation on the (111), (200), (220) and (311) crystallographic planes. The thermal annealing seems to improve the crystallinity of the film as the diffraction peaks observed are slightly better defined than in the pristine layer. Figure 3-2e shows the Arrhenius-like evolution of the area specific resistance (ASR) measured under pure hydrogen atmosphere. A measurement performed in a dense SDC film (cf. later in section 3.4.1) is also presented for comparison purposes. Porous SDC shows an ASR in the range of  $\approx 0.2\text{-}1.0 \text{ } \Omega\cdot\text{cm}^2$  in the 600-750 °C temperature range, while the dense layer presents an ASR two orders of magnitude larger (i.e.  $> 10 \text{ } \Omega\cdot\text{cm}^2$ ) in the same temperature range.

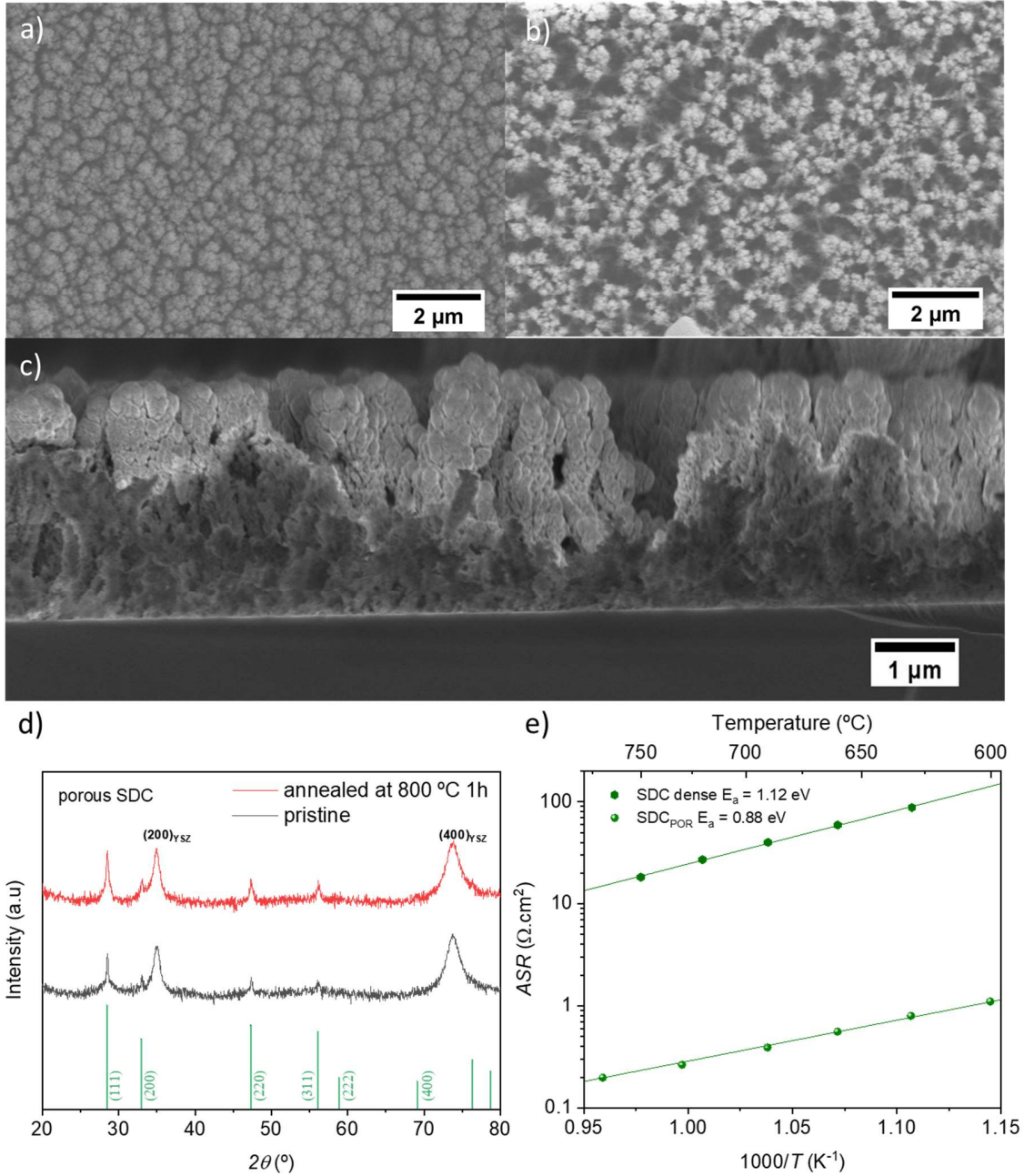


Figure 3-2. SEM micrographs of porous SDC: as deposited (a) and after the thermal treatment (b). Cross section of the thermally treated porous SDC layer (c). XRD patterns obtained for the porous SDC layers pristine and after thermal annealing (d). Reference diffraction patterns are represented on the bottom for SDC ( $Fm-3m$  #225, in green)<sup>21</sup>. The most representative peaks are labelled. YSZ ( $h00$ ) peaks are labelled directly on the top diffraction pattern as a common reference. Evolution of the ASR with temperature for dense and porous SDC (e).

### 3.3 NiCGO thin films for hydrogen electrode application in thin film SOCs

#### 3.3.1 Microstructural characterization of the NiCGO thin film hydrogen electrodes

In order to study the possibilities for maximizing the electrochemical performance and reducing the temperature of operation of fuel electrodes in thin film form, a change in formulation has been explored. For that, the electrochemical properties of novel NiCGO nanocomposite (2 vol% of Ni) layers were fabricated, following the results obtained by Park<sup>18</sup> et al. for the development of an efficient low metal-containing cermet. The films were grown under different conditions (presenting variable microstructure), as described in Table 3-1.

*Table 3-1. Description of the NiCGO samples studied in this work.*

Sample	O <sub>2</sub> pressure (mTorr)	Temperature (°C)	Thermal treatment
NiCGO <sub>5mT-700C</sub>	5	700	-
NiCGO <sub>150mT-700C</sub>	150	700	-
NiCGO <sub>200mT-500C</sub>	200	500	700 °C 1h
NiCGO <sub>200mT-100C</sub>	200	100	700 °C 1h

Figure 3-3a shows a top-view micrograph measured by Atomic Force Microscopy (AFM) of a NiCGO thin film deposited at 700 °C and 5 mTorr of oxygen partial pressure (NiCGO<sub>5mT-700C</sub>). The outcome was the fabrication of a dense electrode, as it can be clearly seen in the smooth topography represented in the micrograph. Similarly, Figure 3-3b depicts a SEM micrograph of a NiCGO thin film deposited at 150 mTorr (NiCGO<sub>150mT-700C</sub>) with the aim to increase the porosity of the thin film, leading to a higher surface area and thus improving the electrochemical activity of the electrode. The micrograph clearly shows the growth of a rougher surface with crystallite sizes of 10-20 nm. The micrograph in Figure 3-3c corresponds to the NiCGO<sub>200mT-500C</sub> sample, fabricated at a higher oxygen partial pressure of 200 mTorr, a lower temperature of 500 °C and annealed at 700 °C for 1 h. The film presents similar microstructure than for the case deposited at 700 °C, with larger crystallites in the range of 25-40 nm in length and seemingly more exposed area due to increased roughness, resulting in a mesoporous surface. Additionally, Figure 3-3d shows the microstructure of NiCGO<sub>200mT-500C</sub>, a layer deposited at 100 °C and thermally annealed at 700 °C for 1 h. The microstructure presents open columnar growth with high porosity, as in the case of the porous SDC discussed in the previous section. This is obtained due to the PLD conditions applied and the similarities in composition between the two films.

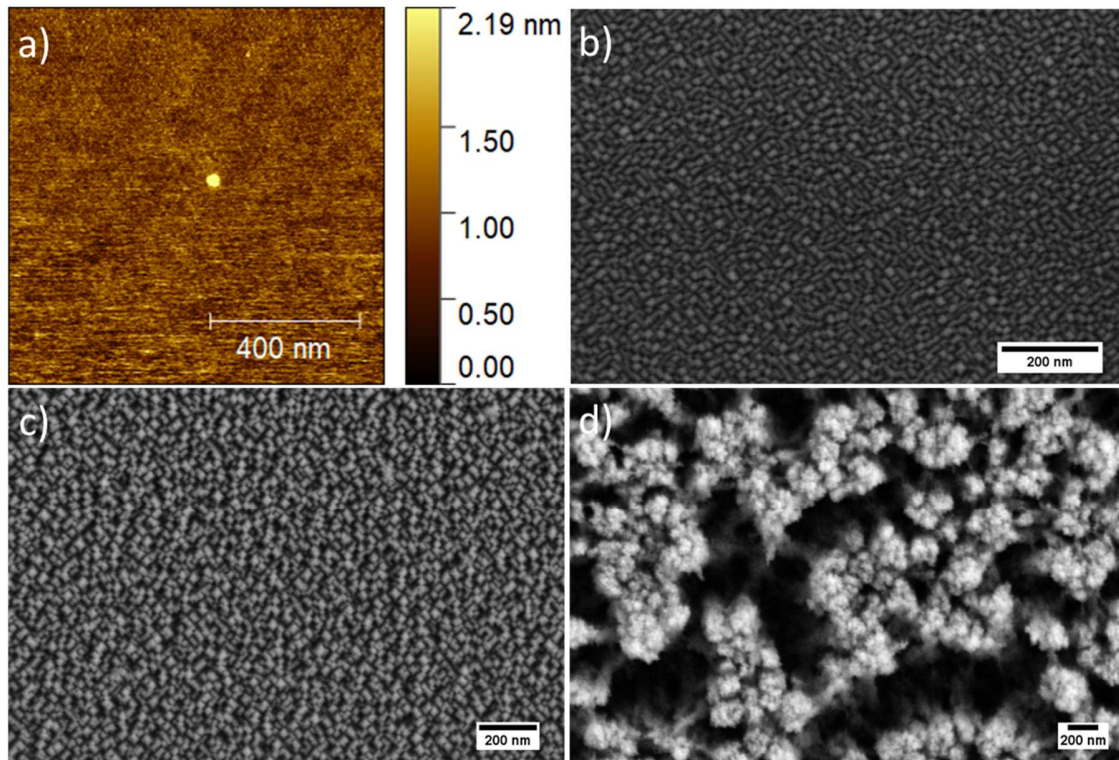


Figure 3-3. Microstructural characterization of as deposited NiCGO-based thin films. AFM micrograph of dense NiCGO<sub>5mT-700C</sub> (a). SEM micrographs for the rest of the NiCGO thin films fabricated: NiCGO<sub>150mT-700C</sub> (b), NiCGO<sub>200mT-500C</sub> (annealed) (c) and NiCGO<sub>200mT-100C</sub> (annealed) (d).

Information on the crystallographic nature of the NiCGO films was retrieved by XRD, as shown in Figure 3-4. NiCGO<sub>5mT-700C</sub> shows epitaxial growth of the CGO phase over the YSZ substrate, due to the unique presence of the (h00) reflections in the XRD pattern, as expected from the similarities with the dense SDC deposition previously described. Minor presence of NiO (111) orientation might be present, as suggested by the peak shoulder located at 37.3°. In the case of NiCGO<sub>150mT-700C</sub>, (h00) CGO orientation is also found to be the one giving the most intense XRD signal. With regard to the annealed NiCGO<sub>200mT-500C</sub> film, only the (200) diffraction peak is observed for the CGO phase. This is expected due to the similarities observed in the microstructure with NiCGO<sub>150mT-700C</sub>. Additionally, a minor (220) peak likely corresponding to the presence of NiO phase is detected. The minor unidentified peak present at 36° could be originated by cross-contamination from the thermal annealing treatment. NiCGO<sub>200mT-100C</sub> shows several diffraction peaks corresponding to orientations of the CGO phase on the (111), (200), (220) and (311) crystallographic planes. This reproduces the same crystalline growth observed for porous SDC in Figure 3-2d. The minor peaks in the 20-30° range (labelled with a star) are ascribed to artefact signals occasionally coming from the sample holder setup.



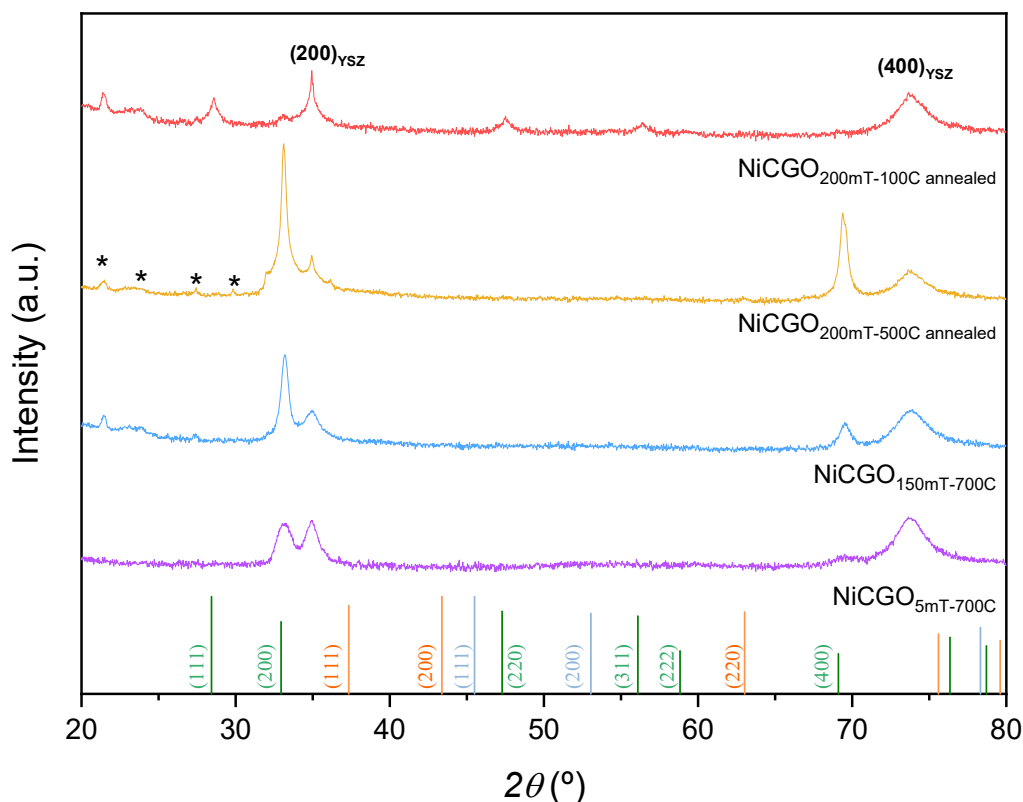


Figure 3-4. XRD patterns measured for all the NiCGO thin films studied. Reference diffraction patterns are represented on the bottom for doped-ceria ( $Fm-3m$  #225, in green)<sup>21</sup>, NiO ( $Fm-3m$  #225, in orange)<sup>22</sup> and Ni ( $Fm-3m$  #225, in light blue)<sup>23</sup>. The most representative peaks are labelled. The star (\*) indicates artefact diffraction signals measured from the setup. YSZ ( $h00$ ) peaks are labelled directly on the top diffraction pattern as a common reference.

### 3.3.2 Electrochemical performance of the NiCGO thin film hydrogen electrodes

Figure 3-5 shows the results of the electrochemical performance obtained for the NiCGO-based anodes and their comparison with reference SDC anodes discussed earlier in the chapter. Hence, Figure 3-5a depicts representative Nyquist plots measured at 700 °C for all the samples studied. All the impedance spectra obtained present a main contribution of the polarization resistance dominated by the low-frequency arc, characteristic of the hydrogen oxidation reaction dominant for these materials. Slight asymmetries in the arcs are attributed to local and minor differences in the films of the symmetric cell measured.

The ASR evolution during the first hours of the NiCGO electrodes is presented in Figure 3-5b. One can conclude that NiCGO<sub>5mT-700C</sub> improves its performance during the first stages of the characterization, most likely due to further reduction of the NiO present in the electrode, while the NiCGO<sub>150mT-700C</sub> increases the polarization resistance, despite being initially lower than for the fully dense NiCGO<sub>5mT-700C</sub> electrode. This could be attributed to

changes in the electrode microstructure, inducing a reduction in the surface area and instability of the active phase. Additionally, NiCGO<sub>200mT-500C</sub> and NiCGO<sub>200mT-100C</sub> showed stable ASR over the first hours of the experiment, suggesting a full reduction of Ni and the absence of microstructure evolution.

Figure 3-5c shows the Arrhenius plot of all the NiCGO electrodes studied, with addition of both dense and porous SDC as reference electrodes for comparison. The performance of all the NiCGO electrodes outperforms the one of dense SDC. In the case of fully dense NiCGO<sub>5mT-700C</sub> the improvement is of one order of magnitude, despite the overall performance is still behind the activity achieved by the porous SDC counterpart. Interestingly, the NiCGO<sub>200mT-100C</sub> layer shows similar ASR values than NiCGO<sub>5mT-700C</sub>. Although higher activity would be expected for NiCGO<sub>200mT-100C</sub> due to the elevated porosity observed, one possible reason for the partially limited performance could be attributed to loss of current percolation along the porous layer. Additional causes might be related to decrease of the active area. The porous layers are mechanically less stable than denser films, so the microstructure of the layer might have suffered partial damage resulting in the loss of the total active material. In the case of NiCGO<sub>150mT-700C</sub> the ASR observed is the highest among the NiCGO films. It should be noted that the initial ASR was similar to that of NiCGO<sub>200mT-100C</sub> and progressively increased (Figure 3-5b), resulting in the values observed in the Arrhenius. This behavior could be attributed to microstructural evolution of the surface. Further characterization would be needed for proper confirmation of this hypothesis. Notably, NiCGO<sub>200mT-500C</sub> shows the best performance of the films studied in this section. The ASR at 700 °C is 0.95 Ω.cm<sup>2</sup>, only a 3-fold factor above the ASR reported for porous SDC. The low values in ASR of NiCGO<sub>200mT-500C</sub> could be attributed both to the increase in the activity resulting of the Ni content in the layer, and the retaining of the mesoporous structure observed in Figure 3-3c. The overall differences in the activity of the films studied with respect to porous SDC could be expected by the difference in the exposed area in each case, being the highest for the reference porous SDC layer. Nonetheless, an additional cause on the differences of the ASR values between the films might fall in the dopant employed. Although Gd and Sm are generally considered to give raise to similar ionic conductivity values in doped ceria, some differences have been reported in the literature<sup>24</sup>. In addition to that, the change in doping from 20 % Sm to 10 % Gd in the NiCGO samples might result in lower ionic conductivity of the ceria phase, as 20 % doping tends to be closer to the maximum ionic conductivities reported<sup>25</sup>. Finally, the thickness of the layers should also be considered as a feasible cause for the differences observed in the performance of the films. On a general basis, porous electrodes fabricated with higher thickness present a larger number of reactions sites, hence resulting in improved performance. All these possibilities should be further studied for reaching a definitive conclusion on the differences in the electrochemical properties of the films analysed in this chapter.

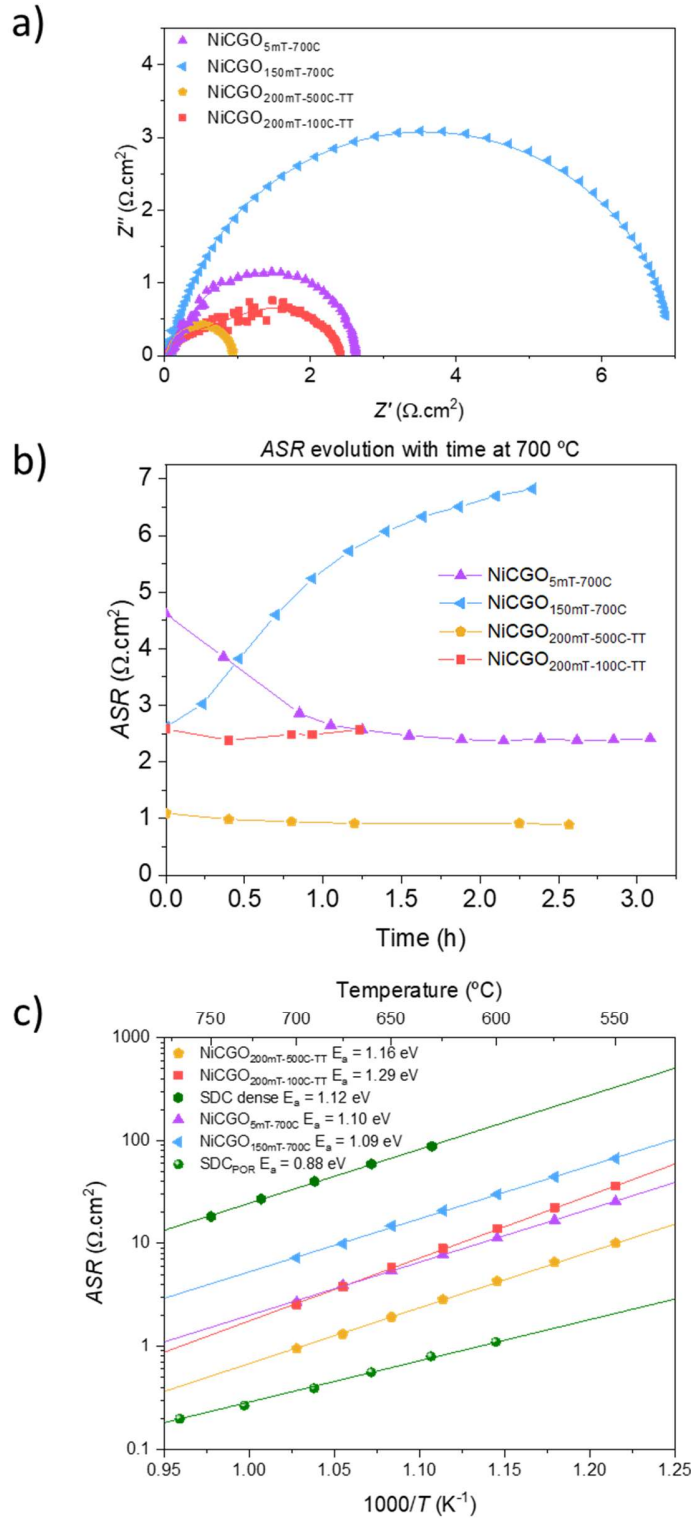


Figure 3-5. Nyquist plots obtained of the NiCGO samples at 700 °C under humidified hydrogen atmosphere (a). ASR evolution with time measured in the beginning of the experiment, at 700 °C (b). Evolution of the ASR with temperature for NiCGO based thin films fabricated under different conditions (c).

### 3.4 Functional layers based on LSCrMn-SDC heterostructures

#### 3.4.1 Development of dense LSCrMn-SDC functional layers for hydrogen and symmetric electrodes

##### 3.4.1.1 Microstructural characterization of the thin film heterostructures

Thin film dense LSCrMn-SDC heterostructures were deposited by PLD following the processes described in Chapter 2, with the goal to fabricate a dual-phase LSCrMn-SDC nanocomposite (LSCrMn-SDC<sub>NC</sub>) and a bilayer corresponding to a thin layer of SDC deposited on top LSCrMn (LSCrMn-SDC<sub>BL</sub>). Figure 3-6 shows the XRD patterns for the dense thin film LSCrMn-SDC electrodes analysed as suitable hydrogen and symmetric electrodes. In addition to the two heterostructures, single dense LSCrMn and SDC phases are represented for comparison purposes. In the case of LSCrMn, the phases presents in all cases a polycrystalline rhombohedral structure with orientation in the (012), (110) and (104) planes. This is coherent with what has been reported in other studies based on LSCrMn<sup>26,27</sup>, and has been confirmed by the Transmission Electron Microscopy (TEM) characterization carried out (see later in the text). The SDC phase presents cubic crystallographic structure with preferential orientation along the (100) plane of the YSZ single crystal substrate. The two LSCrMn-SDC heterostructured films present additional reflections corresponding to the (111) and (220) orientations of the SDC phase. It should be noted though that the (220) SDC reflection is present close to the (024) LSCrMn diffraction peak, so there might be presence of both orientations in the crystallographic structure of the films. Distortions on the peak shape and shifts in the peak positions are ascribed to the existing overlap and the relative intensity of the LSCrMn and SDC phases, as well as to cation interdiffusion in the nanocomposite film (cf. TEM characterization later in the text). From this analysis, it was concluded that phase differentiation between the perovskite LSCrMn phase and the fluorite SDC phase was obtained for all the structures under consideration.

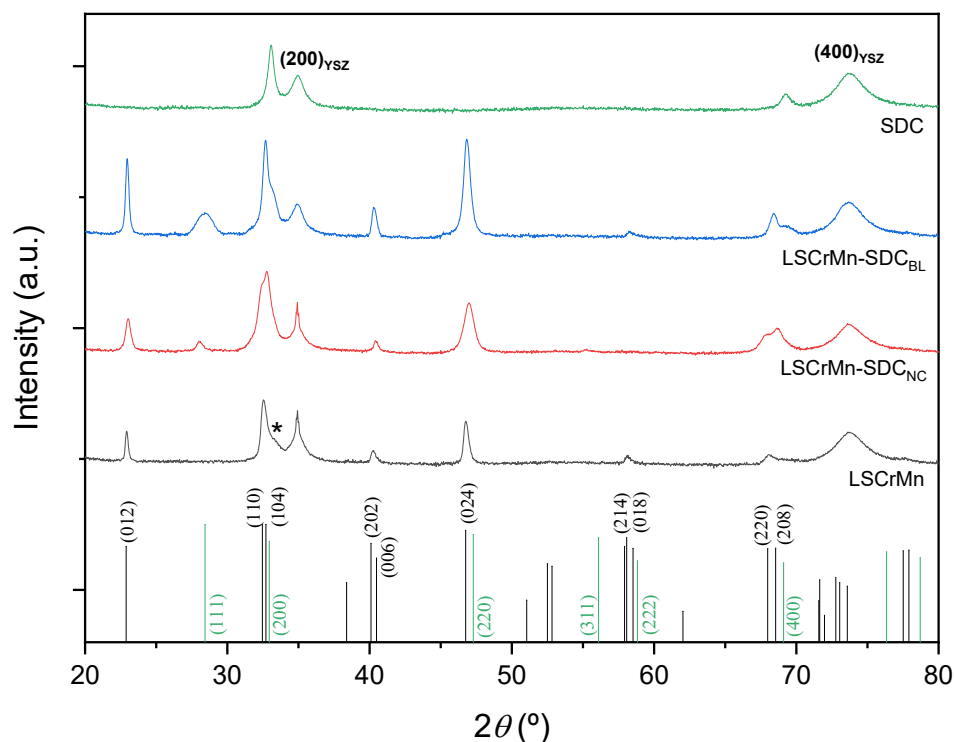


Figure 3-6. X-ray diffraction for all the anode materials under study. Reference diffraction patterns are represented on the bottom for LSCrMn (R-3c #167, in black)<sup>27</sup> and SDC (Fm-3m #225, in green)<sup>21</sup>, respectively. The most representative peaks are labelled. The star (\*) indicates a peak shoulder due to the presence of the (200) orientation of the CGO buffer layer. YSZ (h00) peaks are labelled directly on the SDC diffraction pattern as a common reference.

The microstructure of the two nanostructured films was analysed by atomic force microscopy, as shown in Figure 3-7. The top-view micrographs for LSCrMn-SDC<sub>BL</sub> and LSCrMn-SDC<sub>NC</sub> are presented in Figure 3-7a and b, respectively. Both nanostructures present a dense microstructure with variations in roughness and grain size. The nanocomposite layer shows higher values of roughness ( $R_{ms} = 5.5$  nm) and grain size ( $\approx 30$  nm) with respect to the bilayer, which presents a smoother surface and smaller grain dimension ( $R_{ms} = 2.4$  nm and  $\approx 20$  nm grain size). This is probably due to the disorder present in the nanocomposite deposition, with the perovskite and fluorite phases growing simultaneously.

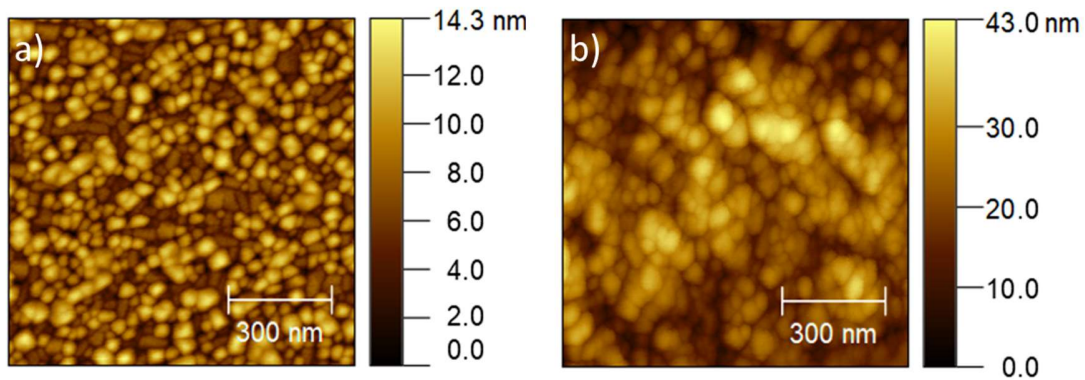


Figure 3-7. Top-view AFM micrographs of the heterostructures studied: LSCrMn-SDC<sub>BL</sub> (2.4 nm  $R_{ms}$ ) (a) and LSCrMn-SDC<sub>NC</sub> (5.5 nm  $R_{ms}$ ) (b).

The cross-section of the two heterostructures were characterized by means of high-resolution transmission electron microscopy (HRTEM), as it can be observed in Figure 3-8. The cross-sectional micrographs shown in Figure 3-8 confirm the dense microstructure of the films. The low magnification micrograph in panel (a) shows that the LSCrMn in the bilayer structure present columnar growth, while panel (d) shows that the nanocomposite is grown following a more disordered geometry. Figure 3-8b and 3e present the selected area electron diffraction (SAED) patterns obtained. In the case of LSCrMn-SDC<sub>BL</sub> the major phase in the film corresponds to the rhombohedral R-3c(H) structure of LSCrMn, while for LSCrMn-SDC<sub>NC</sub> the most important phase is the cubic structure of the SDC. HRTEM micrographs are reported in Figure 3-8c (LSCrMn-SDC<sub>BL</sub> – with the inset representing the related Fourier transform (FT)) and 3f (SDC rich region of the LSCrMn-SDC<sub>NC</sub> film – inset showing FT). In the case of the bilayer, the heterostructure presents clear differentiation in terms of phase and morphology. The LSCrMn perovskite phase presents columnar growth (column width  $\approx$  30 nm), while the SDC layer on top shows full coverage with conformal, crystalline growth. This ordered growth differs from what it is observed for the nanocomposite. In this case, TEM imaging could not be employed to resolve phase alternation nor preferential growth direction in the film.

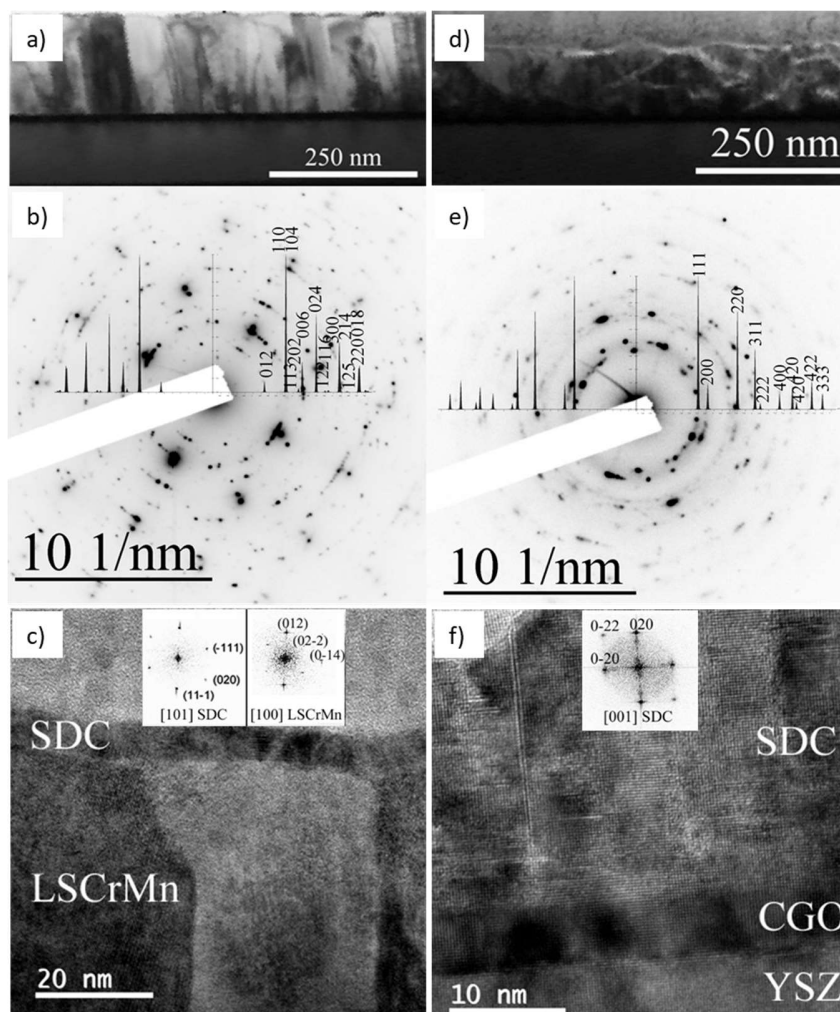


Figure 3-8. Cross-sectional characterization of the heterostructures studied: low magnification TEM, SAED patterns and HRTEM micrographs for LSCrMn-SDC<sub>BL</sub> (a-c) and LSCrMn-SDC<sub>NC</sub> (d-f). Insets in (c) and (f) show the related FT diffraction pattern.

Complementary energy-dispersive X-ray spectroscopy (EDX) mappings have been carried out to shed light on chemical composition of the heterostructures. Figure 3-9a shows the collection of the EDX measurements done with the analysis of Sr (red), La (light blue), Ce (blue), Zr (green) and Y (yellow) signals, in the case of LSCrMn-SDC<sub>BL</sub>. The Sr, La and Ce signals confirm phase differentiation, with the two first contained in the LSCrMn region, and the latter on top of it. The rest of the elements of interest (i.e. Mn, Cr, Sm and Gd) were excluded in the analysis due to overlapping between the peaks in the spectra. Hence, conclusions on phase differentiation and cation intermixing are based on the EDX signals reported. With regard to LSCrMn-SDC<sub>NC</sub>, the same EDX signals are reported in Figure 3-9b. The nanocomposite film presents concentrated Sr signal in localized regions, which are attributed to the perovskite phase (cf. phase discussion later in the text). Nevertheless, Sr is still present in the rest of the film and Ce and La are present with no proper preference along

the film. This analysis suggests the occurrence of strong cation intermixing during the sample fabrication, although some of the mixed signal might also be originated from grain overlapping in the cross-sectional observation.

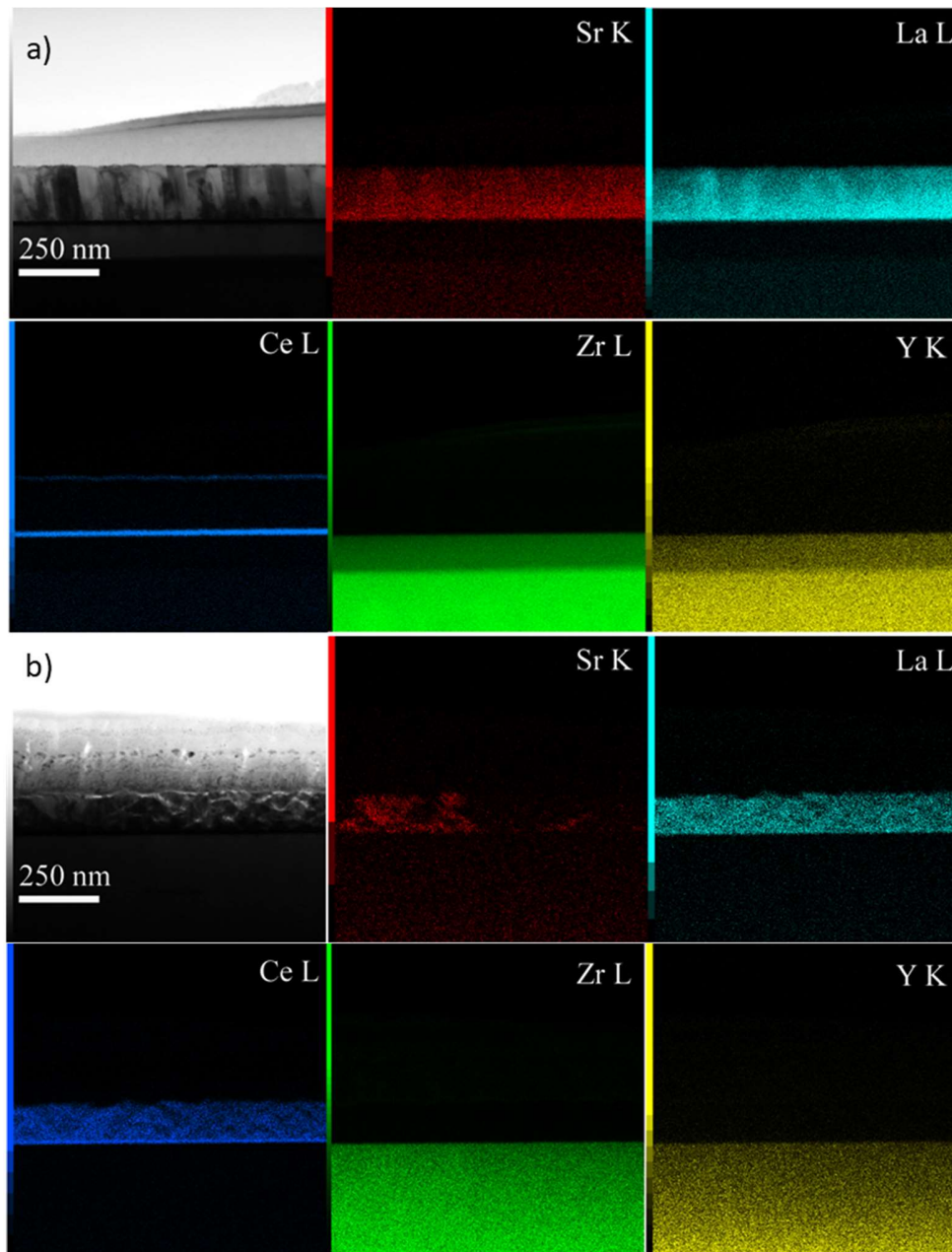


Figure 3-9. EDX elemental distribution maps calculated using the Sr-K, La-L, Ce-L, Zr-L and Y-K and signals for LSCrMn-SDC<sub>BL</sub> (a) and LSCrMn-SDC<sub>NC</sub> (b).

In order to gain further knowledge on the inherent spatial phase identification of the films at the nanometer scale, automated crystal phase and orientation mapping (ACOM) with a precession system (ASTAR) was performed. Figure 3-10 shows an example of phase identification done to the LSCrMn-SDC<sub>NC</sub> film. The overlap between the experimental and



theoretical electron diffraction patterns obtained for different regions of the film (points A-D) allows to assign the corresponding crystallographic structure. The larger the overlap between patterns, the more accurate the phase identification is.

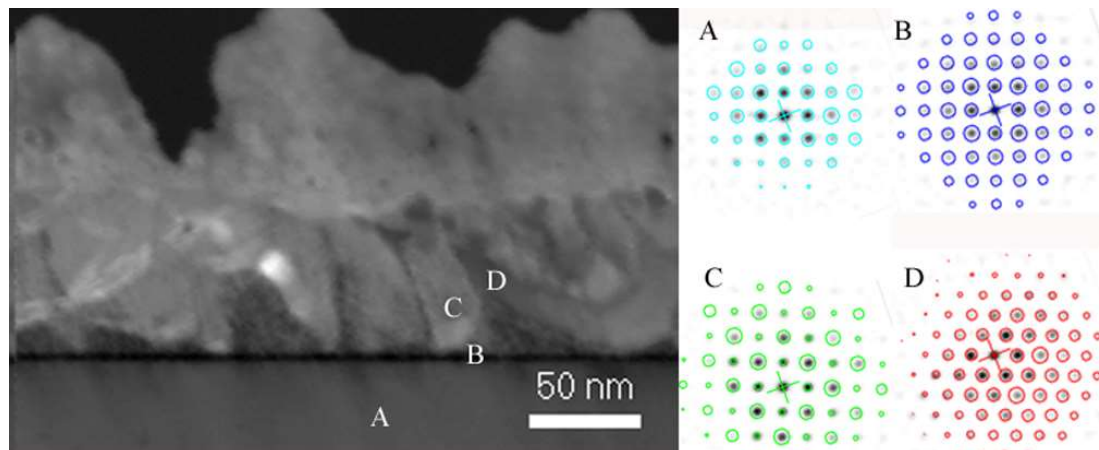


Figure 3-10. LSCrMn-SDC<sub>NC</sub> phase identification by ASTAR. Superposition of the electron diffraction patterns of selected regions (A to D) with the calculated matching phases for: YSZ *Fm3m* 225 (A), CGO *Fm3m* 225 (B), SDC *Fm3m* 225 (C), LSCrMn *R-3c(H)* 167 (D).

The complete identification of the crystallographic phases of the two heterostructures studied can be found in Figure 3-11. Particularly, the ASTAR analyses on LSCrMn-SDC<sub>BL</sub> and LSCrMn-SDC<sub>NC</sub> have been translated into the phase maps represented in Figure 3-11a and c, respectively. The map reveals the presence of areas with different crystallographic structure for both heterostructures, i.e. rhombohedral (assigned to LSCrMn - red), cube-on-cube *Fm3m* fluorite (CGO buffer layer - dark blue) and randomly oriented fluorite (SDC - light blue). For the specific case of LSCrMn-SDC<sub>BL</sub>, both LSCrMn and the SDC top layer present polycrystalline growth (see Figure 3-11b), which is in line with the observations made by XRD. With regard to LSCrMn-SDC<sub>NC</sub>, it has been confirmed that the film presented a major part of cubic fluorite phase, as suspected from the SAED pattern. Nonetheless, perovskite-rich regions with “boat-shape”-like domains can be found in isolated islands. Additionally, preferential growth following the SDC orientation is observed (see Figure 3-11d). More in detail, for the first tens of nanometers the SDC-rich phase shows preferential orientation with epitaxial growth along the [100] axis, following the CGO buffer layer and the YSZ electrolyte.

This behavior is ascribed to the preferential growth of the SDC phase over the CGO/YSZ substrate, allowing for better lattice match, causing the perovskite-rich phases to grow in localized regions, spatially separated. It should be noted that according to this analysis, these differences on phase distribution not only affect the crystallographic order of the films, but also the fraction present of each phase. Specifically, the fluorite phase (although highly intermixed) seems to be predominant over the perovskite. An explanation to this effect is that part of the LSCrMn is dissolved into the SDC-rich phase during film deposition, as suggested by the high presence of intermixed cations observed in the EDX results of Figure

3-9. This is in agreement with observations made in other perovskite-fluorite nanocomposites, in which high levels of intermixing in between the phases was visualized by dedicated atom probe tomography measurements<sup>28</sup>.

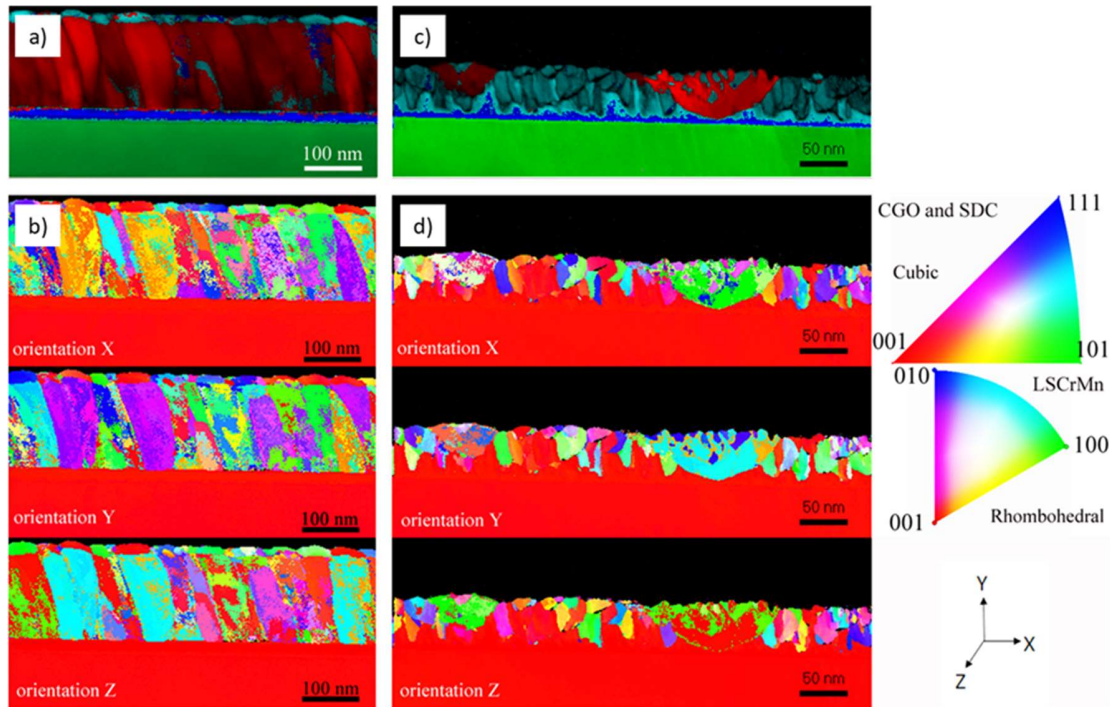


Figure 3-11. ASTAR phase and index analysis maps (top row) and corresponding orientation maps for each direction (bottom rows) of (a-b) LSCrMn-SDC<sub>BL</sub> and (c-d) LSCrMn-SDC<sub>NC</sub> films. Phase maps: YSZ in green, CGO in dark blue, LSCrMn in red and SDC in light blue.

#### 3.4.1.2 Measurement of the sheet conductivity under reducing and oxidizing conditions

Figure 3-12 shows the in-plane conductivity measured under both reducing and oxidizing atmospheres for the two heterostructures under study, and its dependence with temperature. In the case of the conductivity values obtained under 5 % H<sub>2</sub> atmosphere presented in Figure 3-12a, it can be seen that both materials are characterized by linear behavior of  $\ln(\sigma T)$  vs  $1/T$ , indicative of a mechanism of charge transport governed by small polaron hopping<sup>11,29</sup>. Particularly for LSCrMn-SDC<sub>NC</sub>, two linear regimes can be differentiated, most likely because the two phases present in the film (i.e. the separate LSCrMn-rich regions and the SDC-rich matrix discussed in the previous section). In the case of the lower temperature regime, the activation energy ( $E_a$ ) was found to be 0.28 eV, the same as for LSCrMn-SDC<sub>BL</sub>, and hence attributed to the LSCrMn phase. With regard to the higher temperature region, the  $E_a$  increases to 0.44 eV due to the additional SDC contribution to the overall charge transport. Notably, the heterostructuring strategies defined in this work lead to an enhancement of more than three orders of magnitude in

terms of sheet conductivity with respect to state-of-the-art doped ceria electrodes ( $\sigma \approx 7.5 \times 10^{-4} \text{ S.cm}^{-1}$  at  $500 \text{ }^\circ\text{C}$ )<sup>16,30</sup>. Among the two samples studied, the bilayer was found to be the most conductive, most likely due to the continuity of the single LSCrMn layer, which facilitates the electronic transport along the layer. Actual values obtained for the conductivity of the layers were  $\sigma \approx 2.2 \text{ S.cm}^{-1}$  vs  $\sigma \approx 0.3 \text{ S.cm}^{-1}$  for the bilayer and the nanocomposite at  $350 \text{ }^\circ\text{C}$ , respectively.

The sheet conductivity of the two heterostructures was also evaluated in oxidizing conditions, in particular under synthetic air. This was motivated by the possibility of application of the functional layers developed in devices with symmetric cell configuration, with particular interest in the nanocomposite (cf. EIS characterization in the discussion below). The values obtained are represented in Figure 3-12b. It can be seen that the nanocomposite presents relatively low sheet conductivity when compared to the bilayer in the low temperature range ( $\sigma \approx 1.7 \text{ S.cm}^{-1}$  vs  $\sigma \approx 0.08 \text{ S.cm}^{-1}$  for LSCrMn-SDC<sub>BL</sub> and LSCrMn-SDC<sub>NC</sub> at  $350 \text{ }^\circ\text{C}$ , respectively). This is probably due to the presence of the low conductivity of the SDC matrix (more critical in oxidizing conditions than in reducing atmosphere<sup>16,17</sup>), which prevents the formation of a percolating electronic pathway. In relation with the thermal activation, the nanocomposite shows a similar trend than for the measurements under hydrogen atmosphere, observing two linear regimes with different values of activation energy. Notably, the high temperature regime presents a larger  $E_a$  under synthetic air, reaching a value of  $0.72 \text{ eV}$ . This value is coherent with conductivity measurements performed on doped-ceria<sup>30</sup>. Extrapolating the conductivity of LSCrMn-SDC<sub>NC</sub> at typical SOC temperature conditions like  $700 \text{ }^\circ\text{C}$  results in a value of  $\sigma \approx 5.2 \text{ S.cm}^{-1}$ . This value is much higher than what is found to conventional ceria-based thin films<sup>31</sup> (cf. Figure 3-12) and is comparable to the observations made in electronic conductors employed in SOC technologies such as LSM<sup>32</sup> (despite the uncertainty given by the extrapolation).

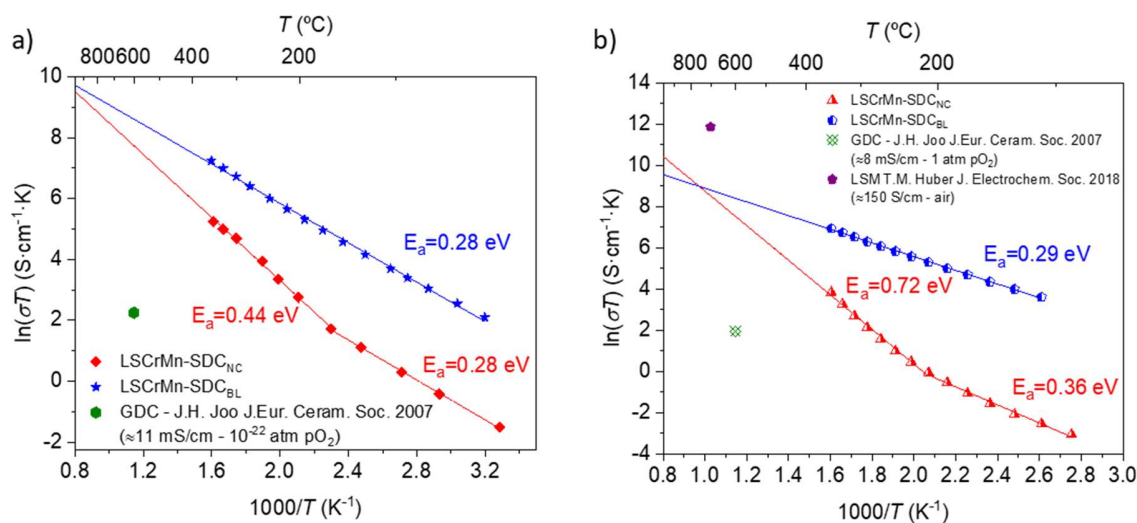


Figure 3-12. Arrhenius representation of the sheet conductivity measured for the different heterostructures as a function of temperature under 5% H<sub>2</sub> in Ar (a) and synthetic air atmosphere (b).

### 3.4.1.3 Electrochemical performance of the heterostructures

The electrochemical properties of the thin films studied in this work have been evaluated by means of impedance spectroscopy. Figure 3-13a shows the Nyquist plot obtained by EIS at 750 °C for the different materials under wet hydrogen atmosphere. The solid line represents the fit result obtained from modelling the corresponding equivalent circuits described in Chapter 2 (see Figure 2-16), in this case the simplified version of the Jamnik-Maier circuit with no limiting contribution from ionic diffusion<sup>33</sup>. All four samples present a clear major arc located in the low frequency region and a secondary minor arc located in the high frequency range, close to the intersection with the real impedance axis (see Figure 3-13a inset). The main arc is ascribed to the surface oxidation reaction, whereas the high frequency contribution could come from minor mass transport limitations (at the film/electrolyte interface or in the bulk material). This is consistent with studies done by Raj on oxygen diffusion and surface exchange studies on the LSCrMn system<sup>34</sup> and by Primdahl<sup>35</sup>, Jung<sup>12</sup> and Nakamura<sup>36</sup> et al. on doped-ceria materials. True capacitances calculated from the high and low frequency arcs are collected in Table 3-2. In the case of the high frequency process, capacitances in the order of 10<sup>-4</sup>-10<sup>-5</sup> F/cm<sup>2</sup> are found, which are representative of diffusion processes<sup>35</sup> or of the double capacitance at the electrolyte/electrode interface<sup>37</sup>. The high frequency contribution can therefore be related to oxygen diffusion along the material or across the interface electrolyte/electrode<sup>35,38</sup>. For the case of the low frequency arc, this is instead associated to the surface reactions, in agreement with previous works found in the literature<sup>12,18,35,36,39</sup>. This interpretation is also supported by the Distribution of Relaxation Times (DRT) analysis presented in Figure 3-13b, which shows two main contributions for the impedance: a minor contribution at lower characteristic times (10<sup>-2</sup>-10<sup>-3</sup> s), and a major peak in the higher region (1-10<sup>-1</sup> s).

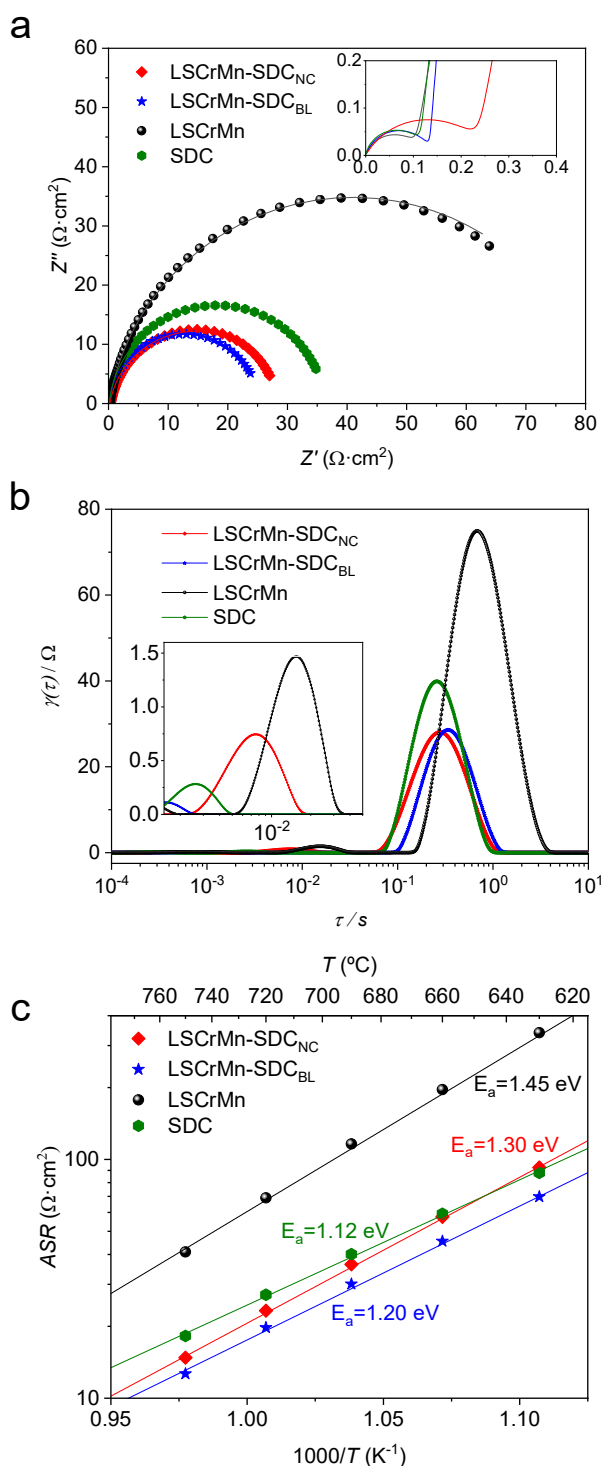


Figure 3-13. Electrochemical characterization of the materials under study in reducing conditions (LSCrMn in black; SDC in green; LSCrMn-SDC<sub>NC</sub> in red; and LSCrMn-SDC<sub>BL</sub> in blue). Nyquist plots obtained at 750 °C (dots), fit result (solid line) and inset with the high frequency region zoomed in (a). DRT analysis of the EIS measurements performed in wet hydrogen atmosphere at 750 °C (b). Arrhenius plot of the ASR (c).

Regarding the capacitance associated to the low frequency arc, it is generally attributed to the sum of the surface process and of the chemical capacitance ( $C_{\text{chem}}$ ) of the films. The latter is expected to be the predominant in systems involving mixed conductors<sup>40</sup>, giving rise to values in the order of  $\approx 10^3$  F/cm<sup>3</sup>. These values are in agreement with what has also been reported in other studies involving perovskite and ceria-based mixed conductors<sup>41-43</sup>. As expected, the LSCrMn single layer shows the highest area specific resistance (ASR  $\approx 41$   $\Omega\cdot\text{cm}^2$  at 750 °C – which takes into account the full polarization arc) among the materials tested<sup>44,45</sup>, while single phase SDC presents a lower polarization ( $\approx 18.2$   $\Omega\cdot\text{cm}^2$ ). Slightly lower ASR values at the reference T = 750 °C characterize LSCrMn-SDC<sub>NC</sub> ( $\approx 14.7$   $\Omega\cdot\text{cm}^2$ ) and LSCrMn-SDC<sub>BL</sub> ( $\approx 12.6$   $\Omega\cdot\text{cm}^2$ ). By analysing the temperature dependence of ASR (Figure 3-13c), one can observe that the two functional heterostructures show the best performance in the full temperature range studied.

The observed enhancement in the HOR kinetics with respect to single phase LSCrMn and SDC suggests a synergistic effect of the two materials in the nanostructures. Most interestingly, such an improvement occurs irrespective of the type of heterostructure chosen, i.e. bilayer or nanocomposite. This is coherent with the microstructural analysis performed in Figure 3-10: In both cases and as inferred from the specific activity of the single phases (cf. Figure 3-13) SDC provides reactive sites for fast HOR, whereas the LSCrMn offers an electronic pathway. Thus, similar catalytic performances are expected owing to the exposed SDC-gas interface and an overall decrease in ASR thanks to the enhanced electronic conductivity with respect to single phase SDC.

*Table 3-2. Capacitance values for the high and low frequency arcs shown in the Nyquist plots in Figure 3-13a.*

Material	C (F/cm <sup>2</sup> )		C <sub>chem</sub> (F/cm <sup>3</sup> )		n
	High Frequency	Low Frequency	High Frequency	Low Frequency	
LSCrMn	2.22 x 10 <sup>-4</sup>	1190.79	0.81	0.91	
LSCrMn-SDC <sub>NC</sub>	7.98 x 10 <sup>-5</sup>	1281.59	0.68	0.91	
LSCrMn-SDC <sub>BL</sub>	1.83 x 10 <sup>-4</sup>	1917.25	0.82	0.96	
SDC	3.19 x 10 <sup>-4</sup>	999.88	0.89	0.94	

Figure 3-14 shows the analysis of the electrochemical properties of the material systems under oxidizing conditions by out-of-plane EIS (Nyquist plot and DRT analysis at 750 °C, and Arrhenius plot of the ASR in panels (a-c), respectively). This allows to further clarify the role of the constituting materials in the heterostructures and to evaluate their

compatibility to be potentially employed in fully symmetric SOC devices. In air at high temperatures, one expects none of the components to be active if taken singularly, as LSCrMn presents a predominant electronic conduction with negligible ionic conductivity<sup>45</sup> while SDC is a pure ionic conductor (cf. Figure 3-14c)<sup>30,42</sup>.

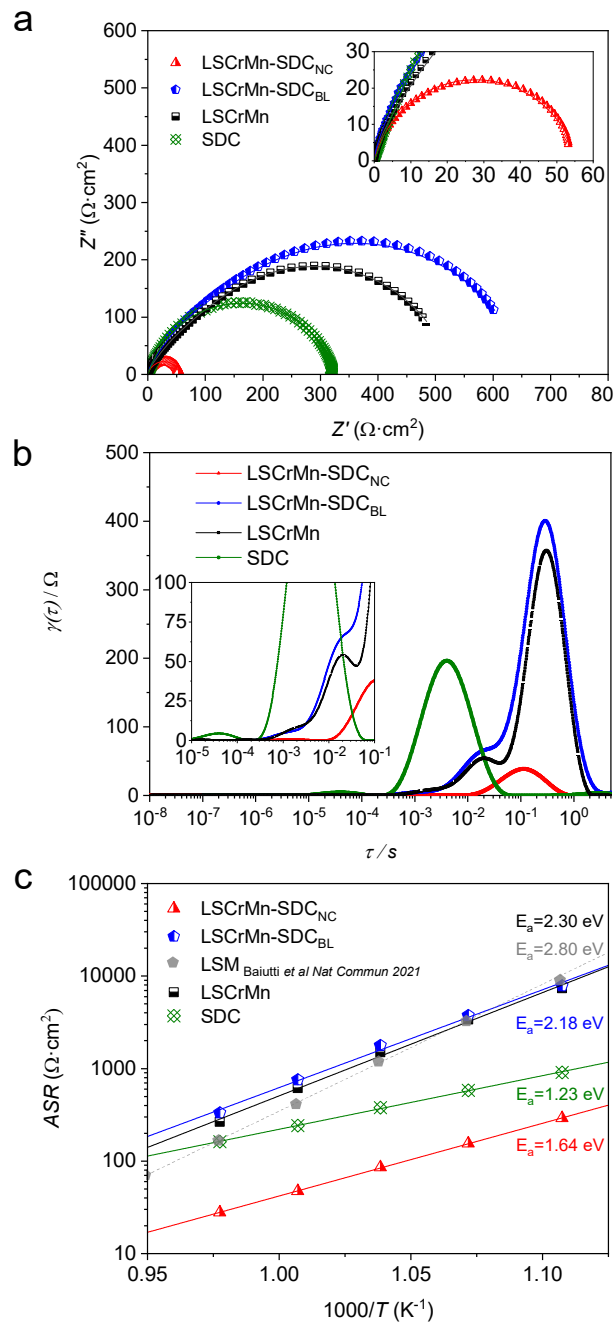


Figure 3-14. Electrochemical characterization of the materials under study in oxidizing conditions (LSCrMn in black; SDC in green; LSCrMn-SDC<sub>NC</sub> in red; and LSCrMn-SDC<sub>BL</sub> in blue). Nyquist plots obtained at 750 °C (dots), fit result (solid line) and inset with the high frequency region zoomed in (a). DRT analysis of the EIS measurements performed in synthetic air at 750 °C (b).

*Arrhenius plot of the ASR with the inclusion of values for LSM and LSM-SDC obtained from the literature<sup>28</sup> (c).*

Interestingly, however, the nanocomposite exhibits a remarkable performance also in air with comparable ASR ( $27.8 \text{ } \Omega \cdot \text{cm}^2$ ) whereas much higher values are measured for all the other systems considered ( $162.1 \text{ } \Omega \cdot \text{cm}^2$ ,  $264.7 \text{ } \Omega \cdot \text{cm}^2$ ,  $330.5 \text{ } \Omega \cdot \text{cm}^2$  for single phase SDC, LSCrMn and the bilayer, respectively, in oxidizing conditions) at  $750 \text{ } ^\circ\text{C}$ . A closer observation of the impedance spectra in Figure 3-14a highlights an evident depression of the arcs for LSCrMn and for LSCrMn-SDC<sub>BL</sub>. This is arguably caused by the appearance of a Warburg-type impedance element in the higher frequency range, indicating that the polarization is co-limited by diffusion and surface reactions and is well in line with the expected poor oxygen diffusivity of LSCrMn under oxidizing conditions (complete Jamnik-Maier equivalent circuit, see Figure 2-16b)<sup>40,46</sup>.

In the cases of the bilayer configuration and of single phase SDC (the latter presenting an almost perfect impedance semicircle with fitting parameter  $n = 0.84^{47,48}$ ), the top ceria layer behaves as a pure ionic conductor<sup>30,42</sup> blocking the surface exchange kinetics. This analysis is supported by the DRT results collected in Figure 3-14b, which show the appearance of an additional high frequency contribution (oxygen diffusion) for LSCrMn and LSCrMn-SDC<sub>BL</sub> films. The DRT plot also shows a shift for the SDC peak towards the lower characteristic times region, with a central peak position of  $\approx 4 \times 10^{-3} \text{ s}$ . This translates into an equivalent capacitance of  $\approx 10^{-5} \text{ F/cm}^2$ , which is in the order of what is observed for double layer capacitances for ionic conductors such as YSZ<sup>49,50</sup>, confirming its behavior as an ionic conductor. Most importantly, the nanocomposite is characterized by faster oxygen reduction kinetics. Here the SDC compensates for the lack of oxygen vacancies and ionic conductivity of the LSCrMn under cathodic conditions (i.e., SDC provides a fast mass transport pathway for out-of-plane oxygen migration), while electronic conductivity (for the oxygen reduction reaction and for current collection) is provided by the perovskite phase. Please note that a simple ZARC element was employed for evaluating the ASR in the case of LSCrMn-SDC<sub>NC</sub> ( $n = 0.86$ ), confirming that surface exchange is limiting. Interestingly, such a clear example of nanoengineered material –in which electronic and ionic conduction pathways are provided separately by the two phases– is achieved here despite the large disorder and cationic intermixing highlighted in Figure 3-9. The temperature dependence of the total ASR presented in Figure 3-14c reports, as a comparison, reference values for a traditional single phase mixed ionic electronic conductor ( $\text{La}_{1-x}\text{Sr}_x\text{MnO}_3$  – LSM). LSCrMn-SDC<sub>NC</sub> surpasses the performance of single phase LSM, validating the thin film nanocomposite approach for the fabrication of systems with ad-hoc tailored performances.

Surface exchange coefficient ( $k_q$ ) values are collected in Figure 3-15 to give details on the surface related electrochemistry. Despite the presence of minor differences on the activity of LSCrMn, LSCrMn-SDC<sub>BL</sub> and LSM –given that their activity is co-limited by oxygen diffusion –, the tendencies observed are similar to the comparison made based on values of



polarization ASR. Nonetheless, further clarification on the effect of thickness on the mass-transport properties of the materials studied is of need. As it has been discussed, the two materials with a continuous LSCrMn layer (i.e. single LSCrMn and LSCrMn-SDC<sub>BL</sub>) also present a diffusion-limited process, hence their performance would be influenced by the thickness of the electrode. Nonetheless, the small thickness difference between the LSCrMn-based structures ( $\leq 10\%$ ) allows to make a comparative analysis between the architectures without expecting a different effect on the performance due to the film thickness. Moreover, as it can be clearly observed from the diffusivity ( $D_q$ ) and  $k_q$  values extracted and reported in Table 3-3 –for the measurements at 750 °C– and in Figure 3-15 for the evolution of  $k_q$  with temperature, both LSCrMn and LSCrMn-SDC<sub>BL</sub> present the highest surface resistance contribution among the rest of the other two materials tested, hence the diffusion contribution does not hinder the conclusions extracted by the analysis.

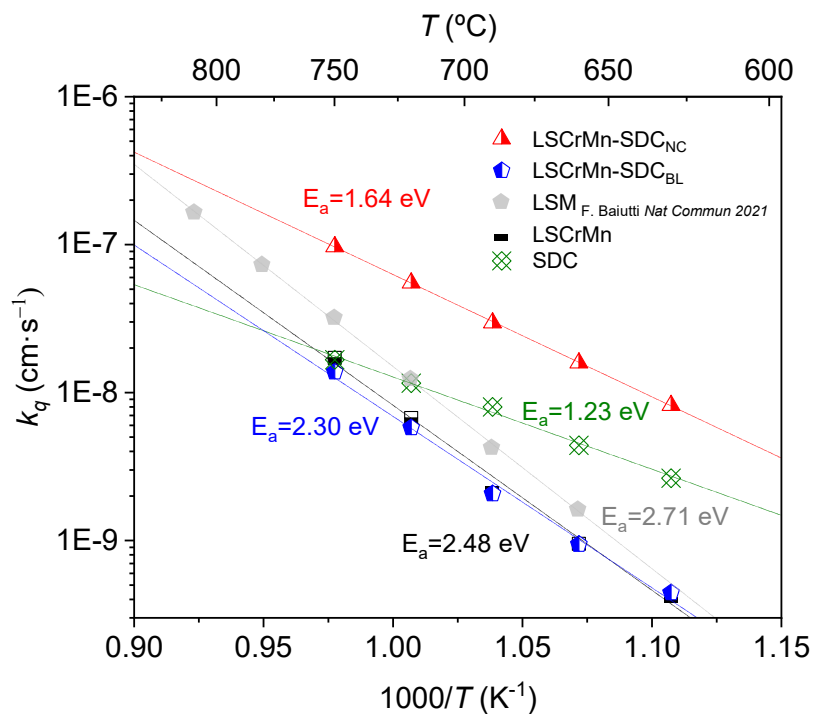


Figure 3-15. Oxygen surface exchange coefficient evolution with temperature of the materials under study.

With regard to the SDC layer, it has been discussed that the measurements in both conditions –reducing and oxidizing– are limited by the reaction on the surface, with no significant mass-transport contribution in the bulk. This is clearly observed when comparing the diffusivity values reported in Table 3-3, which shows a variation of six orders of magnitude between LSCrMn-based materials and SDC. Moreover, if we take the oxygen diffusivity of SDC (taken from the calculations reported in Vives et al. *Ceram. Int.* 2019 at 700 °C<sup>51</sup>) and consider a thickness of 150 nm (i.e. a value comparable to the thickness of the LSCrMn-based materials analysed), a simple calculation would lead to a resistance of  $\approx 3$

$\text{m}\Omega\cdot\text{cm}^2$  at  $700\text{ }^\circ\text{C}$ , which would be even lower when extrapolated to the  $750\text{ }^\circ\text{C}$  that we have considered as reference values. Hence, based on this analysis a direct comparison between a thinner SDC and thicker LSCrMn layers is suitable for drawing conclusions on the electrochemical activity on the surface reaction.

*Table 3-3. Mass-transport parameters calculated from the EIS analysis obtained at  $750\text{ }^\circ\text{C}$  under synthetic air. The SDC oxygen diffusivity value has been taken from Vives et al.<sup>51</sup> for comparison with the values extracted in this study.*

Material	$D_q$ ( $\text{cm}^2/\text{s}$ )	$k_q$ ( $\text{cm}/\text{s}$ )
LSCrMn	4.95E-13	1.72E-08
LSCrMn- SDC <sub>BL</sub>	3.26E-13	1.38E-08
LSCrMn- SDC <sub>NC</sub>	-	9.67E-08
SDC	1.27E-07*	1.67E-08

\*Extracted from Vives et al Ceram. Int. 2019 at  $700\text{ }^\circ\text{C}$

#### 3.4.1.4 Evolution of the electrochemical performance of the LSCrMn-SDC nanocomposite on thermal degradation

With the aim of assessing the suitability of LSCrMn-SDC<sub>NC</sub> as a promising functional layer to be used in symmetric systems, its evolution upon thermal degradation was evaluated. The degradation analysis was carried out in a new sample with a low impedance counter electrode made of Ag paste (see further experimental details in section 2.5.2.2 of Chapter 2). The electrochemical performance (i.e. in terms of ASR values) was analysed for a period of 400 h with the temperature set to  $780\text{ }^\circ\text{C}$ , under synthetic air atmosphere and in Open Circuit Voltage (OCV) conditions (see Figure 3-16a). The performance of the film shows an initial improvement towards lower values of ASR, going from an initial value of  $9.32\ \Omega\cdot\text{cm}^2$  to  $7.14\ \Omega\cdot\text{cm}^2$  after  $\approx 200$  hours. After this period, the degradation rate observed was as low as  $\approx 1.57\ \%/100$  hours. Proper visualization of the evolution of the electrochemical activity during this test can be found in Figure 3-16b-c. These plots show a selection of the EIS spectra obtained during the first 7 h of the experiment (i.e. when the most accentuated decrease of ASR occurs), and for the rest of the measurement. Note that only the low frequency arc was employed for the analysis of the ASR of the LSCrMn-SDC<sub>NC</sub> film, so the degradation observed in the high frequency arc (this contribution is ascribed to the Ag low impedance counter electrode) and the series resistance did not compromise the evaluation of the nanocomposite performance.

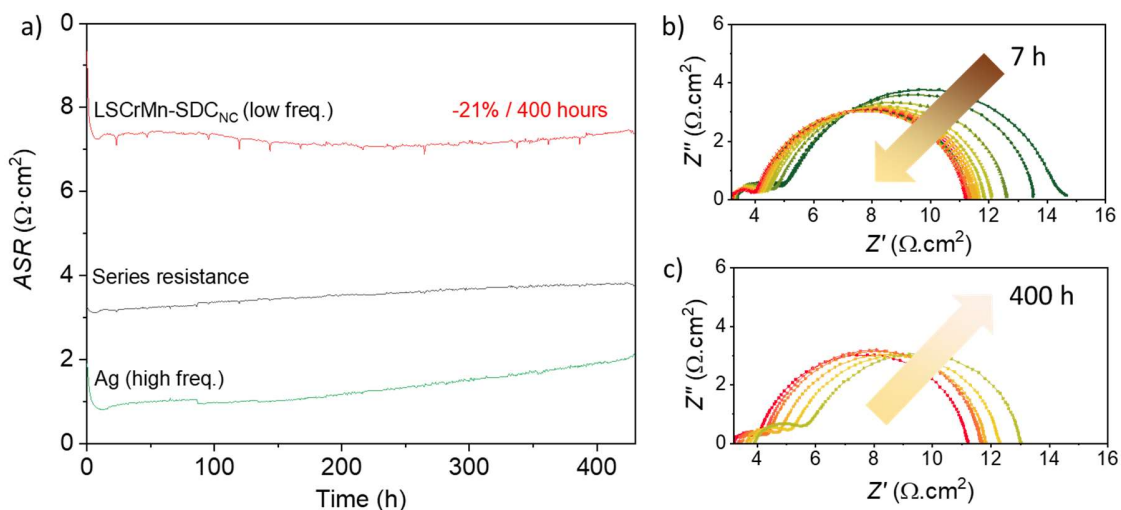


Figure 3-16. Degradation over time of the performance of LSCrMn-SDC<sub>NC</sub> measured at 780 °C under synthetic air atmosphere: low frequency ASR contribution (red), series contribution (black) and high frequency contribution (green) (a). Nyquist plots recorded during the first few hours of measurement (b) and selected plots of the overall period of the degradation experiment (c).

Interestingly, similar behavior has been observed in works dealing with other fluorite-perovskite composite systems<sup>28,52,53</sup>. In these studies, the stabilization effect on the ASR was attributed to suppression of Sr segregation to the surface. This result unveils the promising properties and the potential of the LSCrMn-SDC nanocomposite to be applied as a stable functional layer in combination with porous electrodes. This could potentially prevent the formation of blocking secondary phases –typically found in degraded electrodes– while keeping the high electrochemical activity of well-established porous materials, similar to the system reported in Ref<sup>53</sup>. LSCrMn-SDC<sub>NC</sub> presents better performance in air than prototypical LSM (cf. Figure 3-14b, Figure 3-15 and refs.<sup>28,46</sup>) and outperforms the stability of state-of-the-art La<sub>0.6</sub>Sr<sub>0.4</sub>CoO<sub>3-δ</sub><sup>54</sup>. Additionally, both LSCrMn-SDC<sub>NC</sub> and LSCrMn-SDC<sub>BL</sub> present comparable electrochemical performance than dense SDC in reducing atmosphere. When compared to traditional dense composites, the thin film nanocomposite provides intimate contact in between the constituent phases with no presence of tortuosity. This is reflected in good sheet conductivity (cf. Figure 3-12) and electrochemical activity of the material (cf. Figure 3-13 and Figure 3-14). The findings point LSCrMn-SDC<sub>NC</sub> as a promising candidate to be utilised as functional layers in symmetric solid oxide cell devices<sup>55–58</sup>.

### 3.4.2 Optimization of LSCrMn-SDC thin film microstructure for anode application

Given the potential observed for the dense LSCrMn-SDC heterostructures as functional layer for electrode application, some approaches for enhancing the overall performance through microstructure optimization were explored. A new set of LSCrMn-SDC thin films with increased surface area were studied for application as hydrogen electrodes.

### 3.4.2.1 Structural characterization of microstructure-variant LSCrMn-SDC thin films

With the objective of enhancing the functional properties of the LSCrMn-SDC heterostructures studies, different deposition parameters were tested for optimizing the films microstructure. As in the case of the deposition of porous SDC, higher oxygen partial pressure and lower temperatures were employed in order to increase the roughness and porosity of the functional films. Hence, oxygen pressure was set to 150 mTorr, and different temperatures in the range of 100 °C – 600 °C were fabricated, as summarized in Table 3-4.

*Table 3-4. Summary of the conditions employed in the fabrication of the LSCrMn-SDC films studied in this section.*

Sample	O <sub>2</sub> pressure (mTorr)	Temperature (°C)	Thermal treatment
LSCrMn-SDC <sub>NC-600C</sub>	150	600	-
LSCrMn-SDC <sub>NC-400C</sub>	150	400	800 °C 1h
LSCrMn-SDC <sub>NC-200C</sub>	150	200	800 °C 1h
LSCrMn-SDC <sub>NC-100C</sub>	150	100	800 °C 1h
LSCrMn-SDC <sub>POR*</sub>	200	100	700 °C 1h

\* These conditions are for the porous SDC layer, the dense LSCrMn has been deposited with the same conditions as in Section 3.4.1.

Figure 3-17 shows SEM micrographs of the different films as deposited. For the films deposited at 600 °C and 400 °C (panels (a) and (b), respectively), the microstructure observed presents the characteristics of a 2D layer with additional growth along the z-direction. This could resemble a Stranski-Krastanov mode of thin film growth<sup>59</sup> with island formation, although it could also be a sign of premature columnar growth. In particular, LSCrMn-SDC<sub>NC-600C</sub> exhibits a dense microstructure with additional growth in the form of longitudinal interconnected paths with triangular-like facets, while in the case of LSCrMn-SDC<sub>NC-400C</sub> the islands present are scattered in the form of aggregates in the range of 100-250 nm in diameter, along with a continuous distribution of smaller nucleation sites. No porosity is apparent in LSCrMn-SDC<sub>NC-400C</sub>. LSCrMn-SDC<sub>NC-200C</sub> (see Figure 3-17c) shows a disconnected microstructure characterized by the presence of grains spatially separated by narrow gaps of few tens of nanometers in size, with some additional aggregates on the surface. A similar microstructure is found for LSCrMn-SDC<sub>NC-100C</sub> (see Figure 3-17d), although in this case the gap between the grains was in the order of 10 nm, smaller than for LSCrMn-SDC<sub>NC-200C</sub>.

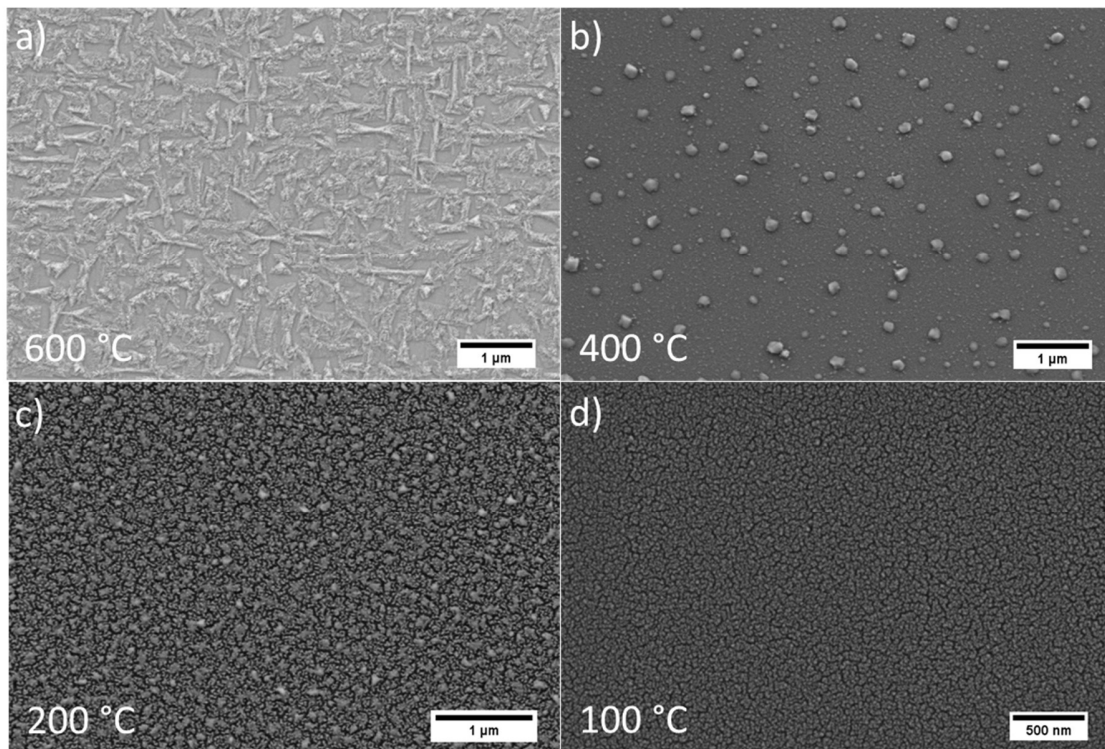


Figure 3-17. SEM micrographs of LSCrMn-SDC<sub>NC</sub> thin films deposited at 150 mTorr and at different temperatures: LSCrMn-SDC<sub>NC-600C</sub> (a), LSCrMn-SDC<sub>NC-400C</sub> (b), LSCrMn-SDC<sub>NC-200C</sub> (c) and LSCrMn-SDC<sub>NC-100C</sub> (d).

Figure 3-18 shows the obtained XRD patterns for the LSCrMn-SDC<sub>NC</sub> materials studied in this section. All the materials have been measured as deposited with the exception of LSCrMn-SDC<sub>NC-100C</sub>, which has been measured after the electrochemical analysis. All the films present diffraction peaks corresponding to the (200) crystallographic plane of the ceria phase, with a shoulder given by the (110) and (104) reflection of the perovskite phase. LSCrMn-SDC<sub>NC-600C</sub> and LSCrMn-SDC<sub>NC-200C</sub> present an additional diffraction peak on the (111) orientation. No secondary phases were observed.

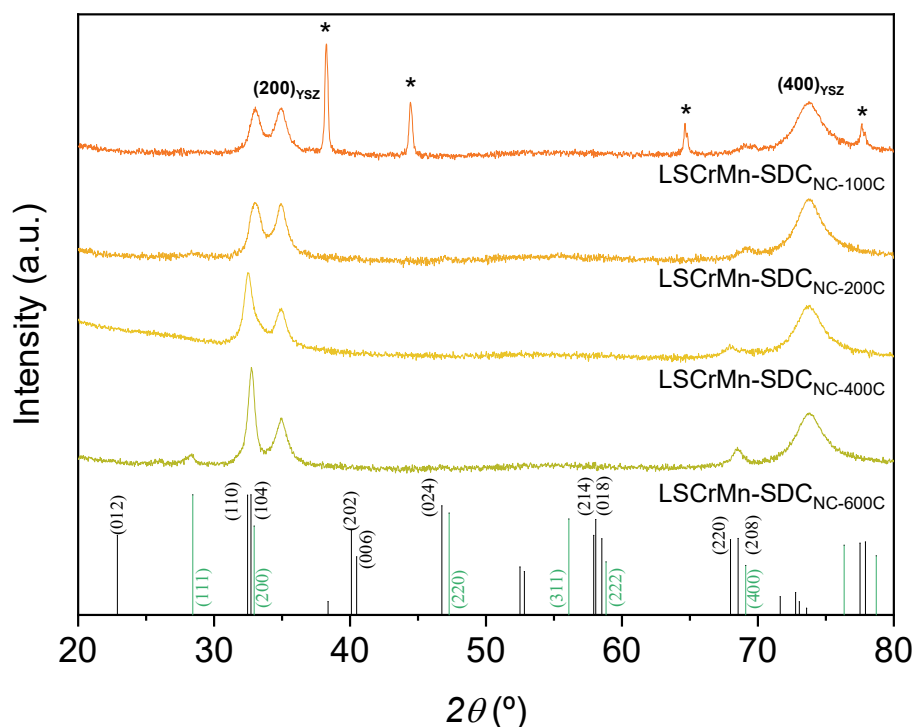


Figure 3-18. XRD diffractograms of the different LSCrMn-SDC<sub>NC</sub> thin films fabricated. The star (\*) refers to diffraction peaks corresponding to gold. Reference diffraction patterns are represented on the bottom for LSCrMn (R-3c #167, in black)<sup>27</sup> and SDC (Fm-3m #225, in green)<sup>21</sup>, respectively. The most representative peaks are labelled. YSZ (h00) peaks are labelled directly on the top diffraction pattern as a common reference.

Additionally, a thin film heterostructure made of dense LSCrMn and porous SDC was fabricated (LSCrMn-SDC<sub>POR</sub>). The dense LSCrMn layer was deposited with the same conditions as in Section 3.4.1, while the porous SDC layer was deposited on top of LSCrMn following the conditions previously described, with the only difference of the thermal treatment, which was performed at 700 °C (see Table 3-4). This was done to prevent the evolution of the LSCrMn layer surface through dopant segregation or other degradation phenomena (e.g. grain growth or microstructure deformation). Figure 3-19a and b show SEM micrographs of the layer before and after thermal annealing, respectively. The microstructure observed was similar to the obtained for single phase porous SDC (see Figure 3-2), only the thermal treatment results in a less pronounced increase of the porosity of the material. This is most likely due to the slightly milder temperature employed for the treatment. Figure 3-19c shows the XRD diffraction patterns measured for LSCrMn-SDC<sub>POR</sub> before and after the thermal treatment. As in the case of single porous SDC, the multilayer shows XRD reflections on the (111), (200), (220) and (311) crystallographic plane orientations. Additionally, several peaks corresponding to crystallographic orientations from the LSCrMn layer can be observed. It should be indicated though that LSCrMn and SDC present high XRD peak overlap corresponding to specific crystallographic planes, so

the peak identification might not be univocal. With regard to the thermal treatment, the annealed layer presents narrower XRD peaks, pointing to the presence of higher crystallinity in the film.

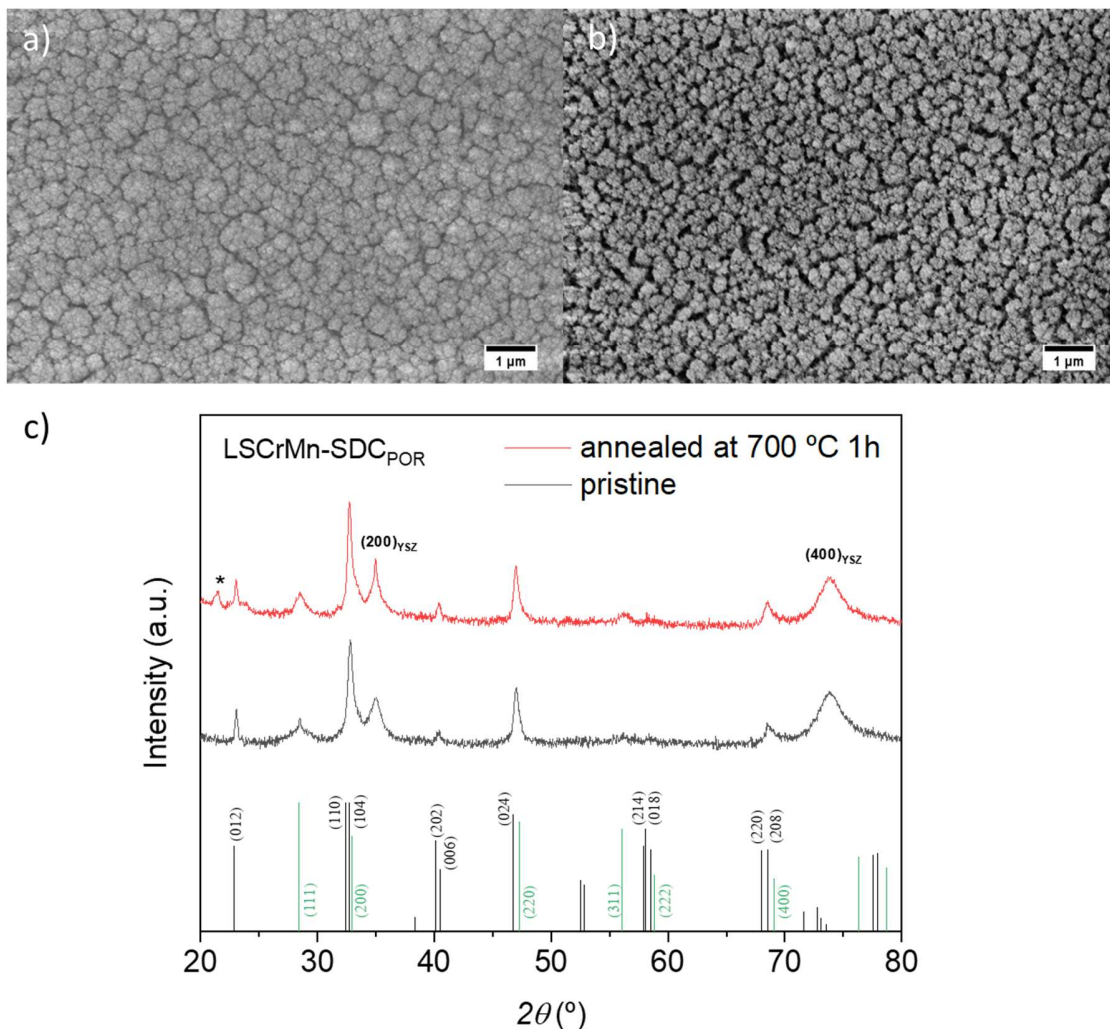


Figure 3-19. SEM micrographs of the LSCrMn-SDC<sub>POR</sub> thin film functional electrode before (a) and after a thermal treatment at 700 °C for 1 h (b). XRD patterns obtained for LSCrMn-SDC<sub>POR</sub> before and after thermal annealing (c). The asterisk (\*) indicates artefact diffraction signals measured from the setup. Reference diffraction patterns are represented on the bottom for LSCrMn (R-3c #167, in black)<sup>27</sup> and SDC (Fm-3m #225, in green)<sup>21</sup>, respectively. The most representative peaks are labelled. YSZ (h00) peaks are labelled directly on the top diffraction pattern as a common reference.

#### 3.4.2.2 Electrochemical performance of microstructure-variant LSCrMn-SDC heterostructures on hydrogen oxidation

The electrochemical properties of the microstructure-variant LSCrMn-SDC materials were studied by impedance spectroscopy under humidified hydrogen atmosphere. Figure 3-20a

shows Nyquist plots obtained for each sample at 750 °C. All the films are mainly dominated by a single arc in the low frequency region characteristic of the hydrogen reaction, as discussed previously<sup>12,35,36</sup>. LSCrMn-SDC<sub>NC-400C</sub> and LSCrMn-SDC<sub>NC-200C</sub> present a slight asymmetry on the arc, most likely caused by minor differences in the thin films of the symmetric cell. An additional minor contribution at high frequencies is present, result of charge-transport processes in the electrolyte-electrode interface. The lowest polarization resistance observed was for the LSCrMn-SDC<sub>POR</sub> heterostructure. The spectra was fitted with an equivalent circuit made of 2 ZARC elements (see Chapter 2). The evolution of the ASR of all the LSCrMn-SDC-based samples analysed so far is reported in Figure 3-20b, including the reference data of the two dense heterostructures discussed in the previous section. Regarding LSCrMn-SDC nanocomposites, a variety of both detrimental and enhancement effects on ASR with respect to dense LSCrMn-SDC<sub>NC</sub> was observed. The nanocomposite grown at 600 °C, LSCrMn-SDC<sub>NC-600C</sub>, showed slightly larger values of ASR and comparable  $E_a$  with respect to the dense material, although the overall difference was not substantially large. Decreasing the deposition temperature to 400 °C and 200 °C lead to the reduction of the ASR below the reference value, approximately by a 2-fold factor, and decreased the  $E_a$  down to 1.10 eV for the sample deposited at 400 °C. Overall, the ASR of the LSCrMn-SDC<sub>NC</sub> samples oscillated in the range of  $\approx 7$ -20  $\Omega\cdot\text{cm}^2$  at 750 °C and the activation energy varied in the 1.10-1.37 eV range. Regarding LSCrMn-SDC<sub>POR</sub>, the electrochemical performance improves substantially –one order of magnitude- with respect to the dense heterostructures, and a 5-fold decrease with respect to the best performing LSCrMn-SDC<sub>NC</sub>. The measured ASR at 750 °C was 1.5  $\Omega\cdot\text{cm}^2$  and the  $E_a$  calculated was 1.44 eV. Despite being the best performance among the LSCrMn-SDC based heterostructures studied in this work, porous SDC presents the lowest ASR on HOR. This is in line with the case of LSCrMn-SDC based materials fabricated with conventional methods, for which the ASR is lower than the obtained in this work. Porous electrodes fabricated by slurry-coating methods have been reported to present  $\approx 0.2$ -0.3  $\Omega\cdot\text{cm}^2$  at 900 °C for the case of LSCrMn<sup>9,60</sup> and  $\approx 0.3$   $\Omega\cdot\text{cm}^2$  at 800 °C for a screen printed LSCrMn-SDC composite<sup>61</sup>. This is out of the values obtained for the thin films studied, even with extrapolation to the same operational temperature. This is most likely related to differences in the thickness of the layers. While the porous SDC layer described in this chapter has an approximate thickness of  $\approx 1$   $\mu\text{m}$  (with lower values expected for LSCrMn-SDC layers given the conditions of deposition chosen), conventional electrodes normally present larger thickness in the order of tens of  $\mu\text{m}$ . This generally leads to lower ASR given the presence of a larger number of reaction sites.



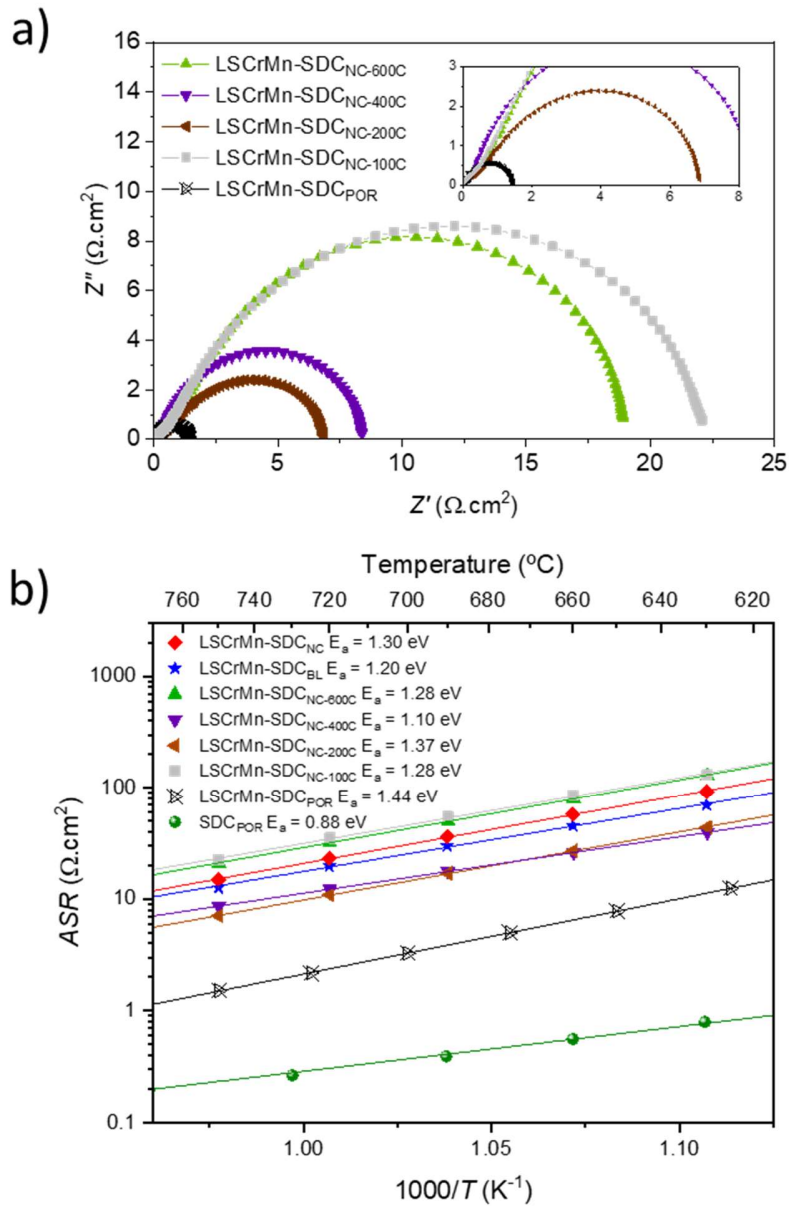


Figure 3-20. Electrochemical characterization of the microstructure-tailored LSCrMn-SDC samples measured under hydrogen atmosphere (LSCrMn-SDC<sub>NC</sub> in red, LSCrMn-SDC<sub>BL</sub> in blue, LSCrMn-SDC<sub>NC-600C</sub> in green, LSCrMn-SDC<sub>NC-400C</sub> in purple, LSCrMn-SDC<sub>NC-200C</sub> in brown, LSCrMn-SDC<sub>NC-100C</sub> in light grey, LSCrMn-SDC<sub>NC-600C</sub> in black and porous SDC in dark green). Nyquist plots measured at 750 °C (a). ASR evolution with temperature (b).

Nonetheless, it should be noted that none of the nanocomposites obtained presented an open volume level of porosity comparable to the case of conventional electrode materials. Figure 3-21 shows SEM micrographs of the LSCrMn-SDC<sub>NC</sub> samples after carrying out the electrochemical measurements. It can be observed that for LSCrMn-SDC<sub>NC-600C</sub> the roughness seems to decrease –the overall microstructure seems less differentiated

than in the as-deposited case–, while for  $\text{LSCrMn-SDC}_{\text{NC-100C}}$  the microstructure densifies through apparent grain coarsening (Figure 3-21a and d, respectively). The evolution of the  $\text{LSCrMn-SDC}_{\text{NC-100C}}$  microstructure is surprising taking into account the thermal treatment performed post-deposition. One possible explanation for this could be that the film did not equilibrate its microstructure within the period of 1 h that the thermal treatment lasted, leading to further evolution during the analysis. The gap observed between the grains of the film prior to the electrochemical characterization seems small enough so the layer can suffer from densification triggered by thermal treatment. Additionally, lattice expansion<sup>62</sup> due to the reducing atmosphere employed during the analysis might have driven the microstructure evolution. The instability of the microstructure is coherent with the worsened ASR of the films with respect to the original dense nanocomposite. In the case of  $\text{LSCrMn-SDC}_{\text{NC-400C}}$ , the microstructure seems to open and become rougher after the electrochemical characterization at high temperature, while keeping the aggregates observed in the film as deposited.  $\text{LSCrMn-SDC}_{\text{NC-200C}}$  shows the smallest microstructure evolution after the electrochemical characterization. The film seems to maintain the overall roughness and some local regions appear to present even larger spatial separation between grains.

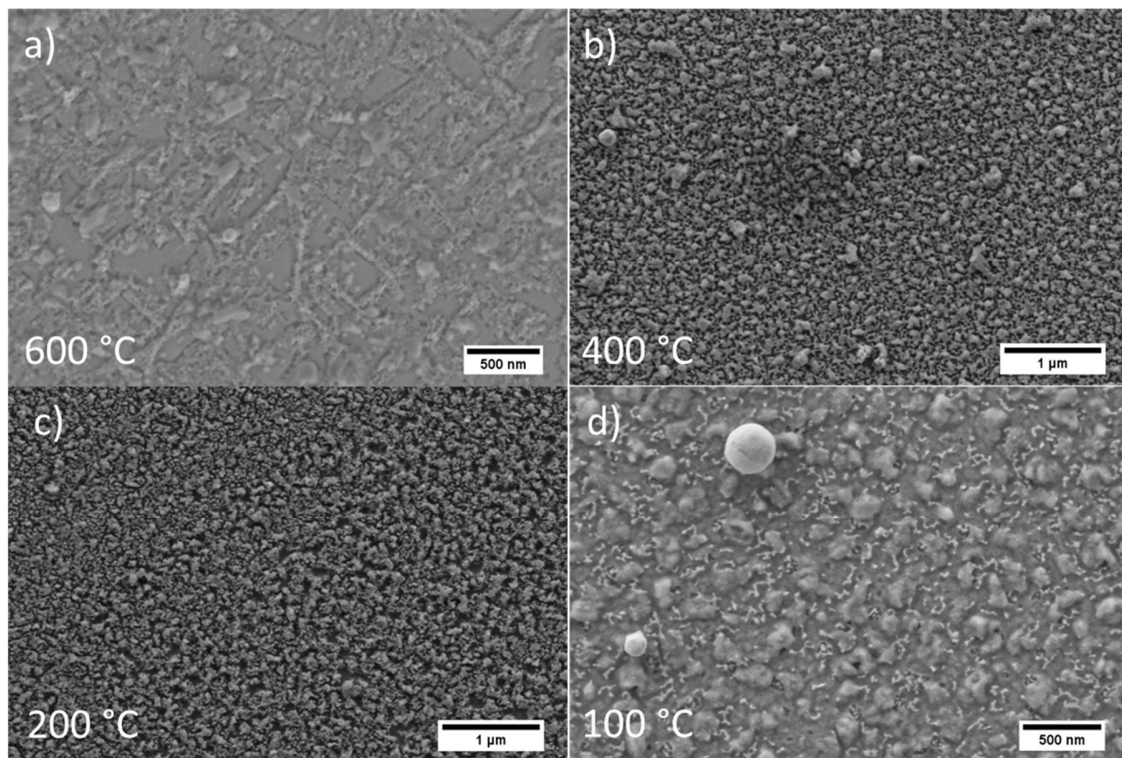


Figure 3-21. SEM micrographs of different  $\text{LSCrMn-SDC}_{\text{NC}}$  films after electrochemical characterization:  $\text{LSCrMn-SDC}_{\text{NC-600C}}$  (a),  $\text{LSCrMn-SDC}_{\text{NC-400C}}$  (b),  $\text{LSCrMn-SDC}_{\text{NC-200C}}$  (c) and  $\text{LSCrMn-SDC}_{\text{NC-100C}}$  (d).

The observed change in the microstructure offers an explanation on the differences in electrochemical performance described between the films. With regard to the electrochemical activity of LSCrMn-SDC<sub>POR</sub>, the difference with single porous SDC can probably be attributed to the presence of the dense LSCrMn layer. Other effects might be due to local differences in the layer thickness with respect to single porous SDC. Additionally, the slight less open porous structure of the SDC phase in the LSCrMn-SDC<sub>POR</sub> sample, with the corresponding decrease of the active area. For single porous SDC, the intimate contact between the porous electrode and the electrolyte results in a large extension of Triple Phase Boundary (TPB) sites, hence increasing the surface redox activity. On the other hand, the most likely scenario in the case of LSCrMn-SDC<sub>POR</sub> is that the LSCrMn layer gives raise to additional interfacial resistances and that the ionic conductivity is not large enough so the active sites are less than the density of TPB sites of the single porous SDC layer. This limitation could be solved by substituting the LSCrMn layer with the LSCrMn-SDC<sub>NC</sub> dense nanocomposite studied in the previous section. The presence of the SDC phase in the dense layer would extend the TPB to all the area in contact with the porous material on top. There is an increasing number of studies that report the use of dense layers in combination with highly active porous electrodes on top. This is the case of oxygen electrode heterostructures like perovskite-fluorite nanocomposites of  $\text{La}_{0.6}\text{Sr}_{0.4}\text{Co}_{0.2}\text{Fe}_{0.8}\text{O}_{3-\delta}$ - $\text{Ce}_{0.9}\text{Gd}_{0.1}\text{O}_{2-\delta}$ <sup>63</sup> and LSM-SDC<sup>53</sup>, or the use of hybrid layers of  $\text{La}_2\text{NiO}_4$  with gradual change from dense to porous microstructure<sup>64</sup>. Nonetheless, the use of these combination of dense interlayers and porous electrodes have been less explored for application in hydrogen electrodes. Given the results presented in this work there is potential for further investigation on the use of LSCrMn-SDC based nanocomposites as hydrogen functional layers in SOCs.

### 3.5 Conclusions

This chapter presented promising approaches for the development of functional hydrogen and symmetric electrodes for SOCs based on different LSCrMn and ceria-based nanomaterials. The work developed aimed to research on the use of novel electrode materials and nanostructures beyond previously developed all-oxide ceria electrodes. First, a series of novel NiCGO cermet thin films with extremely low content of Ni have been studied as potential candidates for hydrogen electrode applications. The microstructure of the films was varied tuning deposition parameters for the fabrication of films with increased level of porosity. The best performing NiCGO electrode was deposited at 500 °C and oxygen pressure of 200 mTorr. The film presented a microstructure characterized by crystallites in the range of 25-40 nm in size and mesoporous-like surface microstructure. The performance of the rest of the NiCGO films were likely determined by the reduced surface area exposed, with the exception of the open-volume NiCGO film. In this case, mechanical instability and sample asymmetry were pointed out as likely causes for the worsened performance. Overall, the performance of the NiCGO materials showed promising electrochemical activity despite it did not surpass the performance of the porous SDC layer. Nonetheless, the mechanical stability of the optimized hydrogen electrodes are expected to overcome the properties of porous SDC given the microstructure observed. Ultimately, further research on the integration of functional layers along with optimized NiCGO materials are expected to offer optimal performance in the development of highly efficient SOC hydrogen electrode.

The second strategy implemented for overcoming the limitations of SDC consisted in fabricating novel nanostructured materials. In particular, the electrochemical performance of LSCrMn-SDC dense heterostructures in either a nanocomposite or a bilayer was evaluated under both reducing and oxidizing atmospheres. The results obtained unveiled a substantial improvement of the performance for both heterostructures, in terms of electrochemical activity and in-plane conductivity (with respect to the single-phase reference materials under anodic conditions) and hence, their potential for catalyzing the hydrogen oxidation reaction in SOCs. Unexpectedly, the LSCrMn-SDC nanocomposite showed high electrochemical activity also under cathodic conditions, along with high stability when tested for over 400 hours. The outstanding properties found for the nanocomposite were attributed to the synergistic effect of the SDC and the LSCrMn phases along the film. The presence of the perovskite phase grown in separate islands along the fluorite matrix was confirmed by HRTEM-ASTAR analysis. Additionally, EDX analysis on the cross section revealed the presence of high cationic intermixing throughout the film, which could be in the origin of high stability of the nanocomposite (according to previous studied of the group). Given the dense nature of the films, the overall electrochemical performance was not comparable to that of single porous SDC. Nonetheless, the remarkable

properties observed makes them promising for application as functional layers in combination with porous electrodes and leave the window open for future material optimization.

Further studies were made for optimizing the microstructure of the LSCrMn-SDC heterostructured layers, in order to enhance the overall electrochemical performance for hydrogen oxidation. PLD parameters were adjusted to lower deposition temperatures while increasing chamber pressures, in order to increase the surface area and overall porosity of the films. The nanocomposites films obtained under these conditions resulted in layers showing different levels of roughness and porosity in their microstructure. The electrochemical activity measured for these films resulted, in some cases, in an improvement of the ASR with respect the dense film. These findings are attributed to the increase of the open-volume porosity in the best performing nanocomposite, and to densification and instability of the microstructure in the worsened heterostructures. A bilayer consisting on a dense LSCrMn film with a porous SDC layer on top was found to be the best performing material (one order of magnitude) among the heterostructures fabricated. Nonetheless, the performance obtained did not reach the activity of a reference porous SDC layer, probably due to the reduction in the active sites as a consequence of the presence of the LSCrMn film and also the slightly reduced surface area of the porous SDC top layer with respect to the reference. With the goal of overcoming these limitations, strategies on the implementation of dense nanocomposite interlayers in combination with porous electrodes have been briefly discussed. The results obtained point to the optimization of a mesoporous microstructure and leave room for further enhancing the activity of the thin film hydrogen electrodes following the principles and strategies explored in the chapter.

## References

- (1) Sirvent, J. de D.; Carmona, A.; Rapenne, L.; Chiabrera, F.; Morata, A.; Burriel, M.; Baiutti, F.; Tarancón, A. Nanostructured  $\text{La}_{0.75}\text{Sr}_{0.25}\text{Cr}_{0.5}\text{Mn}_{0.5}\text{O}_3\text{-Ce}_{0.8}\text{Sm}_{0.2}\text{O}_2$  Heterointerfaces as All-Ceramic Functional Layers for Solid Oxide Fuel Cell Applications. *ACS Appl. Mater. Interfaces* **2022**, *14* (37), 42178–42187. <https://doi.org/10.1021/acsami.2c14044>.
- (2) Setoguchi, T.; Okamoto, K.; Eguchi, K.; Arai, H. Effects of Anode Material and Fuel on Anodic Reaction of Solid Oxide Fuel Cells. *J. Electrochem. Soc.* **1992**, *139* (10), 2875–2880. <https://doi.org/10.1149/1.2068998>.
- (3) Kan, W. H.; Samson, A. J.; Thangadurai, V. Trends in Electrode Development for next Generation Solid Oxide Fuel Cells. *J. Mater. Chem. A* **2016**, *4* (46), 17913–17932. <https://doi.org/10.1039/C6TA06757C>.
- (4) Doppler, M. C.; Fleig, J.; Bram, M.; Opitz, A. K. Hydrogen Oxidation Mechanisms on Ni/Yttria Stabilized Zirconia Anodes: Separation of Reaction Pathways by Geometry Variation of Pattern Electrodes. *J. Power Sources* **2018**, *380*, 46–54. <https://doi.org/10.1016/j.jpowsour.2018.01.073>.
- (5) Doppler, M. C.; Fleig, J.; Bram, M.; Opitz, A. K. Comparison of Electrochemical Hydrogen Oxidation on Different Metal/Ceramic Model Anodes and Mechanistic Implications. *J. Phys. Energy* **2019**, *1* (3), 035001. <https://doi.org/10.1088/2515-7655/ab1ece>.
- (6) Matsuzaki, Y. The Poisoning Effect of Sulfur-Containing Impurity Gas on a SOFC Anode: Part I. Dependence on Temperature, Time, and Impurity Concentration. *Solid State Ion.* **2000**, *132* (3–4), 261–269. [https://doi.org/10.1016/S0167-2738\(00\)00653-6](https://doi.org/10.1016/S0167-2738(00)00653-6).
- (7) Vernoux, P.; Djurado, E.; Guillodo, M. Catalytic and Electrochemical Properties of Doped Lanthanum Chromites as New Anode Materials for Solid Oxide Fuel Cells. *J. Am. Ceram. Soc.* **2004**, *84* (10), 2289–2295. <https://doi.org/10.1111/j.1151-2916.2001.tb01004.x>.
- (8) Rohnke, M.; Falk, M.; Huber, A.-K.; Janek, J. Combining High Temperature Electrochemistry and Time of Flight Secondary Ion Mass Spectrometry: Quasi in Situ Study of Lanthanum Strontium Chromate Manganate Electrodes. *J. Power Sources* **2013**, *221*, 97–107. <https://doi.org/10.1016/j.jpowsour.2012.07.139>.
- (9) Tao, S.; Irvine, J. T. S. Synthesis and Characterization of  $(\text{La}_{0.75}\text{Sr}_{0.25})\text{Cr}_{0.5}\text{Mn}_{0.5}\text{O}_{3-\delta}$ , a Redox-Stable, Efficient Perovskite Anode for SOFCs. *J. Electrochem. Soc.* **2004**, *151* (2), A252. <https://doi.org/10.1149/1.1639161>.
- (10) Zha, S.; Tsang, P.; Cheng, Z.; Liu, M. Electrical Properties and Sulfur Tolerance of  $\text{La}_{0.75}\text{Sr}_{0.25}\text{Cr}_{1-x}\text{Mn}_x\text{O}_3$  under Anodic Conditions. *J. Solid State Chem.* **2005**, *178* (6), 1844–1850. <https://doi.org/10.1016/j.jssc.2005.03.027>.
- (11) Raffaele, R.; Anderson, H. U.; Sparlin, D. M.; Parris, P. E. Transport Anomalies in the High-Temperature Hopping Conductivity and Thermopower of Sr-Doped  $\text{La}(\text{Cr},\text{Mn})\text{O}_3$ . *Phys. Rev. B* **1991**, *43* (10), 7991–7999. <https://doi.org/10.1103/physrevb.43.7991>.

- (12) Jung, W.; Gu, K. L.; Choi, Y.; Haile, S. M. Robust Nanostructures with Exceptionally High Electrochemical Reaction Activity for High Temperature Fuel Cell Electrodes. *Energy Environ. Sci.* **2014**, *7* (5), 1685–1692. <https://doi.org/10.1039/c3ee43546f>.
- (13) Chueh, W. C.; Hao, Y.; Jung, W.; Haile, S. M. High Electrochemical Activity of the Oxide Phase in Model Ceria-Pt and Ceria-Ni Composite Anodes. *Nat. Mater.* **2012**, *11* (2), 155–161. <https://doi.org/10.1038/nmat3184>.
- (14) Jung, W.; Dereux, J. O.; Chueh, W. C.; Hao, Y.; Haile, S. M. High Electrode Activity of Nanostructured, Columnar Ceria Films for Solid Oxide Fuel Cells. *Energy Environ. Sci.* **2012**, *5* (9), 8682–8689. <https://doi.org/10.1039/c2ee22151a>.
- (15) Rojek-Wöckner, V. A.; Opitz, A. K.; Brandner, M.; Mathé, J.; Bram, M. A Novel Ni/Ceria-Based Anode for Metal-Supported Solid Oxide Fuel Cells. *J. Power Sources* **2016**, *328*, 65–74. <https://doi.org/10.1016/j.jpowsour.2016.07.075>.
- (16) Joo, J. H.; Choi, G. M. Electrical Conductivity of Thin Film Ceria Grown by Pulsed Laser Deposition. *J. Eur. Ceram. Soc.* **2007**, *27* (13–15), 4273–4277. <https://doi.org/10.1016/j.jeurceramsoc.2007.02.135>.
- (17) Schmitt, R.; Nanning, A.; Kraynis, O.; Korobko, R.; Frenkel, A. I.; Lubomirsky, I.; Haile, S. M.; Rupp, J. L. M. A Review of Defect Structure and Chemistry in Ceria and Its Solid Solutions. *Chem. Soc. Rev.* **2020**, *49* (2), 554–592. <https://doi.org/10.1039/C9CS00588A>.
- (18) Park, J. H.; Lee, J.-H.; Yoon, K. J.; Kim, H.; Ji, H.-I.; Yang, S.; Park, S.; Han, S. M.; Son, J.-W. A Nanoarchitected Cermet Composite with Extremely Low Ni Content for Stable High-Performance Solid Oxide Fuel Cells. *Acta Mater.* **2021**, *206*, 116580. <https://doi.org/10.1016/j.actamat.2020.116580>.
- (19) Bianchini, M. Integration of Ceramic Thin Films in Silicon Technology for Energy Conversion and Oxygen Sensing, Universitat Autònoma de Barcelona, 2022.
- (20) Dhakal, T.; Mukherjee, D.; Hyde, R. H.; Srikanth, H.; Mukherjee, P.; Witanachchi, S. Enhancement in Ferroelectricity in V-Doped ZnO Thin Film Grown Using Laser Ablation. *MRS Proc.* **2009**, *1199*, 1199-F03-44. <https://doi.org/10.1557/PROC-1199-F03-44>.
- (21) Artini, C.; Pani, M.; Carnasciali, M. M.; Buscaglia, M. T.; Plaisier, J. R.; Costa, G. A. Structural Features of Sm- and Gd-Doped Ceria Studied by Synchrotron X-Ray Diffraction and  $\mu$ -Raman Spectroscopy. *Inorg. Chem.* **2015**, *54* (8), 4126–4137. <https://doi.org/10.1021/acs.inorgchem.5b00395>.
- (22) Cairns, R. W.; Ott, E. X-Ray Studies of the System Nickel—Oxygen—Water. I. Nickelous Oxide and Hydroxide. *J. Am. Chem. Soc.* **1933**, *55* (2), 527–533. <https://doi.org/10.1021/ja01329a013>.
- (23) Häglund, J.; Fernández Guillermet, A.; Grimvall, G.; Körling, M. Theory of Bonding in Transition-Metal Carbides and Nitrides. *Phys. Rev. B* **1993**, *48* (16), 11685–11691. <https://doi.org/10.1103/PhysRevB.48.11685>.
- (24) Zha, S.; Xia, C.; Meng, G. Effect of Gd (Sm) Doping on Properties of Ceria Electrolyte for Solid Oxide Fuel Cells. *J. Power Sources* **2003**, *115* (1), 44–48. [https://doi.org/10.1016/S0378-7753\(02\)00625-0](https://doi.org/10.1016/S0378-7753(02)00625-0).
- (25) Koettgen, J.; Martin, M. The Ionic Conductivity of Sm-Doped Ceria. *J. Am. Ceram. Soc.* **2020**, *103* (6), 3776–3787. <https://doi.org/10.1111/jace.17066>.

- (26) Zhang, S.; Wan, Y.; Xu, Z.; Xue, S.; Zhang, L.; Zhang, B.; Xia, C. Bismuth Doped  $\text{La}_{0.75}\text{Sr}_{0.25}\text{Cr}_{0.5}\text{Mn}_{0.5}\text{O}_{3-\delta}$  Perovskite as a Novel Redox-Stable Efficient Anode for Solid Oxide Fuel Cells. *J. Mater. Chem. A* **2020**, *8* (23), 11553–11563. <https://doi.org/10.1039/D0TA03328F>.
- (27) El-Fadli, Z.; Redouane Metni, M.; Sapiña, F.; Martinez, E.; José-Vicente Folgado, and; Beltrán, A. Electronic Properties of Mixed-Valence Manganates: The Role of Mn Substitutional Defects. *Chem. Mater.* **2002**, *14* (2), 688–696. <https://doi.org/10.1021/cm010655e>.
- (28) Baiutti, F.; Chiabrera, F.; Acosta, M.; Diercks, D.; Parfitt, D.; Santiso, J.; Wang, X.; Cavallaro, A.; Morata, A.; Wang, H.; Chroneos, A.; MacManus-Driscoll, J.; Tarancon, A. A High-Entropy Manganite in an Ordered Nanocomposite for Long-Term Application in Solid Oxide Cells. *Nat. Commun.* **2021**, *12* (1), 2660. <https://doi.org/10.1038/s41467-021-22916-4>.
- (29) Varshney, D.; Dodiya, N. Electrical Resistivity of the Hole Doped  $\text{La}_{0.8}\text{Sr}_{0.2}\text{MnO}_3$  Manganites: Role of Electron–Electron/Phonon/Magnon Interactions. *Mater. Chem. Phys.* **2011**, *129* (3), 896–904. <https://doi.org/10.1016/j.matchemphys.2011.05.034>.
- (30) Harrington, G. F.; Sun, L.; Yildiz, B.; Sasaki, K.; Perry, N. H.; Tuller, H. L. The Interplay and Impact of Strain and Defect Association on the Conductivity of Rare-Earth Substituted Ceria. *Acta Mater.* **2019**, *166*, 447–458. <https://doi.org/10.1016/j.actamat.2018.12.058>.
- (31) Morales, M.; Pesce, A.; Slodczyk, A.; Torrell, M.; Piccardo, P.; Montinaro, D.; Tarancón, A.; Morata, A. Enhanced Performance of Gadolinia-Doped Ceria Diffusion Barrier Layers Fabricated by Pulsed Laser Deposition for Large-Area Solid Oxide Fuel Cells. *ACS Appl. Energy Mater.* **2018**, *1* (5), 1955–1964. <https://doi.org/10.1021/acsaem.8b00039>.
- (32) Huber, T. M.; Navickas, E.; Sasaki, K.; Yildiz, B.; Hutter, H.; Tuller, H.; Fleig, J. Interplay of Grain Size Dependent Electronic and Ionic Conductivity in Electrochemical Polarization Studies on Sr-Doped  $\text{LaMnO}_3$  (LSM) Thin Film Cathodes. *J. Electrochem. Soc.* **2018**, *165* (9), F702–F709. <https://doi.org/10.1149/2.1081809jes>.
- (33) Baumann, F. S.; Fleig, J.; Habermeier, H.-U.; Maier, J. Impedance Spectroscopic Study on Well-Defined  $(\text{La,Sr})(\text{Co,Fe})\text{O}_{3-\delta}$  Model Electrodes. *Solid State Ion.* **2006**, *177* (11–12), 1071–1081. <https://doi.org/10.1016/j.ssi.2006.02.045>.
- (34) Raj, E.; Kilner, J.; Irvine, J. Oxygen Diffusion and Surface Exchange Studies on  $(\text{La}_{0.75}\text{Sr}_{0.25})_{0.95}\text{Cr}_{0.5}\text{Mn}_{0.5}\text{O}_{3-\delta}$ . *Solid State Ion.* **2006**, *177* (19–25), 1747–1752. <https://doi.org/10.1016/j.ssi.2006.04.011>.
- (35) Primdahl, S.; Liu, Y. L. Ni Catalyst for Hydrogen Conversion in Gadolinia-Doped Ceria Anodes for Solid Oxide Fuel Cells. *J. Electrochem. Soc.* **2002**, *149* (11), A1466–A1472. <https://doi.org/10.1149/1.1514234>.
- (36) Nakamura, T.; Kobayashi, T.; Yashiro, K.; Kaimai, A.; Otake, T.; Sato, K.; Mizusaki, J.; Kawada, T. Electrochemical Behaviors of Mixed Conducting Oxide Anodes for Solid Oxide Fuel Cell. *J. Electrochem. Soc.* **2008**, *155* (6), B563–B569. <https://doi.org/10.1149/1.2901047>.



- (37) Holtappels, P.; Vinke, I. C.; de Haart, L. G. J.; Stimming, U. Reaction of Hydrogen/Water Mixtures on Nickel-Zirconia Cermet Electrodes: II. AC Polarization Characteristics. *J. Electrochem. Soc.* **1999**, *146* (8), 2976–2982. <https://doi.org/10.1149/1.1392038>.
- (38) Murray, E. P.; Barnett, S. A. (La,Sr)MnO<sub>3</sub>-(Ce,Gd)O<sub>2-x</sub> Composite Cathodes for Solid Oxide Fuel Cells. *Solid State Ion.* **2001**, *143* (3–4), 265–273. [https://doi.org/10.1016/S0167-2738\(01\)00871-2](https://doi.org/10.1016/S0167-2738(01)00871-2).
- (39) Burnat, D.; Nasdaurk, G.; Holzer, L.; Kopecki, M.; Heel, A. Lanthanum Doped Strontium Titanate - Ceria Anodes: Deconvolution of Impedance Spectra and Relationship with Composition and Microstructure. *J. Power Sources* **2018**, *385*, 62–75. <https://doi.org/10.1016/j.jpowsour.2018.03.024>.
- (40) Jamnik, J.; Maier, J. Generalised Equivalent Circuits for Mass and Charge Transport: Chemical Capacitance and Its Implications. *Phys. Chem. Chem. Phys.* **2001**, *3* (9), 1668–1678. <https://doi.org/10.1039/b100180i>.
- (41) Chueh, W. C.; Haile, S. M. Electrochemical Studies of Capacitance in Cerium Oxide Thin Films and Its Relationship to Anionic and Electronic Defect Densities. *Phys. Chem. Chem. Phys.* **2009**, *11* (37), 8144–8148. <https://doi.org/10.1039/b910903j>.
- (42) Lai, W.; Haile, S. M. Impedance Spectroscopy as a Tool for Chemical and Electrochemical Analysis of Mixed Conductors: A Case Study of Ceria. *J. Am. Ceram. Soc.* **2005**, *88* (11), 2979–2997. <https://doi.org/10.1111/j.1551-2916.2005.00740.x>.
- (43) Rupp, G. M.; Limbeck, A.; Kubicek, M.; Penn, A.; Stöger-Pollach, M.; Friedbacher, G.; Fleig, J. Correlating Surface Cation Composition and Thin Film Microstructure with the Electrochemical Performance of Lanthanum Strontium Cobaltite (LSC) Electrodes. *J Mater Chem A* **2014**, *2* (19), 7099–7108. <https://doi.org/10.1039/C3TA15327D>.
- (44) Jiang, S.; Chen, X.; Chan, S.; Kwok, J.; Khor, K. (La<sub>0.75</sub>Sr<sub>0.25</sub>)(Cr<sub>0.5</sub>Mn<sub>0.5</sub>)O<sub>3</sub>/YSZ Composite Anodes for Methane Oxidation Reaction in Solid Oxide Fuel Cells. *Solid State Ion.* **2006**, *177* (1–2), 149–157. <https://doi.org/10.1016/j.ssi.2005.09.010>.
- (45) Kharton, V. V.; Tsipis, E. V.; Marozau, I. P.; Viskup, A. P.; Frade, J. R.; Irvine, J. T. S. Mixed Conductivity and Electrochemical Behavior of (La<sub>0.75</sub>Sr<sub>0.25</sub>)<sub>0.95</sub>Cr<sub>0.5</sub>Mn<sub>0.5</sub>O<sub>3-δ</sub>. *Solid State Ion.* **2007**, *178* (1–2), 101–113. <https://doi.org/10.1016/j.ssi.2006.11.012>.
- (46) Usiskin, R. E.; Maruyama, S.; Kucharczyk, C. J.; Takeuchi, I.; Haile, S. M. Probing the Reaction Pathway in (La<sub>0.8</sub>Sr<sub>0.2</sub>)<sub>0.95</sub>MnO<sub>3+δ</sub> Using Libraries of Thin Film Microelectrodes. *J. Mater. Chem. A* **2015**, *3* (38), 19330–19345. <https://doi.org/10.1039/c5ta02428e>.
- (47) Harrington, S. P.; Devine, T. M. Analysis of Electrodes Displaying Frequency Dispersion in Mott-Schottky Tests. *J. Electrochem. Soc.* **2008**, *155* (8), C381. <https://doi.org/10.1149/1.2929819>.
- (48) Brug, G. J.; van der Eeden, A. L. G.; Sluyters-Rehbach, M.; Sluyters, J. H. The Analysis of Electrode Impedances Complicated by the Presence of a Constant Phase Element. *J. Electroanal. Chem. Interfacial Electrochem.* **1984**, *176* (1–2), 275–295. [https://doi.org/10.1016/S0022-0728\(84\)80324-1](https://doi.org/10.1016/S0022-0728(84)80324-1).
- (49) Hendriks, M. G. H. M.; ten Elshof, J. E.; Bouwmeester, H. J. M.; Verweij, H. The Electrochemical Double-Layer Capacitance of Yttria-Stabilised Zirconia. *Solid State Ion.* **2002**, *146* (3–4), 211–217. [https://doi.org/10.1016/S0167-2738\(01\)01017-7](https://doi.org/10.1016/S0167-2738(01)01017-7).

- (50) Pornprasertsuk, R.; Cheng, J.; Huang, H.; Prinz, F. Electrochemical Impedance Analysis of Solid Oxide Fuel Cell Electrolyte Using Kinetic Monte Carlo Technique. *Solid State Ion.* **2007**, *178* (3–4), 195–205. <https://doi.org/10.1016/j.ssi.2006.12.016>.
- (51) Vives, S.; Ramel, D.; Meunier, C. Molecular Dynamics Study in the  $\text{Ce}_{0.9}\text{M}_{0.1}\text{O}_{1.95}$  (M=Gd, Sm) Doped and Co-Doped  $\text{CeO}_2$  Systems: Structure and Oxygen Diffusion. *Ceram. Int.* **2019**, *45* (17), 21625–21634. <https://doi.org/10.1016/j.ceramint.2019.07.158>.
- (52) Choi, M.; Ibrahim, I. A. M.; Kim, K.; Koo, J. Y.; Kim, S. J.; Son, J.-W.; Han, J. W.; Lee, W. Engineering of Charged Defects at Perovskite Oxide Surfaces for Exceptionally Stable Solid Oxide Fuel Cell Electrodes. *ACS Appl. Mater. Interfaces* **2020**, *12* (19), 21494–21504. <https://doi.org/10.1021/acsmi.9b21919>.
- (53) Machado, M.; Baiutti, F.; Bernadet, L.; Morata, A.; Nuñez, M.; Ouweltjes, J. P.; Fonseca, F. C.; Torrell, M.; Tarancón, A. Functional Thin Films as Cathode/Electrolyte Interlayers: A Strategy to Enhance the Performance and Durability of Solid Oxide Fuel Cells. *J. Mater. Chem. A* **2022**, *10* (33), 17317–17325. <https://doi.org/10.1039/D2TA03641J>.
- (54) Cai, Z.; Kubicek, M.; Fleig, J.; Yildiz, B. Chemical Heterogeneities on  $\text{La}_{0.6}\text{Sr}_{0.4}\text{CoO}_{3-\delta}$  Thin Films—Correlations to Cathode Surface Activity and Stability. *Chem. Mater.* **2012**, *24* (6), 1116–1127. <https://doi.org/10.1021/cm203501u>.
- (55) Ma, W.; Kim, J. J.; Tsvetkov, N.; Daio, T.; Kuru, Y.; Cai, Z.; Chen, Y.; Sasaki, K.; Tuller, H. L.; Yildiz, B. Vertically Aligned Nanocomposite  $\text{La}_{0.8}\text{Sr}_{0.2}\text{CoO}_3/(\text{La}_{0.5}\text{Sr}_{0.5})_2\text{CoO}_4$  Cathodes – Electronic Structure, Surface Chemistry and Oxygen Reduction Kinetics. *J. Mater. Chem. A* **2015**, *3* (1), 207–219. <https://doi.org/10.1039/C4TA04993D>.
- (56) Acosta, M.; Baiutti, F.; Tarancón, A.; MacManus-Driscoll, J. L. Nanostructured Materials and Interfaces for Advanced Ionic Electronic Conducting Oxides. *Adv. Mater. Interfaces* **2019**, *6*, 1900462. <https://doi.org/10.1002/admi.201900462>.
- (57) Gupta, S.; Zhong, Y.; Mahapatra, M.; Singh, P. Processing and Electrochemical Performance of Manganese-Doped Lanthanum-Strontium Chromite in Oxidizing and Reducing Atmospheres. *Int. J. Hydrog. Energy* **2015**, *40* (39), 13479–13489. <https://doi.org/10.1016/j.ijhydene.2015.07.153>.
- (58) Bernadet, L.; Moncasi, C.; Torrell, M.; Tarancón, A. High-Performing Electrolyte-Supported Symmetrical Solid Oxide Electrolysis Cells Operating under Steam Electrolysis and Co-Electrolysis Modes. *Int. J. Hydrog. Energy* **2020**, *45* (28), 14208–14217. <https://doi.org/10.1016/j.ijhydene.2020.03.144>.
- (59) Venables, J. *Introduction to Surface and Thin Film Processes*; Cambridge University Press: Cambridge, UK; New York, 2000.
- (60) Ruiz-Morales, J. C.; Canales-Vázquez, J.; Peña-Martínez, J.; López, D. M.; Núñez, P. On the Simultaneous Use of  $\text{La}_{0.75}\text{Sr}_{0.25}\text{Cr}_{0.5}\text{Mn}_{0.5}\text{O}_{3-\delta}$  as Both Anode and Cathode Material with Improved Microstructure in Solid Oxide Fuel Cells. *Electrochimica Acta* **2006**, *52* (1), 278–284. <https://doi.org/10.1016/j.electacta.2006.05.006>.
- (61) He, S.; Chen, H.; Li, R.; Ge, L.; Guo, L. Effect of  $\text{Ce}_{0.8}\text{Sm}_{0.2}\text{O}_{1.9}$  Interlayer on the Electrochemical Performance of  $\text{La}_{0.75}\text{Sr}_{0.25}\text{Cr}_{0.5}\text{Mn}_{0.5}\text{O}_{3-\delta}$ – $\text{Ce}_{0.8}\text{Sm}_{0.2}\text{O}_{1.9}$  Composite Anodes for Intermediate-Temperature Solid Oxide Fuel Cells. *J. Power Sources* **2014**, *253*, 187–192. <https://doi.org/10.1016/j.jpowsour.2013.12.071>.

- (62) Tao, S.; Irvine, J. T. S. Phase Transition in Perovskite Oxide  $\text{La}_{0.75}\text{Sr}_{0.25}\text{Cr}_{0.5}\text{Mn}_{0.5}\text{O}_{3-\delta}$  Observed by in Situ High-Temperature Neutron Powder Diffraction. *Chem. Mater.* **2006**, *18* (23), 5453–5460. <https://doi.org/10.1021/cm061413n>.
- (63) Develos-Bagarinao, K.; Ishiyama, T.; Kishimoto, H.; Shimada, H.; Yamaji, K. Nanoengineering of Cathode Layers for Solid Oxide Fuel Cells to Achieve Superior Power Densities. *Nat. Commun.* **2021**, *12* (1), 3979. <https://doi.org/10.1038/s41467-021-24255-w>.
- (64) Stangl, A.; Riaz, A.; Rapenne, L.; Caicedo, J. M.; Sirvent, J. de D.; Baiutti, F.; Jiménez, C.; Tarancón, A.; Mermoux, M.; Burriel, M. Tailored Nano-Columnar  $\text{La}_2\text{NiO}_4$  Cathodes for Improved Electrode Performance. *J. Mater. Chem. A* **2022**, *10*, 2528–2540. <https://doi.org/10.1039/D1TA09110G>.

*4. Study of the  $\text{La}_{0.8}\text{Sr}_{0.2}\text{Mn}_x\text{Co}_y\text{Fe}_{1-x-y}\text{O}_3$  perovskite family as suitable cathodes in solid oxide fuel cells*

4.1 Motivation .....	133
4.2 Optimization of the deposition procedure.....	135
4.3 Development of high throughput characterization methods .....	138
4.3.1 Structural, compositional and optical characterization.....	138
4.3.1.1 Distribution of the B-cation by high throughput X-Ray Fluorescence .....	138
4.3.1.2 Characterization of the crystallographic structure by X-Ray Diffraction.....	140
4.3.1.3 Structural characterization by Raman Spectroscopy .....	142
4.3.1.4 Analysis of the optical properties by spectroscopic ellipsometry.....	145
4.3.2 Functional characterization .....	147
4.3.2.1 Analysis of the mass transport properties by Isotopic Exchange Depth Profiling-Secondary Ion Mass Spectrometry.....	147
4.3.2.2 Electrochemical characterization by impedance spectroscopy mapping .....	152
4.4 Study of the evolution of LSMCF thin films facing thermal degradation .....	156
4.4.1 Electrochemical performance during thermal degradation.....	156
4.4.2 Structural and chemical evolution of the thin film surface and subsurface.....	157
4.4.2.1 Evolution of surface microstructure and appearance of segregated phases ....	158
4.4.2.2 A-site cation structural and chemical evolution at the surface and sub-surface level .....	161
4.4.2.3 Effect of the surface evolution with degradation of the electrochemical performance.....	174
4.4.3 Evolution of the distribution and nature of B-site cations and vacancy-defects beyond the surface and subsurface.....	175
4.4.3.1 Compensation of the B-site cations upon thermal annealing.....	175
4.4.3.2 Evolution of vacancy-related defects and their correlation with cation.....	178
4.5 Guidelines for the selection of a thin film LSMCF compound .....	186
4.6 Conclusions .....	188
References.....	190

## 4.1 Motivation

This chapter is dedicated to the systematic investigation of the  $\text{La}_{0.8}\text{Sr}_{0.2}\text{Mn}_x\text{Co}_y\text{Fe}_{1-x-y}\text{O}_3$  (LSMCF) perovskite family and their properties for application as oxygen electrodes in solid oxide cells (SOCs). The three single materials, namely  $\text{La}_x\text{Sr}_{1-x}\text{MnO}_3$  (LSM),  $\text{La}_x\text{Sr}_{1-x}\text{CoO}_3$  (LSC) and  $\text{La}_x\text{Sr}_{1-x}\text{FeO}_3$  (LSF) are well-known cathode materials and have been extensively discussed in the community<sup>1-3</sup> (cf. Chapter 1 for an extensive description on oxygen electrode materials). This is also the case for binary systems like  $\text{La}_x\text{Sr}_{1-x}\text{Mn}_y\text{Co}_{1-y}\text{O}_3$ <sup>4,5</sup> (LSMC) and  $\text{La}_x\text{Sr}_{1-x}\text{Co}_y\text{Fe}_{1-y}\text{O}_3$ <sup>6,7</sup> (LSCF), with the latter being one of the best performing and most established cathode materials employed. All of these materials present different characteristics that makes them suitable for application in solid oxide energy systems. LSM is an electronic conductor that presents high thermodynamical stability in SOC operating conditions<sup>8</sup> and a decent thermal expansion match with the generally employed yttria-stabilized zirconia (YSZ) electrolyte<sup>9</sup>. Nevertheless, the electrochemical activity of LSM is characterized by high thermal activation and is typically limited to operating temperatures above 800 °C. In contrast, Co-containing materials like LSC and LSCF are characterized by mixed ionic electronic conduction and superior electrochemical activity but are more prone to suffer from degradation phenomena due to higher chemical instability through dopant segregation phenomena. In particular, the presence of Sr segregated phases into the electrode surface has been associated to performance degradation in a large number of studies over the years and for a variety of electrode compositions<sup>10-14</sup>. It is therefore of interest to explore the material space represented by the LSMCF, B-site co-doped system, pursuing the ideal tradeoff between thermo-chemo-mechanical stability and electrochemical activity. Such a goal requires putting in place advanced strategies of combinatorial material synthesis and high-throughput characterization, which have been developed in the frame of the present thesis and presented in this chapter. The work described here has been carried out according to two main strategies. The first consisted in carrying out a thorough characterization of the compositional, structural and functional properties of the complete LSMCF library by making use of high-throughput methodologies. These approaches allow to carry out the full characterization of the material library under the same conditions, reducing the experimental uncertainty associated to sample variability. Secondly, a discrete set of LSMCF compounds were selected for the study of the changes affecting the structural and electrochemical properties driven by thermal degradation. Particular focus was given to study of the phenomenon of dopant segregation. Advanced characterization techniques for analyzing the chemistry of surface, subsurface and deeper regions of the degraded films were employed. The experimental work developed is intended to generate relevant information on the chemical, structural and functional properties for the full LSMCF library. The ultimate goal behind this work would be to predict correlation features between these properties in the form of

performance descriptors based on predictive analyzes methodologies –out of the scope of this thesis–.

In Section 4.2 of this chapter, details on the optimization of the fabrication process by combinatorial pulsed laser deposition (PLD) are described. Particularly, thickness characterization of the parent materials and the resulting combinatorial film is described, along with a discussion on the composition distribution of the LSMCF film. In Section 4.3, high-throughput methodologies are employed for fully characterize the LSMCF perovskite library. In particular, Section 4.3.1 presents the methodologies employed for the structural, compositional and optical characterization of LSMCF. For this purpose high-throughput X-Ray Fluorescence (XRF), X-Ray Diffraction (XRD), Raman Spectroscopy and Spectroscopic Ellipsometry techniques were employed. In Section 4.3.2 the oxygen mass transport kinetics of the LSMCF material library is studied by means of Isotopic Exchange Depth Profiling (IEDP) coupled with Secondary Ion Mass Spectrometry (SIMS). Additionally, the electrochemical activity on the oxygen reduction reaction in terms of polarization resistance and thermal activation has been studied by Electrochemical Impedance Spectroscopy (EIS).

Section 4.4 focuses on the study of the evolution of LSMCF-based materials when exposed to thermal degradation. Section 4.4.1 shows the evolution over time of the electrochemical performance of single perovskites, along with representative LSMCF co-doped materials. A study on the evolution of a selection of LSMCF compounds on prolonged thermal annealing with focus on the structural and chemical changes induced by dopant segregation is presented in section 4.4.2. The evolution of the surface microstructure has been analyzed by Atomic Force Microscopy (AFM), while the surface and subsurface regions are studied by Low Energy Ion Scattering (LEIS) depth profiles, showing the rearrangement along the off-plane axis of the A-site cations. The chemical nature of the surface species has been characterized by X-Ray Photoelectron Spectroscopy (XPS). Section 4.4.3 introduces additional characterization focused on the identification of the B-site cation distribution and the presence of the major defects involved in the thermal ageing. The analysis has been performed by deeper LEIS profiling and Positron Annihilation Spectroscopy (PAS). Finally, in Section 4.5, guidelines for the proper selection of the composition of interest of a LSMCF compound are discussed, based on the more relevant results obtained through the chapter.

## 4.2 Optimization of the deposition procedure

Thin film libraries of LSMCF have been prepared by combinatorial pulsed laser deposition on Si (100) and 8 % mol YSZ (100) wafer substrates. An interlayer of  $\text{Ce}_{0.8}\text{Gd}_{0.2}\text{O}_2$  (CGO) was also fabricated by large area PLD for the cases in which secondary reactions in the electrode-electrolyte interface were to be avoided (i.e. for functional characterization at high temperatures). During this process, each parent material (LSC, LSF and LSM) was sequentially ablated into the substrate and spatially separated by rotating  $120^\circ$ . The number of laser pulses per cycle of deposition was adjusted to deposit a layer of approximately 1 nm of thickness. This low thickness allowed for the rearrangement of the B-cation into a single perovskite phase, in which the distribution of Mn, Co and Fe content follows the geometry of the deposition<sup>5</sup>. A detailed description on the combinatorial deposition methodology can be found in Chapter 2. Figure 4-1 shows the characterization of the thickness distribution of deposited plumes for each of the parent materials as well as for the resulting combinatorial film deposited. The thickness map was obtained by Spectroscopic Ellipsometry. In particular, Figure 4-1a-c shows the deposition of the LSC, LSM and LSF films, respectively. It can be observed that all of the plumes are characterized by similar geometries, with LSC presenting a more circular pattern with respect to LSM and LSF, for which the plumes seem to be slightly more elongated in the vertical axis (i.e. the direction of laser incidence). Additionally, the LSF plume seemed to present the narrowest region around the peak maximum. This could be attributed to several experimental factors. Local differences in the setup might lead to differences in the spot geometry and hence, in the plume shape. The deposition kinetics is also expected to vary for different materials, even for the same experimental conditions<sup>15</sup>, e.g. in case of differences in the optical absorption. For the combinatorial deposition, the growth rates of each parent material were extracted from the maxima obtained in the plume characterization. With that, the number of laser pulses per cycle were adjusted and the combinatorial deposition was carried out. Figure 4-1d shows the thickness map of the fabricated LSMCF film. From it, it is clear that the nature of the geometries observed for the single materials is maintained. The Co- and Mn-rich regions present wider distribution in thickness while the Fe-rich region presents a narrower maximum. The LSMCF combinatorial film analyzed in Figure 4-1d showed thickness values in the 30-50 nm range, approximately. Although differences in thickness have been proven to show changes on the electrochemical performance of solid oxide fuel cell (SOFC) cathodes<sup>16</sup>, it is expected that this may not play a substantial role in this system. This hypothesis is based on two reasons. First, the absolute range of thicknesses present in the LSMCF is much lower than typically employed thin film electrodes (i.e. thickness  $\ll$  100 nm), hence the contribution of ion diffusion through the film thickness on the polarization resistance is expected to be minimized. In second place, a large extension of the combinatorial LSMCF film is expected to present electrochemical performances dominated by the surface activity, as it is the case of the LSC and LSF parent materials<sup>2,17</sup>. With regard



to the Mn-rich region, generally known to be co-limited by both bulk ionic transport and surface activity, the large extension of the sample in the lateral dimension is expected to keep the spatial change in the B-cation composition as the main cause of electrochemical activity evolution along the sample. Overall, the thickness distribution obtained during the characterization of the plumes and the LSMCF combinatorial film is in good agreement with the results published by Saranya and Chiabrera et al. on the LSMC and LSM<sub>y</sub> systems<sup>5,18</sup> – i.e. preceding works from the group based on combinatorial approaches –, guaranteeing the reproducibility of the method.

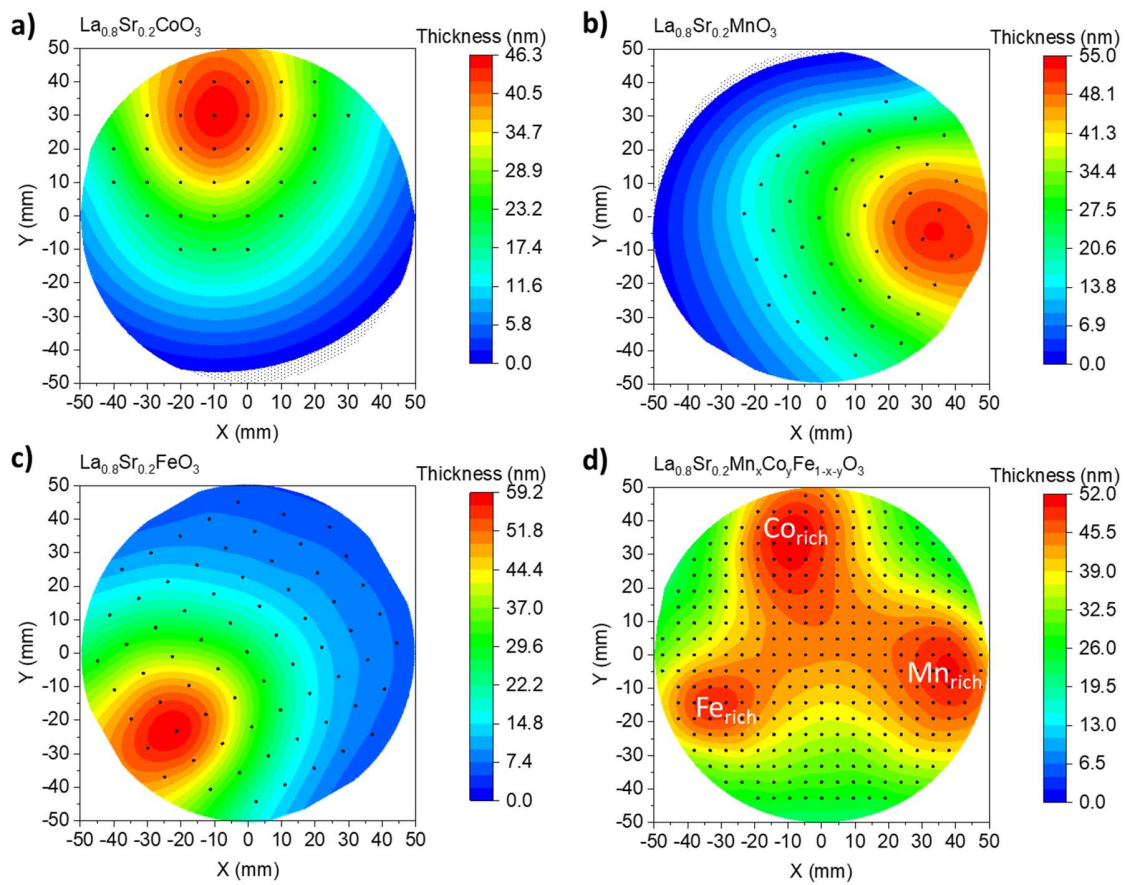


Figure 4-1. Characterization of the deposition geometry and thickness distribution of the parent materials and LSMCF combinatorial films studied in this chapter: thickness maps of LSC, LSM, LSF and LSMCF films deposited on 10 cm Si (100) wafers, respectively (a-d).

The deposited LSMCF combinatorial thin films were characterized by energy dispersive X-ray spectroscopy (EDX), in order to confirm the relative distribution of the Mn, Co and Fe cations along the wafer. The obtained maps for the normalized contents of Fe, Co and Mn are shown in Figure 4-2a-c, respectively. From each map it can be appreciated that the relative content of each B-cation along the XY coordinates of the wafer substrate follows the same trend as from the thickness measurements performed. These results confirmed the successful deposition of combinatorial LSMCF thin films as intended, obtaining the ternary

LSMCF perovskite family widespread on large area substrates. It should be noted that compositions close to the single constituents (i.e. B-content  $\approx 1$  for one cation) are present near the edges of the sample. In particular, in the cases in which the LSMCF film was deposited on 3-inch substrates (dashed lines in Figure 4-2), the relative B-cation content was limited to a maximum up to 0.8. Because of this limitation and in order to offer a complete discussion on the LSMCF library, LSM, LSC and LSF thin films deposited on 10x10 mm<sup>2</sup> substrates were also studied in this work.

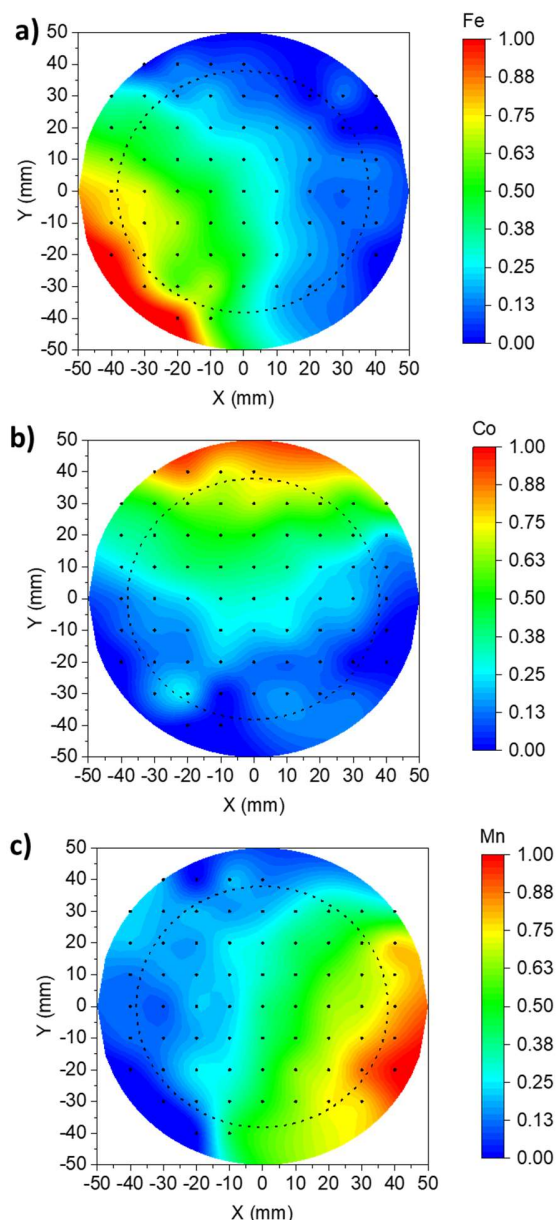


Figure 4-2. EDX maps showing the relative presence of Fe, Co and Mn cations in the deposited LSMCF thin films, respectively (a-c). The dashed circle is a reference to the 3-inch substrates employed for the fabrication of the samples to be characterized by electrochemical methods.

## 4.3 Development of high throughput characterization methods

### 4.3.1 Structural, compositional and optical characterization

#### 4.3.1.1 Distribution of the B-cation by high throughput X-Ray Fluorescence\*

In order to properly evaluate the properties studied for the LSMCF system, a through characterization of the cation spatial distribution along the wafer was needed. Despite the initial characterization made by EDX allowed to visualize the relative distribution of the B-cations up to an extent, a more sensitive tool is required for characterization of the complete LSMCF library. With that aim, XRF measurements were performed in a synchrotron facility. An example of the results of the XRF pattern fitting routine is reported in Figure 4-3 for different XY sample coordinates: the center of the sample (0;0), the deposition centers of Mn (30;0), Fe (-30;-18), and Co (-12;36). A good agreement between experimental points (black hollow circles) and the total fitting profile (black line) is observed for all the coordinates.

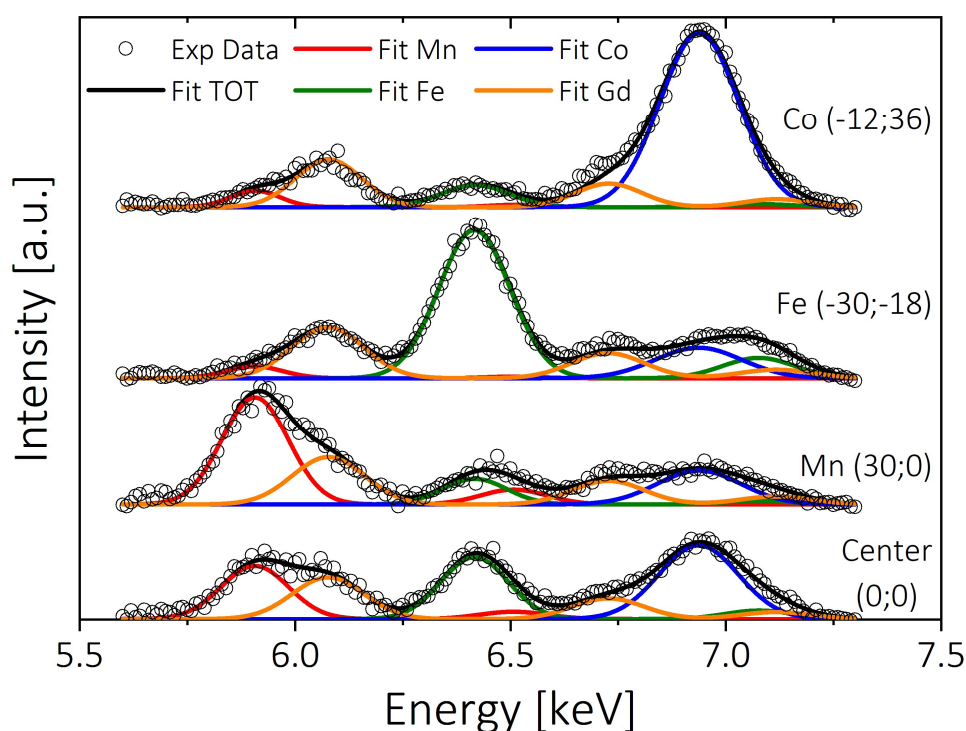


Figure 4-3. Examples of XRF spectra and fitting curves for different XY sample coordinates: the center of the sample (0;0), the deposition centers of Mn (30;0), Fe (-30;-18), and Co (-12;36). The experimental data are reported as black circles, while the curves represent the total fitting (black), the functions of Mn (red), Fe (green), Co (blue), and Gd (orange).

\* High throughput XRF measurements were performed at SOLEIL Synchrotron, DIFFABS beamline. Data analysis was performed by Dr. Giulio Cordaro at Université Paris-Saclay, CentraleSupélec, CNRS, Laboratoire SPMS.

The resulting B-cation distribution is presented in Figure 4-4, which shows the normalized intensity of Co, Mn and Fe in panels (a-c), respectively. The distribution of these elements are representative of the contribution of LSM, LSF and LSC during the deposition to the final composition obtained at each position. The results obtained correspond to the LSMCF film deposited on the 3-inch YSZ substrate, so the outermost region of the combinatorial film was not analyzed (cf. Figure 4-2). The visualization of the overall distribution of all three cations along the wafer coordinates is reported in panel (d). It is clearly observed that the B-cations are distributed as intended from the deposition conditions and in line with the observations made in Figure 4-1 and Figure 4-2. The Co signal is highest in the top part of the wafer ( $y=40$  mm,  $x=0$  mm). With regard to the Mn and Fe signals, these are located in the bottom part of the wafer, in the right ( $y=-10$  mm,  $x=30$  mm) and left ( $y=-20$  mm,  $x=-30$  mm) regions, respectively, with the Mn maximum signal being slightly displaced upwards with respect to Fe. This is in agreement with the thickness distribution observed in Figure 4-1d. Note that none of the single elements intensity signals reaches value of 1. This is caused by the reduced diameter of the sample measured, which keeps the purest compositions out of the analysis, i.e. certain degree of B-site intermixing is always present. The obtained information on the distribution of Mn, Co and Fe cations allowed the correlation of each sample position with a specific LSMCF composition. Therefore, it has been possible to represent the results of the oxygen mass transport properties of LSMCF discussed in Section 4.3.2.1. as ternary diagrams, hence facilitating the interpretation of the composition-dependent results.

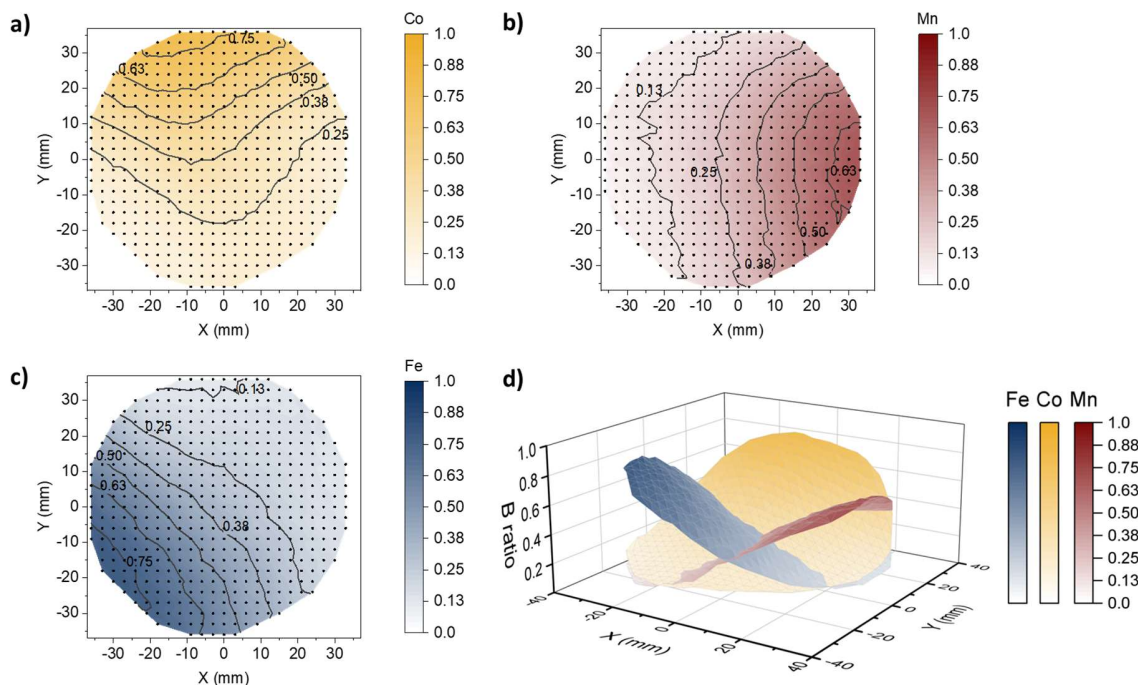


Figure 4-4. Normalized B-ratios obtained by XRF of Co (a), Mn (b) and Fe (c) signals. B-ratio map showing the three contributions altogether (d).

#### 4.3.1.2 Characterization of the crystallographic structure by X-Ray Diffraction<sup>†</sup>

The crystallographic structure of the combinatorial LSMCF thin film on top of a CGO-buffer/YSZ single crystal wafer was characterized by XRD in an automatized lab-scale diffractometer to obtain a representative analysis of the crystallographic structure as in a prototypical cell architecture. Figure 4-5a shows several diffraction patterns obtained in different regions of the LSMCF wafer. In general terms it can be observed that the perovskite film grows following the direction of the (100) and (110) crystallographic planes, except in the case of the Co-rich region, which only shows the (100) orientation. The CGO layer presents the (200) orientation, resulting from strongly oriented growth on top of the YSZ substrate, as both phases present good cube-on-cube crystallographic match. It should be noted that the (220) orientation of the ceria phase is located close to the (200) reflection of the perovskite, so an additional CGO orientation might be present. Nonetheless this is unlikely due to the proper accommodation of the (100) orientation on the YSZ substrate. In parallel, the (110) orientation of the perovskite phase falls close to the (200) orientation of the CGO. Again, this is due to close crystallographic match, in this case with the half diagonal of the CGO cubic structure. This can be visualized in Figure 4-5a either as the presence of two diffraction peaks, or a shoulder peak corresponding to the LSMCF phase being partially shadowed by the more intense CGO peak.

The LSMCF peaks present in the 20-80° 2 $\theta$  angular range are indexed as (100), (110), (200), (220), and (300) reflections of the  $Pm-3m$  cubic cell (space group n° 221). However, the (300) peak ( $\approx 72.5^\circ$  2 $\theta$ ) partially overlaps with the YSZ (400). Therefore, the precise identification of the position results very complex. The presence of the peaks along the (110) direction is localized only in the bottom part of the sample, with the highest intensity in the LSF-rich region (Figure 4-5b). In this area, the identification and fitting of both the (110) and (220) reflections were performed. The (110) peaks are reduced in intensity in the LSM area and completely disappear in the region close to the center of the LSC deposition. The reduced number of LSMCF peaks does not allow the simultaneous calculation of the lattice parameter and the sample displacement. Therefore, the sample displacement is determined using the variation of the CGO(200) and (400) peak positions, fixing the lattice parameter equal to 5.426 Å<sup>19</sup>. The LSMCF lattice parameter was obtained subsequently using the sample displacement correction. The introduction of this correction does not significantly change the distribution of the results, but it was necessary due to the evident sample curvature due to tensile stress applied by the highly oriented depositions on the single crystal substrate.

---

<sup>†</sup> High throughput XRD measurements were performed and analyzed at Université Paris-Saclay, CentraleSupélec, CNRS, Laboratoire SPMS with the collaboration of Dr. Guilhem Dezanneau and Dr. Giulio Cordaro. Data analysis was performed by Dr. Giulio Cordaro.

Figure 4-5b shows the variation of the pseudo-cubic lattice parameter of the perovskite phase, with values in the range of 3.85-3.96 Å. The region with the smallest lattice parameter,  $a = 3.85$  Å, corresponds to the Co-rich region, as expected from the lower ionic radii of Co when compared to the other two cations, and in line with what has been reported in the literature for LSC thin films<sup>20</sup>, and specifically for LSC with 20 % Sr doping<sup>21</sup>. The evolution of the cell parameter in this region is coherent with the shape observed for the XRF Co signal in Figure 4-4. There is a progressive increase of the lattice parameter with the addition of Mn, reaching a relative maximum at  $a = 3.93$  Å, as expected for LSM<sup>22,23</sup>. Finally, the largest lattice parameter present in the LSMCF film corresponds to the Fe-rich region, reaching a value of  $a \approx 3.96$  Å, in agreement with values found in other LSF thin film studies<sup>24,25</sup>. Interestingly, the lattice parameter slightly decrease between the Mn-rich and Fe-rich regions. This can be attributed to the partial incorporation of Co. As depicted in Figure 4-4a, even for the bottom part of the sample an amount down to approximately 20 % of Co can be expected, therefore the lowering in the lattice parameter.

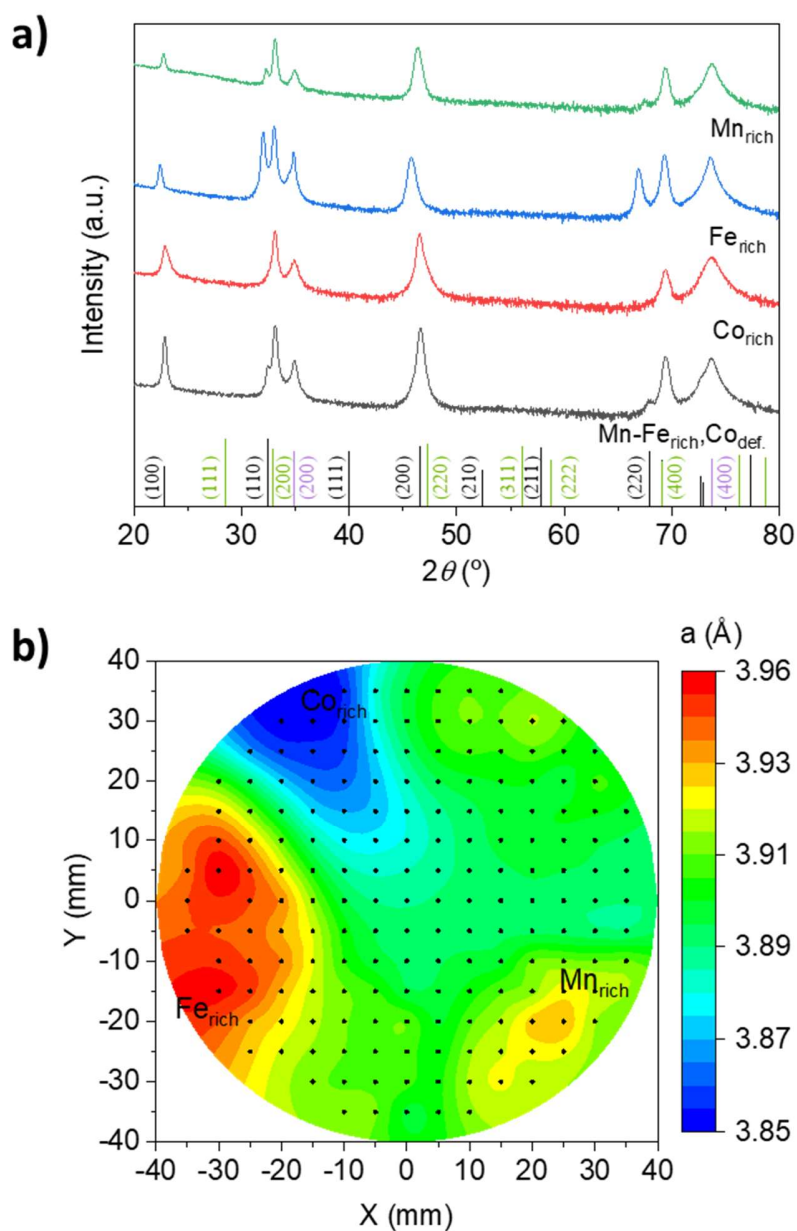


Figure 4-5. Characterization of the crystallographic structure measured by XRD for the LSMCF combinatorial film deposited on a CGO/YSZ wafer. Examples of diffraction patterns obtained at different coordinates (a). Reference diffraction patterns are represented on the bottom for the structure of a cubic perovskite ( $Pm-3m$  #221, in black)<sup>26</sup>, SDC ( $Fm-3m$  #225, in green)<sup>27</sup> and YSZ ( $Fm-3m$  #225, in purple)<sup>28</sup>. Map of the pseudo-cubic lattice parameter obtained from the XRD analysis (b).

#### 4.3.1.3 Structural characterization by Raman Spectroscopy

The combinatorial LSMCF thin film was analyzed by means of Raman Spectroscopy, with the goal to gain additional insight on the structural properties caused by the distribution of the different B-cations along the LSMCF film, complementary to the XRF and XRD

measurements discussed. The characterization was performed in a LSMCF thin film deposited directly on a silicon substrate, in contrast to the XRF and XRD measurements performed on CGO/YSZ substrates. This was chosen in order to avoid additional Raman peaks coming from the substrate that might hinder the identification of the LSMCF active peaks. Figure 4-6a shows the Raman spectra obtained for reference LSF, LSC and LSM parent materials, while in Figure 4-6b representative Raman spectra measured on each cation richest region are plotted. Without taking into account the silicon substrate contribution to the Raman signal (indicated with a star in the plot), it can be clearly observed that the main contribution present in the spectra is located in the 600-700  $\text{cm}^{-1}$  range. This region of interest can be further appreciated in the zoomed inset of both panels. The feature of the peak (or peaks) varies considerably depending on the composition of the B-site. Starting with the reference films, in the case of the LSM spectrum the peak is centered approximately at 620  $\text{cm}^{-1}$ . LSF presents the same contribution, in addition to the appearance of a shoulder shifted towards higher wavenumbers, around 660  $\text{cm}^{-1}$ . Interestingly, LSC shows one main peak at 660  $\text{cm}^{-1}$ . With regard to the LSMCF film, the spectra represented in Figure 4-6b for the Fe-, Mn- and Co-rich regions resemble the reference materials within the combinatorial film. The Mn-rich portion shows similar shape than for LSM, with a peak at 630  $\text{cm}^{-1}$ , slightly stiffer than for the single phase. This can be attributed to the small presence of Fe and Co cations, which are expected to deviate the vibrational modes towards higher Raman shifts, in line with the observations made for LSF and LSC. Consequently, by increasing the Fe content in the LSMCF film the peak shifts towards a central position located at 650  $\text{cm}^{-1}$ . Additionally, moving to the Co-rich region results in a further increase of the Raman shift peak position centered at  $\approx 665 \text{ cm}^{-1}$ , while showing a small shoulder located at  $\approx 620 \text{ cm}^{-1}$ .

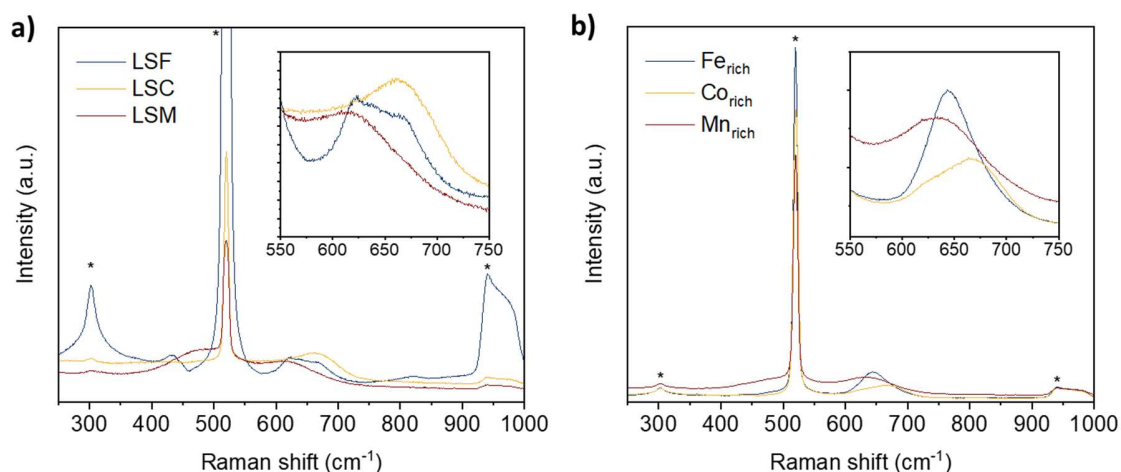


Figure 4-6. Raman Spectroscopy characterization of combinatorial LSMCF thin films. Raman spectra obtained for three parent material reference samples (a), as well as for Co, Fe and Mn-rich regions in the LSMCF film (a). Peaks corresponding to the silicon substrate are marked with an star (\*).



Figure 4-7 shows the evolution of the different Raman features selected to interpret the spectra obtained along the LSMCF film. Figure 4-7a depicts the evolution of the Raman shift value at the maximum intensity of the signal measured in the 550-700  $\text{cm}^{-1}$  range, i.e. the region of interest. Interestingly, the shape of the map recalls the one obtained for the evolution of the lattice parameter in Figure 4-5b. Both present clear differentiated areas for the Co-rich and Fe-rich regions, and a rather large region on the right side with data values close to the characteristic of the Mn-rich zone. Although presenting a similar shape, the evolution of both features (i.e. the lattice parameter and the Raman shift) do not present the same evolution progression on the B-cation. While the lattice parameter increases its value when moving from the Co-rich to the Fe-rich regions (with intermediate values found in the Mn-rich case), the Raman shift finds its maximum in the Co-rich area and its minimum in the Mn-rich region. Hence, the evolution of the structural properties observed by Raman cannot be directly correlated to the evolution in the lattice parameter, i.e. the evolution of the Raman peak in this region is not due to a simple mass effect (cf. later discussion). In parallel, Figure 4-7b shows the result of treating the Raman signal as the convolution of three peaks centered at 664, 649 and 620  $\text{cm}^{-1}$ , respectively. Each map shows the normalized intensity for each of the peaks defined, resembling the importance of each contribution along the film. This analysis is complementary to the map shown in Figure 4-7a, as it allows to also appreciate the presence of minor vibrational modes in regions presenting more than one contribution. For instance, the presence of the 620  $\text{cm}^{-1}$  mode can be observed along the major part of the film, including the part dominated by the 665  $\text{cm}^{-1}$  Raman shift (Co-rich region), as in the spectra presented in Figure 4-6b.

In the work by Minh et al.<sup>29</sup> they attribute the changes in the vibrational mode of LSM with the addition of Fe or Co (among other substituent cations). In particular, they observe changes in peak shift for the vibrational mode located at frequencies above 630  $\text{cm}^{-1}$ , corresponding to the  $A_g$  high frequency mode. They do not attribute these changes to the differences in the mass of the B cation, but rather to the ionic radius. The  $A_g$  mode is characteristic of the vibration through the metal-oxygen bond broken asymmetry<sup>30</sup>, ie. Mn-O-M. In this case, different radius of the substituent metals lead to stiffer or weaker chemical bonds, which translates to the shift in the frequency observed.

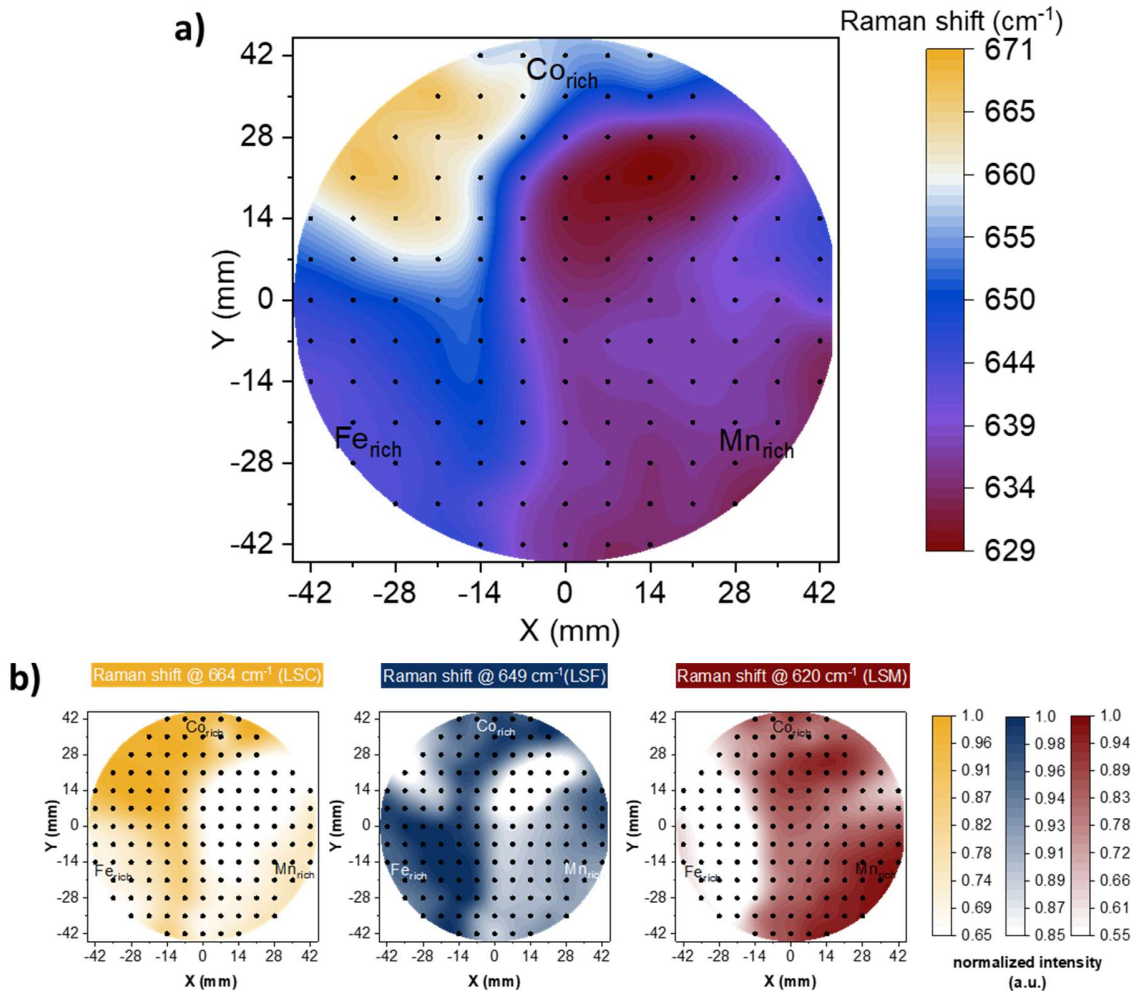


Figure 4-7. Mapping of the Raman shift position at the peak maxima in the 550-700  $\text{cm}^{-1}$  range (a). Mapping of the relative intensity of each characteristic peak resulting from fitting the region of interest with three different peaks centered at 664, 649 and 620  $\text{cm}^{-1}$ , respectively (b).

#### 4.3.1.4 Analysis of the optical properties by spectroscopic ellipsometry

The optical properties of the combinatorial LSMCF thin film were obtained by means of spectroscopic ellipsometry, following the process described in Chapter 2. Figure 4-8a shows a collection of several spectra obtained for different regions of the wafer, namely Co-, Fe- and Mn-rich region, as well as a measurement from a fully intermixed central position. With regard to the Co-rich region, this is characterized by presenting the highest optical absorption activity in the low energy regime (approximately below 3 eV), while Mn- and Fe-rich perovskites present higher larger absorption beyond this point. In the case of the Mn-rich region, despite the relative low absorption in the 2-3 eV range, it appears to get close to a relative peak maximum close to 1.5 eV energies. This is in agreement with observations made in studies related to the optical properties of LSM and their evolution with Sr-doping<sup>31</sup>. The Fe-rich spectra also shows a partial increase of the optical absorption

coefficient around 1.5 eV (although less evident than for the Mn-rich region), also related to Sr-doping, and an additional optical feature at  $\approx 3$  eV, related to the electronic transition O 2p-Fe  $e_g$ <sup>24,25</sup>.

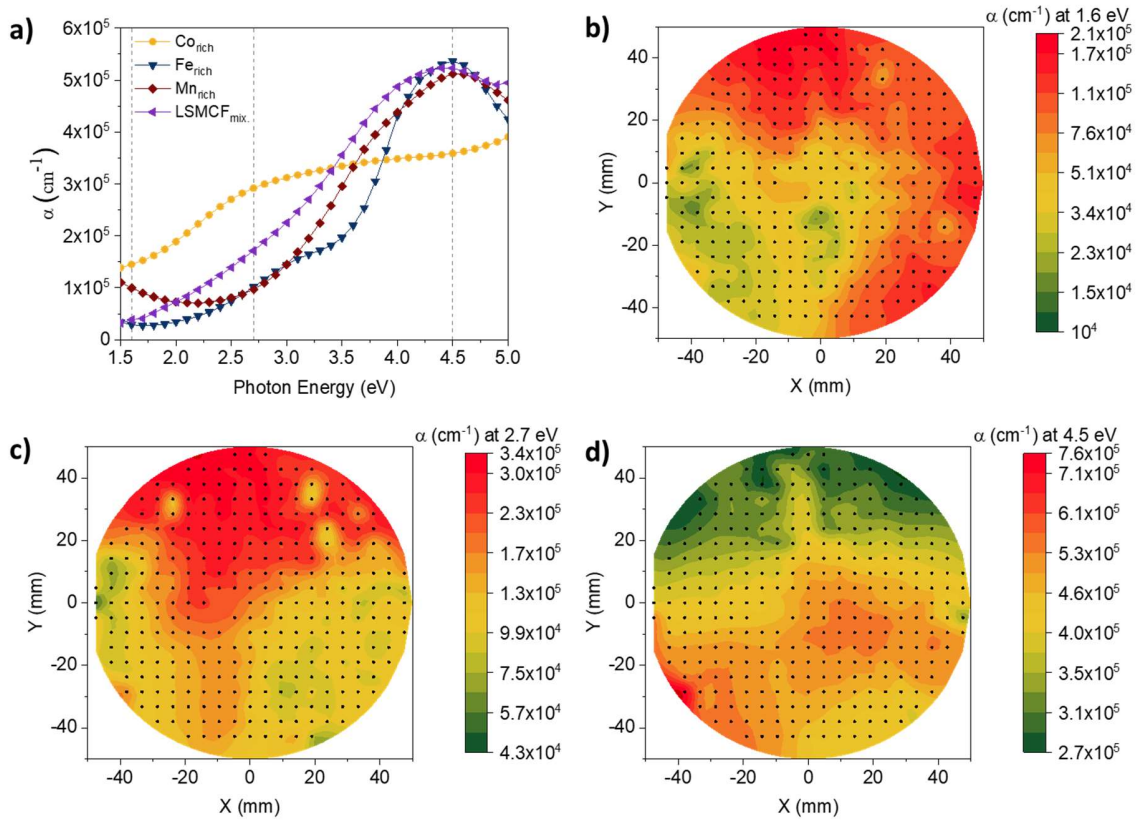


Figure 4-8. Characterization of the optical properties of the LSMCF combinatorial thin film. Optical absorption coefficient spectra obtained in different regions of the film: Co, Fe and Mn-rich regions, and an example of a fully intermixed position in the center of the wafer (a). XY maps of the optical absorption coefficient at 1.6, 2.7 and 4.5 eV, respectively (b-d). Vertical dashed lines at these energies are placed in the spectra in (a) to facilitate the comparison with the maps.

Figure 4-8b-c show the map of the optical absorption coefficient calculated at 1.6, 2.7 and 4.5 eV for the whole LSMCF film, respectively. The trends observed are coherent with the observations made in Figure 4-8a. For Figure 4-8b, it can be seen that the regions showing the highest absorption are the Co- and Mn-rich areas of the film. In the case of Figure 4-8c, the Co-rich area is dominant in absorption and the Mn- and Fe-rich counterparts show similar values. Finally, in Figure 4-8d, the Mn- and Fe- rich regions are the most absorbing, with the Co-rich area being the lowest, as expected.

## 4.3.2 Functional characterization

### 4.3.2.1 Analysis of the mass transport properties by Isotopic Exchange Depth Profiling-Secondary Ion Mass Spectrometry<sup>†</sup>

The oxygen mass transport properties were measured IEDP-SIMS. The sample analyzed consisted in a LSMCF combinatorial film deposited on a Si (100) wafer substrate. The conditions of the isotopic exchange set were 400 °C for a period of 30 min (see further experimental details in Chapter 2). Figure 4-9 shows a set of examples of the  $^{18}\text{O}$  fraction ( $f(^{18}\text{O})$ ) profiles obtained for different LSMCF compounds. One can clearly differentiate two oxygen regimes. For regions with high content in manganese, the profile presents an exponential-like decay in the  $^{18}\text{O}$  fraction in the  $z$ -direction. This behavior is characteristic of poor mixed ionic electronic conductors. In the particular case of perovskite systems, it is often observed in chromite<sup>32,33</sup> and manganite<sup>34,35</sup> materials. On the other hand, in the case of Fe- and Co-rich regions the profile presents a flat shape, as a result of the fast exchange occurring in these materials. This behavior is characteristic of transport mechanisms dominated by the surface exchange and with no limitation on the oxygen diffusion through the film. The isotopic fraction shows the same value throughout the film, until reaching the interface with the substrate. In this mechanism, only the differences in the oxygen exchange happening in the surface can be analyzed (i.e. the surface exchange coefficient) and this will be determined by the value of the isotopic oxygen fraction at the end of the annealing. Due to the nature of the LSMCF thin films –i.e. progressive evolution of the B-cation–, intermediate cases between these two mass transport models are to be expected in punctual cases. For these examples, the profiles were treated as in the second model, as they cannot be considered to be representative of a regular exponential decay-like profile. In this cases, the value of  $f(^{18}\text{O})$  was averaged through the film thickness in order to obtain a calculation on the surface exchange coefficient ( $k^*$ ). This approximation allowed to progressively study the oxygen exchange properties of the LSMCF system, and although it should not be considered as an exact calculation, it offers a reasonable estimation on the coefficient values in this boundary region. The exchanged profiles presenting the decay in the  $^{18}\text{O}$  fraction were fitted by using Crank's solution<sup>36</sup> to Fick's second law of diffusion in the case of semi-infinite mediums (please refer to Chapter 2 for further explanation on the modelling process). This analysis allowed to extract the oxygen surface exchange coefficient and oxygen diffusivity ( $D^*$ ) parameters for this set of LSMCF compounds. In parallel,  $k^*$  values for the region of the LSMCF thin film showing planar profiles were directly calculated by solving the differential equation assuming oxygen transport at constant flux (see equation (2-21) in Chapter 2).

---

<sup>†</sup> High throughput IEDP-SIMS was performed at Imperial College London, Department of Materials, Surface Analysis Facility, with the collaboration of Dr. Sarah Fearn and Dr. Andrea Cavallaro.

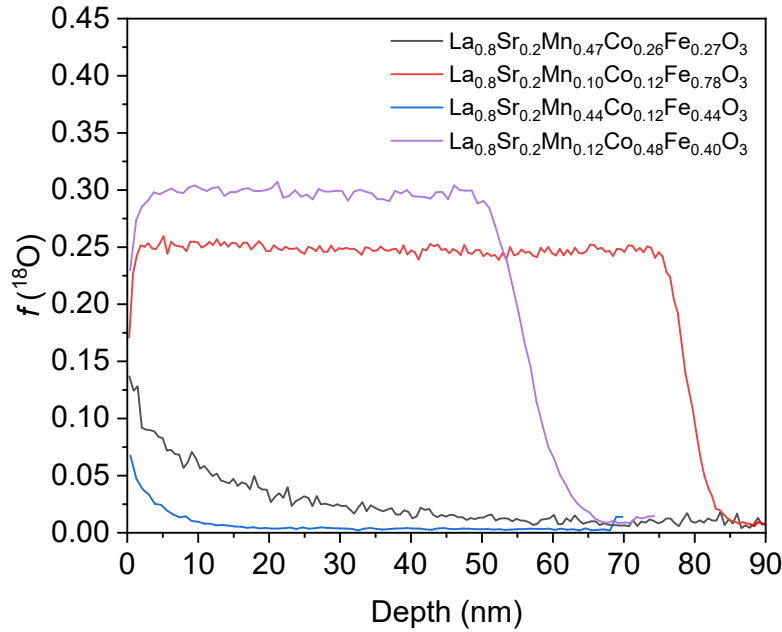


Figure 4-9.  $^{18}\text{O}$  fraction depth profiles obtained by IEDP-SIMS for local positions of the LSMCF thin film.

The results of the analysis carried out on the isotopic exchange profiles obtained along the whole LSMCF thin film are reported in Figure 4-10. In particular, the calculated oxygen diffusivity coefficient is shown in Figure 4-10a. The figure shows the evolution of  $k^*$  along the ternary LSMCF system, differentiating between both the  $k^*$  values calculated through Crank's solution (solid symbols) and  $k^*$  directly calculated assuming an only surface exchange-limited model (i.e. incorporation of  $^{18}\text{O}$  at constant flux in the surface), represented with open symbols. The analyzed  $k^*$  varies from values in the order of  $10^{-12}$  cm/s for the Mn-rich compounds to  $2 \times 10^{-9}$  cm/s for both the Co- and Fe-rich regions. Similarly, in Figure 4-10b the  $D^*$  values calculated applying the semi-infinite medium solution are represented with solid symbols, while for the rest of the compounds, the  $D^*_{\text{min}}$  coefficient was calculated (open symbol).  $D^*_{\text{min}}$  corresponds to the diffusivity value beyond which the relation  $D^*/k^* \gg L$  can start to be satisfied (i.e. the condition for oxygen transport limited by surface incorporation, exclusively) and has been calculated by taking  $D^*_{\text{min}}/k^* = L$ .  $D^*/k^*$  corresponds to the critical length (i.e. the length determining the relative importance of ionic diffusion relative to surface exchange<sup>37,38</sup>) while  $L$  is the thin film thickness. The oxygen diffusivity calculated for the LSMCF library presents values in the range of  $10^{-17}$  to  $10^{-14}$  cm<sup>2</sup>/s, although the real values for the  $k$ -limited model are expected to be considerably larger (cf. later discussion in the text).

Figure 4-10c shows the relation between the logarithm values of both  $k^*$  and  $D^*$ , calculated for the regions modeled with the semi-infinite medium solution. The plot presents a clear linear relation between the two parameters. This correlation is well-known in the community<sup>39-41</sup> and has been extensively investigated for a wide range of mixed ionic

electronic conductor materials, including LSMC<sup>5</sup>. In this work, it is clear that the linearity is kept for a large variety of compositions (165 points corresponding to analyzed profiles are represented, with each point presenting an RGB color representative of the relative Mn,Co, Fe composition, as shown in the figure). Assuming that linearity is kept for the rest of the compositions for which the  $D^*$  could not be experimentally obtained, one could consider extrapolating the real values of  $D^*$  for this region from the obtained values of  $k^*$ . Considering that  $k^*$  in the Co,Fe rich region oscillates in the  $10^{-10}$ - $10^{-9}$  cm/s range, approximate values between  $5 \times 10^{-15}$ - $10^{-13}$  cm<sup>2</sup>/s would be expected.

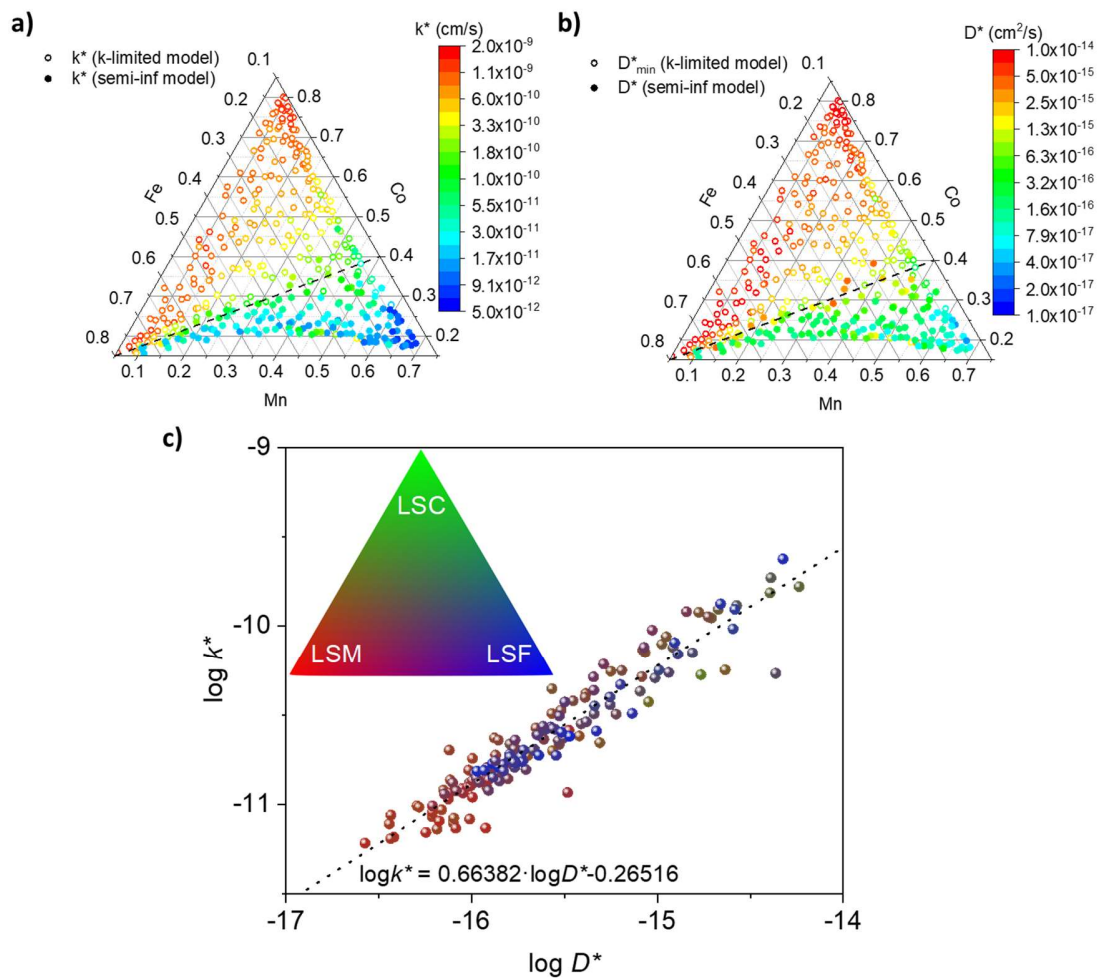


Figure 4-10. Oxygen mass transport parameter mappings obtained by IEDP-SIMS. Oxygen surface exchange coefficient  $k^*$  (a) and oxygen diffusivity coefficient  $D^*$  (b) obtained by the models indicated. The dashed line indicates the approximate boundary between the two models. Plot of the relationship between the logarithm of the experimental values of the oxygen surface exchange coefficient and the oxygen diffusivity (semi-infinite model) obtained for the LSMCF system (c).

Then, taking the linear expression obtained from the fitting in Figure 4-10c, a value of the oxygen diffusivity can then be estimated ( $D^*_{\text{calc}}$ ) for the k-limited region. The resulting  $D^*$  map is presented in Figure 4-11a. It can be seen that as previously estimated, the diffusivity

in this region is larger than the initially estimated by  $D^*_{\min}$ , reaching values up to  $10^{-13}$  cm<sup>2</sup>/s. The LSMCF library then is fully characterized to present  $D^*$  values in the range of  $10^{-13}$ - $10^{-17}$  cm<sup>2</sup>/s for the whole system. Additionally, Figure 4-11b shows the ternary diagram of the  $k^*/D^*$  ratio calculated for the whole system with the  $k^*$  and  $D^*$  values obtained from the analysis. The  $k^*/D^*$  ratio is directly related to the broadening of the active zone in MIECs<sup>42,43</sup>. Being the inverse of the critical length, this broadening is interpreted as the extension of the area that is active to the oxygen reduction reaction (ORR). In this sense, a decrease in the ratio translates into larger activation of the electrode area, i.e. the ionic transport through the electrode towards the electrolyte becomes less limiting. Interestingly, for the points calculated with the semi-infinite model, a progressive decrease in the  $k^*/D^*$  ratio can be observed when moving from the Mn-rich region, towards higher contents of Fe and Co. This trend is progressively respected when introducing the values calculated with the k-limiting model (then, using the  $D^*_{\text{calc}}$  value), reaching values down to  $10^4$  cm<sup>-1</sup>. Similarly, Figure 4-11c shows the map obtained for the  $k^* \cdot D^*$  product. The value of this product provides a clear metric of the behavior of a material as an oxygen electrode in SOCs<sup>38,43</sup>. The  $k^* \cdot D^*$  product varies from a lower limit of  $10^{-28}$  cm<sup>3</sup>/s<sup>2</sup> for the Mn rich region and progressively increases to a maximum limit of  $4 \times 10^{-22}$  cm<sup>3</sup>/s<sup>2</sup> for higher amount of Co and Fe. Comparing the observed  $k^*/D^*$  ratio and  $k^* \cdot D^*$  product with bulk LSC and LSM-based materials in the same temperature<sup>43,44</sup>, one can observe that LSM presents  $k^*/D^*$  ratios in the order of  $\approx 10^{10}$  cm<sup>-1</sup> and  $k^* \cdot D^*$  values of  $\approx 10^{-33}$  cm<sup>3</sup>·s<sup>-2</sup>, while the Mn-rich region reported in this work presents values of  $10^5$  cm<sup>-1</sup> and  $10^{-28}$ , respectively, an indication of enhanced performance. Comparing with LSC, values in the range of  $\approx 10^5$ - $10^6$  cm<sup>-1</sup> and  $\approx 10^{-25}$  cm<sup>3</sup>/s<sup>2</sup> for the  $k^*/D^*$  ratio and  $k^* \cdot D^*$  product respectively have been reported for the same nominal composition (i.e. 20 % Sr doping)<sup>43</sup>. This is within the range of values observed in this work, supporting the approximation made by considering  $D^*_{\text{calc}}$  diffusivity value.

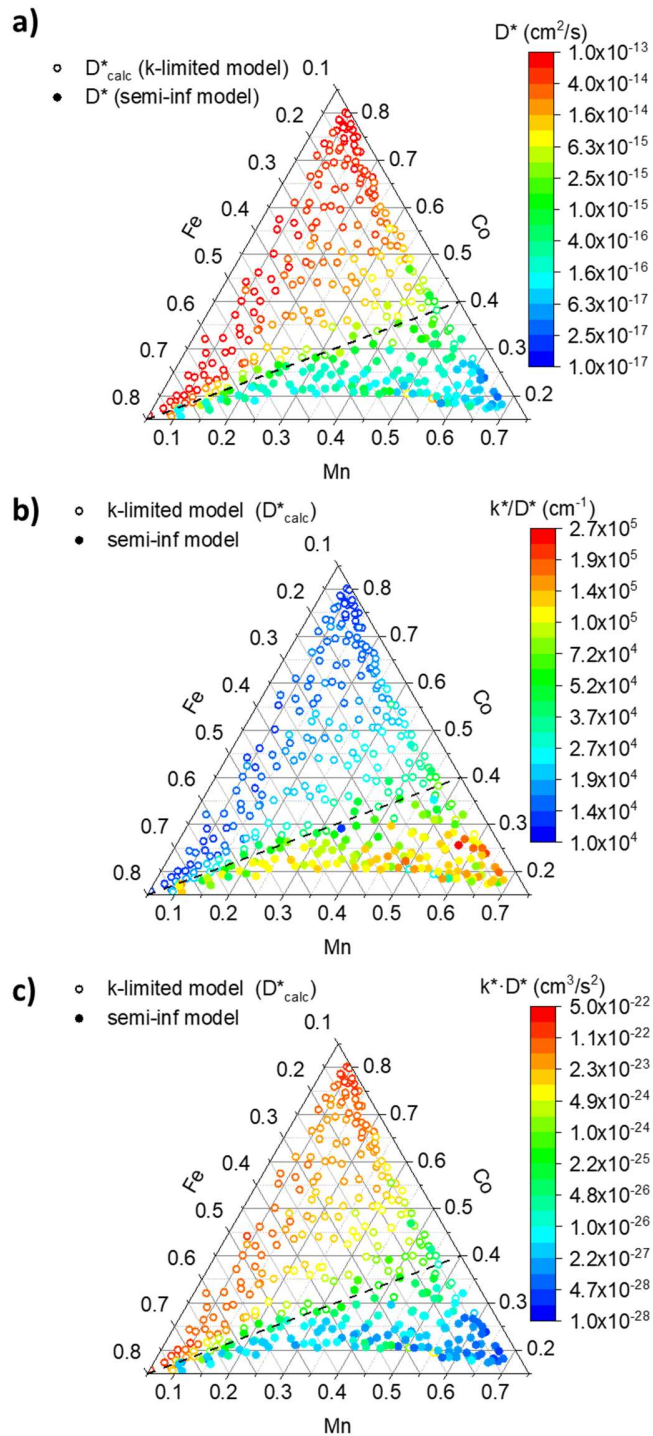


Figure 4-11. Oxygen diffusivity coefficient mapping with the addition of the  $D^*_{\text{calc}}$  coefficient calculated (a),  $k^*/D^*$  ratio (b) and  $k^* \cdot D^*$  product (c) maps calculated from the analysis performed. The dashed lines indicate the approximate boundary between the two models.

The fact that, in general terms, the observed activity is higher than conventional bulk counterparts, suggests the presence of enhancing contributions to the oxygen mass



transport activity. Although this work has focused on the analysis of the whole library studied by assuming one averaged path for the oxygen transport, specific features such as transport through grain boundaries might have an important role on the improved performance of the system. In fact, fast(er) diffusion through grain boundaries and the increase of active catalytic sites through grain boundary engineering are phenomena that are being reported in recent years. Examples of these phenomena in relation to the LSMCF perovskite library can be found in the independent works reported by Saranya<sup>45</sup>, Chiabrera<sup>18</sup> and Navickas<sup>22</sup> et al., for the case of LSM thin films. Saranya et al.<sup>5</sup> also reported grain-boundary fast ionic transport in co-doped LSMC thin films. Most interestingly, Thoreton et al.<sup>46</sup> recently published a work in which they observe an additional grain boundary contribution in oxygen diffusion profiles for LSCF. Hence, the presence of an additional transport path through grain boundary engineering is likely to be present in the LSMCF electrodes studied in this chapter.

#### 4.3.2.2 Electrochemical characterization by impedance spectroscopy mapping

The electrochemical activity of the LSMCF ternary system has been analyzed by means of EIS mapping. The LSMCF thin film has been measured in a high-temperature chamber with a hot stage in an asymmetric configuration –i.e. employing a half-cell like configuration in which the counter electrode is a low impedance silver porous electrode–. Figure 4-12a shows the Nyquist plot of four representative compositions of the system measured (i.e. four points out of the total amount of points measured), at a set temperature of 725 °C. The relative composition was measured by EDX. It should be taken into account that certain degree of temperature inhomogeneity is to be expected along the Si wafer. Calculations of the real temperature at each point measured have been carried out according to the procedure described in Chapter 2, so this issue does not have an impact in the discussion given for the rest of the section. All of the impedance spectra were fitted with the generalized modified Jamnik-Maier equivalent circuit (the equivalent circuit can be found in Chapter 2, Figure 2-16b), in order to obtain a proper fit of the area specific resistance (ASR), irrespective of the different contributions present for each composition. It can be observed that the polarization resistance is larger with the higher amount of Mn, and lower for the Co,Fe-rich regions. This is expected as Mn-rich perovskites are known to present poor ionic conductivity and sluggish oxygen exchange at the surface, even in thin film form<sup>47</sup>. Nonetheless, the ASR value observed in this case is not as high as in the case of single LSM<sup>16,47</sup>, probably due to the presence Co and Fe, even at relatively low amounts (Co+Fe = 0.3). Regarding the rest of the compounds studied, the region with the highest content of Co presents the lowest ASR, although does not substantially change than in the case of the Fe-rich compound. The overall variation in ASR observed for these compounds was in the range of 6–21  $\Omega\cdot\text{cm}^2$ . The combinatorial film was then measured at different temperatures so the Arrhenius electrochemical activity was analyzed. The ASR evolution with temperature of the same

exemplary compositions along with the activation energy calculated is reported in Figure 4-12b. Reference values obtained for single LSM, LSC and LSF parent materials measured in a ProboStat setup in the frame of the present thesis are also included in the plot. This is done in order to offer a coherent discussion on the performance of the combinatorial LSMCF thin film materials characterized in this work in comparison to well-known materials characterized in an already established experimental setup. The overall ASR observed in the intermixed LSMCF is considerably lower than in the case of single LSM and also than LSF, with a reduced difference. Variation on the values of activation energies extracted for the materials studied could also be observed, with a general decrease when shifting from Mn-rich to Co,Fe-rich compounds.

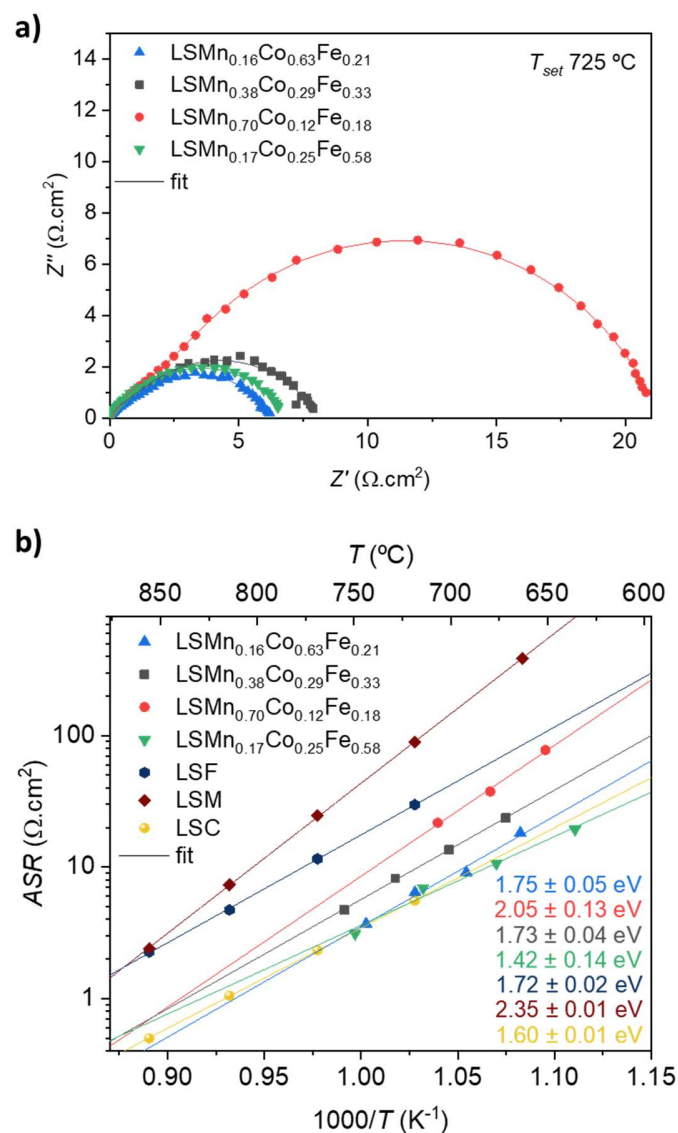


Figure 4-12. Electrochemical characterization of exemplary compounds of the combinatorial LSMCF thin film: Nyquist plots measured at a set temperature of 750 °C (a) and Arrhenius-like

plot showing ASR evolution with temperature with inclusion of reference values of LSM, LSC and LSF parent materials (b).

The collection of the total amount of compounds analyzed by EIS mapping is summarized in Figure 4-13. Values of the calculated activation energies ( $E_a$ ) and pre-exponential factors ( $ASR_0$ ) are represented in Figure 4-13a-b, respectively. Additionally, the error of the  $E_a$  calculated is plotted in Figure 4-13c, in order to facilitate the interpretation of the features extracted from the analysis and the reliability of the measurements carried out.

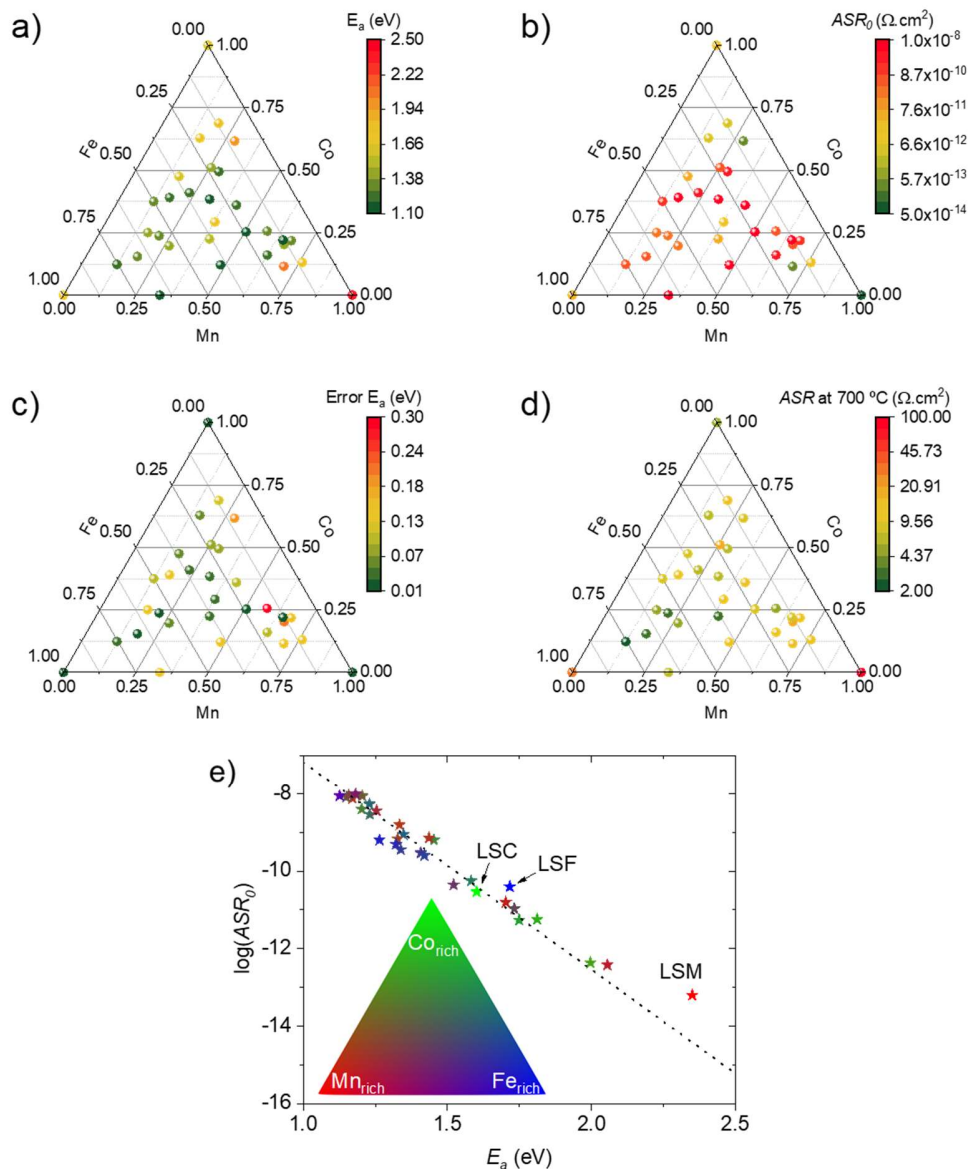


Figure 4-13. Electrochemical characterization resulting of EIS mapping:  $E_a$  (a), pre-exponential factor  $ASR_0$  (b), Absolute error in the  $E_a$  fit (c) and ASR calculated at 700 °C (d). Plot of the logarithm of the pre-exponential factor vs the activation energy measured. The distribution in color depicts the relative composition of Mn, Co and Fe following the RGB triangle depicted (e).

With the  $E_a$  and  $ASR_0$  values extracted, an equivalent ASR was calculated at a temperature of 700 °C (see Figure 4-13d). Unlike for direct measurements, the extraction of the ASR from  $E_a$  and  $ASR_0$  allows removing uncertainties coming from temperature inhomogeneity. Reference values from single phase LSM, LSC and LSF have been included in the analysis for comparison, as indicated above. Interestingly, low  $E_a$  has been extracted for most of the intermixed LSMCF compounds. Specifically, except some points closer to the Mn and Co-rich regions which present  $E_a$  values in a 1.6 – 2.0 eV, many of the points representative of higher intermixed compositions show lower  $E_a$ , approximately in the 1.1–1.50 eV range. These are considerably lower than the values reported for the parent materials (i.e. 1.60 eV, 1.72 eV and 2.35 eV for LSC, LSF and LSM, respectively, see Figure 4-12b and Figure 4-13a). Additionally, most of the  $E_a$  error values are confined in values below 0.15 eV, with few points presenting larger values of 0.2 – 0.3 eV, an indicative of the robustness of the method. With regard to the pre-exponential factor calculated from the ASR Arrhenius analysis, it follows a similar trend than the  $E_a$ , although complementary –i.e. the  $E_a$  decreasing trend is translated into an  $ASR_0$  increasing trend (cf. discussion later in the text) –. Hence, most of the intermixed compounds present high values of  $ASR_0$  in the order of  $10^{-11}$ – $10^{-8}$   $\Omega\cdot\text{cm}^2$ , while lower values of  $10^{-14}$ – $0^{-12}$   $\Omega\cdot\text{cm}^2$  can be found closer to the Mn- and Co- rich edges. The equivalent ASR calculated for 700 °C shown in Figure 4-13d offers a straightforward comparison on the relative performance of materials compiled in this study. The lowest ASR values down to  $\approx 2$   $\Omega\cdot\text{cm}^2$  are concentrated in the Fe-rich region, with relative B-cation compositions in the following ranges: 12–27 % of Mn, 12–25 % of Co and 50–75 % of Fe. Increasing the content in Co and Mn progressively results in larger values of ASR, with the higher values observed in the Mn-rich compounds.

Figure 4-13e shows the plot of the logarithmic value of the pre-exponential factor of the Arrhenius analysis represented as a function of the activation energy, for the LSMCF electrode materials measured. Each point has been coloured according to the RGB system to show the relative B-cation composition, as seen in the inset of the plot. It can be clearly observed that these two factors follow a linear correlation that covers all the points of the LSMCF perovskite family, including the parent materials. Interestingly, the relation between the two electrochemical parameters results in a compensation effect: as the activation energy value decreases, the pre-exponential factor increases, as previously observed in Figure 4-13a-b. Additionally, the high degree of linearity obtained for these measurements validates the methodology employed in this work. While low  $E_a$  values are generally advantageous for the performance of SOFCs (i.e. the lower the  $E_a$ , the more one can decrease the operational temperature while keeping high electrochemical activity), low values of  $ASR_0$  are also desirable as it also promotes lowering of the ASR. Hence, such behaviour seems to hinder further optimization of the system. As being related to Arrhenius-like thermally activated electrochemistry, the linear relation between  $ASR_0$  and  $E_a$  has been discussed previously in the literature, where is generally referred as the Meyer-Neldel rule<sup>48</sup> or compensation law. Particularly in the field of SOFCs, in the work published

by Berenov et al.<sup>49</sup> they authors report the appearance of these relations for oxygen diffusion in different perovskite systems. It is of particular interest that, contrary to the observations made in the work described in this chapter, the systems reported in Ref.<sup>49</sup> deal with several systems (e.g. ferrites, cobaltites, chromites, manganites and titanates) in which the A-site doping is varied. The result is the characterization of several linear relations, each one for the particular B-cation studied in each case. On the contrary, the findings covered in this section present a common linear relation in a system with fixed A-site and irrespectively of the three B-cations studied. It should be noted though that the relation discussed in Ref.<sup>49</sup> deals with the  $E_a$  of oxygen diffusion, while in here the  $E_a$  of the total polarization resistance is considered. Additionally, they report a linear trend between the different B-cations through the common value of diffusion coefficient at iso-kinetic temperatures ( $D_{00}$ ) and the Meyer-Neldel energy ( $E_{MNE}$ ), so deeper mechanistic relations between the different systems might be present.

## 4.4 Study of the evolution of LSMCF thin films facing thermal degradation

### 4.4.1 Electrochemical performance during thermal degradation

The findings obtained in the previous sections unveiled the promising properties of LSMCF B-site co-doped cathodes for limiting Sr segregation related phenomena driven by thermal degradation. In order to relate these effects with the evolution of the electrochemical properties, degradation experiments were performed while keeping track of the ASR for a period of approximate 100 h at 700 °C. The test was carried out for the parent materials LSC and LSF, and for two intermixed LSMCF with composition  $\text{La}_{0.8}\text{Sr}_{0.2}\text{Mn}_{0.42}\text{Co}_{0.31}\text{Fe}_{0.27}\text{O}_3$  and  $\text{La}_{0.8}\text{Sr}_{0.2}\text{Mn}_{0.1}\text{Co}_{0.17}\text{Fe}_{0.73}\text{O}_3$ , as shown in Figure 4-14. The two LSMCF compounds were selected in order to investigate the performance on degradation of different co-doped systems. In particular,  $\text{La}_{0.8}\text{Sr}_{0.2}\text{Mn}_{0.42}\text{Co}_{0.31}\text{Fe}_{0.27}\text{O}_3$  was selected in the basis of studying a highly disordered compound (i.e. closer to B-site equimolarity), whereas  $\text{La}_{0.8}\text{Sr}_{0.2}\text{Mn}_{0.1}\text{Co}_{0.17}\text{Fe}_{0.73}\text{O}_3$  was chosen based on the high activity observed in the mass-transport properties characterized by IEDP-SIMS for the Fe-rich region (see Figure 4-10). For information on LSM degradation the data values reported in Ref.<sup>50</sup> were taken into account. Given that the electrochemical performance of thin films is generally found to be affected by microstructural features and differences in the nominal stoichiometry<sup>16,18</sup>, the comparison with LSM degradation is focused exclusively on the performance on degradation –i.e. the evolution of ASR over time with respect to the initial performance–. For this, the  $\text{ASR}(t)/\text{ASR}_{t=0}$  ratio ( $\text{ASR}_{t=0}$  being the initial ASR value at  $t = 0$  h) was plotted, as reported in Figure 4-14. The dashed line indicates the reference value in which the  $\text{ASR}/\text{ASR}_{t=0}$  has a value of 1, i.e. all the values above the reference are an indicative of performance degradation. LSC –one of the best performing materials in terms of ASR (as discussed in Section 4.3.2.2)– shows progressive worsening over time. Particularly, it can be clearly seen that LSC presents the fastest degradation rate among the materials analyzed, keeping a

linear trend on ASR evolution, resulting in an increase of one order of magnitude by the end of the measurement. A similar case is visualized for LSF, which shows clear performance degradation over time. Nonetheless, unlike the degradation behavior observed for LSC, the ASR/ASR<sub>0</sub> ratio for LSF reaches a stabilized plateau after the first 20 h of measurement, resulting in an approximately 2.5-fold worsening factor on the ASR. The overall degradation is lower for LSM than for the LSF or LSC counterparts, with a final ASR ≈ 1.6 times larger than at the start of the test. Note in addition that LSM presents much larger initial resistance values. With regard to the La<sub>0.8</sub>Sr<sub>0.2</sub>Mn<sub>0.1</sub>Co<sub>0.17</sub>Fe<sub>0.73</sub>O<sub>3</sub> sample, it shows smaller degradation rate with respect to the parent materials analyzed, even showing ASR/ASR<sub>0</sub> values below 1 in the initial stages of the measurement, indicating enhanced electrochemical activity. The final ASR/ASR<sub>0</sub> ratio measured was ≈ 1.2. Most interestingly, in the case of La<sub>0.8</sub>Sr<sub>0.2</sub>Mn<sub>0.42</sub>Co<sub>0.31</sub>Fe<sub>0.27</sub>O<sub>3</sub> the ASR/ASR<sub>0</sub> ratio is maintained below 1 for the whole time of the analysis, with a final value of ≈ 0.95, reflecting a 5 % of performance enhancement.

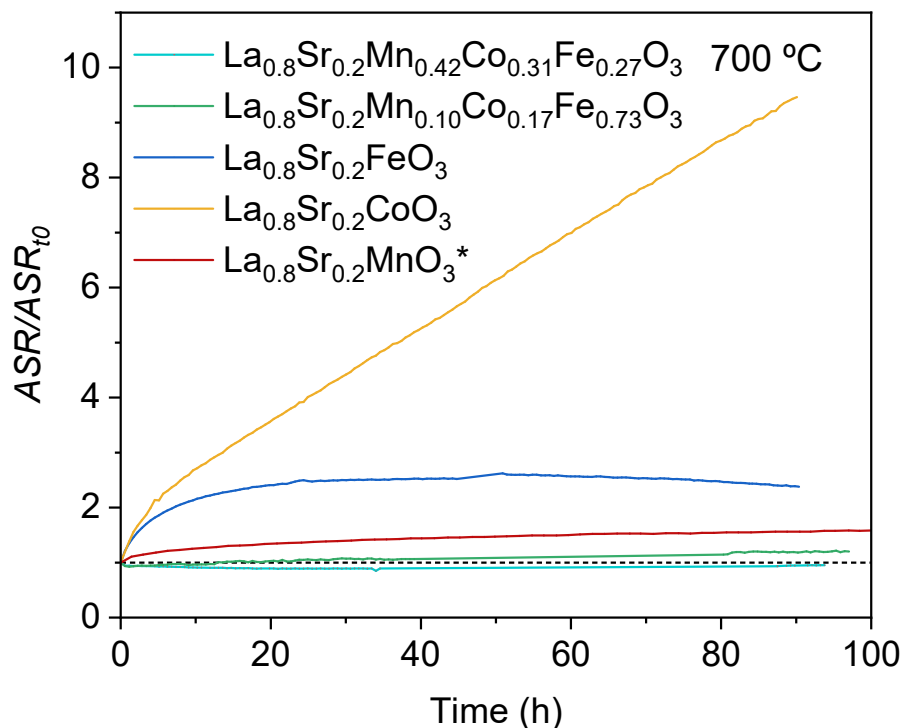


Figure 4-14. Degradation experiments measuring the evolution of the electrochemical performance evolution with time on thermal annealing for 100 h. \*Values on the degradation of LSM have been adapted from Baiutti et al.<sup>50</sup>

#### 4.4.2 Structural and chemical evolution of the thin film surface and subsurface

Given the observation made in the previous subsection on the evolution of the electrochemical performance on thermal degradation, a systematic study on the structural and chemical evolution of LSMCF combinatorial thin films was performed. This was

evaluated by comparing the cationic distribution of an as-deposited sample (grown on a CGO/YSZ substrate) with one that was thermally treated at 800 °C for a period of 100 h. The same thermal process was carried out to reference samples of the three parent materials. A selection of compositions were then characterized in order to analyze the evolution of the surface, subsurface and bulk in terms of segregation of dopant species, cation rearrangement and evolution of defects.

#### 4.4.2.1 Evolution of surface microstructure and appearance of segregated phases

The surface of the perovskite LSMCF-based films under study was investigated by AFM. Figure 4-15 shows the top-view micrographs obtained for the reference parent materials before and after the annealing, as well as individual line scans, in order to facilitate the comprehension on the differences observed in the microstructure.

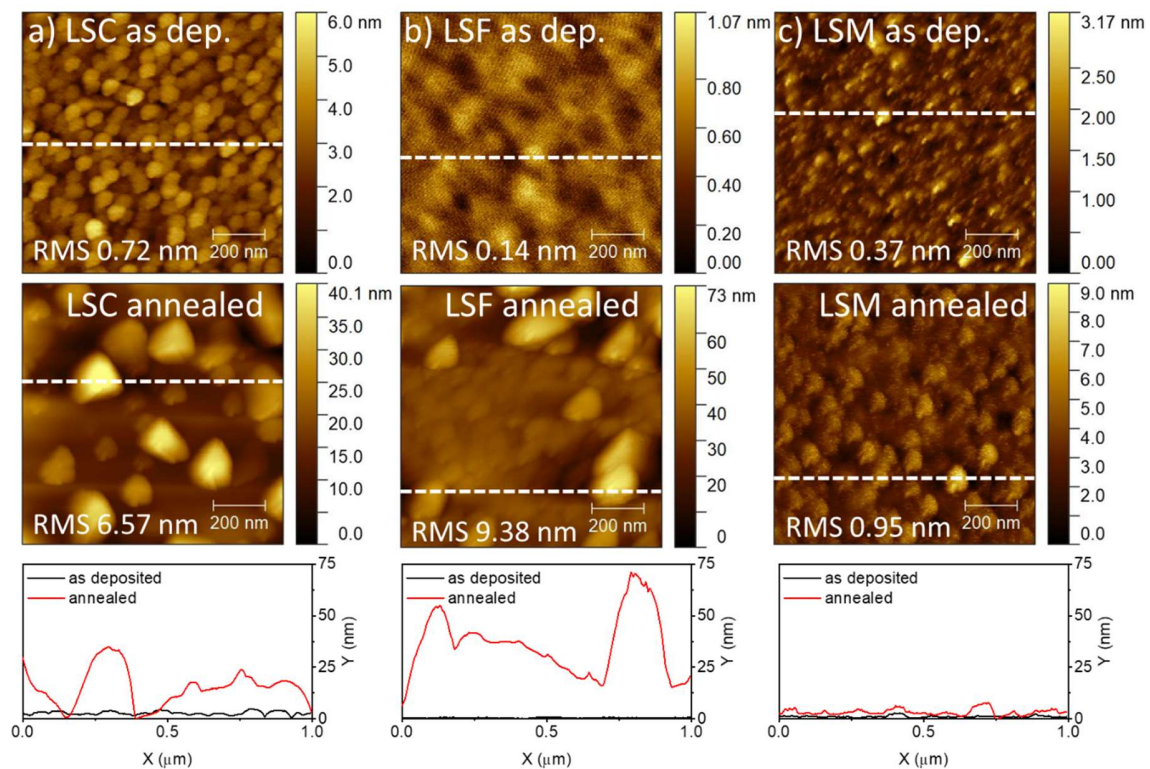


Figure 4-15. Surface microstructural characterization of the parent materials by AFM. Micrographs of the surface of LSC, LSF and LSM, as deposited and annealed (800 °C – 100 h), along with exemplary line scans (indicated in the topography micrographs with a white dashed line), respectively (a-c).

The evolution of LSC can be observed in Figure 4-15a. The as-deposited film presents a homogeneous surface with low roughness ( $R_{ms} = 0.72$  nm) and grains of around 60 nm in size. In the case of the annealed LSC, the roughness increases substantially, up to 6.57 nm,

and the appearance of shard-shaped segregated particles of the order of 130-200 nm of lateral size and up to 40 nm of height (better seen in the line scan) is observed. The LSF film follows a similar behavior (Figure 4-15b), with the presence of a smooth surface with  $R_{ms} = 0.14$  nm with less defined grains than in the case of LSC. Annealing of LSF results in the formation of a rough layer ( $R_{ms} = 9.38$  nm) with large shard-like segregated phases on the surface, with lateral size in the range of 150-250 nm, and height of up to 70 nm, as depicted in the line scan. Most interesting is the case of LSM –panel (c)–, which presents a smooth surface in the pristine state ( $R_{ms} = 0.37$  nm) with particularly small grains. In the case of the annealed sample the roughness is increased but maintained at a low value ( $R_{ms} = 0.95$  nm), grain growth is observed to values of 60-70 nm and no significant segregation of particles is appreciated. This suggests a clear difference in the behavior on thermal degradation of LSM in contrast to LSC and LSF, in which LSM do not present significant segregation when faced to prolonged exposure to high temperature conditions.

With regard to the LSMCF combinatorial thin films analyzed, Figure 4-16 shows the collection of AFM micrographs obtained for the as deposited and thermally annealed samples, along with the relative B-cation distribution measured by EDX, and the roughness  $R_{ms}$  values. The films are characterized by the presence of a small amount of segregated phases already observed in the as deposited state, with no apparent dependence on the relative composition of the B-cation. The roughness values vary in the range of 0.6-3.67 nm, with most of the samples showing values close-to or below 1 nm. Some small nucleates are also visible in some of the micrographs. The difference in the as deposited state with regards to the parent materials may be explained by the nature of the deposition process, as combinatorial PLD deposition is expected to result in a slightly more disordered growth. Particularly, the cycled repetition of few laser pulses during target ablation in the combinatorial deposition with respect to the continuum ablation of the parent material films might facilitate the thin film growth favored by a 2D+island nucleation type of growth<sup>51</sup>. Additionally, the cycling process of combinatorial PLD derives in longer deposition times (e.g. 1-2 hours) than for conventional depositions (e.g. 10-20 minutes). This can result in favoured growth of nucleation sites occurring during the deposition, as well as facilitating the appearance of segregated species due to the long exposition to the high temperature.



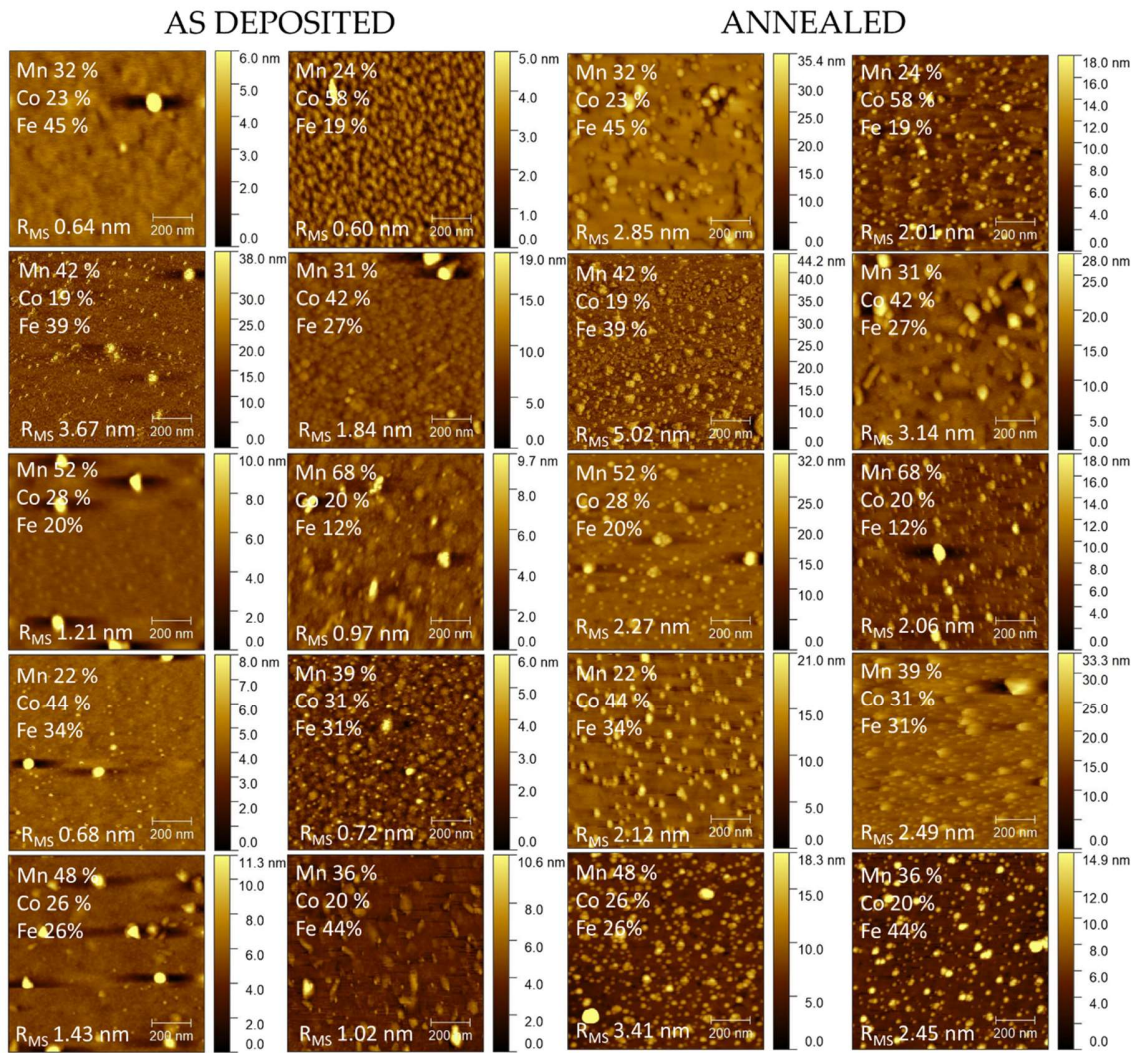


Figure 4-16. AFM micrographs of the combinatorial LSMCF films as deposited and after thermal annealing at 800 °C for 100 h. The relative composition of the B-cation and the  $R_{MS}$  roughness value are indicated in each micrograph.

Regarding the thermally annealed LSMCF materials, a higher presence of segregated phases can be clearly observed all of the films, with particle growth of the previously observed nucleates. Grain growth of the base perovskite film is also observed in the cases with Fe content at 45 % and 27 %, while for the rest of the films the segregated particles do not make possible to differentiate the microstructure of the perovskite phase. The roughness values calculated vary in the 2.01-5.02 nm range, following progressive increase with respect to the as deposited samples with equivalent composition. Interestingly, despite the evident increase in roughness and the visible increase of segregated phases, none of the LSMCF films show the drastic increase in roughness and growth of segregated particles as the observed for single LSC and LSF in Figure 4-15. This indicates that the LSMCF combinatorial

films present higher stability for facing segregation mechanisms induced by thermal annealing.

#### 4.4.2.2 A-site cation structural and chemical evolution at the surface and sub-surface level

The surface and subsurface chemistry of the films was analyzed by Low Energy Ion Scattering. Figure 4-17 presents the LEIS spectra obtained for the LSC, LSF and LSM parent materials –panels (a-c)–, as well as for an individual LSMCF compound –panel (d)– with a Ne<sup>+</sup> primary beam at 5 keV, both before and after the thermal treatment. The spectra was measured after a first ablation with Ar<sup>+</sup> sputtering beam, in order to remove the first atomic layer, mostly characterized by the presence of hydrocarbons. The peaks present in the region 1200-1400 eV correspond to the signals of Mn, Fe and Co. These peaks show a certain degree of overlapping, as only two peaks can be properly distinguished in Figure 4-17d. The Sr and La peaks can be found at 2100 and 2800 eV, respectively. The B/La+Sr and Sr/La+Sr ratios indicated in each panel have been calculated in each case by the ratio between the corresponding peak areas. Note that for the co-doped LSMCF film the overall B-cation contribution has been calculated due to the overlap present between the Mn,Co and Fe peaks. It can be observed that for LSC and LSF single chip samples, B/La+Sr is considerably lower after the thermal treatment (from 0.33 to 0.07 for LSC and from 0.64 to 0.29 for LSF), while the Sr/La+Sr signal is higher (increase from 0.34 to 0.47 for LSC and from 0.30 to 0.42 for LSF). In the case of LSM, both the B/La+Sr and Sr/La+Sr ratios decrease after thermal annealing, even though the Mn-peak stays practically unchanged. The decrease in the ratios can be explained then by the drastic lowering of the Sr peak area and the respective increase in the La peak contribution. This suggests that the LSM outermost surface is favoured to present La-O termination upon thermal annealing. Finally, for the case of the LSMCF sample there is a decrease in both the B/La+Sr (0.64 to 0.24) and Sr/La+Sr (0.29 to 0.25) ratios after performing the annealing treatment, although for the Sr contribution the decrease is not substantially large.

Although this analysis corresponds only to the outermost atomic layer of the films, and a screening in depth is needed for deeper understanding (cf. later in the text), some initial considerations can be here introduced. Both LSC and LSF present a significant decrease of the B-cation presence in the top surface, which is translated to an increase of the Sr content. This is coherent with the visual observations made by AFM microscopy in Figure 4-15a-b and is an indicative of the Sr segregation phenomena experienced by these materials. With regard to LSM, the major difference in the spectra is found in the decrease of the Sr peak after thermal annealing and a minor increase in the La signal, resulting in a Sr/La+Sr ratio of 0.08. These changes go in the opposite direction than for LSC and LSF, which is coherent with the absence of segregated species observed in the AFM micrographs. Equilibration towards a La-enriched surface stoichiometry is suggested by this behavior. In the case of the

LSMCF film (in particular, the example with stoichiometry of  $\text{La}_{0.8}\text{Sr}_{0.2}\text{Mn}_{0.32}\text{Co}_{0.23}\text{Fe}_{0.45}\text{O}_3$ ), the main change is observed in the decrease of the B/La+Sr ratio after thermal annealing, with minor decrease of the Sr/La+Sr signal. This suggests the formation of an preferential A-site surface termination, with seemingly preference of La over Sr in comparison to the as deposited state for the Mn-containing materials.

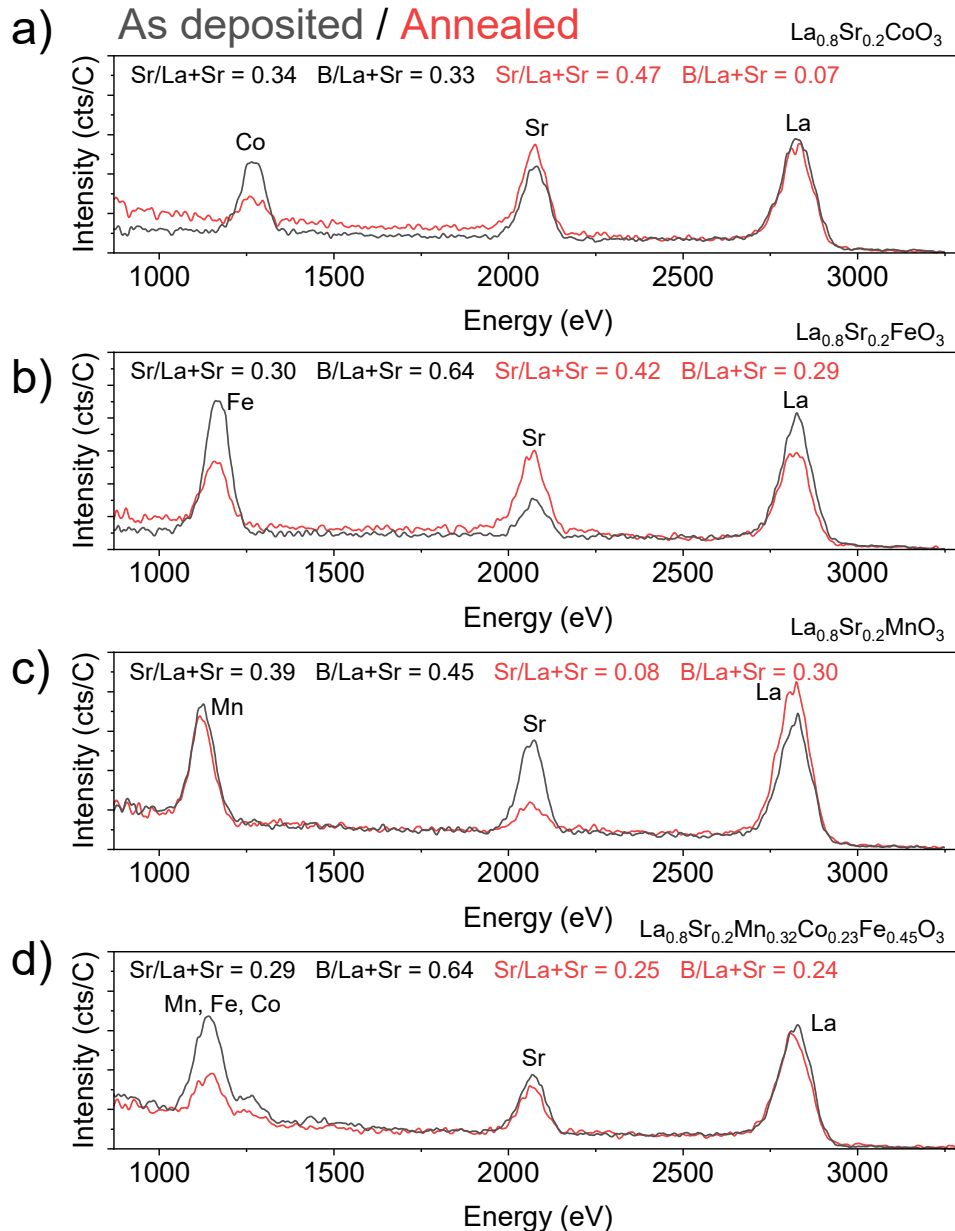


Figure 4-17. LEIS spectra obtained with a  $\text{Ne}^+$  primary ion for the perovskites studied before and after thermal annealing: parent materials LSC (a), LSF (b), LSM (c) and a example of a LSMCF film (d).

Depth profiles were measured by alternating the  $\text{Ne}^+$  LEIS spectra with  $\text{Ar}^+$  sputtering. B/La+Sr and Sr/La+Sr profiles were obtained by calculating the ratios between the area of

the peaks of interest (i.e. the area of the peaks shown above). Figure 4-18 shows the collection of profiles measured for the reference single constituent samples of LSC, LSF and LSM. The differences between the three materials are evident, even in the as deposited case. While all the films present Sr-enrichment close to the surface after the deposition, the thermal treatment performed on the parent materials results in a dramatic increase of the Sr/La+Sr ratio for both LSC and LSF, reaching values over 0.4 at the top surface, i.e. over double the nominal stoichiometry. It is such an increase in the relative content of Sr that the nominal 0.2 content is not recovered for the 10 nm region analyzed (i.e. the considered surface and subsurface active regions), despite the progressive decay observed. Further characterization on deeper regions are discussed in the next section. The severe enrichment experienced for these two materials aligns perfectly with the observed microstructure in Figure 4-15, taking into account the size of the segregated particles, which is in the order of tens of nm. This results in the relative loss of active surface of the perovskite material due to the appearance of the segregated phases. The measured ratio results then from an averaged contribution of both the film and the segregated particles. Following the observations made previously, LSM does not show further Sr-enrichment in the surface region after the thermal treatment. In fact, the Sr/La+Sr profile shows an almost planar shape with Sr dropping at the outermost surface, which can be attributed to a thermodynamical equilibrium state which facilitates the recovering of La-O-terminated layers to the surface<sup>52</sup>.

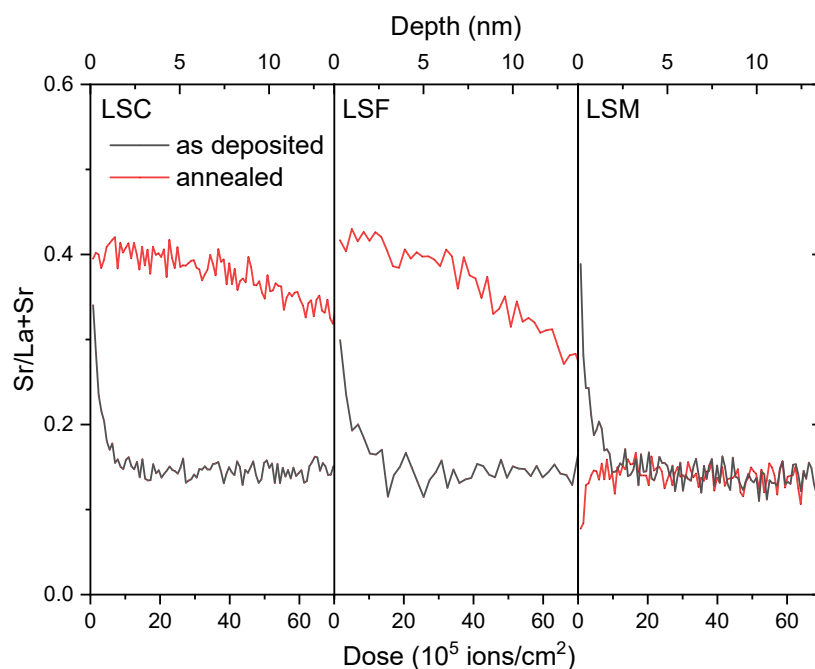


Figure 4-18. LEIS depth profiles of the LSC, LSF and LSM films obtained for the surface and subsurface region showing the Sr/La+Sr ratio. The dark line corresponds to the film as deposited and the red after the thermal annealing at 800 °C for 100 h.

The overall profiles analyzed for the combinatorial samples are shown in Figure 4-19. It can be observed that, although there are differences in the cation distribution along the several compositions analyzed, the profiles obtained show similar shapes and features. All of the as deposited films present Sr-enrichment on the outermost surface, in the same way as observed for the parent materials discussed. Hence, it is clear that the fabrication process resulted in the deposition of LSMCF-based films already presenting Sr-enrichment in the outermost surface, irrespectively of the B-cation content. This systematic behavior of Sr-enrichment is broken after performing the thermal annealing. In general terms, all of the Sr/La+Sr annealed profiles present lower values with respect to the as deposited counterpart.

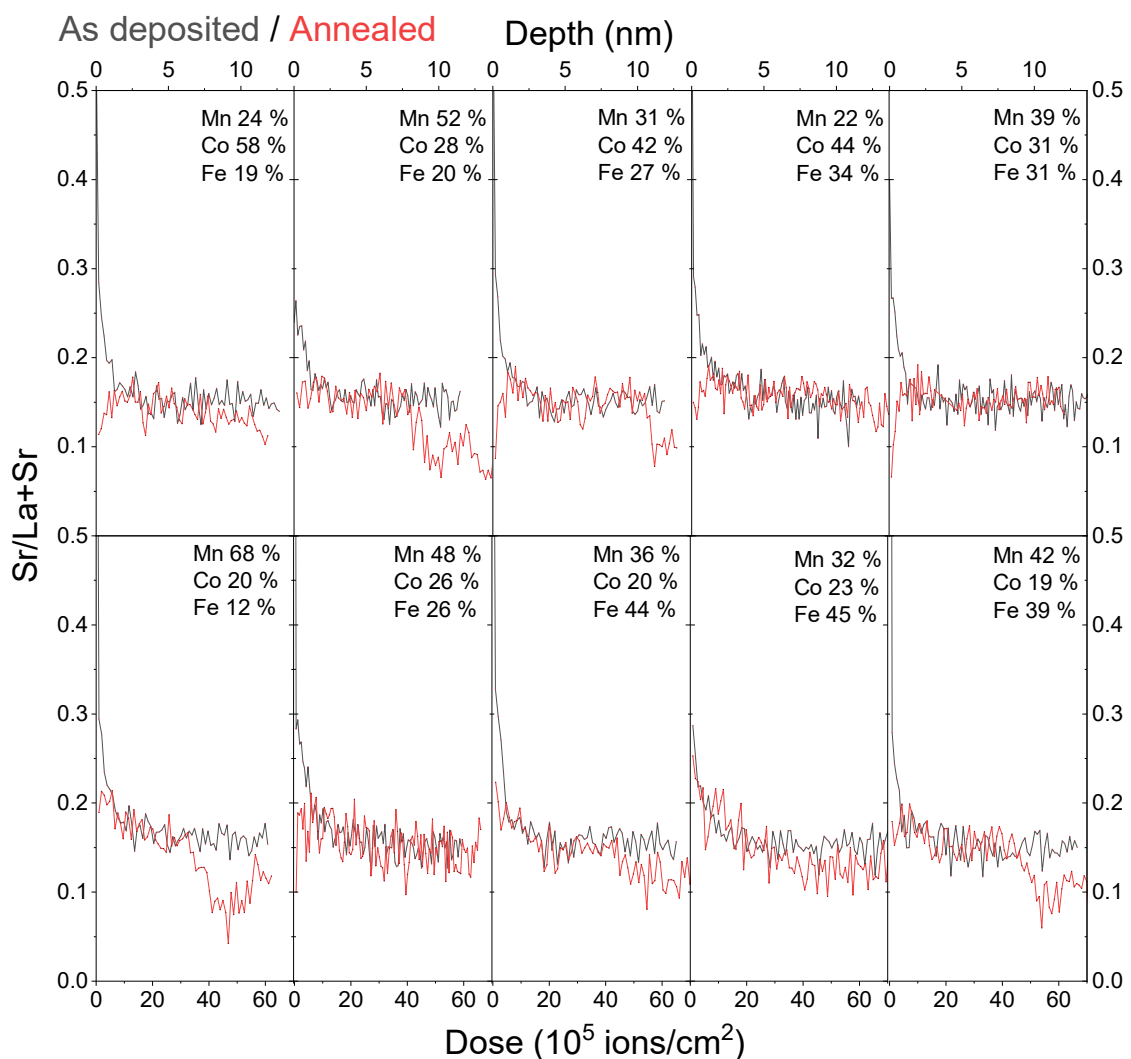


Figure 4-19. LEIS depth profiles of the LSMCF films obtained for the surface and subsurface region showing the Sr/La+Sr ratio. The dark line corresponds to the film as deposited and the red after the thermal annealing at 800 °C for 100 h.

This is more evident in the top surface level (i.e. the first 1 nm of the profile), for which the Fe-rich samples present slightly lower Sr-enrichment (e.g. Fe 44-45 % films), while for the rest the Sr signal appears to equilibrate close to the nominal stoichiometric value and even decrease for the outermost atomic layers, as observed for LSM in Figure 4-18. Additionally, in the case of the subsurface (i.e. region right below the surface within the first 10 nm) a decrease of the Sr/La+Sr signal in some of the films analyzed can be appreciated (e.g. the films with Fe content of 20 %, 27 %, 12 % and 39 %).

In order to obtain a more general analysis on the Sr rearrangement in the surface and subsurface areas, the Sr/La+Sr LEIS profiles were integrated over the first 2 nm (surface) and the 2 to 10 nm regions (subsurface) and normalized over the depth. This calculation results in the weighted value of the Sr/La+Sr stoichiometry over these two regions, and is reported in Figure 4-20. Figure 4-20a reports the value of Sr/La+Sr for the surface and subsurface regions in the as deposited case. It can be seen that the surface region exhibits Sr/La+Sr values close to the nominal stoichiometry of 0.2 in all cases, included the parent materials, as previously commented on the profile discussion above. The subsurface however presents Sr content below the nominal stoichiometric value. A possible cause to this phenomenon might be derived from the migration of Sr into the surface, which might have led to a Sr-deficient subsurface. Additionally slight deviations from the nominal stoichiometry might be related to experimental uncertainties for full quantification (e.g. for LEIS analysis, the analysis of material standards and calibration processes is highly desired). For this reason, the Sr/La+Sr values obtained for the as deposited samples in the subsurface ( $\approx 0.16$ ) will be employed as a reference value to evaluate the relative Sr enrichment. Following this reference, all the as deposited samples present a Sr-enriched surface. Figure 4-20b shows the surface and subsurface Sr/La+Sr signal after the annealing performed. Interestingly, for the co-doped LSMCF films, both the surface and subsurface regions present Sr content close or lower than the nominal stoichiometric values, contrary to the observed phenomenon in the as deposited samples. If we compare then with the Sr content analyzed for the aged parent materials, while a similar behavior is observed for LSM –with the Sr/La+Sr ratio below 0.2– a dramatic increase of the Sr content is observed for pure LSC and LSF. This is better shown in Figure 4-20c, which shows the enrichment factor (calculated from the ratio between the Sr/La+Sr signal after the annealing over the as deposited values measured for the surface and subsurface, respectively). The resulting value can be interpreted as the factor determining the migration of Sr cations driven by thermal evolution under the conditions applied. This factor allows to get a clear view on the effect of the annealing treatment on the films. It can be clearly seen how the overall surface Sr/La+Sr content decreases (surface enrichment factor  $< 1$ ) for LSM and all the LSMCF films analyzed. This is also the case of the subsurface region, though for some films the Sr/La+Sr content was kept (enrichment factor in the subsurface  $\leq 1$ ). The overall Sr/La+Sr ratio decrease in the LSMCF thin films after performing the thermal treatment might be unexpected considering the segregation phenomena observed in Figure 4-16. Nonetheless, this seems to be a recurrent topic

emerging on the literature, as there are studies which either show complete Sr-enrichment<sup>53</sup> caused by the segregated phases or report the presence of Sr depleted layers prior to the outermost surface<sup>54-56</sup>. Regarding LSC and LSF, both present enrichment factors > 2 for both the surface and subsurface, reaching a value of 2.70 in the subsurface. This is in total agreement with the microstructure evolution discussed previously, confirming the involvement of Sr in the appearance of the segregated phases.

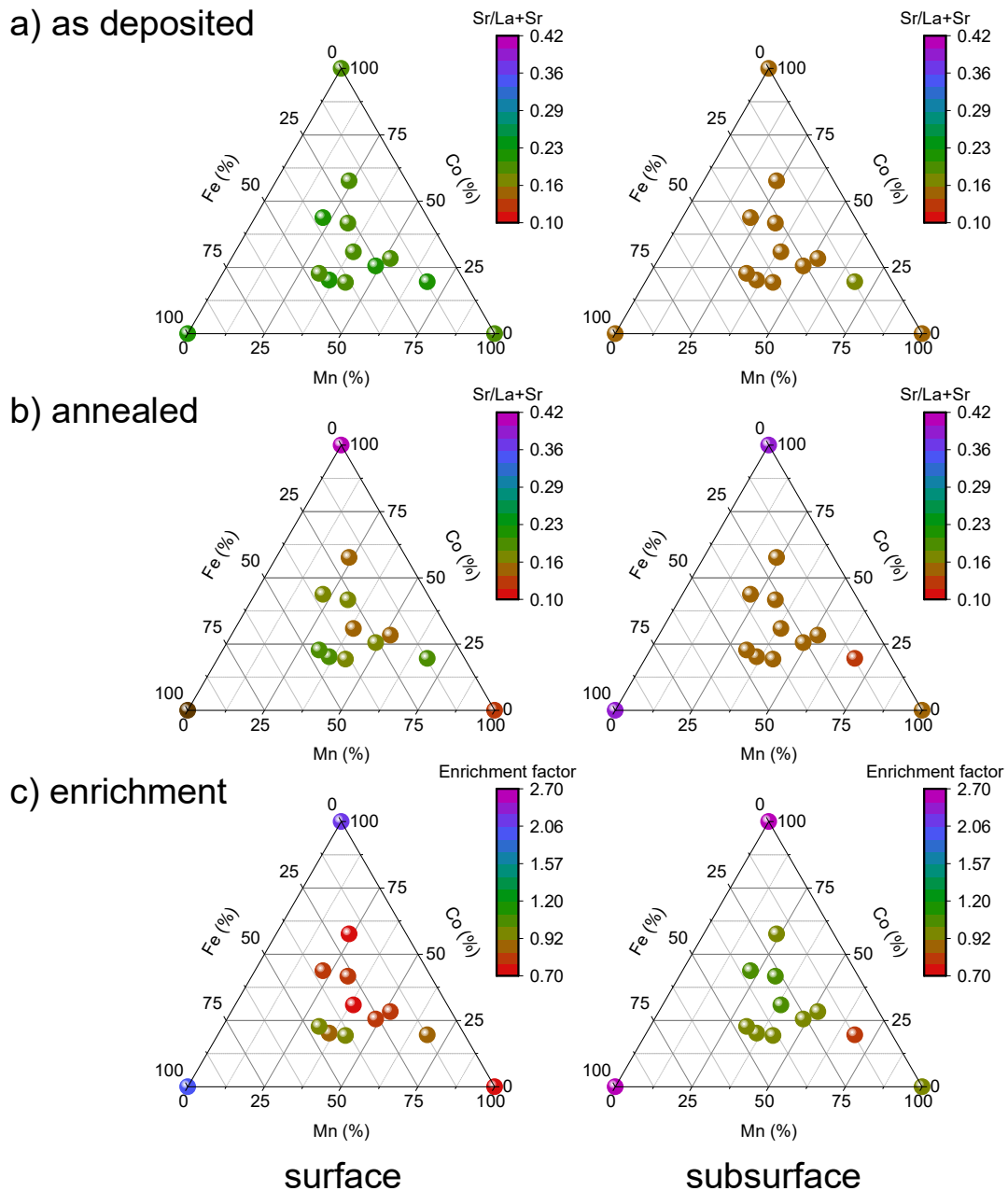


Figure 4-20. LEIS analysis extracted from LSMCF depth profiles measured. The integrated Sr/La+Sr is calculated and normalized in two regions of interest: surface (2 nm depth) and

*subsurface (2-10 nm of depth). As deposited (a), annealed (b) and the enrichment factor calculated (c) are shown for each region.*

In order to gain clarity on the nature of the surface chemistry involved in the evolution observed after thermal annealing, the films were analyzed by XPS. XPS spectra for C 1s, O 1s, Mn 3d, Co 3d, Fe 3d, La 3d and Sr 3d were measured in order to fully characterize the chemical environment. Figure 4-21a shows an example of a XPS survey spectrum measured for the  $\text{La}_{0.8}\text{Sr}_{0.2}\text{Mn}_{0.32}\text{Co}_{0.23}\text{Fe}_{0.45}\text{O}_3$  thin film. The main peak contributions involved in the analysis have been highlighted, for easier comprehension. Particular focus was given to the Sr 3d signal, with the goal to identify the chemical composition of the dopant segregated species and further understand cation rearrangement in the LSMCF films. Figure 4-21b-e shows the Sr 3d XPS spectra obtained for the LSC, LSF and LSM parent materials studied, as well as for one example of the intermixed LSMCF compounds, both as deposited and after the thermal treatment. Three different Sr-related species have been considered for the analysis of these spectra. The signal attributed to the Sr-O bond in the perovskite lattice, labeled as  $\text{Sr}_{\text{latt}}$ , can be found in the lower binding energy range, with the  $3d_{5/2}$  peak centered in the 131.7-132.3 eV range. Sr bonds corresponding to species such as SrO,  $\text{Sr}(\text{OH})_2$  and  $\text{SrCO}_3$  (referred from now on as  $\text{Sr}_{\text{mix}}$ ) present the  $3d_{5/2}$  peak positioned in the 132.7-13.3 eV range. Finally, sulfate species in the form of  $\text{SrSO}_4$ , if present, can be located at even stiffer bounds placed in the 133.7-134.2 eV range ( $\text{Sr}_{\text{sulf}}$ ). The  $3d_{3/2}$  doublet peak has been fitted considering a shift of  $1.8 (\pm 0.1)$  eV in the higher energy direction. It should be pointed out that peak identification and XPS analysis of the Sr 3d signal in thermally degraded perovskites is not straight-forward. Although there is a general consensus in differentiating between the *lattice/bulk* component, corresponding to the Sr-O bond in the perovskite structure (e.g. the works from Cai<sup>57</sup>, Celikbilek<sup>55</sup> or Tripković<sup>58</sup> et al.), and the surface (i.e. a generalized contribution for the possible strontium segregated species present, such as SrO,  $\text{Sr}(\text{OH})_2$ ,  $\text{SrCO}_3$ , or  $\text{SrSO}_4$ ), some works go further in identifying the surface species. This is the case of the exemplary studies from Kim<sup>59</sup> and Siebenhofer<sup>60</sup> et al. These two works differ in the identification of the Sr species for the  $3d_{5/2}$  peak contribution located at  $\approx 134$  eV. While in the first case this is attributed to be the contribution of strontium carbonate precipitates, in the latter this is identified to be originated from strontium sulfate. Peak identification made in this chapter has been performed by attributing this peak to the presence of  $\text{SrSO}_4$  after confirming the appearance of sulfur XPS signal in the survey measured prior to the experiment (see Figure 4-21a), and in agreement with the works by Vasquez<sup>61,62</sup> on the study of Sr compounds (including  $\text{SrCO}_3$  and  $\text{SrSO}_4$ ) by XPS. In these works, Sr  $3d_{5/2}$  peak was found to be centered at 132.9 and 134.05 eV for  $\text{SrCO}_3$  and  $\text{SrSO}_4$ , respectively, in line with the values observed in this work. All the fitted contributions have been differentiated in the spectra showed in Figure 4-21. A detailed list of the binding energies fitted for the Sr contributions and La can be found in Table 4-1 and Table 4-2 for the as deposited and thermally treated samples, respectively. The XPS spectra in Figure 4-21 offer further details in the chemical nature of the Sr species involved in the evolution of the materials under



study. Both as deposited LSC and LSF present all three Sr-peak contributions with relatively comparable intensities, being  $Sr_{latt}$  the major of them. In the case of the thermally annealed acquired spectra though, the peak associated to  $SrSO_4$  becomes the main peak observed by a large extent, while the other two peaks are practically indistinguishable. This is coherent with the topography observed for the two aged samples, characterized by the growth of large segregated particles. The sharp edges observed in the particles have been attributed to the presence of  $SrSO_4$  in other studies<sup>58</sup>. In the case of LSM, the as deposited XPS spectra shows the presence of all three Sr contributions, with the most intense peaks being  $Sr_{latt}$  and the intermediate  $Sr_{mix}$  peak. After the thermal annealing the LSM film increases the relative peak of  $Sr_{latt}$  with respect to the rest, in line with observations made of the topographical surface area in Figure 4-15. In the case of the  $La_{0.8}Sr_{0.2}Mn_{0.32}Co_{0.23}Fe_{0.45}O_3$  sample, the as deposited spectra presents the highest relative presence of  $Sr_{latt}$ , in contrast to the parent materials. Nonetheless, the spectra after the annealing shows the decrease of the perovskite signal, and the respective increase of the other surface-related signals.

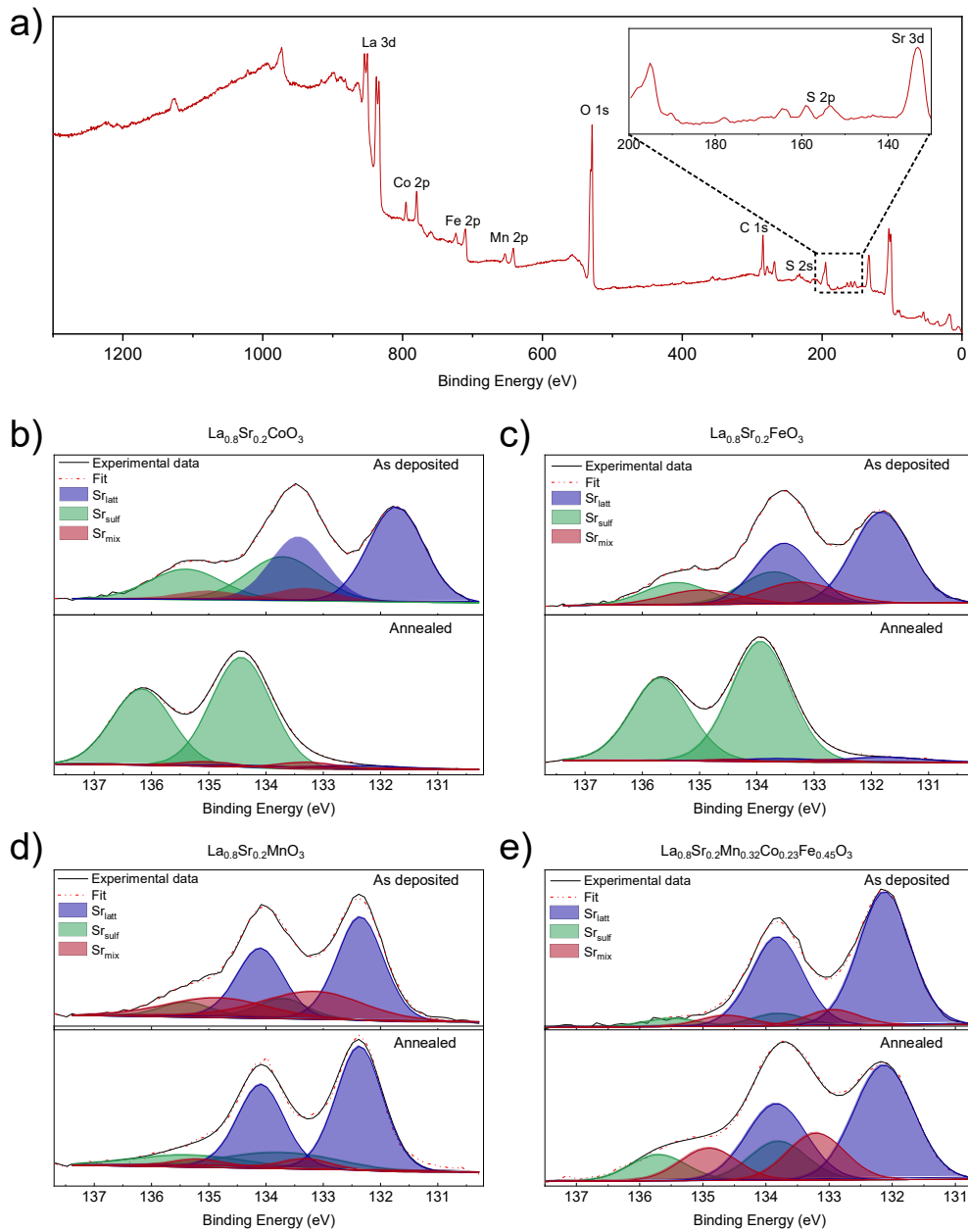


Figure 4-21. XPS survey spectrum obtained for the annealed  $\text{La}_{0.8}\text{Sr}_{0.2}\text{Mn}_{0.32}\text{Co}_{0.23}\text{Fe}_{0.45}\text{O}_3$  showing the main representative peaks of the system: La 3d, Co 2p, Fe 2p, Mn 2p, O 1s, C 1s, S 2p and Sr 3d. peaks (a). XPS spectra obtained for the parent materials LSC, LSF and LSM, and an intermixed  $\text{La}_{0.8}\text{Sr}_{0.2}\text{Mn}_{0.32}\text{Co}_{0.23}\text{Fe}_{0.45}\text{O}_3$  sample, respectively (b-e). Each plot shows both the measurement as deposited and after the thermal annealing at 800 °C for 100 h.

In this sense, the intermixed LSMCF sample seem to present an intermediate behavior between the observations made for LSC or LSF and LSM. The initial state of the thin film shows a large contribution of  $\text{Sr}_{\text{latt}}$  and considerably low peak areas for the other two contributions. Thermal annealing results then in a decrease of the  $\text{Sr}_{\text{latt}}$  signal with the

corresponding increase of both Sr<sub>mix</sub> and Sr<sub>sulf</sub> peaks. Nonetheless, the increase in the segregated particles-related XPS signals do not reach the drastic increase experienced by LSC and LSF.

*Table 4-1. Main values calculated from the XPS fitting of the as deposited LSMCF films: peak binding energy of the different Sr contributions and La, and normalized atomic percentage calculated.*

Composition	Peak BE (eV) - 3d <sub>5/2</sub>				Normalized Atomic %			
	Sr <sub>latt</sub>	Sr <sub>mix</sub>	Sr <sub>sulf</sub>	La	Sr <sub>latt</sub>	Sr <sub>mix</sub>	Sr <sub>sulf</sub>	La
La <sub>0.8</sub> Sr <sub>0.2</sub> CoO <sub>3</sub>	131.72	133.3	133.7	833.82	11.76	1.56	4.06	82.62
La <sub>0.8</sub> Sr <sub>0.2</sub> FeO <sub>3</sub>	131.82	133.26	133.7	833.65	20.51	6.36	4.84	68.28
La <sub>0.8</sub> Sr <sub>0.2</sub> MnO <sub>3</sub>	132.35	133.16	133.7	834.21	19.31	10.91	2.25	67.53
La <sub>0.8</sub> Sr <sub>0.2</sub> Mn <sub>0.24</sub> Co <sub>0.58</sub> Fe <sub>0.19</sub> O <sub>3</sub>	131.88	132.7	133.81	834.2	16.58	8.00	2.02	73.40
La <sub>0.8</sub> Sr <sub>0.2</sub> Mn <sub>0.48</sub> Co <sub>0.37</sub> Fe <sub>0.15</sub> O <sub>3</sub>	132.05	133.08	133.75	834.13	9.87	7.97	2.91	79.25
La <sub>0.8</sub> Sr <sub>0.2</sub> Mn <sub>0.38</sub> Co <sub>0.43</sub> Fe <sub>0.19</sub> O <sub>3</sub>	131.91	132.7	133.7	833.99	8.80	8.25	4.22	78.74
La <sub>0.8</sub> Sr <sub>0.2</sub> Mn <sub>0.18</sub> Co <sub>0.55</sub> Fe <sub>0.27</sub> O <sub>3</sub>	131.8	132.93	133.73	834.11	7.01	7.93	7.62	77.44
La <sub>0.8</sub> Sr <sub>0.2</sub> Mn <sub>0.60</sub> Co <sub>0.25</sub> Fe <sub>0.15</sub> O <sub>3</sub>	132.46	133.05	134.2	834.46	12.84	6.54	1.91	78.71
La <sub>0.8</sub> Sr <sub>0.2</sub> Mn <sub>0.52</sub> Co <sub>0.28</sub> Fe <sub>0.20</sub> O <sub>3</sub>	132.17	132.7	133.72	834.39	12.16	7.32	4.74	75.78
La <sub>0.8</sub> Sr <sub>0.2</sub> Mn <sub>0.31</sub> Co <sub>0.42</sub> Fe <sub>0.27</sub> O <sub>3</sub>	131.98	132.7	133.71	834.21	19.13	4.17	4.56	72.14
La <sub>0.8</sub> Sr <sub>0.2</sub> Mn <sub>0.22</sub> Co <sub>0.44</sub> Fe <sub>0.34</sub> O <sub>3</sub>	131.91	132.7	133.7	834.1	18.84	3.41	4.83	72.92
La <sub>0.8</sub> Sr <sub>0.2</sub> Mn <sub>0.23</sub> Co <sub>0.44</sub> Fe <sub>0.33</sub> O <sub>3</sub>	132.06	132.8	134	834.17	9.69	5.12	5.47	79.72
La <sub>0.8</sub> Sr <sub>0.2</sub> Mn <sub>0.55</sub> Co <sub>0.26</sub> Fe <sub>0.19</sub> O <sub>3</sub>	132.42	132.82	134.07	834.36	14.56	3.46	3.55	78.42
La <sub>0.8</sub> Sr <sub>0.2</sub> Mn <sub>0.39</sub> Co <sub>0.31</sub> Fe <sub>0.31</sub> O <sub>3</sub>	132.07	133.24	133.9	834.21	14.55	5.26	3.10	77.09
La <sub>0.8</sub> Sr <sub>0.2</sub> Mn <sub>0.28</sub> Co <sub>0.32</sub> Fe <sub>0.40</sub> O <sub>3</sub>	132.02	132.7	133.93	834.01	9.69	5.60	5.19	79.52
La <sub>0.8</sub> Sr <sub>0.2</sub> Mn <sub>0.68</sub> Co <sub>0.20</sub> Fe <sub>0.12</sub> O <sub>3</sub>	132.41	133.05	133.7	834.37	26.53	6.24	1.17	66.06
La <sub>0.8</sub> Sr <sub>0.2</sub> Mn <sub>0.48</sub> Co <sub>0.26</sub> Fe <sub>0.26</sub> O <sub>3</sub>	132.25	132.78	133.91	834.32	20.60	5.72	2.48	71.20
La <sub>0.8</sub> Sr <sub>0.2</sub> Mn <sub>0.36</sub> Co <sub>0.20</sub> Fe <sub>0.44</sub> O <sub>3</sub>	132.29	132.73	133.89	834.17	23.85	4.84	3.26	68.05
La <sub>0.8</sub> Sr <sub>0.2</sub> Mn <sub>0.32</sub> Co <sub>0.23</sub> Fe <sub>0.45</sub> O <sub>3</sub>	132.12	132.87	133.74	833.59	25.38	1.74	2.56	70.32
La <sub>0.8</sub> Sr <sub>0.2</sub> Mn <sub>0.58</sub> Co <sub>0.21</sub> Fe <sub>0.21</sub> O <sub>3</sub>	132.23	133.17	134.18	834.36	10.54	5.72	1.81	81.93
La <sub>0.8</sub> Sr <sub>0.2</sub> Mn <sub>0.42</sub> Co <sub>0.19</sub> Fe <sub>0.39</sub> O <sub>3</sub>	132.13	132.7	133.9	834.28	19.22	5.14	2.28	73.36
La <sub>0.8</sub> Sr <sub>0.2</sub> Mn <sub>0.36</sub> Co <sub>0.17</sub> Fe <sub>0.47</sub> O <sub>3</sub>	132.27	132.8	133.97	833.67	14.17	8.21	1.56	76.06

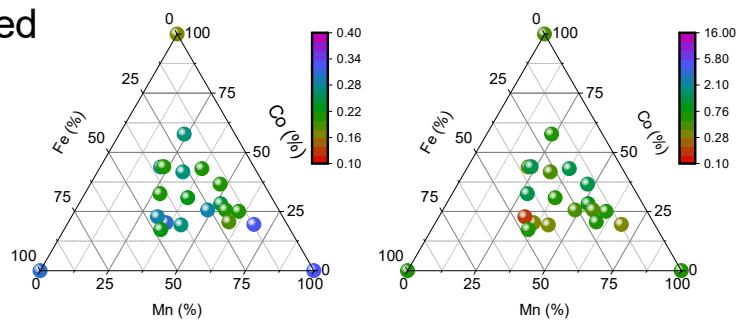
Table 4-2. Main values calculated from the XPS fitting of the thermally treated LSMCF films: peak binding energy of the different Sr contributions and La, and normalized atomic percentage calculated.

Composition	Peak BE (eV) - 3d <sub>5/2</sub>				Normalized Atomic %			
	Sr <sub>latt</sub>	Sr <sub>mix</sub>	Sr <sub>sulf</sub>	La	Sr <sub>latt</sub>	Sr <sub>mix</sub>	Sr <sub>sulf</sub>	La
La <sub>0.8</sub> Sr <sub>0.2</sub> CoO <sub>3</sub>	132.29	133.3	134.43	834.31	2.36	4.22	32.12	61.30
La <sub>0.8</sub> Sr <sub>0.2</sub> FeO <sub>3</sub>	131.8	132.7	133.93	833.68	3.69	1.03	34.91	60.38
La <sub>0.8</sub> Sr <sub>0.2</sub> MnO <sub>3</sub>	132.37	133.3	133.71	833.96	14.97	1.19	2.53	81.31
La <sub>0.8</sub> Sr <sub>0.2</sub> Mn <sub>0.24</sub> Co <sub>0.58</sub> Fe <sub>0.19</sub> O <sub>3</sub>	131.86	133.14	133.74	834.1	14.27	6.63	2.81	76.28
La <sub>0.8</sub> Sr <sub>0.2</sub> Mn <sub>0.48</sub> Co <sub>0.37</sub> Fe <sub>0.15</sub> O <sub>3</sub>	132.02	133.13	133.83	834.13	9.07	3.82	5.11	82.00
La <sub>0.8</sub> Sr <sub>0.2</sub> Mn <sub>0.38</sub> Co <sub>0.43</sub> Fe <sub>0.19</sub> O <sub>3</sub>	131.97	133.06	133.81	834.19	8.67	4.23	3.94	83.15
La <sub>0.8</sub> Sr <sub>0.2</sub> Mn <sub>0.18</sub> Co <sub>0.55</sub> Fe <sub>0.27</sub> O <sub>3</sub>	131.73	132.71	133.74	833.88	11.43	6.40	3.16	79.01
La <sub>0.8</sub> Sr <sub>0.2</sub> Mn <sub>0.60</sub> Co <sub>0.25</sub> Fe <sub>0.15</sub> O <sub>3</sub>	132.16	133.1	133.75	834.28	12.79	3.62	4.36	79.23
La <sub>0.8</sub> Sr <sub>0.2</sub> Mn <sub>0.52</sub> Co <sub>0.28</sub> Fe <sub>0.20</sub> O <sub>3</sub>	132.12	132.7	133.71	834.37	14.37	6.53	6.53	72.56
La <sub>0.8</sub> Sr <sub>0.2</sub> Mn <sub>0.31</sub> Co <sub>0.42</sub> Fe <sub>0.27</sub> O <sub>3</sub>	131.85	132.7	133.75	834.19	12.78	4.02	6.44	76.76
La <sub>0.8</sub> Sr <sub>0.2</sub> Mn <sub>0.22</sub> Co <sub>0.44</sub> Fe <sub>0.34</sub> O <sub>3</sub>	131.88	133.03	133.75	834.22	9.85	6.50	4.47	79.19
La <sub>0.8</sub> Sr <sub>0.2</sub> Mn <sub>0.23</sub> Co <sub>0.44</sub> Fe <sub>0.33</sub> O <sub>3</sub>	131.89	133.09	133.89	834.22	7.93	5.58	5.36	81.13
La <sub>0.8</sub> Sr <sub>0.2</sub> Mn <sub>0.55</sub> Co <sub>0.26</sub> Fe <sub>0.19</sub> O <sub>3</sub>	132.22	133.12	133.75	834.28	12.13	3.03	6.23	78.61
La <sub>0.8</sub> Sr <sub>0.2</sub> Mn <sub>0.39</sub> Co <sub>0.31</sub> Fe <sub>0.31</sub> O <sub>3</sub>	131.98	133.19	133.7	834.31	10.68	4.21	5.24	79.88
La <sub>0.8</sub> Sr <sub>0.2</sub> Mn <sub>0.28</sub> Co <sub>0.32</sub> Fe <sub>0.40</sub> O <sub>3</sub>	131.87	132.91	133.7	834.03	9.01	5.05	5.12	80.82
La <sub>0.8</sub> Sr <sub>0.2</sub> Mn <sub>0.68</sub> Co <sub>0.20</sub> Fe <sub>0.12</sub> O <sub>3</sub>	132.21	132.7	133.7	834.38	22.06	5.94	2.18	69.82
La <sub>0.8</sub> Sr <sub>0.2</sub> Mn <sub>0.48</sub> Co <sub>0.26</sub> Fe <sub>0.26</sub> O <sub>3</sub>	132.17	132.7	133.7	834.38	13.75	7.73	4.08	74.44
La <sub>0.8</sub> Sr <sub>0.2</sub> Mn <sub>0.36</sub> Co <sub>0.20</sub> Fe <sub>0.44</sub> O <sub>3</sub>	132.12	133.18	133.79	834.28	19.96	3.05	5.40	71.59
La <sub>0.8</sub> Sr <sub>0.2</sub> Mn <sub>0.32</sub> Co <sub>0.23</sub> Fe <sub>0.45</sub> O <sub>3</sub>	132.14	133.2	133.7	834.27	20.82	3.35	8.37	67.47
La <sub>0.8</sub> Sr <sub>0.2</sub> Mn <sub>0.58</sub> Co <sub>0.21</sub> Fe <sub>0.21</sub> O <sub>3</sub>	131.82	132.94	133.7	833.88	11.62	6.04	1.94	80.40
La <sub>0.8</sub> Sr <sub>0.2</sub> Mn <sub>0.42</sub> Co <sub>0.19</sub> Fe <sub>0.39</sub> O <sub>3</sub>	132.18	132.7	133.78	834.29	13.61	7.43	4.50	74.45
La <sub>0.8</sub> Sr <sub>0.2</sub> Mn <sub>0.36</sub> Co <sub>0.17</sub> Fe <sub>0.47</sub> O <sub>3</sub>	132.16	133.1	133.7	834.07	13.57	5.02	5.99	75.42

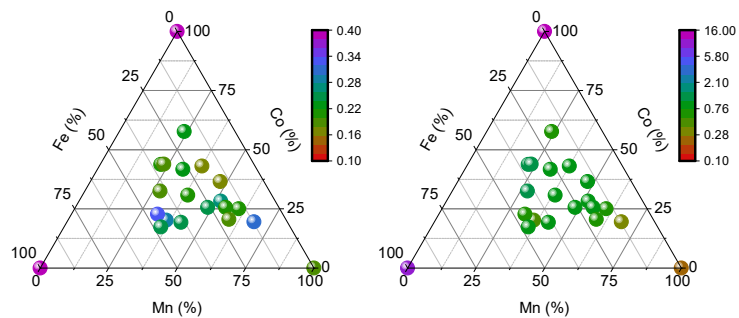
In order to extend the analysis to the full set of materials characterized, Sr/La+Sr and Sr<sub>surf</sub>/Sr<sub>latt</sub> ratios and their evolution after thermal annealing (i.e. the enrichment factor) have been evaluated. In this analysis, Sr<sub>surf</sub> corresponds to the sum of the peak area contributions of Sr<sub>mix</sub> and Sr<sub>sulf</sub>, so the overall segregation effect is discussed. The results for the as deposited, annealed and the enrichment ratios are summarized in panels (a-c) of Figure 4-22, respectively. In line with the observations made with LEIS, the overall Sr/La+Sr decreases after thermal treatment on all the combinatorial films and LSM (enrichment factor < 1), while it increases in the case of LSC and LSF. Interestingly, the Sr<sub>surf</sub>/Sr<sub>latt</sub> ratio reveals an overall increase of the Sr content in the form of surface species with respect to the presence in the perovskite lattice. Notably, the Sr<sub>surf</sub>/Sr<sub>latt</sub> enrichment factor is kept at relatively low values (1-3 range) for most of the LSMCF films, with a couple of examples presenting values below 1 –sign that the surface species are slightly decreased in those–, comparable to single LSM. Hence, Sr enrichment on thermal annealing is much lower in the LSMCF materials than the

observed for LSC and LSF, which present enrichment factors up to 30. This means that the LSMCF co-doped samples present one order of magnitude less Sr segregation than for single LSC/LSF under the conditions tested. It should be pointed out that the LSMCF films studied in this section present variable composition on the perovskite B-cation. Specifically, the samples analyzed cover the ranges of [17-68] % of Mn, [17-57] % of Co and [12-47] % of Fe. Thus, within this broad range of compositions there does not seem to be significant differences on the resilience to Sr segregation phenomena. A direct comparison with the poor performance observed for LSC and LSF parent materials suggest that an addition of Mn within the range studied is key to enhance the stability of LSCF-based oxygen electrodes.

a) as deposited



b) annealed



c) enrichment

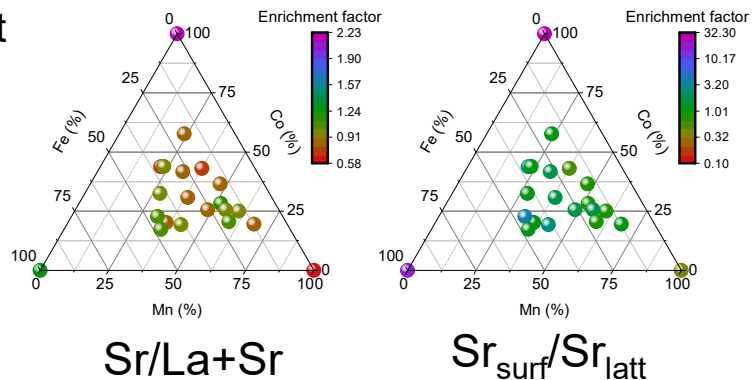


Figure 4-22. Characterization by XPS of the surface chemistry of LSMCF films:  $Sr/La+Sr$  and  $Sr_{surf}/Sr_{latt}$  ratios measured before and after thermal degradation, and the enrichment factor calculated, respectively (a-c).

Further details on the evolution of the strontium segregated species are given in Figure 4-23, in which the  $Sr_{latt}$ ,  $Sr_{mix}$  and  $Sr_{sulf}$  contributions with respect to the overall strontium signal ( $Sr_{total}$ ) are represented. In particular, the pristine state –panel (a)– shows clear dominance of the  $Sr_{latt}$  peak for all the composition range, with most of the cases showing values over 60% of relative content. The  $Sr_{mix}$  and  $Sr_{sulf}$  signals are characterized by higher presence of the first and lower presence of the sulfate peak, with most of the cases below the 20 % range. Figure 4-23b shows the normalized intensities of the peaks after the thermal treatment. The differences already introduced for the parent materials in the discussion of Figure 4-21 are clearly observed here, with presence of the  $Sr_{sulf}$  contribution for LSC and LSF and  $Sr_{latt}$  for LSM. The LSMCF co-doped materials do not present an obvious change in the  $Sr_{latt}/Sr_{total}$  ratio, although some decrease is observed. With regard to the  $Sr_{mix}$  and  $Sr_{sulf}$  analysis, a decrease of the  $Sr_{mix}$  relative content is observed in most of the cases, while increase of the  $Sr_{sulf}$  overall content is also visualized. From this analysis the enrichment factor (annealed/as deposited) for each peak was calculated, as represented in Figure 4-23c.

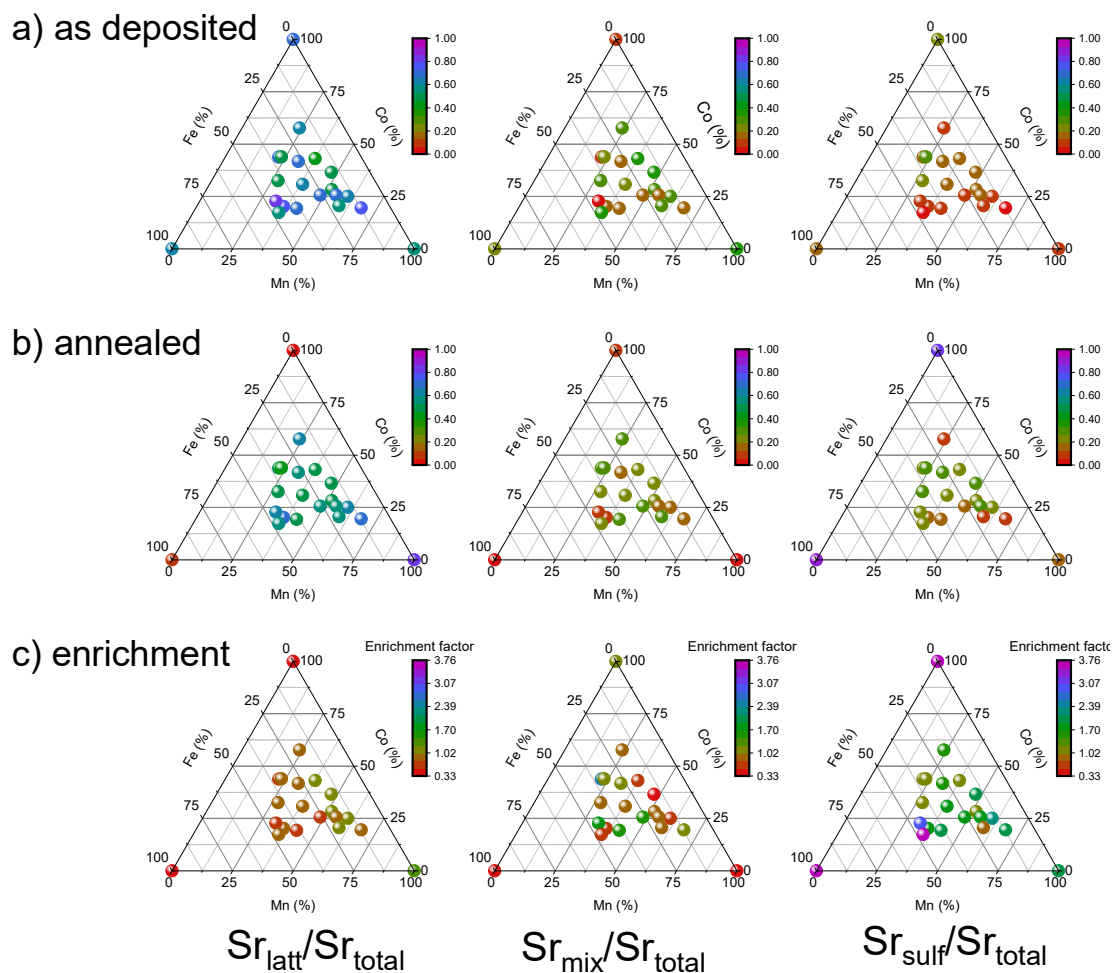


Figure 4-23. Characterization by XPS of the strontium species present in LSMCF films: lattice ( $Sr_{latt}$ ), oxide-carbonates-hydroxides ( $Sr_{mix}$ ) and sulfates ( $Sr_{sulf}$ ) contributions vs the overall

*strontium signal ( $Sr_{total}$ ). Ratios as deposited (a), after thermal annealing (b) and the enrichment factor calculated (c).*

The analysis of the enrichment factor allows to make a general valuation of the behavior of the overall set of compositions on thermal degradation and for facing segregation phenomena. This indicates a drastic increase in the  $Sr_{sulf}/Sr_{total}$  ratio for both LSC and LSF (factor > 3.7). While LSC also shows increase of the  $Sr_{mix}/Sr_{total}$  ratio (enrichment >1), this is not the case for LSF. For the rest of the compounds analyzed, i.e. LSM and LSMCF co-doped materials, a much milder increase of the  $Sr_{sulf}/Sr_{total}$  ratio is generally observed (with only two Fe-rich cases reaching enrichment >2). A generalized decrease of the  $Sr_{mix}/Sr_{total}$  ratio is also observed for the Mn-containing compounds. Notably, LSM and most of the rather stable LSMCF compositions show a  $Sr_{latt}/Sr_{total}$  enrichment factor  $\geq 1$ . This is a clear indicative of the stability of these materials, i.e. the perovskite phase remains present in the surface after the prolonged exposure to the thermal degradation treatment.

#### 4.4.2.3 Effect of the surface evolution with degradation of the electrochemical performance

The characterization performed on the surface evolution of the LSMCF thin films allowed to analyze different types of responses upon Sr segregation. In this sense, the electrochemical performance characterized during thermal degradation in section 4.4.1 can be explained taking into account the structural and chemical analyzes carried out for the LSMCF-based thin films after long thermal annealing. The evolution observed for both LSC and LSF microstructures, i.e. strong Sr enrichment analyzed by LEIS and XPS, is coherent with the fast degradation on the electrochemical performance. The smaller electrochemical degradation rate for LSF with respect to the similar surface evolution characterized could be attributed to the milder temperature conditions for the electrochemical degradation test. Thus, LSF seems to withstand degradation better than LSC at 700 °C, and then show comparable degradation at higher temperatures. This can also be attributed to the different behavior observed between LSC and LSF with regard to formation of strontium carbonate-related species. As indicated in the XPS analysis, LSF seems to be less prone to this kind of Sr segregation and more sensitive to sulfate formation only, while LSC is sensitive to both. The degradation behavior of the electrochemical performance of LSM is also coherent with the surface evolution observed, for which the sulfate contribution has been found to increase its presence -although the total amount of Sr decreases upon thermal annealing. With regard to the LSMCF films analyzed, the observed evolution in surface microstructure and composition is coherent with the small electrochemical degradation observed for the analyzed Fe-rich compound  $La_{0.8}Sr_{0.2}Mn_{0.1}Co_{0.17}Fe_{0.73}O_3$ . Note that the strongest enrichment of Sr surface (and sulfate) species was indeed observed for the Fe-richest compounds studied by XPS, in line with the degradation measured. The absence of degradation for the Mn-rich  $La_{0.8}Sr_{0.2}Mn_{0.42}Co_{0.31}Fe_{0.27}O_3$  film can be attributed to the enrichment factors observed

in the LSMCF highly intermixed regions for the Sr/La+Sr, the surface and the sulfate components in LEIS and XPS, suggesting the presence of a more equilibrated surface with stable electrochemical performance.

#### 4.4.3 Evolution of the distribution and nature of B-site cations and vacancy-defects beyond the surface and subsurface

The findings obtained on the surface and subsurface segregation chemistry evolution of the LSMCF thin films raised the question on the compensation mechanisms triggered by the Sr kinetics observed upon thermal evolution. In order to offer a more complete picture on the cationic rearrangement of the perovskite, and to shed light in the compensation mechanisms that might play a role in the stability observed, further analysis based on LEIS depth profiling and Positron Annihilation Spectroscopy (PAS) are discussed in this section.

##### 4.4.3.1 Compensation of the B-site cations upon thermal annealing

While previous LEIS discussion presented in this chapter has been exclusively focused on the A-site evolution through the evaluation of the Sr/La+Sr ratio, analyzing the evolution of the B-site cations might offer valuable information on the overall thermal ageing process. Figure 4-24 shows the B/La+Sr ratio for the LSC, LSF and LSM single perovskites as deposited and after carrying out the thermal treatment, respectively. It can be clearly seen that the B-cation content largely differs depending on the composition. Both LSC and LSF present B-site deficiency with respect to the nominal stoichiometry (i.e. B/La+Sr ratio of 1), with LSC approaching values of 0.4-0.5 and LSF values close to 0.6 when going towards the subsurface and bulk (i.e. depths below 5 nm). Taking these values as reference, both materials show a local B-site accumulation in the immediate subsurface ( $\approx 2-4$  nm range of depth), reaching values up to  $\approx 0.7$  for LSC and  $\approx 0.9$  for LSF. The observed relative B-cation enrichment in the subsurface is in line with the conclusions made in several studies dealing with Sr-segregation phenomena in LSC-related films<sup>53-55,63</sup>. In the case of LSM, the film shows the B/La+Sr ratio closest to the nominal value of 1, with local deficiency in the surface and immediate subsurface, which progressively increases until reaching values close to 0.9. The observed deficiency in the top 2 nm is in good agreement with the Sr-enrichment observed in section 4.4.2.2. Overall, the differences observed in the B/La+Sr ratio among the three pristine parent materials can be attributed to different target ablation and plasma dynamics during the PLD deposition of the films. The proper transfer of the target stoichiometry into the thin film deposited has been known to be a critical factor in PLD. The presence of cation off-stoichiometries might rise from preferential ablation<sup>64</sup> and background gas interaction effects<sup>65</sup>, which could explain the differences observed for the different materials. Additionally, the presence of surface particles and preferential sputtering effects during the LEIS profiling are likely to result in an underestimation of the B-cation with respect to the regular perovskite stoichiometry.



For this reason, the B/La+Sr analysis performed in this section will be treated as a semi-quantitative discussion with a major focus on the relative evolution of the signal after thermal annealing and for the different samples under study. In the case of the annealed samples, a drastic decrease in the B/La+Sr ratio can be observed for both LSC and LSF. This decrease in the B-cation presence is attributed to the relative loss of signal caused by the large segregation of strontium related species discussed in the previous section. Regarding the annealed LSM, the B/La+Sr signal shows a similar shape than in the as deposited measurement with a slightly more pronounced decay in the top surface. This is most likely due to the rearrangement of the La-O-termination layers mentioned, similarly to the decay observed in the Sr/La+Sr ratio in Figure 4-18.

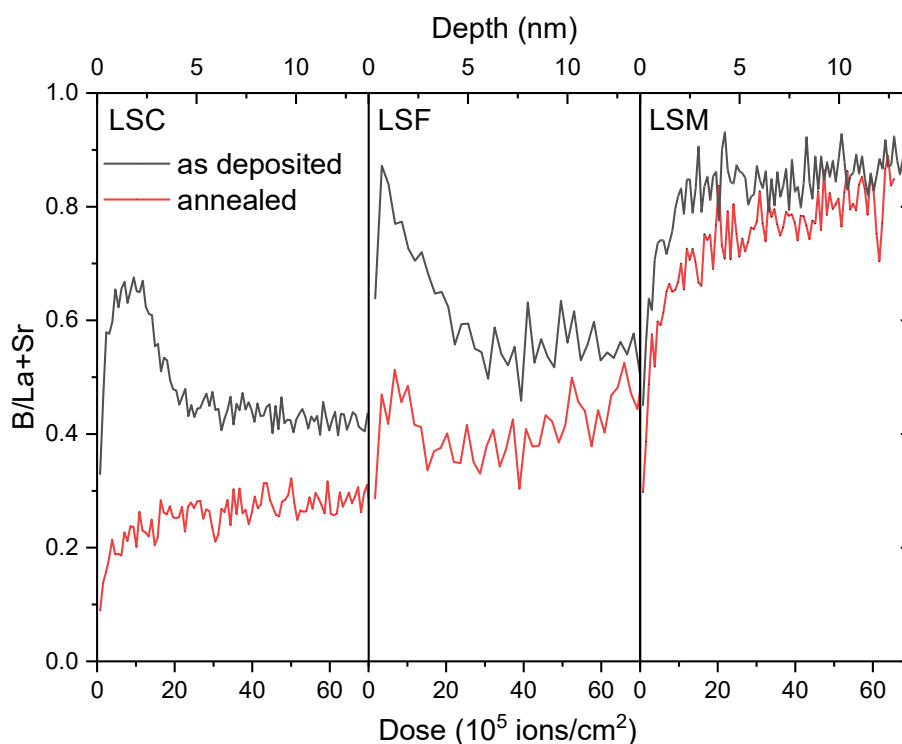


Figure 4-24. LEIS depth profiles of the LSC, LSF and LSM films obtained for the surface and subsurface region showing the B/La+Sr ratio. The dark line corresponds to the film as deposited and the red after the thermal annealing at 800 °C for 100 h.

Additionally, Figure 4-25 shows the collection of B/La+Sr ratios measured by LEIS profiling both as deposited and after performing the thermal annealing. In general terms, the pristine samples all present similar distribution than the observed for the parent materials in Figure 4-24. Most of the films present a B-site enriched region in the 2-4 nm range with respect to the rest of the film, similar to the cases of LSC and LSF. This is less evident for the two films with the highest amount of Mn (i.e. Mn 68 % and Mn 48 %), for which the overall B/La+Sr

ratio is higher than for the other films, presenting less differentiation over the subsurface even though the maximum signal is also found in the 1-2 nm depth region.

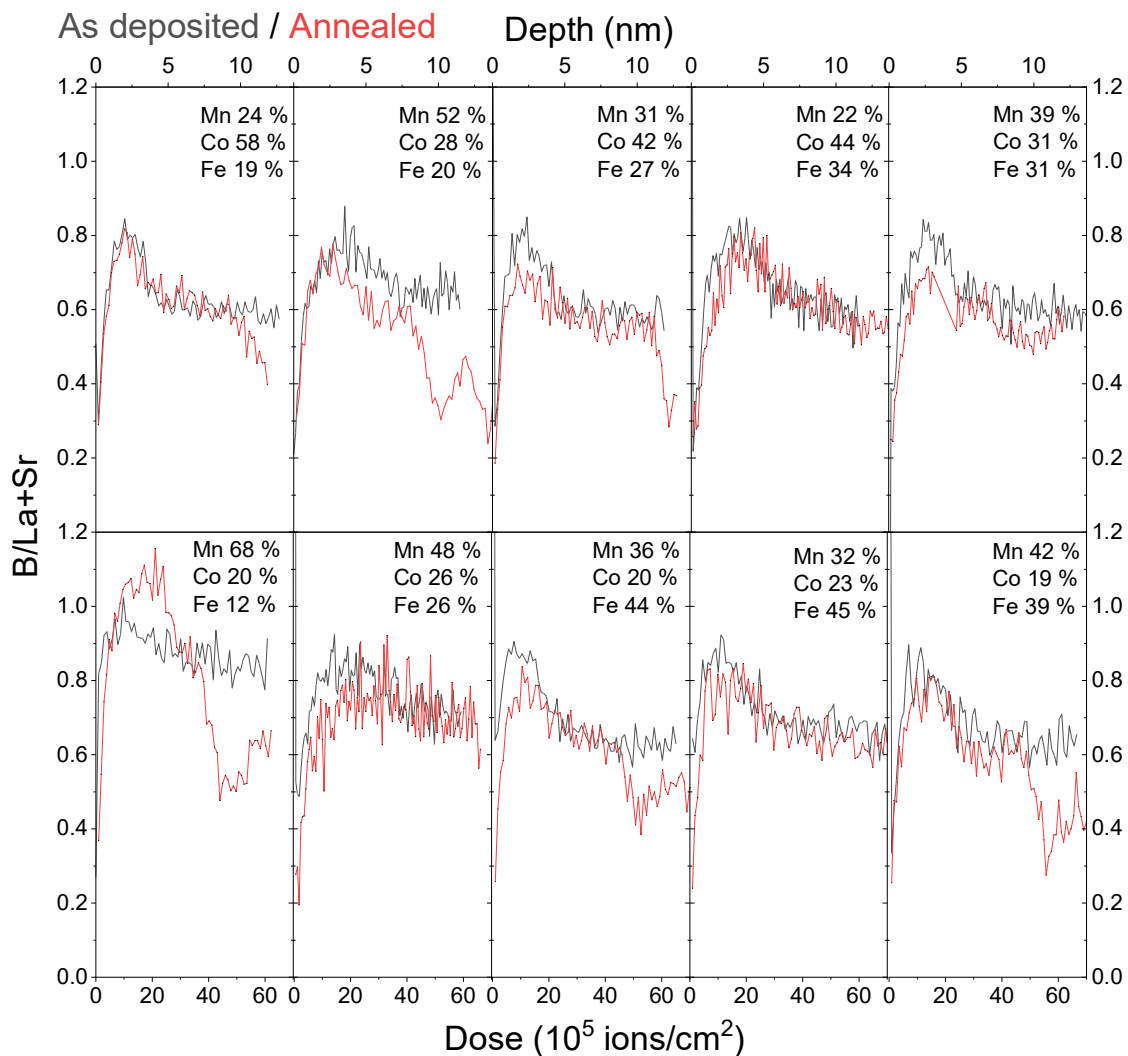


Figure 4-25. LEIS depth profiles of the LSMCF films obtained for the surface and subsurface region showing the B/La+Sr ratio. The dark line corresponds to the film as deposited and the red after the thermal annealing at 800 °C for 100 h.

In the case of the thermally annealed films, the B/La+Sr ratio seems to present similar features than in the as deposited case for the first few nm. Interestingly, there seems to be a local drop when reaching subsurface depth values close to the 10 nm range (e.g. more evident for the cases with Mn at 68 %, 52%, 42 %, 36 % and 31 %). These variations of the B/La+Sr ratio are in contrast to the observations made for the parent materials, which do not present such drops towards the subsurface level. Interestingly, although the B/La+Sr profiles of the LSMCF have resembled more the ones of LSC and LSF in the pristine state, the structural stability facing thermal degradation observed have suggested that the addition of Mn plays a role. Nonetheless, the resulting cation distribution on the surface and

subsurface do not resemble either the one observed for LSM. As an additional remark on the B/La+Sr ratio, Table 4-3 shows the values calculated from EDX analyses of the as deposited samples. This was done in order to gain clarity on the B-site deficiency of the films on the bulk level, and its translation into LEIS profiles. It can be seen that most of the films present B-site deficiency, with values ranging in the 0.81-1.02 range, slightly larger than the values measured by LEIS profiling. This difference results in a reasonable variation given the different characterization techniques employed. Nonetheless, the relative variation in the B/La+Sr ratio among the LSMCF combinatorial films studied present similar evaluation than for the LEIS profiles, showing seemingly higher ratios for Mn-rich compositions and a decrease for the films with low content of Mn.

*Table 4-3. B/La+Sr ratio calculated by EDX for the as deposited combinatorial LSMCF samples studied by LEIS.*

LSMCF sample (B-site composition)	B/La+Sr
Mn <sub>0.24</sub> Co <sub>0.58</sub> Fe <sub>0.19</sub>	0.91
Mn <sub>0.52</sub> Co <sub>0.28</sub> Fe <sub>0.20</sub>	0.81
Mn <sub>0.31</sub> Co <sub>0.42</sub> Fe <sub>0.27</sub>	0.84
Mn <sub>0.22</sub> Co <sub>0.44</sub> Fe <sub>0.34</sub>	0.83
Mn <sub>0.39</sub> Co <sub>0.31</sub> Fe <sub>0.31</sub>	0.84
Mn <sub>0.68</sub> Co <sub>0.20</sub> Fe <sub>0.12</sub>	1.02
Mn <sub>0.48</sub> Co <sub>0.26</sub> Fe <sub>0.26</sub>	0.92
Mn <sub>0.36</sub> Co <sub>0.20</sub> Fe <sub>0.44</sub>	0.92
Mn <sub>0.32</sub> Co <sub>0.23</sub> Fe <sub>0.45</sub>	1.02
Mn <sub>0.42</sub> Co <sub>0.19</sub> Fe <sub>0.39</sub>	0.86

#### 4.4.3.2 Evolution of vacancy-related defects and their correlation with cation

The deeper regions of the films beyond the surface and subsurface were investigated by means of positron annihilation lifetime spectroscopy (PALS) and deeper LEIS depth profiling. Figure 4-26 show the depth profiles obtained by PALS for the collection of combinatorial LSMCF thin films analyzed. In particular, the evolution in depth of two identified defect annihilation lifetimes ( $\tau_i$ ) is represented for each compound, before and after performing the thermal treatment. Lifetime values of reference cation defects are indicated in the dashed horizontal lines, specifically for B-site ( $V_B \approx 0.196$  ns) and A-site vacancies ( $V_A \approx 0.282$  ns)<sup>66</sup>. The reference values have been selected in analogy with previous reports on LaMnO<sub>3</sub>. The lifetime values for A- and B-site defects in other perovskites such SrTiO<sub>3</sub> or BiFeO<sub>3</sub> do not differ substantially. It should be noted that in general terms the lifetime scales with the size of the defect (larger open volumes lead to

longer annihilation times for positrons), hence some minor variability is expected. For that, a general  $V_A$  and  $V_B$  notation is employed for characterizing the defect nature, as it is not possible to identify the chemical nature of the defect further than its position in the lattice (e.g. impossibility to distinguish between Sr and La-related defects, or between Mn,Co and Fe, as well as considering the additional presence of clusters of defects). Regarding the profiles measured, it is evident that the thermal treatment performed provokes a significant alteration on the defect landscape. The as deposited films present in most of the cases values of  $\tau_1$  below the reference for  $V_B$ . This could be attributed to several reasons such as the presence of substitutions, differences towards lower lattice parameter (which could be expected, according to the variation observed in Figure 4-5), relaxation of defects or the presence of dislocation associated with monovacancies<sup>67</sup>. After the thermal treatment  $\tau_1$  increases getting closer to the  $V_B$  reference value, even above it. The larger values of  $\tau_1$  can be attributed to association of the metal vacancy with oxygen vacancies ( $V_O^{\bullet\bullet}$ ), leading to the formation of defect complexes, as proposed for STO<sup>68</sup>. Moreover, the increase in the value of  $\tau_1$  seems to be more concentrated in the subsurface region, up to approximately 20 nm of depth. It should be noted that the Mn-rich composition presents lifetime values above the reference both before and after the thermal treatment. With respect to  $\tau_2$ , all of the films analyzed present values above the reference for  $V_A$ , both in the pristine and the annealed state. This is representative of vacancy agglomerations, or clusters, likely consisting in a mixture of Sr, La, Mn, Co, Fe, Co and oxygen vacancy complexes.

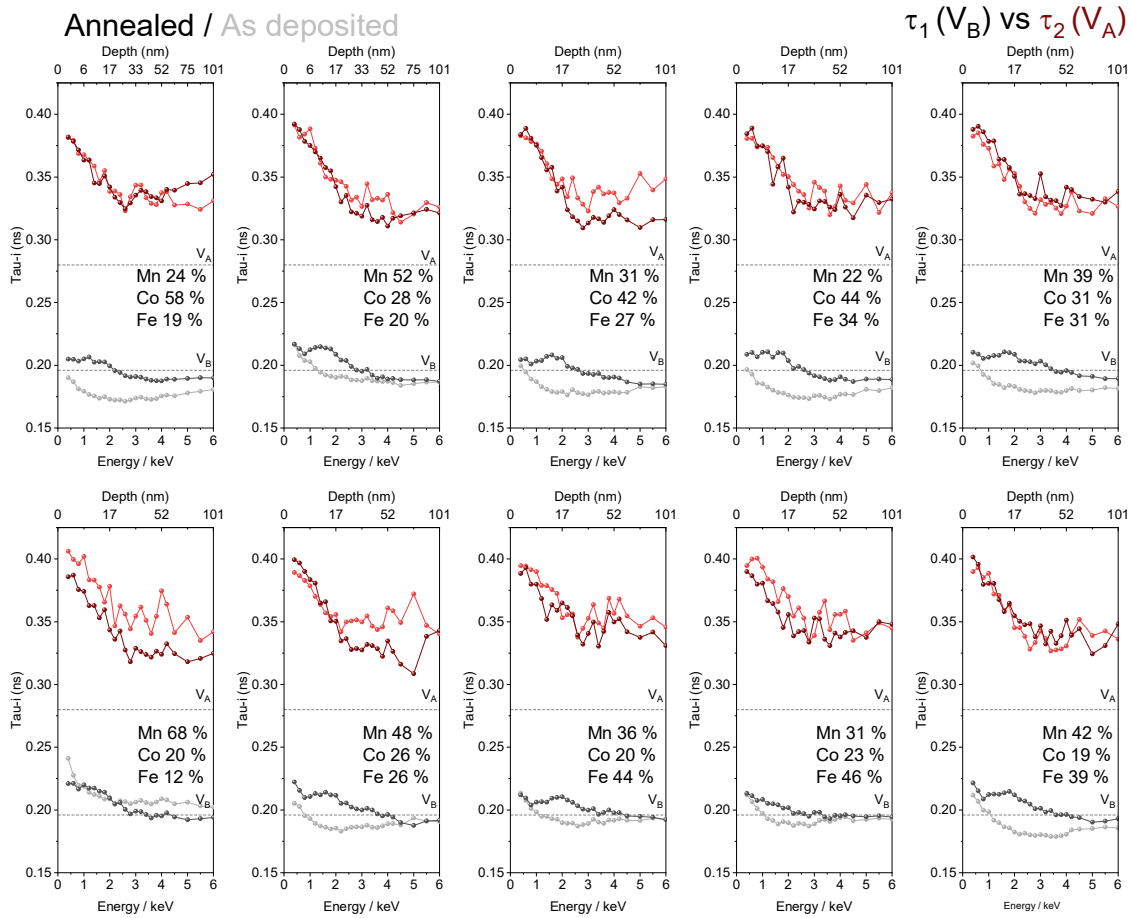


Figure 4-26. PALS profiles of the combinatorial LSMCF thin films with the two time constants,  $\tau_1$  (in grey as deposited and black after thermal annealing) and  $\tau_2$  (in red as deposited and dark red after thermal annealing).

Moreover, Figure 4-27 shows the depth profiles showing the relative intensity of each of the two defect contributions identified. It can be observed that the  $V_B$  vacancies are the majority defect, in comparison to  $V_A$ -associated vacancies. Nonetheless, the thermal treatment provokes the generalized reduction of the relative intensity of  $V_B$  with respect to the pristine state, and the higher presence of the  $V_A$  complexes. This behavior is attributed to the migration of Sr towards the surface, as confirmed by AFM and XPS in the previous section. This is particularly acute for regions beyond the subsurface, i.e. for depths below 15 nm and extended through the film ( $\approx 80$  nm). Most interestingly, these relative changes in the intensity of the annealed defects, despite being clearly more present than in the pristine state (in the case of  $V_A$  complexes), do not show a smooth signal through the film (e.g. in the form of a plateau or a progressive decay). Contrary to that, changes in the defect intensity beyond the subsurface are shown present oscillations, suggesting an inhomogeneous or even layered redistribution in the film after the annealing.

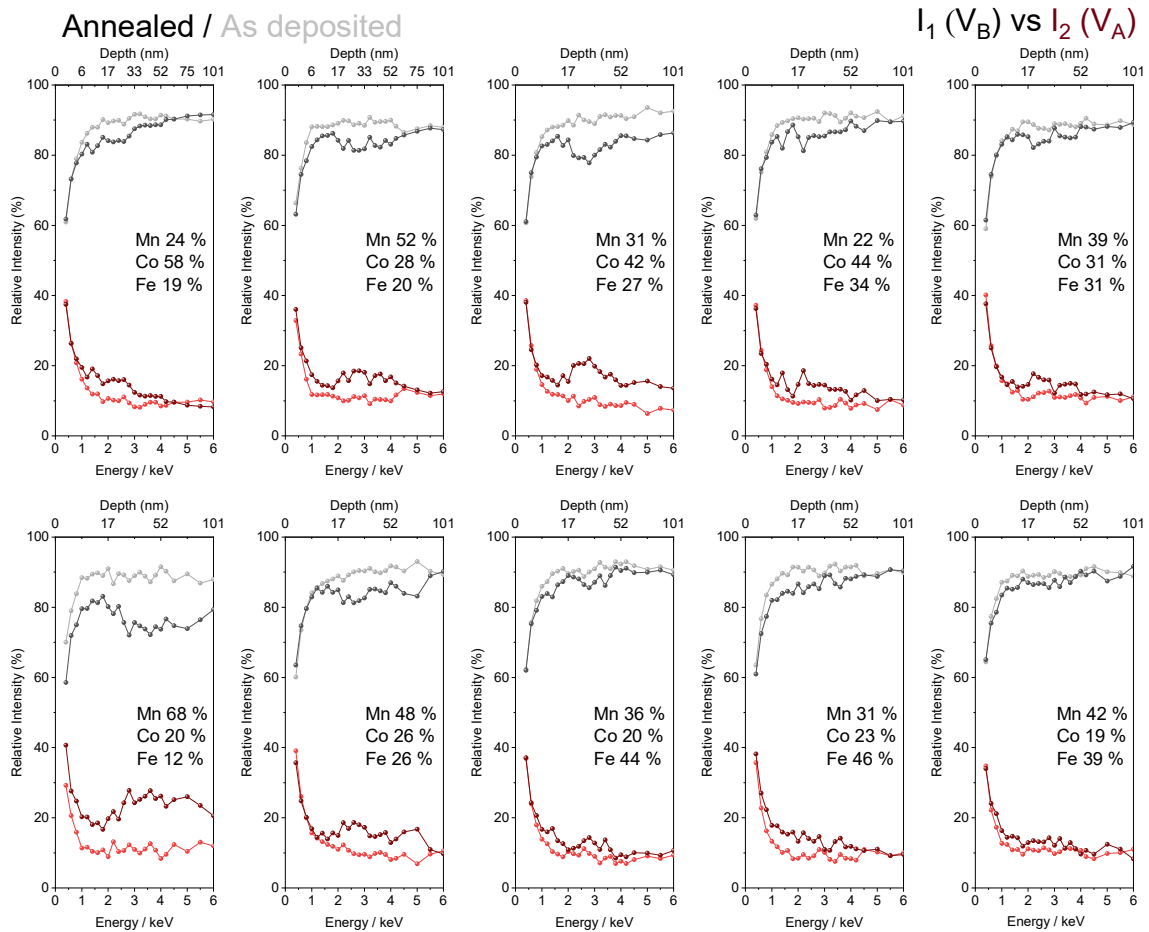


Figure 4-27. PALS profiles of the combinatorial LSMCF thin films with the relative intensity of the two time constants,  $I_1$  (in grey as deposited and black after thermal annealing) and  $I_2$  (in red as deposited and dark red after thermal annealing).

Doppler-Broadening-Variable Energy Positron Annihilation Spectroscopy (DB-VEPAS) was employed in order to gain more insight in the defect density present in the combinatorial LSMCF thin films and caused by the defect evolution just discussed. Broadening occurs during positron annihilation due to the differences in momentum of the positron and the electrons. In general terms, the intensity of the S-parameter is directly related to the presence of vacancy defects, while the W-parameter is determined by the chemical nature surrounding the defect (see Chapter 2 for further details in the technique). S-W plots are then employed to examine atomic surrounding of the defect site and the defect size<sup>69</sup>. This is the case of Figure 4-28, which shows the S-W plot for the collection of pristine and annealed films measured, at a given penetration depth of 27 nm, approximately. Co, Fe and Mn reference metallic samples were also included in the DB-VEPALS analysis. Co and Fe reference samples are considered as defect free, however Mn can present some residual defects or even oxides. The depth selected for the analysis is right in the region where the maximum change in the defect type intensity has been observed, hence is valid for

evaluating the evolution of the films. The defect density of the pristine samples is quite similar since most of the data points agglomerate in a localized position. Nonetheless, a larger data spread is visible for the annealed samples with an overall increase of defect density with respect to the pristine samples. This confirms the evolution of the defect structure of the films after the annealing with respect to the pristine state, indicating a higher presence of defects as a result of the thermal treatment. Additionally, the S-W plot indicates larger decoration (i.e. atomic proximity) of the defect site by Mn in the case of pristine samples. This is reflexed by the line between the data points belonging to the films and the Mn reference. After annealing however, larger Fe and Co decoration is found. Taking into account that the thermal treatment leads to an increase of the  $V_A$ -associated vacancies –as seen by VEPALS results–, this suggests that these defects are more present in positions surrounded by Fe and Co. This is in agreement to the observations made that Co,Fe-rich materials (and in particular LSC/LSF parent materials) lead to higher degradation than in the case of Mn-containing materials.

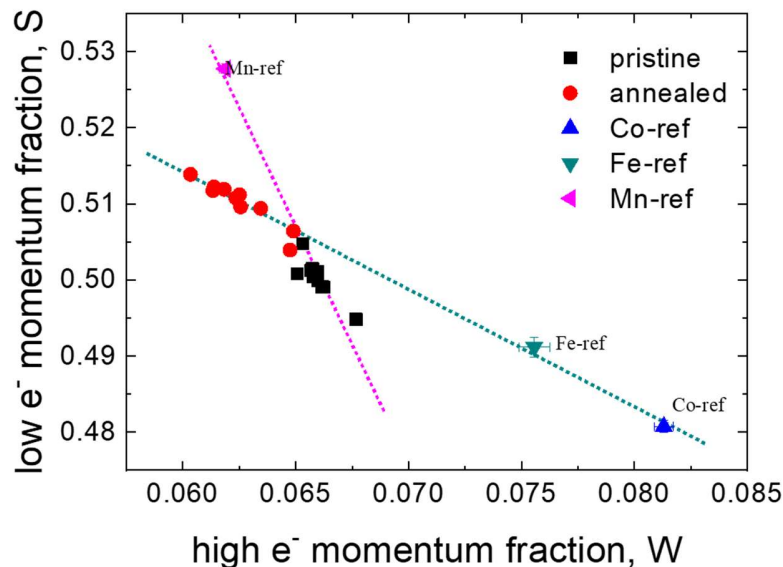


Figure 4-28. S-W plot indicating relative changes of defect decoration for depth (~27 nm) corresponding to  $E_p=2.65$  keV.

With the aim to shed light on the defect evolution observed and the compensation mechanisms triggered by Sr segregation, deeper LEIS analysis ( $\approx 40$  nm) was performed for a selection of compounds, reaching the region beyond the surface and subsurface discussed previously. The obtained profiles along with the PALS measurements collected for the same materials after the thermal treatment are shown in Figure 4-29. The LEIS profiles represented in panels (a,c) show the presence of oscillations in the cation detection, visualized as stiff valley-like drops of the B/La+Sr and Sr/La+Sr ratios. The decrease in both signals indicates the presence of La-enrichment in these regions. Most interestingly, the variations in the cation signals can be associated into the variations observed in the depth

profiles obtained by PALS. In particular, the intensity plots in panel (b,d) follow a similar trend as the variation in the cation signal observed in the LEIS profiles of panels (a,c). In this sense, the regions in which the B/La+Sr ratio presents a major decrease in the LEIS profiles can be correlated to the variation of  $I_1$  in the PALS profiles, suggesting higher presence of  $V_B$  vacancies –i.e. a variation of the B/La+Sr can be associated with a variation in the  $V_B$  intensity–. Similarly, the drop in this region of the relative presence of  $V_A$  can be correlated not only to the increase of  $V_B$  vacancies but also to the increase of the La content. This is also suggested by the decrease in the Sr-signal in the LEIS profile. Similarly, the regions in which the perovskite recovers the B/La+Sr and Sr/La+Sr stoichiometry can be related to the lowering of the  $I_1$  intensity.

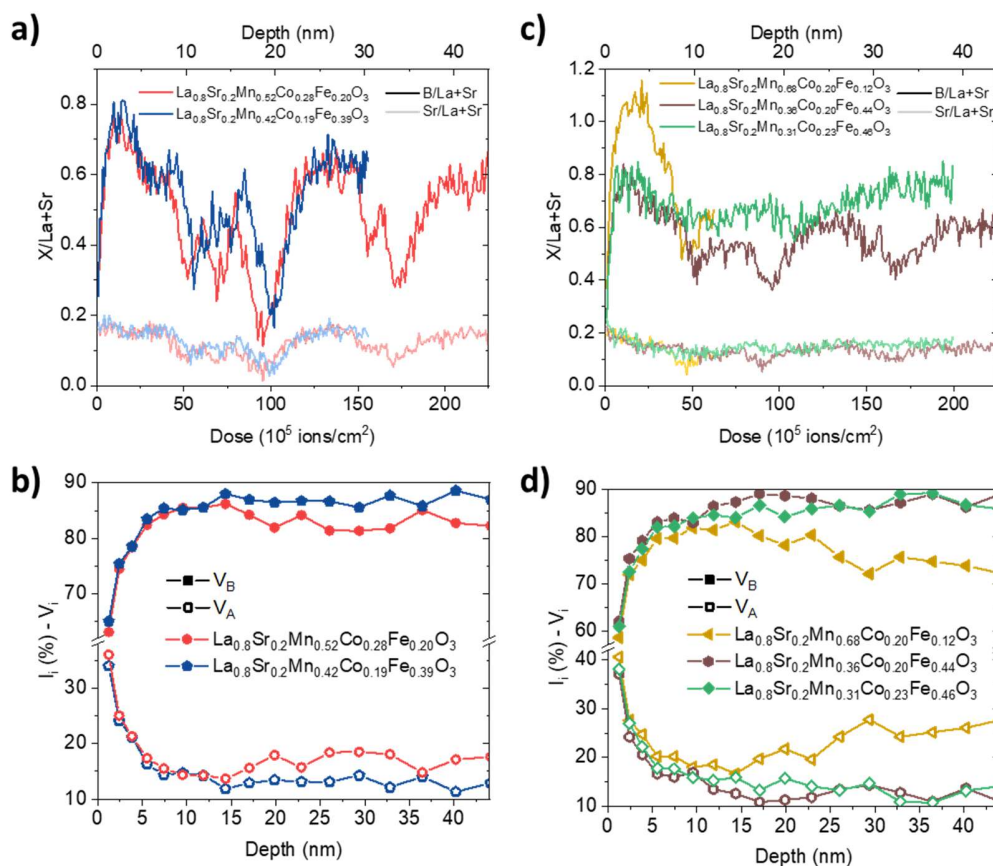


Figure 4-29. Characterization of the cations and defects present in the bulk level for a selection of combinatorial films after thermal degradation. LEIS depth profiles measured for 40 nm of depth (a-b), PALS profiles showing the evolution of the defect relative intensities (c) and characteristic times (d).

There are different possibilities that may lead to this scenario. One likely scenario could be relating the oscillations in the cation ratios (i.e. decrease of B and Sr, and increase of La) to local formation of the  $A_2BO_4$  perovskite structure. Thermal decomposition of single perovskites into Ruddlesden-Popper (RP) structure has been observed in the past for LSM



at high temperature ( $>900\text{ }^{\circ}\text{C}$ )<sup>8</sup> and suggested for LSCF<sup>13</sup>. In the latter work, Oh et al. observed similar cation rearrangement in the subsurface of the LSCF material, right below the presence of Sr precipitates. It is unclear if the local changes in the cation arrangement observed in this work -likely inducing changes in the crystallographic structure- are responsible for the stabilization effect observed in the appearance of segregated strontium species. Independent works by Sase et al.<sup>70</sup> and Crumlin et al.<sup>71</sup> observed enhancement of the electrochemical performance of LSC films decorated with top layers of LSC<sub>214</sub> (i.e. LaSrCoO<sub>4</sub> RP structure), while more recently Lee et al. observed minimization of Sr particle segregation for the same types of heterostructures<sup>72</sup>. Despite these examples, formation of the RP structure cannot be confirmed only by LEIS analysis. Additionally, the possibility of keeping the single perovskite structure while presenting highly off-stoichiometric localized regions should also be considered.

In order to gain clarity on the differences between the annealed LSMCF films and the single parent materials along the whole film, deeper LEIS profiles of LSC, LSM and LSF after the thermal treatment were measured, as shown in Figure 4-30. Contrary to the observations made in Figure 4-18 (limited to the top 10 nm), which showed drastic levels of Sr-enrichment for LSF and LSC far above the stoichiometric value, the deeper profiles in Figure 4-30 show that the nominal stoichiometry level is eventually recovered. Both LSC and LSF materials reach the reference Sr content (i.e. the value observed for LSM) at depths in the 20-25 nm range, going even below this value in deeper regions. The Sr-deficiency in the bulk is then attributed to the migration of Sr cations towards the surface during the thermal treatment process. Complementary, both materials show a gradual increase of the B/La+Sr ratio, sign of recovery of the as deposited perovskite stoichiometry (see Figure 4-24).

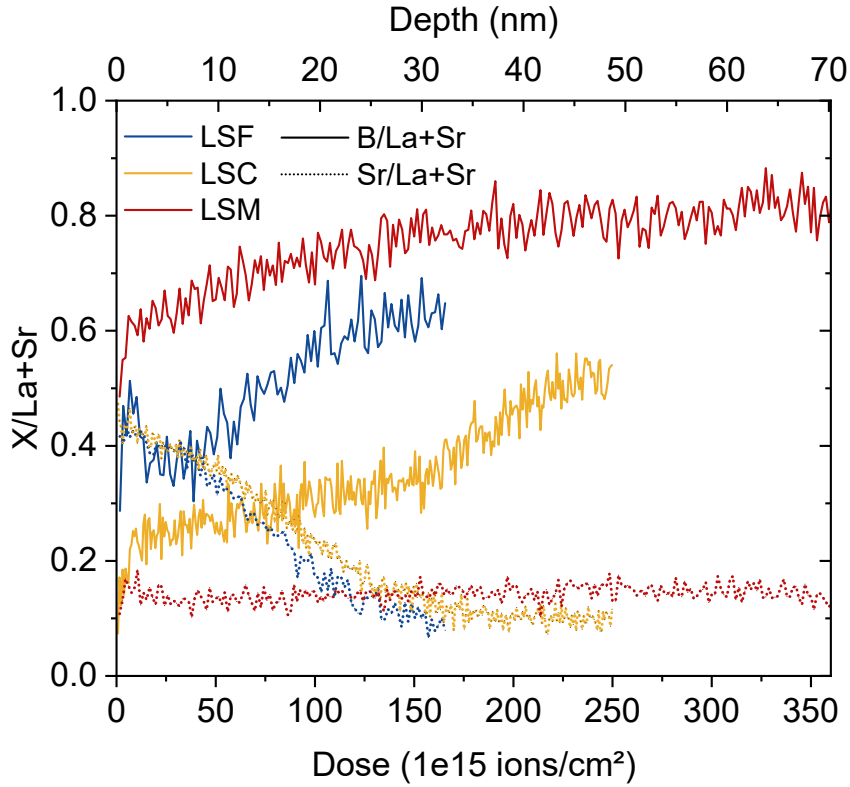


Figure 4-30. LEIS profiles obtained for the annealed parent materials with depths up to 70 nm.

It is relevant that none of the parent materials show the oscillating features observed for the annealed LSMCF thin films. From the studies performed in this work it can be confirmed that Mn addition to LSCF rich perovskites results in higher resistance to dopant segregation. Additionally, local changes in the chemical nature of the films resulting in severe off-stoichiometric regions for depths beyond the subsurface have been observed. It has been discussed that this kind of behavior has been observed in other perovskite electrodes based on LSCF<sup>13</sup> and it could be attributed to the appearance of RP-like phases presenting the structure  $A_2BO_4$ . Nonetheless, confirmation of this phenomenon would require of direct visualization of the crystallographic structure by HRTEM and obtaining localized compositional information by EDX. The resulting disorder is suspected to play a role in hindering the continuous migration of Sr towards the surface of LSMCF co-doped materials.

## 4.5 Guidelines for the selection of a thin film LSMCF compound

The  $\text{La}_{0.8}\text{Sr}_{0.2}\text{Mn}_x\text{Co}_y\text{Fe}_{1-x-y}\text{O}_3$  perovskite family has been proven to present a series of a large variety of structural and functional properties that makes the system suitable for application as SOC electrodes. Regarding the structural properties, all of the representative compounds studied present good compatibility between the B-cations present, showing polycrystalline growth of the perovskite phase. Hence, the selection of a proper LSMCF compound (or compounds) will be determined by the functional properties related to i) the oxygen transport kinetics, ii) the electrochemical activity for the oxygen reduction reaction and iii) the performance evolution upon thermal degradation.

Regarding the oxygen mass transport properties, the results obtained by IEDP-SIMS at 400 °C reveal high kinetic activity along the region Co- and Fe-rich regions, and for values of Mn content below 0.2. For the regions closer to either Co or Fe, values of the  $k^* \cdot D^*$  product as high as  $4 \times 10^{-3} \text{ cm}^3/\text{s}^2$  can be found, indicative of high oxygen electrochemical activity and the maximum found for the LSMCF system. The lower and upper bounds for the relative B-cation content in order to maximize the oxygen kinetics would be as follows: [0-0.2] of Mn, [0-0.2] or [0.7 – 0.8] of Co and [0-0.2] or [0.7 – 0.8] of Fe.

The electrochemical activity measurement by EIS for the LSMCF library resulted in the characterization of activation energies with promising values in the range of 1.1-1.5 eV. This behavior was observed for a large variety of compounds, concentrated in the region delimited by [0.12 – 0.7] of Mn, [0 – 0.5] of Co and [0.12 – 0.75] of Fe. Additionally, the lowest values for the ASR were mostly found in the concentrated area above 0.5 of Fe content and below 0.25 of both Co and Mn content. According to these two conditions, LSMCF compounds with Fe over 0.5 and Co, Mn contents below 0.25 present the most promising performance.

The studies performed on the evolution of the LSMCF thin films facing thermal degradation unveiled the favorable properties of the intermixed LSMCF thin films with respect to single LSC and LSF. Studies performed on the evolution of the electrochemical activity over time showed an increase of 20 % on the ASR after 100 h of experiment for a  $\text{La}_{0.8}\text{Sr}_{0.2}\text{Mn}_{0.1}\text{Co}_{0.17}\text{Fe}_{0.73}\text{O}_3$  and a decrease of 5 % on the final ASR for a LSMCF with composition  $\text{La}_{0.8}\text{Sr}_{0.2}\text{Mn}_{0.42}\text{Co}_{0.31}\text{Fe}_{0.27}\text{O}_3$ . Structural and chemical characterization of degraded LSMCF materials showed a generalized resistance to segregation and surface microstructure evolution is observed for all of the LSMCF thin films. In terms of the enrichment calculated by XPS for Sr surface species, all of the films present lower values than LSC and LSF, which show drastic enrichment of  $\text{SrSO}_4$  related species. On the perspective of Sr-segregation and evolution of the electrochemical performance an intermixed composition of [0.25 – 0.7] of Mn, [0.25 – 0.6] of Co and [0.12 – 0.4] of Fe is recommended.

Balancing all the conclusions derived from this study, the region with [0.1 – 0.2] of Mn, [0.1 – 0.35] of Co and [0.5 – 0.8] of Fe is selected as the most promising region in the system. In particular, a hypothetical  $\text{La}_{0.8}\text{Sr}_{0.2}\text{Mn}_{0.15}\text{Co}_{0.35}\text{Fe}_{0.5}\text{O}_3$  compound and further degradation experiments in the Fe-rich (> 50 %) region would be interesting subjects of study.

## 4.6 Conclusions

This chapter has presented an extensive research study on the structural and functional properties of the  $\text{La}_{0.8}\text{Sr}_{0.2}\text{Mn}_x\text{Co}_y\text{Fe}_{1-x-y}\text{O}_3$  library of oxygen electrode materials for SOC application. A set of samples deposited by combinatorial PLD was studied in terms of composition distribution, structural and optical properties, electrochemical activity and oxygen transport kinetics, and behavior on thermal degradation. First, high throughput methodologies were employed for characterizing the films deposited. A complete analysis of the distribution of Mn, Co and Fe along the samples was achieved by high throughput XRF. Similarly, automatized measurements by XRD and spectroscopic ellipsometry in lab-scale facilities allowed to obtain full maps of the evolution of the lattice parameter and the optical properties along the LSMCF film. Regarding the study of the functional properties of the perovskite library, high-throughput IEDP-SIMS allowed to characterize the oxygen mass transport kinetic parameters, i.e. surface exchange and diffusivity coefficients, for several hundreds of compositions. The results obtained unveiled the promising properties of the thin film cathode library, particularly for increased Fe- and Co- rich regions, with values surpassing the activity of similar-composition conventional electrodes. The evolution of the electrochemical performance and its dependence on temperature was analyzed by EIS mapping in an automatized high temperature chamber. The experiments performed allowed for the mapping of the activation energy, pre-exponential factor and area specific resistance of a set of LSMCF compounds. A particularly promising low activation energy was observed in several of the intermixed compounds studied.

The second goal of the work discussed in this chapter was focused on the performance and evolution of the LSMCF thin films facing thermal degradation. For that, different characterization techniques and analyses were performed on a selection of pristine and annealed LSMCF thin films. Particular focus was given to the systematic study of the dopant segregation phenomena for this family of perovskites. For that, LEIS surface and depth profiling analyses were employed in order to account for the rearrangement of the LSMCF cations along the surface and subsurface regions. XPS spectroscopy was also utilized for the chemical characterization of the surface species involved in the surface evolution. The appearance of segregated phases was visualized by AFM. Thin film bulk reconstruction was performed by deeper LEIS profiling and characterization of the defects present through the film was achieved by positron annihilation spectroscopy. The results unveiled the promising performance of the highly intermixed LSMCF cathode materials with respect to the parent materials LSC, LSF and LSM. In particular, the LSMCF compounds showed apparent stabilization on segregation with reduced degradation evolution. This effect reflected a drastic difference when compared to single LSC and LSF materials, which showed a dramatic increase on the presence of strontium segregated species in the surface. Specifically, sulfate species were found to be the ones increasing the most their relative presence after thermal degradation. Local changes in the perovskite structure with presence

of off-stoichiometric regions were observed for the co-doped films. A brief discussion on the matter and its possible relation with the stabilization effect observed is offered. These findings were cross checked by tracking the evolution of the electrochemical performance by impedance spectroscopy of the parent materials reference electrodes and two examples of intermixed LSMCF compound. The slowest degradation rate was found for the intermixed LSMCF with high Fe-content while the more intermixed LSMCF sample even showed enhancement over the degradation experiment. This confirmed the promising properties of co-doped perovskites towards degradation phenomena in SOCs. In the final section of the chapter the overall effects of the functional properties characterized have been balanced in order to choose a region of interest on the LSMCF library as electrode compounds with promising performance for application in SOCs.

## References

- (1) Fleig, J.; Kim, H. R.; Jamnik, J.; Maier, J. Oxygen Reduction Kinetics of Lanthanum Manganite (LSM) Model Cathodes: Partial Pressure Dependence and Rate-Limiting Steps. *Fuel Cells* **2008**, *8* (5), 330–337. <https://doi.org/10.1002/fuce.200800025>.
- (2) Schmid, A.; Nenning, A.; Opitz, A.; Kubicek, M.; Fleig, J. High Oxygen Exchange Activity of Pristine  $\text{La}_{0.6}\text{Sr}_{0.4}\text{FeO}_{3-\delta}$  Films and Its Degradation. *J. Electrochem. Soc.* **2020**, *167* (12), 124509. <https://doi.org/10.1149/1945-7111/abac2b>.
- (3) la O', G. J.; Ahn, S.-J.; Crumlin, E.; Orikasa, Y.; Biegalski, M. D.; Christen, H. M.; Shao-Horn, Y. Catalytic Activity Enhancement for Oxygen Reduction on Epitaxial Perovskite Thin Films for Solid-Oxide Fuel Cells. *Angew. Chem. Int. Ed.* **2010**, *49* (31), 5344–5347. <https://doi.org/10.1002/anie.201001922>.
- (4) Rossiny, J.; Fearn, S.; Kilner, J. A. A.; Zhang, Y.; Chen, L.; Yang, S.; Evans, J. R.; Zhang, T.; Yates, K.; Cohen, L. F. Characterisation of Combinatorial Libraries of Perovskite Materials for SOFC Cathode Applications. *ECS Trans.* **2007**, *7* (1), 1005–1013. <https://doi.org/10.1149/1.2729196>.
- (5) Saranya, A. M.; Morata, A.; Pla, D.; Burriel, M.; Chiabrera, F.; Garbayo, I.; Hornés, A.; Kilner, J. A.; Tarancón, A. Unveiling the Outstanding Oxygen Mass Transport Properties of Mn-Rich Perovskites in Grain Boundary-Dominated  $\text{La}_{0.8}\text{Sr}_{0.2}(\text{Mn}_{1-x}\text{Co}_x)_{0.85}\text{O}_{3\pm\delta}$  Nanostructures. *Chem. Mater.* **2018**, *30* (16), 5621–5629. <https://doi.org/10.1021/acs.chemmater.8b01771>.
- (6) Benson, S. J.; Waller, D.; Kilner, J. A. Degradation of  $\text{La}_{0.6}\text{Sr}_{0.4}\text{Fe}_{0.8}\text{Co}_{0.2}\text{O}_{3-\delta}$  in Carbon Dioxide and Water Atmospheres. *J. Electrochem. Soc.* **1999**, *146*, 1305. <https://doi.org/10.1149/1.1391762>.
- (7) Celikbilek, O.; Thieu, C.-A.; Agnese, F.; Cali, E.; Lenser, C.; Menzler, N. H.; Son, J.-W.; Skinner, S. J.; Djurado, E. Enhanced Catalytic Activity of Nanostructured, A-Site Deficient  $(\text{La}_{0.7}\text{Sr}_{0.3})_{0.95}(\text{Co}_{0.2}\text{Fe}_{0.8})\text{O}_{3-\delta}$  for SOFC Cathodes. *J. Mater. Chem. A* **2019**, *7* (43), 25102–25111. <https://doi.org/10.1039/C9TA07697B>.
- (8) Mizusaki, J. Nonstoichiometry and Thermochemical Stability of the Perovskite-Type  $\text{La}_{1-x}\text{Sr}_x\text{MnO}_{3-\delta}$ . *Solid State Ion.* **1991**, *49*, 111–118. [https://doi.org/10.1016/0167-2738\(91\)90076-N](https://doi.org/10.1016/0167-2738(91)90076-N).
- (9) Anderson, H. Review of P-Type Doped Perovskite Materials for SOFC and Other Applications. *Solid State Ion.* **1992**, *52* (1–3), 33–41. [https://doi.org/10.1016/0167-2738\(92\)90089-8](https://doi.org/10.1016/0167-2738(92)90089-8).
- (10) Dulli, H.; Dowben, P. A.; Liou, S.-H.; Plummer, E. W. Surface Segregation and Restructuring of Colossal-Magneto-resistant Manganese Perovskites  $\text{La}_{0.65}\text{Sr}_{0.35}\text{MnO}_3$ . *Phys. Rev. B* **2000**, *62* (22), R14629–R14632. <https://doi.org/10.1103/PhysRevB.62.R14629>.
- (11) Kubicek, M.; Limbeck, A.; Frömling, T.; Hutter, H.; Fleig, J. Relationship between Cation Segregation and the Electrochemical Oxygen Reduction Kinetics of  $\text{La}_{0.6}\text{Sr}_{0.4}\text{CoO}_{3-\delta}$  Thin Film Electrodes. *J. Electrochem. Soc.* **2011**, *158* (6), B727–B734. <https://doi.org/10.1149/1.3581114>.
- (12) Huber, A.-K.; Falk, M.; Rohnke, M.; Luerssen, B.; Amati, M.; Gregoratti, L.; Hesse, D.; Janek, J. In Situ Study of Activation and De-Activation of LSM Fuel Cell Cathodes –

- Electrochemistry and Surface Analysis of Thin-Film Electrodes. *J. Catal.* **2012**, *294*, 79–88. <https://doi.org/10.1016/j.jcat.2012.07.010>.
- (13) Oh, D.; Gostovic, D.; Wachsmann, E. D. Mechanism of  $\text{La}_{0.6}\text{Sr}_{0.4}\text{Co}_{0.2}\text{Fe}_{0.8}\text{O}_3$  Cathode Degradation. *J. Mater. Res.* **2012**, *27* (15), 1992–1999. <https://doi.org/10.1557/jmr.2012.222>.
- (14) Niania, M.; Podor, R.; Britton, T. B.; Li, C.; Cooper, S. J.; Svetkov, N.; Skinner, S.; Kilner, J. In Situ Study of Strontium Segregation in  $\text{La}_{0.6}\text{Sr}_{0.4}\text{Co}_{0.2}\text{Fe}_{0.8}\text{O}_{3-\delta}$  in Ambient Atmospheres Using High-Temperature Environmental Scanning Electron Microscopy. *J. Mater. Chem. A* **2018**, *6* (29), 14120–14135. <https://doi.org/10.1039/C8TA01341A>.
- (15) Ojeda-G-P, A.; Döbeli, M.; Lippert, T. Influence of Plume Properties on Thin Film Composition in Pulsed Laser Deposition. *Adv. Mater. Interfaces* **2018**, *5* (18), 1701062. <https://doi.org/10.1002/admi.201701062>.
- (16) Chiabrera, F.; Morata, A.; Pacios, M.; Tarancón, A. Insights into the Enhancement of Oxygen Mass Transport Properties of Strontium-Doped Lanthanum Manganite Interface-Dominated Thin Films. *Solid State Ion.* **2017**, *299*, 70–77. <https://doi.org/10.1016/j.ssi.2016.08.009>.
- (17) Tsvetkov, N.; Lu, Q.; Yildiz, B. Improved Electrochemical Stability at the Surface of  $\text{La}_{0.8}\text{Sr}_{0.2}\text{CoO}_3$  Achieved by Surface Chemical Modification. *Faraday Discuss.* **2015**, *182*, 257–269. <https://doi.org/10.1039/C5FD00023H>.
- (18) Chiabrera, F.; Garbayo, I.; López-Conesa, L.; Martín, G.; Ruiz-Caridad, A.; Walls, M.; Ruiz-González, L.; Kordatos, A.; Núñez, M.; Morata, A.; Estradé, S.; Chronos, A.; Peiró, F.; Tarancón, A. Engineering Transport in Manganites by Tuning Local Nonstoichiometry in Grain Boundaries. *Adv. Mater.* **2019**, *31* (4), 1805360. <https://doi.org/10.1002/adma.201805360>.
- (19) Yashima, M.; Takizawa, T. Atomic Displacement Parameters of Ceria Doped with Rare-Earth Oxide  $\text{Ce}_{0.8}\text{R}_{0.2}\text{O}_{1.9}$  (R = La, Nd, Sm, Gd, Y, and Yb) and Correlation with Oxide-Ion Conductivity. *J. Phys. Chem. C* **2010**, *114* (5), 2385–2392. <https://doi.org/10.1021/jp910925t>.
- (20) Kubicek, M.; Rupp, G. M.; Huber, S.; Penn, A.; Opitz, A. K.; Bernardi, J.; Stöger-Pollach, M.; Hutter, H.; Fleig, J. Cation Diffusion in  $\text{La}_{0.6}\text{Sr}_{0.4}\text{CoO}_{3-\delta}$  below 800 °C and Its Relevance for Sr Segregation. *Phys. Chem. Chem. Phys.* **2014**, *16* (6), 2715. <https://doi.org/10.1039/c3cp51906f>.
- (21) Cai, Z.; Kuru, Y.; Han, J. W.; Chen, Y.; Yildiz, B. Surface Electronic Structure Transitions at High Temperature on Perovskite Oxides: The Case of Strained  $\text{La}_{0.8}\text{Sr}_{0.2}\text{CoO}_3$  Thin Films. *J. Am. Chem. Soc.* **2011**, *133* (44), 17696–17704. <https://doi.org/10.1021/ja2059445>.
- (22) Navickas, E.; Huber, T. M.; Chen, Y.; Hetaba, W.; Holzlechner, G.; Rupp, G.; Stöger-Pollach, M.; Friedbacher, G.; Hutter, H.; Yildiz, B.; Fleig, J. Fast Oxygen Exchange and Diffusion Kinetics of Grain Boundaries in Sr-Doped  $\text{LaMnO}_3$  Thin Films. *Phys. Chem. Chem. Phys.* **2015**, *17* (12), 7659–7669. <https://doi.org/10.1039/C4CP05421K>.
- (23) Chiabrera, F.; Garbayo, I.; Pla, D.; Burriel, M.; Wilhelm, F.; Rogalev, A.; Núñez, M.; Morata, A.; Tarancón, A. Unraveling Bulk and Grain Boundary Electrical Properties in  $\text{La}_{0.8}\text{Sr}_{0.2}\text{Mn}_{1-y}\text{O}_{3\pm\delta}$  Thin Films. *APL Mater.* **2019**, *7* (1), 013205. <https://doi.org/10.1063/1.5054576>.



- (24) Tang, Y.; Chiabrera, F.; Morata, A.; Garbayo, I.; Alayo, N.; Tarancón, A. Pushing the Study of Point Defects in Thin Film Ferrites to Low Temperatures Using In Situ Ellipsometry. *Adv. Mater. Interfaces* **2021**, *8*, 2001881. <https://doi.org/10.1002/admi.202001881>.
- (25) Scafetta, M. D.; Xie, Y. J.; Torres, M.; Spanier, J. E.; May, S. J. Optical Absorption in Epitaxial  $\text{La}_{1-x}\text{Sr}_x\text{FeO}_3$  Thin Films. *Appl. Phys. Lett.* **2013**, *102* (8), 081904. <https://doi.org/10.1063/1.4794145>.
- (26) Al-Shakarchi, E. K.; Mahmood, N. B. Three Techniques Used to Produce  $\text{BaTiO}_3$  Fine Powder. *J. Mod. Phys.* **2011**, *02* (11), 1420–1428. <https://doi.org/10.4236/jmp.2011.211175>.
- (27) Artini, C.; Pani, M.; Carnasciali, M. M.; Buscaglia, M. T.; Plaisier, J. R.; Costa, G. A. Structural Features of Sm- and Gd-Doped Ceria Studied by Synchrotron X-Ray Diffraction and  $\mu$ -Raman Spectroscopy. *Inorg. Chem.* **2015**, *54* (8), 4126–4137. <https://doi.org/10.1021/acs.inorgchem.5b00395>.
- (28) Lamas, D. G.; Walsöe De Reca, N. E. X-Ray Diffraction Study of Compositionally Homogeneous, Nanocrystalline Ytria-Doped Zirconia Powders. *J. Mater. Sci.* **2000**, *35* (22), 5563–5567. <https://doi.org/10.1023/A:1004896727413>.
- (29) Minh, N. V. Raman Scattering Study of Perovskite Manganites. *J. Phys. Conf. Ser.* **2009**, *187*, 012011. <https://doi.org/10.1088/1742-6596/187/1/012011>.
- (30) Souza Filho, A. G.; Faria, J. L. B.; Guedes, I.; Sasaki, J. M.; Freire, P. T. C.; Freire, V. N.; Mendes Filho, J.; Xavier, M. M.; Cabral, F. A. O.; de Araújo, J. H.; da Costa, J. A. P. Evidence of Magnetic Polaronic States in  $\text{La}_{0.70}\text{Sr}_{0.30}\text{Mn}_{1-x}\text{Fe}_x\text{O}_3$  Manganites. *Phys. Rev. B* **2003**, *67* (5), 052405. <https://doi.org/10.1103/PhysRevB.67.052405>.
- (31) Nomerovannaya, L. V.; Makhnev, A. A.; Romyantsev, A. Y. Evolution of the Optical Properties of Single-Crystal  $\text{La}_{1-x}\text{Sr}_x\text{MnO}_3$ . *Phys. Solid State* **1999**, *41* (8), 1322–1326. <https://doi.org/10.1134/1.1130991>.
- (32) Sha, Z.; Cali, E.; Shen, Z.; Ware, E.; Kerherve, G.; Skinner, S. J. Significantly Enhanced Oxygen Transport Properties in Mixed Conducting Perovskite Oxides under Humid Reducing Environments. *Chem. Mater.* **2021**, *33* (21), 8469–8476. <https://doi.org/10.1021/acs.chemmater.1c02909>.
- (33) Baiutti, F.; Chiabrera, F.; Diercks, D.; Cavallaro, A.; Yedra, L.; López-Conesa, L.; Estradé, S.; Peiró, F.; Morata, A.; Aguadero, A.; Tarancón, A. Direct Measurement of Oxygen Mass Transport at the Nanoscale. *Adv. Mater.* **2021**, *33* (48), 2105622. <https://doi.org/10.1002/adma.202105622>.
- (34) Navickas, E.; Chen, Y.; Lu, Q.; Wallisch, W.; Huber, T. M.; Bernardi, J.; Stöger-Pollach, M.; Friedbacher, G.; Hutter, H.; Yildiz, B.; Fleig, J. Dislocations Accelerate Oxygen Ion Diffusion in  $\text{La}_{0.8}\text{Sr}_{0.2}\text{MnO}_3$  Epitaxial Thin Films. *ACS Nano* **2017**, *11* (11), 11475–11487. <https://doi.org/10.1021/acsnano.7b06228>.
- (35) Chiabrera, F. M.; Baiutti, F.; Börgers, J. M.; Harrington, G. F.; Yedra, L.; Liedke, M. O.; Kler, J.; Nandi, P.; Sirvent, J. de D.; Santiso, J.; López-Haro, M.; Calvino, J. J.; Estradé, S.; Butterling, M.; Wagner, A.; Peiró, F.; De Souza, R. A.; Tarancón, A. The Impact of Mn Nonstoichiometry on the Oxygen Mass Transport Properties of  $\text{La}_{0.8}\text{Sr}_{0.2}\text{Mn}_y\text{O}_{3+\delta}$  Thin Films. *J. Phys. Energy* **2022**, *4* (4), 044011. <https://doi.org/10.1088/2515-7655/ac98df>.
- (36) Crank, J. *The Mathematics of Diffusion*, 2nd ed.; Clarendon Press: Oxford, 1975.

- (37) Deng, H.; Zhou, M.; Abeles, B. Diffusion-Reaction in Mixed Ionic-Electronic Solid Oxide Membranes with Porous Electrodes. *Solid State Ion.* **1994**, *74* (1–2), 75–84. [https://doi.org/10.1016/0167-2738\(94\)90439-1](https://doi.org/10.1016/0167-2738(94)90439-1).
- (38) Adler, S. B.; Lane, J. A.; Steele, B. C. H. Electrode Kinetics of Porous Mixed-Conducting Oxygen Electrodes. *J. Electrochem. Soc.* **1996**, *143* (11), 3554–3564. <https://doi.org/10.1149/1.1837252>.
- (39) Kilner, J. Surface Exchange of Oxygen in Mixed Conducting Perovskite Oxides. *Solid State Ion.* **1996**, *86–88*, 703–709. [https://doi.org/10.1016/0167-2738\(96\)00153-1](https://doi.org/10.1016/0167-2738(96)00153-1).
- (40) De Souza, R. A.; Kilner, J. A. Oxygen Transport in  $\text{La}_{1-x}\text{Sr}_x\text{Mn}_{1-y}\text{Co}_y\text{O}_{3\pm\delta}$  Perovskites. *Solid State Ion.* **1999**, *126* (1–2), 153–161.
- (41) Wang, L.; Merkle, R.; Mastrov, Y. A.; Kotomin, E. A.; Maier, J. Oxygen Exchange Kinetics on Solid Oxide Fuel Cell Cathode Materials—General Trends and Their Mechanistic Interpretation. *J. Mater. Res.* **2012**, *27* (15), 2000–2008. <https://doi.org/10.1557/jmr.2012.186>.
- (42) Fleig, J.; Maier, J. The Polarization of Mixed Conducting SOFC Cathodes: Effects of Surface Reaction Coefficient, Ionic Conductivity and Geometry. *J. Eur. Ceram. Soc.* **2004**, *24* (6), 1343–1347. [https://doi.org/10.1016/S0955-2219\(03\)00561-2](https://doi.org/10.1016/S0955-2219(03)00561-2).
- (43) Tarancón, A.; Skinner, S. J.; Chater, R. J.; Hernández-Ramírez, F.; Kilner, J. A. Layered Perovskites as Promising Cathodes for Intermediate Temperature Solid Oxide Fuel Cells. *J. Mater. Chem.* **2007**, *17* (30), 3175. <https://doi.org/10.1039/b704320a>.
- (44) Bouwmeester, H. J. M.; Burggraaf, A. J. Dense Ceramic Membranes for Oxygen Separation. In *Fundamentals of Inorganic Membrane Science and Technology*; Elsevier, 1996; Vol. 4, pp 435–528. [https://doi.org/10.1016/S0927-5193\(96\)80013-1](https://doi.org/10.1016/S0927-5193(96)80013-1).
- (45) Saranya, A. M.; Pla, D.; Morata, A.; Cavallaro, A.; Canales-Vázquez, J.; Kilner, J. A.; Burriel, M.; Tarancón, A. Engineering Mixed Ionic Electronic Conduction in  $\text{La}_{0.8}\text{Sr}_{0.2}\text{MnO}_{3+\delta}$  Nanostructures through Fast Grain Boundary Oxygen Diffusivity. *Adv. Energy Mater.* **2015**, *5* (11), 1500377. <https://doi.org/10.1002/aenm.201500377>.
- (46) Thoreton, V.; Niania, M.; Druce, J.; Tellez, H.; Kilner, J. Oxygen Diffusion in Ceramic Mixed Conducting  $\text{La}_{0.6}\text{Sr}_{0.4}\text{Co}_{0.2}\text{Fe}_{0.8}\text{O}_{3-\delta}$ : The Role of Grain and Twin Boundaries. *J. Electrochem. Soc.* **2022**, *169*, 044513. <https://doi.org/10.1149/1945-7111/ac6396>.
- (47) Usiskin, R. E.; Maruyama, S.; Kucharczyk, C. J.; Takeuchi, I.; Haile, S. M. Probing the Reaction Pathway in  $(\text{La}_{0.8}\text{Sr}_{0.2})_{0.95}\text{MnO}_{3+\delta}$  Using Libraries of Thin Film Microelectrodes. *J. Mater. Chem. A* **2015**, *3* (38), 19330–19345. <https://doi.org/10.1039/c5ta02428e>.
- (48) Tassis, D. H.; Dimitriadis, C. A.; Valassiades, O. The Meyer–Neldel Rule in the Conductivity of Polycrystalline Semiconducting  $\text{FeSi}_2$  Films. *J. Appl. Phys.* **1998**, *84* (5), 2960–2962. <https://doi.org/10.1063/1.368402>.
- (49) Berenov, A. V.; MacManus-Driscoll, J. L.; Kilner, J. A. Observation of the Compensation Law during Oxygen Diffusion in Perovskite Materials. *Int. J. Inorg. Mater.* **2001**, *3* (8), 1109–1111. [https://doi.org/10.1016/S1466-6049\(01\)00107-6](https://doi.org/10.1016/S1466-6049(01)00107-6).
- (50) Baiutti, F.; Chiabrera, F.; Acosta, M.; Diercks, D.; Parfitt, D.; Santiso, J.; Wang, X.; Cavallaro, A.; Morata, A.; Wang, H.; Chronos, A.; MacManus-Driscoll, J.; Tarancón, A. A High-Entropy Manganite in an Ordered Nanocomposite for Long-Term Application

- in Solid Oxide Cells. *Nat. Commun.* **2021**, *12* (1), 2660. <https://doi.org/10.1038/s41467-021-22916-4>.
- (51) Venables, J. *Introduction to Surface and Thin Film Processes*; Cambridge University Press: Cambridge, UK ; New York, 2000.
- (52) Sha, Z.; Shen, Z.; Calì, E.; Kilner, J. A.; Skinner, S. J. Understanding Surface Chemical Processes in Perovskite Oxide Electrodes. *J. Mater. Chem. A* **2023**, *11*, 5645–5659. <https://doi.org/10.1039/D3TA00070B>.
- (53) Chen, Y.; Téllez, H.; Burriel, M.; Yang, F.; Tsvetkov, N.; Cai, Z.; McComb, D. W.; Kilner, J. A.; Yildiz, B. Segregated Chemistry and Structure on (001) and (100) Surfaces of  $(\text{La}_{1-x}\text{Sr}_x)_2\text{CoO}_4$  Override the Crystal Anisotropy in Oxygen Exchange Kinetics. *Chem. Mater.* **2015**, *27* (15), 5436–5450. <https://doi.org/10.1021/acs.chemmater.5b02292>.
- (54) Niania, M. A. R.; Rossall, A. K.; Van den Berg, J. A.; Kilner, J. A. The Effect of Sub-Surface Strontium Depletion on Oxygen Diffusion in  $\text{La}_{0.6}\text{Sr}_{0.4}\text{Co}_{0.2}\text{Fe}_{0.8}\text{O}_{3-\delta}$ . *J. Mater. Chem. A* **2020**, *8* (37), 19414–19424. <https://doi.org/10.1039/D0TA06058E>.
- (55) Celikbilek, O.; Cavallaro, A.; Kerherve, G.; Fearn, S.; Chaix-Pluchery, O.; Agüadero, A.; Kilner, J. A.; Skinner, S. J. Surface Restructuring of Thin-Film Electrodes Based on Thermal History and Its Significance for the Catalytic Activity and Stability at the Gas/Solid and Solid/Solid Interfaces. *ACS Appl. Mater. Interfaces* **2020**, *12* (30), 34388–34401. <https://doi.org/10.1021/acsami.0c08308>.
- (56) Yu, Y.; Ludwig, K. F.; Woicik, J. C.; Gopalan, S.; Pal, U. B.; Kaspar, T. C.; Basu, S. N. Effect of Sr Content and Strain on Sr Surface Segregation of  $\text{La}_{1-x}\text{Sr}_x\text{Co}_{0.2}\text{Fe}_{0.8}\text{O}_{3-\delta}$  as Cathode Material for Solid Oxide Fuel Cells. *ACS Appl. Mater. Interfaces* **2016**, *8* (40), 26704–26711. <https://doi.org/10.1021/acsami.6b07118>.
- (57) Cai, Z.; Kubicek, M.; Fleig, J.; Yildiz, B. Chemical Heterogeneities on  $\text{La}_{0.6}\text{Sr}_{0.4}\text{CoO}_{3-\delta}$  Thin Films—Correlations to Cathode Surface Activity and Stability. *Chem. Mater.* **2012**, *24* (6), 1116–1127. <https://doi.org/10.1021/cm203501u>.
- (58) Tripković, Đ.; Wang, J.; Küngas, R.; Mogensen, M. B.; Yildiz, B.; Hendriksen, P. V. Thermally Controlled Activation and Passivation of Surface Chemistry and Oxygen-Exchange Kinetics on a Perovskite Oxide. *Chem. Mater.* **2022**, *34* (4), 1722–1736. <https://doi.org/10.1021/acs.chemmater.1c03901>.
- (59) Kim, D.; Hunt, A.; Waluyo, I.; Yildiz, B. Cation Deficiency Enables Reversal of Dopant Segregation at Perovskite Oxide Surfaces under Anodic Potential. *J. Mater. Chem. A* **2023**, *11* (13), 7299–7313. <https://doi.org/10.1039/D2TA09118F>.
- (60) Siebenhofer, M.; Haselmann, U.; Nenning, A.; Friedbacher, G.; Ewald Bumberger, A.; Wurster, S.; Artner, W.; Hutter, H.; Zhang, Z.; Fleig, J.; Kubicek, M. Surface Chemistry and Degradation Processes of Dense  $\text{La}_{0.6}\text{Sr}_{0.4}\text{CoO}_{3-\delta}$  Thin Film Electrodes. *J. Electrochem. Soc.* **2023**, *170* (1), 014501. <https://doi.org/10.1149/1945-7111/acada8>.
- (61) Vasquez, R. P. X-Ray Photoelectron Spectroscopy Study of Sr and Ba Compounds. *J. Electron Spectrosc. Relat. Phenom.* **1991**, *56* (3), 217–240. [https://doi.org/10.1016/0368-2048\(91\)85005-E](https://doi.org/10.1016/0368-2048(91)85005-E).
- (62) Vasquez, R. P.  $\text{SrSO}_4$  by XPS. *Surf. Sci. Spectra* **1992**, *1* (1), 117–121. <https://doi.org/10.1116/1.1247681>.

- (63) Niania, M.; Sharpe, M.; Webb, R.; Kilner, J. A. The Surface of Complex Oxides; Ion Beam Based Analysis of Energy Materials. *Nucl. Instrum. Methods Phys. Res. Sect. B Beam Interact. Mater. At.* **2020**, *480*, 27–32. <https://doi.org/10.1016/j.nimb.2020.07.022>.
- (64) Wicklein, S.; Sambri, A.; Amoroso, S.; Wang, X.; Bruzzese, R.; Koehl, A.; Dittmann, R. Pulsed Laser Ablation of Complex Oxides: The Role of Congruent Ablation and Preferential Scattering for the Film Stoichiometry. *Appl. Phys. Lett.* **2012**, *101* (13), 131601. <https://doi.org/10.1063/1.4754112>.
- (65) Chen, J.; Döbeli, M.; Stender, D.; Conder, K.; Wokaun, A.; Schneider, C. W.; Lippert, T. Plasma Interactions Determine the Composition in Pulsed Laser Deposited Thin Films. *Appl. Phys. Lett.* **2014**, *105* (11), 114104. <https://doi.org/10.1063/1.4895788>.
- (66) Keeble, D. J.; Wicklein, S.; Dittmann, R.; Ravelli, L.; Mackie, R. A.; Egger, W. Identification of A - and B -Site Cation Vacancy Defects in Perovskite Oxide Thin Films. *Phys. Rev. Lett.* **2010**, *105* (22), 226102. <https://doi.org/10.1103/PhysRevLett.105.226102>.
- (67) Čížek, J.; Melikhova, O.; Barnovská, Z.; Procházka, I.; Islamgaliev, R. K. Vacancy Clusters in Ultra Fine Grained Metals Prepared by Severe Plastic Deformation. *J. Phys. Conf. Ser.* **2013**, *443*, 012008. <https://doi.org/10.1088/1742-6596/443/1/012008>.
- (68) Keeble, D. J.; Mackie, R. A.; Egger, W.; Löwe, B.; Pikart, P.; Hugenschmidt, C.; Jackson, T. J. Identification of Vacancy Defects in a Thin Film Perovskite Oxide. *Phys. Rev. B* **2010**, *81* (6), 064102. <https://doi.org/10.1103/PhysRevB.81.064102>.
- (69) Clement, M.; de Nijs, J. M. M.; Balk, P.; Schut, H.; van Veen, A. Analysis of Positron Beam Data by the Combined Use of the Shape- and Wing-Parameters. *J. Appl. Phys.* **1996**, *79* (12), 9029–9036. <https://doi.org/10.1063/1.362635>.
- (70) Sase, M.; Hermes, F.; Yashiro, K.; Sato, K.; Mizusaki, J.; Kawada, T.; Sakai, N.; Yokokawa, H. Enhancement of Oxygen Surface Exchange at the Hetero-Interface of (La,Sr)CoO<sub>3</sub>/(La,Sr)<sub>2</sub>CoO<sub>4</sub> with PLD-Layered Films. *J. Electrochem. Soc.* **155** (8), B793–B797.
- (71) Crumlin, E. J.; Mutoro, E.; Ahn, S.-J.; la O', G. J.; Leonard, D. N.; Borisevich, A.; Biegalski, M. D.; Christen, H. M.; Shao-Horn, Y. Oxygen Reduction Kinetics Enhancement on a Heterostructured Oxide Surface for Solid Oxide Fuel Cells. *J. Phys. Chem. Lett.* **2010**, *1* (21), 3149–3155. <https://doi.org/10.1021/jz101217d>.
- (72) Lee, D.; Lee, Y.-L.; Hong, W. T.; Biegalski, M. D.; Morgan, D.; Shao-Horn, Y. Oxygen Surface Exchange Kinetics and Stability of (La,Sr)<sub>2</sub>CoO<sub>4±δ</sub>/La<sub>1-x</sub>Sr<sub>x</sub>MO<sub>3-δ</sub> (M = Co and Fe) Hetero-Interfaces at Intermediate Temperatures. *J. Mater. Chem. A* **2015**, *3* (5), 2144–2157. <https://doi.org/10.1039/C4TA05795C>.



5. *Integration of thin film electrode materials in highly functional solid oxide cells*

5.1 Motivation .....	199
5.2 Symmetric solid oxide fuel cells.....	202
5.2.1 Thin film characterization and cell configuration.....	202
5.2.2 Electrochemical characterization.....	204
5.2.3 Microstructural characterization after operation.....	210
5.3 Single crystal supported thin film solid oxide cells.....	211
5.3.1 Characterization in fuel cell mode .....	212
5.3.2 Characterization in electrolysis mode.....	214
5.4 Integration of thin film solid oxide fuel cells in silicon supported devices: micro solid oxide fuel cells.....	218
5.4.1 Cell architecture and device setup .....	219
5.4.2 Electrochemical characterization.....	221
5.4.3 Post-mortem structural characterization .....	222
5.5 Remarks on the experimental limitations for the operation of thin film-based solid oxide cells .....	227
5.6 Conclusions .....	230
5.7 Future work.....	232

## 5.1 Motivation

This chapter describes the advances carried out during this thesis towards the implementation of thin film electrode materials in solid oxide cell (SOC) and micro-solid oxide fuel cell ( $\mu$ SOFC) systems. Established state-of-the-art thin film materials have been employed for the fabrication and assembly of full devices in different configurations. Thin film SOCs (TF-SOCs) were produced in an electrolyte supported architecture by employing YSZ single crystal substrates. These devices were utilized as model devices and allowed for the study of different types of TF-SOCs. First, the use of symmetric SOCs (SSOCs) based on thin film materials is explored. SSOCs are devices that employ the same material as both the oxygen and hydrogen electrode<sup>1,2</sup>. This configuration presents several advantages in terms of reduction of manufacturing cost and thermomechanical stresses due to the use of a single electrode material, as well as mitigating potential device failure mechanisms due to redox-cycling mechanisms. Redox-cycling processes are normally investigated in hydrogen electrodes as they induce undesired mechanical stresses due to reoxidation of the metallic phase in cermet electrodes (typically Ni in Ni/YSZ composites). The second type of device configuration studied in this chapter was the use of thin film reversible SOCs (RSOCs)<sup>3,4</sup>. This device configuration is based on the alternate operation in electrolysis (SOEC) or fuel cell (SOFC) mode depending on the energy needs. In this sense, the RSOC is able to either supply electrical power or to store chemical energy (through production of hydrogen). A more detailed description on SSOCs and RSOCs can be found in Chapter 1.

In Section 5.2, the use of symmetric SOFCs based on the application of  $\text{La}_{0.9}\text{Sr}_{0.1}\text{CrO}_3$  (LSCr) thin films as both anode and cathode materials is explored. Lanthanum chromites have been proposed over time as suitable electrode candidates for symmetric applications<sup>2,5-7</sup>. This has been majorly explained by their high stability under reducing conditions. Nonetheless, their electrochemical performance is not considerably high and its application window has normally been conditioned to the high temperature range and the use of bulk materials. Interestingly, recent studies have reported the presence of grain boundary enhancement effects on the oxygen mass transport properties of LSCr thin films<sup>8</sup>, leading to higher electrochemical activity than the typically observed in bulk systems. Symmetric LSCr electrodes were then chosen as the model material in this section in order to prove the concept on the operation of a thin film SSOC. Measurements of the cell electrochemical properties and their performance on redox cycling –i.e. oxidant to reducing atmosphere exchange– are presented and discussed, with focus on possible performance recovery effects observed after the cycling process.

Section 5.3 presents the results obtained for thin film RSOCs fabricated with  $\text{La}_{0.8}\text{Sr}_{0.2}\text{CoO}_3$  (LSC82) as the oxygen electrode and porous  $\text{Ce}_{0.8}\text{Sm}_{0.2}\text{O}_2$  (SDC) as the hydrogen electrode. The use of Co-containing materials as the oxygen electrode is normally a preferred option found in the literature related to thin film devices, due to its high electrochemical activity at



lower temperatures<sup>9</sup>. Regarding the use of SDC, it is one of the few all-oxide-based materials presenting high electrochemical activity for hydrogen conversion<sup>10,11</sup>. More details on the properties of these materials can be found in Chapter 1, in the dedicated section to the review of state-of-the-art SOC materials. The electrochemical properties and structural characterization can also be found in Chapter 3 for SDC and Chapter 4 for LSC82. The fabricated cells were also supported on yttria-stabilized zirconia (YSZ) single crystal substrates and employed as model thin film-based devices. Two different current collectors were applied to the porous SDC electrode, consisting in either a layer of sputtered gold or platinum. The variable current collecting layer was exclusively studied in the porous electrode since more drastic differences were expected due to the open microstructure. The resulting cells were characterized both in SOFC and SOEC modes in order to study the suitability of employing the devices as RSOCs. Electrochemical operation over time was also performed for the first cell, in order to study its resistance against degradation.

Section 5.4 deals with the studies made for the implementation of thin film materials in a free-standing  $\mu$ SOFC membrane supported in silicon. These devices have promising interest for the development of portable power systems for application in the consumer and industrial electronics sectors<sup>12-14</sup>. The characterization of two cells is presented, one based on the application of LSC82 and porous SDC as the electrodes –following the selection of materials utilized in section 5.3–. The second microcell presented  $\text{La}_{0.6}\text{Sr}_{0.4}\text{CoO}_3$  (LSC64) as the oxygen electrode and an additional  $\text{La}_{0.75}\text{Sr}_{0.25}\text{Cr}_{0.5}\text{Mn}_{0.5}\text{O}_3$  (LSCrMn) layer between the electrolyte and the porous SDC. The second architecture was selected with the expectation to show enhanced cell performance as a result of the higher Sr doping<sup>15</sup> in the cathode material and improved electrical percolation in the anode side. Post-mortem analyses were also carried out in order to shed light on the causes behind the performance observed and the device limitations present. A discussion on the limitations experienced for the operation of the TF-SOCs with special focus in the  $\mu$ SOFCs is given. A perspective on the future work beyond the systems described is included in the end of the chapter. Given the variety of devices studied in this chapter and in order to ease its reading, Figure 5-1 shows a schematic of the different devices and architectures studied and specified by chapter section.

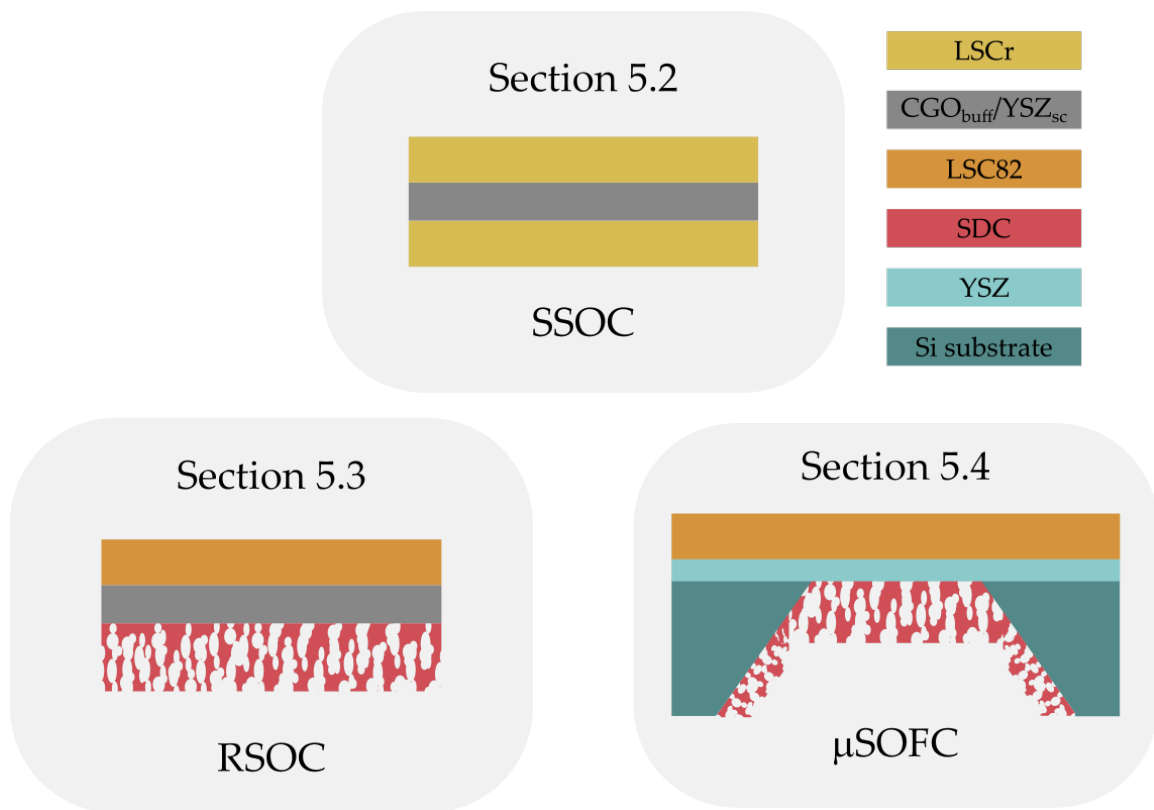


Figure 5-1. Schematic of the different devices studied in the chapter specified for each section.

## 5.2 Symmetric solid oxide fuel cells

This section deals with the investigation made for the use of LSCr thin films as symmetric electrodes to be employed in SOFCs. With that aim, a symmetric cell was fabricated in a single crystal electrolyte supported architecture and tested under different operational conditions.

### 5.2.1 Thin film characterization and cell configuration

LSCr thin film electrodes were deposited by pulsed laser deposition (PLD) on top of YSZ electrolyte substrates, following the procedure described in Chapter 2 for the fabrication of dense thin films. Figure 5-2a shows the X-Ray Diffraction (XRD) measurement obtained for the film. From the pattern it can be concluded that LSCr presents highly polycrystalline structure. In particular, XRD reflections on the (100), (110), (111) and (211) crystallographic orientations – considering a pseudo-cubic structure – can be observed. Despite LSCr-based materials has been reported to present orthorhombic<sup>16</sup> and rhombohedral<sup>17</sup> structures, the pseudo-cubic notation has been employed for simplicity reasons. This is due to the difficulty of properly identifying these phases when the total amount of material is low (e.g. in the case of thin films) and the structure allows lower levels of symmetry (i.e. cubic symmetry). The inset shows the topography of the LSCr thin film obtained by Atomic Force Microscopy (AFM). The microstructure observed is characterized by irregular grain morphology – probably due to the polycrystalline structure– and low roughness ( $R_{ms} = 0.3$  nm). Figure 5-2b shows the evolution of the area specific resistance (ASR) with temperature, measured both under synthetic air and wet hydrogen atmospheres. It can be seen that LSCr presents lower values of ASR ( $\approx 55 \text{ } \Omega \cdot \text{cm}^2$  at  $750 \text{ } ^\circ\text{C}$ ) in hydrogen atmosphere than in air ( $\approx 90 \text{ } \Omega \cdot \text{cm}^2$  at  $750 \text{ } ^\circ\text{C}$ ). This is also the case for the activation energy, which shows lower values under hydrogen ( $E_a = 1.19 \text{ eV}$ ) with respect to the measurements in air ( $E_a = 2.22 \text{ eV}$ ). This behavior is similar to the observed in the chromite materials studied in Chapter 3, showing comparable performance to the single phases studied and slightly worse than the optimized nanocomposite. These results validate then the suitability of the LSCr thin film to be employed as a model symmetric electrode in the device studied in this chapter.

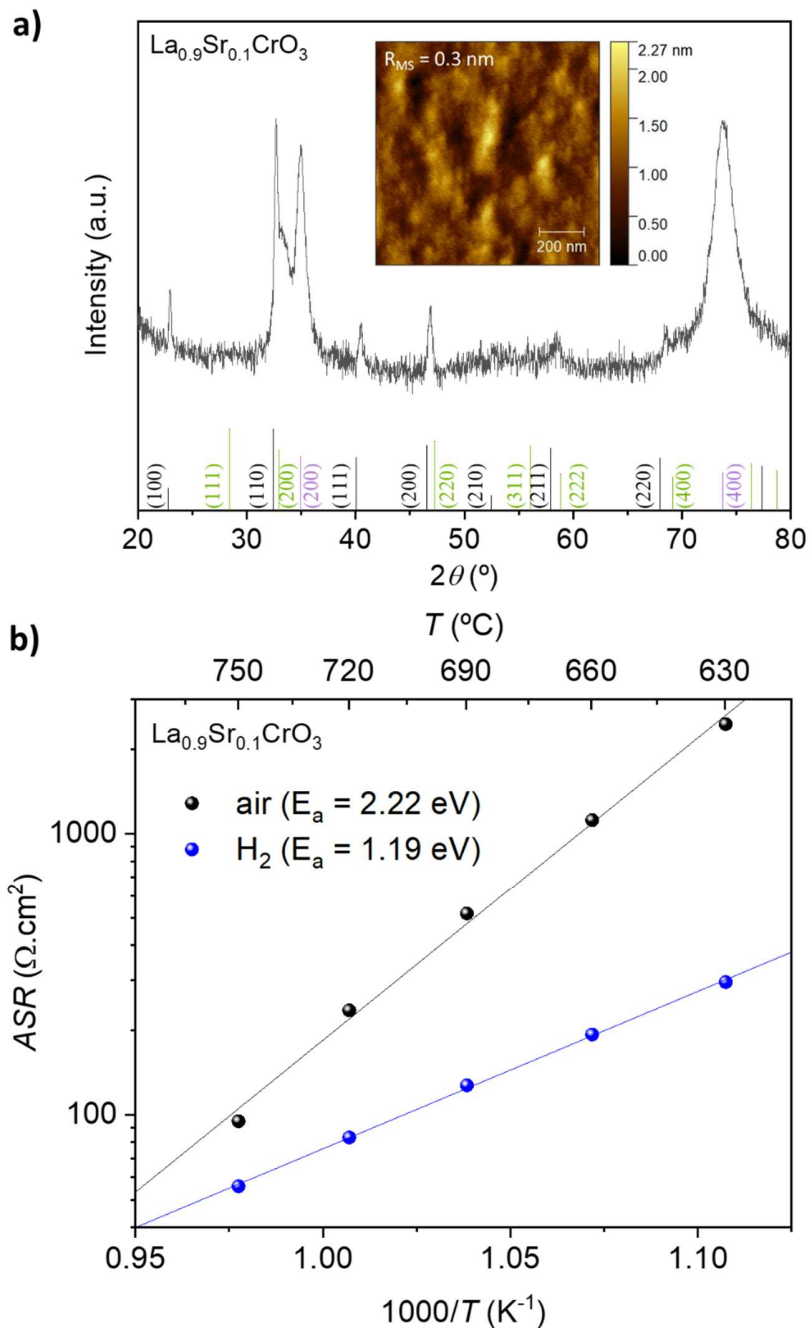


Figure 5-2. Characterization of the LSCr thin film studied as symmetric electrode in SOFCs: XRD diffraction pattern with reference patterns of a cubic perovskite ( $Pm\text{-}3m$  #221, in black)<sup>18</sup>, SDC ( $Fm\text{-}3m$  #225, in green)<sup>19</sup> and YSZ ( $Fm\text{-}3m$  #225, in purple)<sup>20</sup>, top-view AFM micrograph of the film (inset) (a). Evolution of the ASR with temperature of the LSCr thin film both under air and  $\text{H}_2$  atmospheres.

The final device architecture is described in Table 5-1. In summary, both films were deposited at each side of the YSZ substrate, with the corresponding  $\text{Ce}_{0.8}\text{Gd}_{0.2}\text{O}_2$  (CGO) buffer layers deposited to avoid undesired electrolyte-electrode secondary reactions. Gold

paste was applied on top of the films as current collectors (CC) in order to facilitate current percolation between the device and the electrical connections.

Table 5-1. Components of the symmetric SOFC measured.

CC	Hydrogen Electrode	Electrolyte	Oxygen Electrode	CC
Au <sub>paste</sub>	La <sub>0.9</sub> Sr <sub>0.1</sub> CrO <sub>3</sub>	CGO <sub>buff</sub> /YSZ/CGO <sub>buff</sub>	La <sub>0.9</sub> Sr <sub>0.1</sub> CrO <sub>3</sub>	Au <sub>paste</sub>

The symmetric thin film SOFC was measured under fuel cell mode, with wet hydrogen in the fuel chamber ( $\approx 3\%$  H<sub>2</sub>O) and synthetic air in the oxygen chamber. The cell was measured under two different gas configurations, by exchanging the hydrogen and oxygen chamber in the inner and outer chambers of the ProboStat station, as schematized in Figure 5-3. The two chamber conditions were defined as follows: configuration A corresponded to the hydrogen chamber being the inner chamber of the station, while configuration B was set the opposite. The chambers were purged with Ar before performing the exchange.

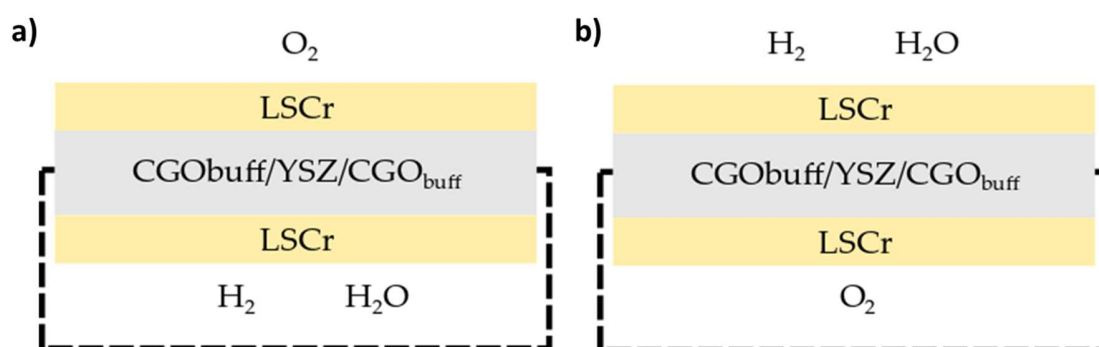


Figure 5-3. Schematic of the two atmosphere conditions employed for the cycling experiment: configuration A with H<sub>2</sub>/H<sub>2</sub>O in the inner chamber and O<sub>2</sub> in the outer chamber (a) and configuration B with the opposite distribution of gases (b).

### 5.2.2 Electrochemical characterization

The symmetric SOFC was then subjected to a cycling operation process for a period of over 70 h. At each step of the experiment the cell was operated in galvanostatic conditions. I-V, electrochemical impedance spectroscopy (EIS) and open circuit voltage (OCV) measurements were performed between steps in order to study the electrochemical evolution of the symmetric cell. A summary of the overall characterization conditions is collected in Table 5-2.

Table 5-2. Description of the setup conditions employed in the cycling of the symmetric LSCr SOFC.

Cycle	Inner chamber	Outer chamber	Configuration	Temperature (°)
-------	---------------	---------------	---------------	-----------------

1	Wet H <sub>2</sub>	Synthetic air	A	650
1	Synthetic air	Wet H <sub>2</sub>	B	650
2	Wet H <sub>2</sub>	Synthetic air	A	650
2	Synthetic air	Wet H <sub>2</sub>	B	650
3	Wet H <sub>2</sub>	Synthetic air	A	650
3	Synthetic air	Wet H <sub>2</sub>	B	650
4	Wet H <sub>2</sub>	Synthetic air	A	700
4	Synthetic air	Wet H <sub>2</sub>	B	700
5	Wet H <sub>2</sub>	Synthetic air	A	700
5	Synthetic air	Wet H <sub>2</sub>	B	700
6	Wet H <sub>2</sub>	Synthetic air	A	750
6	Synthetic air	Wet H <sub>2</sub>	B	750
7	Wet H <sub>2</sub>	Synthetic air	A	750
7	Synthetic air	Wet H <sub>2</sub>	B	750
8	Wet H <sub>2</sub>	Synthetic air	A	750

The overall electrochemical operation performed in the symmetric SOFC is represented in Figure 5-4. In particular, measurements of the OCV analyzed at the start of each galvanostatic step are collected in panel (a). It can be seen that the OCV recorded oscillated in the 0.8-1.0 V range for most of the cases, and that a general trend towards lower OCV values was observed for configuration B (points in red color). This can be attributed to the presence of gas leaking between the chambers. This was generally controlled by adjusting the flow at each chamber, which allowed to control the OCV value within a certain range. Nevertheless, exchanging the chamber gases required the readjustment of the gas flows, with the consequent differences in the OCV measurements performed. Panel (b) shows the current density applied at each step of the experiment (absolute values have been considered for simplicity of representation). In general, values between 0.4 mA/cm<sup>2</sup> and 4 mA/cm<sup>2</sup> could be applied for the experimental conditions set. It can be observed that in the end of the first stage of the test (T = 650 °C), the current density had to be adjusted to lower values in order to operate the cell within a reasonable voltage value. This was also the case at the beginning of the operation at 700 °C. This could be attributed to two reasons: i) partial degradation of the cell and ii) differences (in particular, lowering) of OCV values due to gas leaks. Degradation could affect the LSCr thin films, most likely in the form of dopant segregated species and microstructure and surface evolution, as observed in other chormite-perovskites<sup>21,22</sup>. Additionally, loss of current percolation caused by current collector temperature evolution (dewetting)<sup>23,24</sup> is to be expected at these temperatures. Nonetheless, the differences in the OCV at the beginning of the operation step seems to be the most likely reason, as the decrease in the current density applied coincide with the observation of lower values of OCV ( $\leq 0.8$  V).

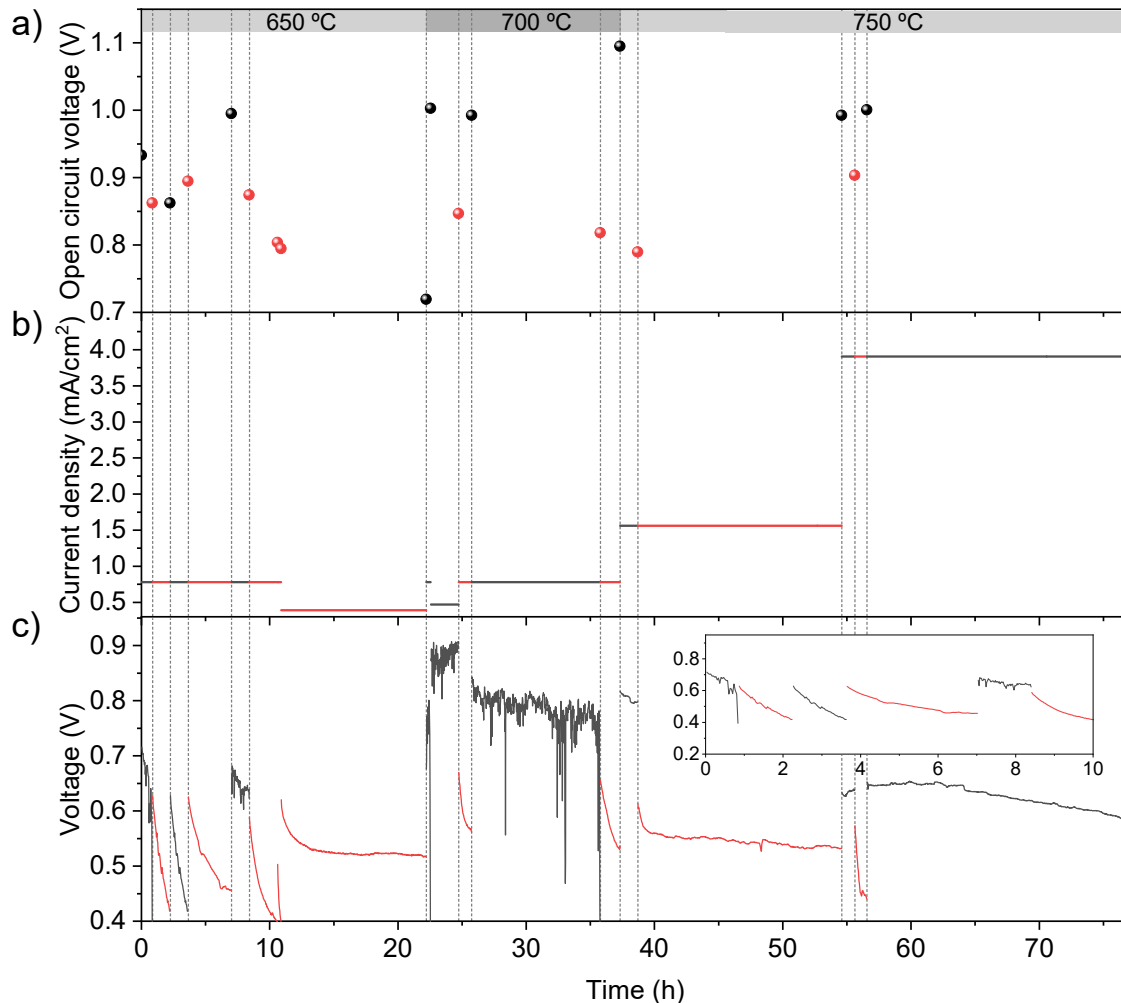


Figure 5-4. Electrochemical characterization of the reversible LSCr-based SOFC under constant current and at different temperatures: OCV recorded right before each operation step (a), current density fixed through the cell (b) and voltage measurement during operation (c). Values colored in black correspond to configuration A, while red was assigned to measurements performed in configuration B. The inset in panel (c) shows a zoomed-in over the first 10 h of measurement.

Finally, Figure 5-4c shows the evolution over time of the cell voltage at each operating step. It should be pointed out that the measurements were paused if the voltage dropped below 0.4 V, in order to preserve the integrity of the cell. In such cases, the measurement was either restarted after checking the OCV, the applied current was readjusted to lower values or the step was skipped to the next configuration. During the initial stages of the cycling test, it can be seen that the performance drops progressively within 1-2 hours (see inset for a zoom in the first 10 h of analysis), as highlighted by the decrease of the voltage value. Interestingly, the voltage seems to stabilize during the third cycle with configuration B (10-20 h range), and then subsequently for the rest of the cycles performed for similar periods of time (> 10 h). Additionally to the stabilization of the voltage observed during these stages of the experiment, a generalized recovery on the performance is observed after each cycling

process –i.e. operation under the two different chamber configurations. By comparing the measurements performed for the same configuration, either A or B, between cycles in which the same current density was applied, one can clearly observe that for the latter measurement the voltage was recovered to higher values. This was observed throughout the whole experiment. For instance, measurement steps 1B, 2A and 2B at 650 °C were recorded by applying  $\approx 0.78 \text{ mA/cm}^2$  with similar initial OCV values and showed recovery of the voltage after each of the measurements. This was also observed clearly in steps 4B and 5B measured at 700 °C with the same current density, as with the previous example. In this case, the voltage measured in the beginning of step 5B was larger than the observed in the end of 4B, sign of performance recovery. Finally, measurements performed at 750 °C, in particular 7A and 8A, show similar values of voltage after the voltage drop observed in step 7B. This suggests promising stability of the symmetric cell performance upon redox cycling. For proper evaluation of this effect through the cycling experiment, j-V and EIS spectra were recorded before and after each galvanostatic operation step.

Figure 5-5 shows the collection of j-V –panel (a)– and j-P –panel (b)– measurements recorded throughout the redox cycling operation. Despite the measurements performed at 650 °C and 700 °C show high variability of the OCV values (as commented previously), performance recovery can be observed similarly than for the cases previously discussed under galvanostatic operation –e.g. comparing  $1A_f$  (end of step 1A) and  $2A_0$  (start of step 2A). Most interestingly, the measurements performed at 750 °C show much more stable OCV, only oscillating within the 0.9-1 V range, which allows to perform a more reliable analysis of the phenomena. In this stage, cell performance degradation is observed when comparing the measurements before and after the galvanostatic steps, while performance recovery is observed at the subsequent cycle, i.e. after operation under reverse atmosphere. In this sense, it can be seen that the performance in cycle 6 is worse than at cycle 7 and 8. In fact, the maximum power density peak ( $\approx 3.25 \text{ mW/cm}^2$ ) is reached for step  $7A_0$ , with steps  $7B_0$  and  $8A_0$  almost as high in power ( $\approx 3.1 \text{ mW/cm}^2$ ). These measurements confirm the recovery on the electrochemical performance, i.e. power generation, as a result of the redox cycling process.



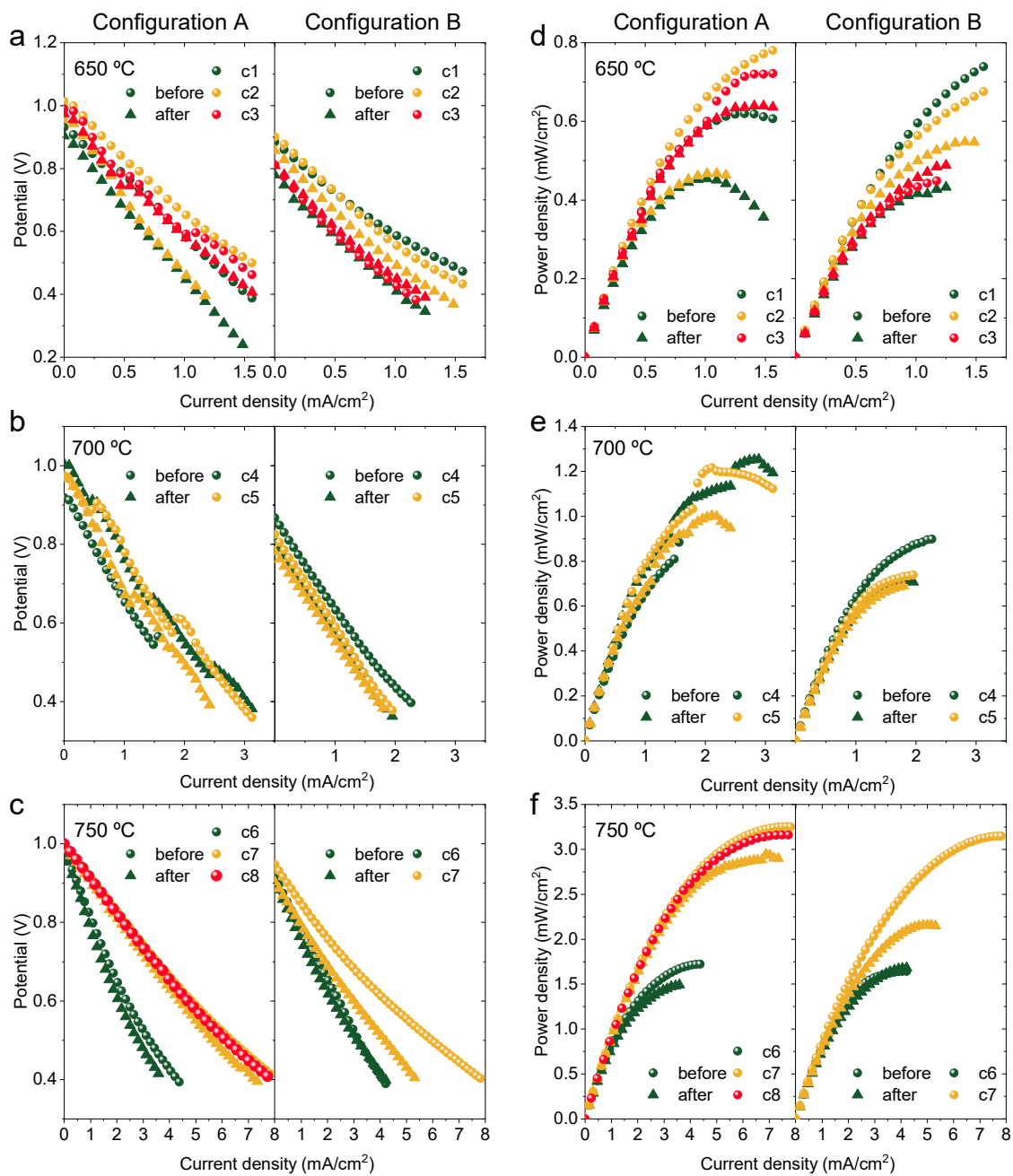


Figure 5-5. Electrochemical characterization of the symmetric LSCr cell under the two configurations set:  $j$ -V at different temperatures (a-c) and corresponding  $j$ -P curves (d-f).

Figure 5-6 shows the Nyquist plots obtained by impedance spectroscopy analysis under OCV conditions at the different temperatures set for the redox cycling experiment. In order to facilitate the interpretation the presence of noisy points in the lower frequency regime has been removed from some of the spectra. In general terms, it can be observed that improvement in terms of ASR can be visualized when moving between cycles with the same

configuration, similar to the enhancement observed in the previous analyses. Particularly, in the case of the measurements performed at 650 °C –panel (a)–, a general trend towards higher ASR is observed, with partial recovery of lower ASR values in between redox cycles. For the measurements obtained at 700 °C –panel (b), redox cycles 4 and 5– an initial ASR decreasing trend is observed, with step 4B<sub>0</sub> presenting the lowest polarization resistance ( $\approx 200 \text{ } \Omega \cdot \text{cm}^2$ ). Then the ASR increases in steps 4B<sub>i</sub>, 5A<sub>0</sub> and 5A<sub>i</sub>. Interestingly, the ASR decreases again for steps 5B<sub>0</sub> and 5B<sub>i</sub>.

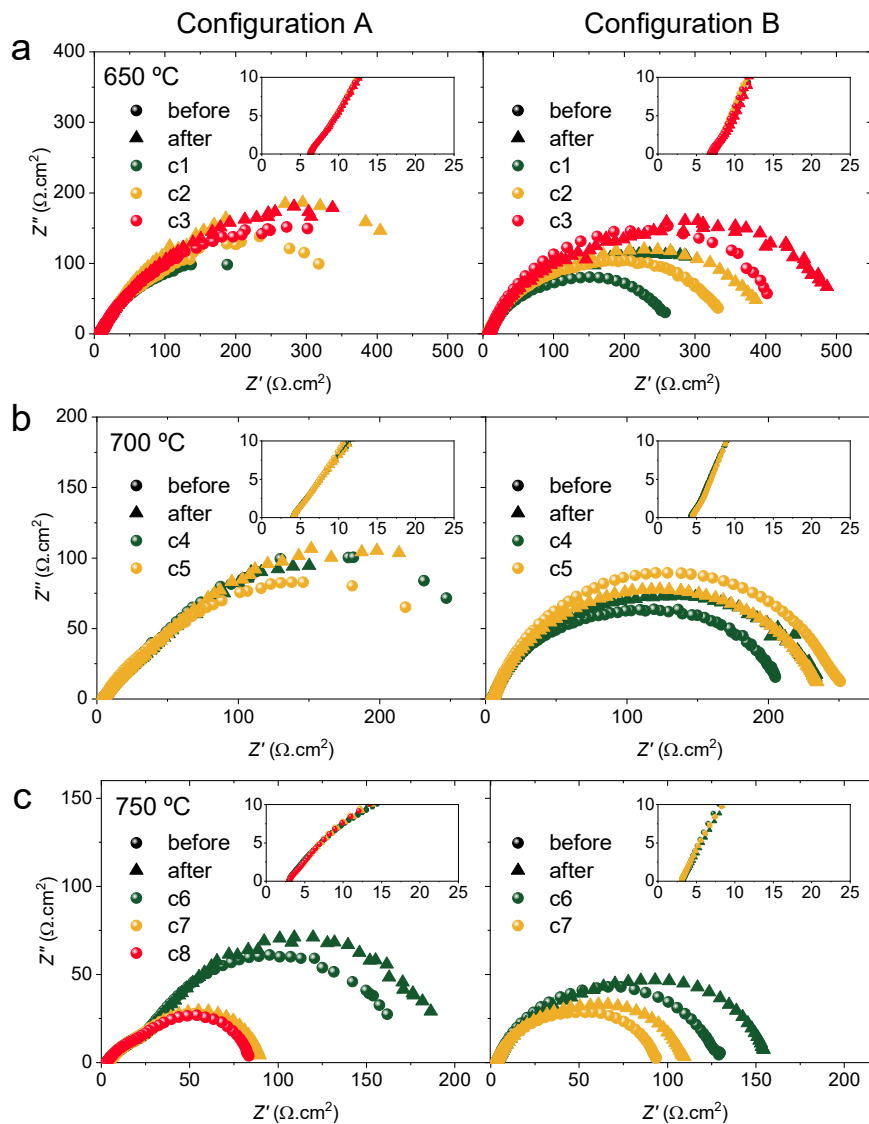


Figure 5-6. Nyquist plots obtained for configurations A and B before and after each operation step and at different temperatures: 650 °C (a), 700 °C (b) and 750 °C (c). Note that the presence of noisy points in the lower frequency range was removed in some of the plots of configuration A to ease interpretation of the spectra. The insets show a zoomed-in region in the high frequency range for each spectra.

Despite partial enhancement is suggested by the changes in ASR described, it should be pointed out that the differences in the ASR might also be partially attributed to changes in the gas atmosphere 'sensed' by the electrodes, due to the presence of leakages. Hence, the EIS spectra presented in Figure 5-6c is expected to offer a better representation of the evolution observed on redox cycling, due to the more stable OCV registered in this sequence of measurements. The spectra show an overall decreasing trend of the ASR with partial increase before and after each galvanostatic step and subsequent lowering at each of the steps and cycles performed. Interestingly, the lowest ASR observed in this sequence was registered for step 8A<sub>0</sub>, that is the final step of the cycling experiment.

### 5.2.3 Microstructural characterization after operation

Microstructural characterization of the symmetric SOFC cell was performed after the redox cycling experiment by Scanning Electron Microscopy (SEM) microscopy, as depicted in Figure 5-7, for both the film exposed to the inner –panels (a-d)– and outer chamber –panels (e-f)–. At first sight, it can be observed that the gold current collector presents severe dewetting after the high temperature exposure during the electrochemical characterization. While some areas remain interconnected, as in the case in Figure 5-7a, some others present agglomeration of gold particles (Figure 5-7b). This might cause loss of active surface area due to poor current percolation, leading to possible increase of the series and polarization resistances as well as to drop of the OCV values. Additionally, it can be observed that the surface of the film evolves considerably after the electrochemical characterization performed. Portions of the electrode area keep a dense-like microstructure (central region in Figure 5-7c), while others show increased roughness and even some open mesoporous regions (Figure 5-7d). This evolution of the microstructure towards more surface-exposed area might be responsible of the lowering observed in the ASR values in the final stages of the redox cycling experiment. The electrode facing the inner chamber of the station show similar microstructure evolution, with agglomerated gold particles and increased roughness, as in Figure 5-7e. Most interestingly, the film microstructure presents faceted nanoparticles dispersed on the surface. Taking into account that the outer chamber was exposed to synthetic air by the end of the experiment, the presence of dopant segregated species like strontium sulfates and carbonates might be responsible of the surface evolution<sup>21,22</sup>. In particular, segregation of SrSO<sub>4</sub> species typically show faceted particles<sup>25</sup> like the ones observed in Figure 5-7f. Additional Cr-rich secondary phases might also be present, due to the facile evaporation of Cr, forming oxides like Cr<sub>2</sub>O<sub>3</sub><sup>26</sup>. Moreover, Cr interaction with Sr species could also result in the formation of SrCrO<sub>4</sub><sup>27</sup> in the surface. Nonetheless, further chemical and structural characterization analyses (e.g. X-Ray Photoelectron Spectroscopy, Energy-dispersive X-ray Spectroscopy, XRD) would be needed.

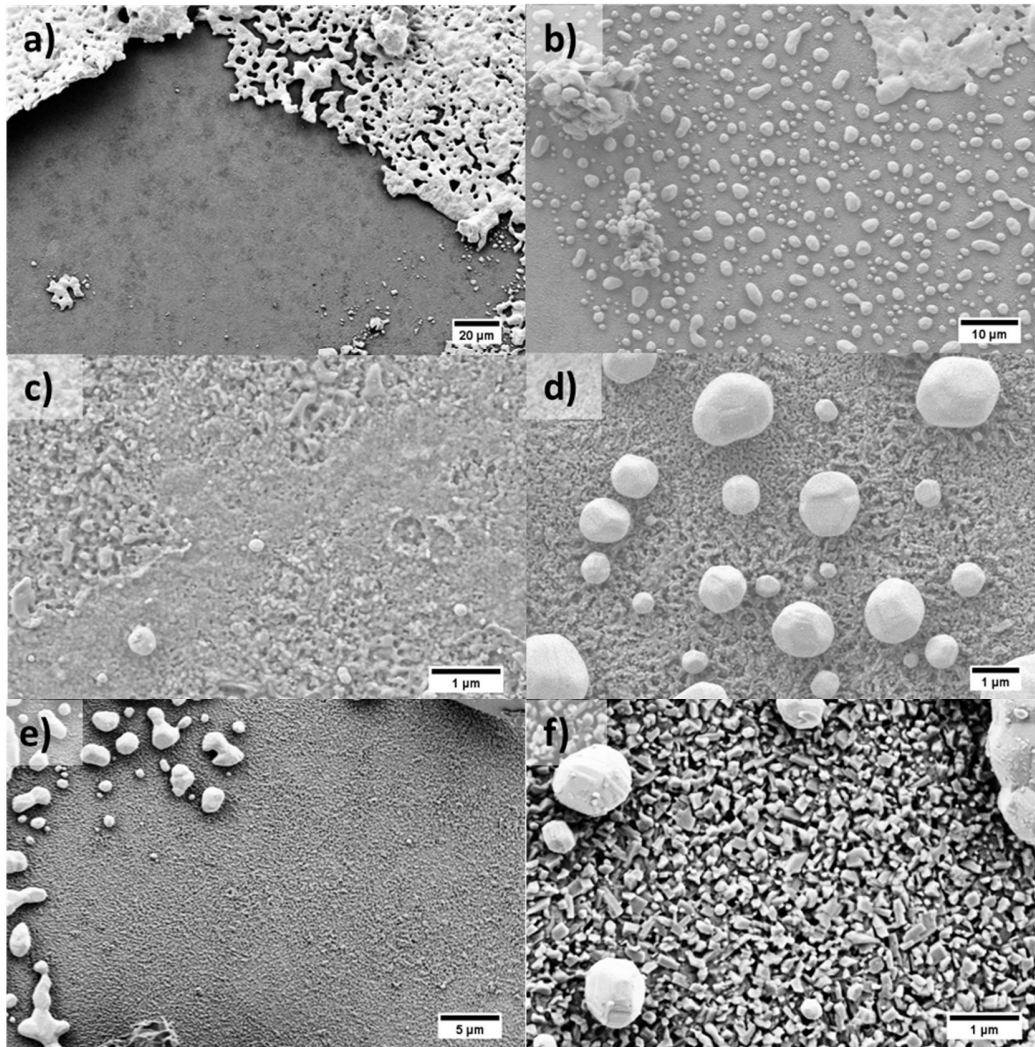


Figure 5-7. SEM characterization performed after the measurement: film exposed to the inner chamber (a-d) and film exposed to the outer chamber (e-f).

### 5.3 Single crystal supported thin film solid oxide cells

With the aim of studying the feasibility of employing thin film electrode materials in fully functional SOCs, different cells have been fabricated and characterized. The electrode materials selected for the device were porous SDC in the case of the hydrogen electrode and LSC82 in the case of the oxygen electrode. Details on the properties of these materials can be found in the Motivation section and in Chapters 3 and 4, respectively. The selected electrodes consist in state-of-the-art materials with well-known electrochemical performance. The goal defined was to integrate both films into an electrolyte supported cell and to characterize them under SOFC and SOEC modes. These analyses would then be extended to the integration in silicon technologies (cf. Section 5.4). Table 5-3 summarizes the components of the two TF-SOCs characterized in this section. It can be observed that the

two cells are almost identical in composition, with the exception of the current collector employed in the hydrogen electrode side. In this case, either a sputtered layer of gold or platinum were utilized. This was done in order to explore the effect on the current collector employed in the hydrogen electrode side ( $CC_{hy}$ ), as SDC is intrinsically a poor electronic conductor and hence, the performance of the device might be severely affected by the collection of current from this electrode. Gold paste was applied in the oxygen electrode ( $CC_{ox}$ ) in order to guarantee proper current collection and electrical contact. The resulting devices were characterized both under fuel and electrolysis cell conditions in order to study their suitability as reversible SOCs.

Table 5-3. Component description of the TF-SOCs fabricated and analyzed.

Sample	$CC_{hy}$	Hydrogen Electrode	Electrolyte	Oxygen Electrode	$CC_{ox}$
Cell #1	Au <sub>sput</sub>	Porous SDC	YSZ/CGO <sub>buff</sub>	LSC82	Au <sub>paste</sub>
Cell #2	Pt <sub>sput</sub>	Porous SDC	YSZ/CGO <sub>buff</sub>	LSC82	Au <sub>paste</sub>

### 5.3.1 Characterization in fuel cell mode

SOFC measurements were performed for both cell #1 and cell #2. The fuel atmosphere set was a mixture of 97% of H<sub>2</sub> and 3% of steam water, while synthetic air was set as the cathode atmosphere. Figure 5-8 summarizes the electrochemical characterization performed on the cells studied. In particular, Figure 5-8a the current-voltage and current-power curves measured at 500, 600, and 700 °C for cell #1. The three measurements performed present OCV voltages in the 1.0-1.1 V range, an indicative of a good gas-tight sealing between the anodic and cathodic chambers. A peak power density of  $\approx 15$  mW/cm<sup>2</sup> was reached at 700 °C. Figure 5-8b shows the EIS spectra obtained for cell #1 at different temperatures and with DC excitation both under OCV and with 0.6 V of bias. It can be clearly seen that the total polarization is limited by two different contributions, differentiated by two arcs in the Nyquist. These two contributions are comparable at higher temperatures and become more easily differentiated when decreasing the temperature, with one of the arcs being the main contribution to the ASR. A general lowering on the polarization resistance is observed for the measurements under bias. The activity increase is more evident the lower the temperature, with a total polarization of  $\approx 110$   $\Omega$ .cm<sup>2</sup> under bias with respect to  $\approx 200$   $\Omega$ .cm<sup>2</sup> in OCV conditions, at 500 °C. In the case measured at 700 °C, the ASR values measured under bias and in OCV were  $\approx 10.6$   $\Omega$ .cm<sup>2</sup> and  $\approx 12$   $\Omega$ .cm<sup>2</sup>, respectively. In the case of the Pt-sputtered cell (cell #2, see Figure 5-8c), it also presented high values of OCV ( $> 1.05$  V in all cases), suggesting a stable sealing. The maximum output power density generated for this was over 30 mW/cm<sup>2</sup> at 700 °C, resulting in improved performance with respect to cell #1 – i.e. the one with gold sputtering as current collector–. Interestingly, this was confirmed by the EIS measurements presented in Figure 5-8d. A similar behavior than for cell #1 can be

observed, with comparable resistance contributions at higher temperatures and one more predominant arc at 500 °C. The lowest values of ASR were 4.1  $\Omega\cdot\text{cm}^2$  and 6.4  $\Omega\cdot\text{cm}^2$ , measured under 0.6 V of bias and under OCV, at 700 °C. This is roughly a 2-2.5-fold factor with respect to the ASR values obtained for cell #1, which coincides with the 2-fold factor observed for the power density measured. It should be pointed out that the main contribution in the Nyquist spectra experiencing the differences in the current collector layer employed is the lower frequency arc. This suggests that both of the TF-SOFCs are limited by the electrochemical activity of the anode. Most interestingly, the impedance spectra allows to analyse the potential drop caused by the electrolyte resistance (i.e. the series contribution in the Nyquist). In the case of cell #2, the series ASR at 700 °C has a value of  $\approx 4.4 \Omega\cdot\text{cm}^2$ , which for a work voltage of 0.6 V would translate into a potential drop of  $\approx 0.21$  V (considering a current density of  $\approx 48.4 \text{ mA}/\text{cm}^2$ ). In the case of operation at 500 °C, considering a series ASR of  $\approx 70.6 \Omega\cdot\text{cm}^2$  and current density of  $\approx 4.68 \text{ mA}/\text{cm}^2$  at 0.6 V, the potential drop increase up to 0.33 V in the electrolyte. These values highlight the necessity of minimizing the electrolyte contribution for realistic operation beyond the model single crystal-based devices shown in this section.

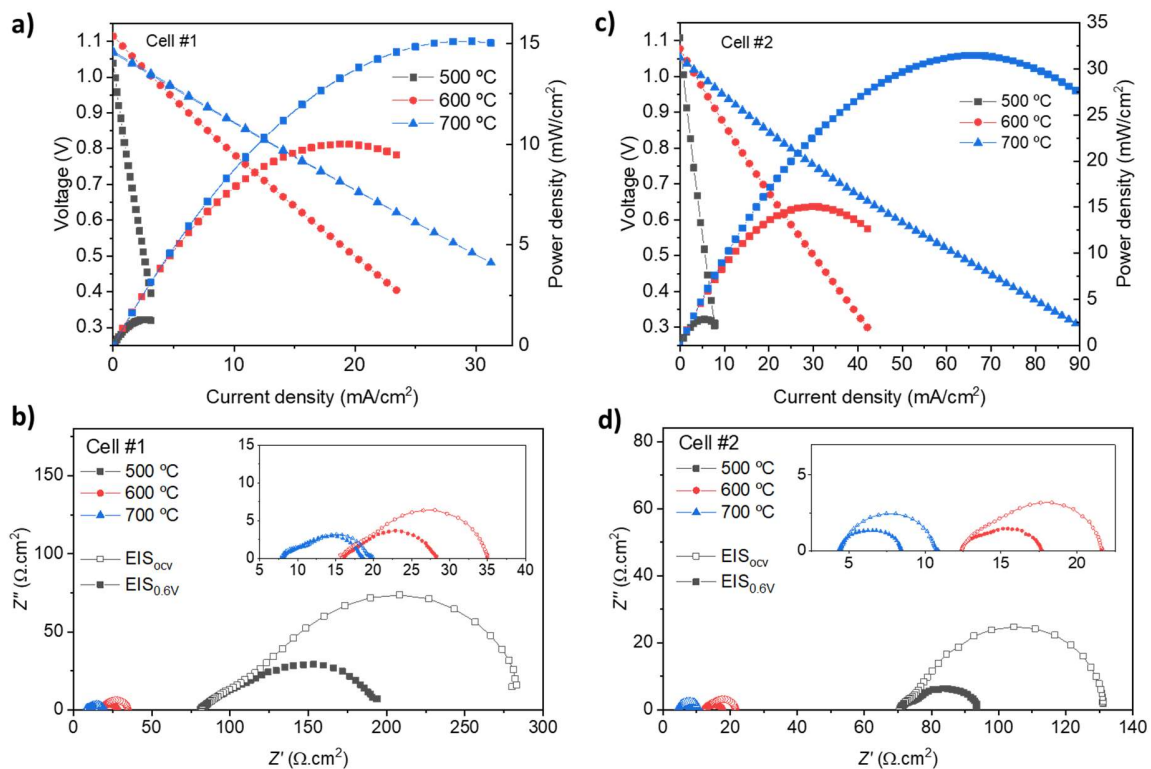


Figure 5-8. Electrochemical characterization of the TF-SOFCs in fuel mode:  $j$ - $V/P$  and Nyquist plots measured in OCV and under 0.6 V of bias for cell #1 (a-b) and cell #2 (c-d).

Given the motivation of studying the use of thin film SOC materials in microelectronics reversible applications (e.g. powering IoT nodes), it would be interesting to discuss the window of operation that these cells could present. In this sense, assuming ideal behavior

for reactants and products of the electrochemical reaction, hydrogen consumption rates can be estimated taking into account the hydrogen semireaction and the current measured (see equations (1-1) and (1-5) in Chapter 1). For instance, a hypothetical device that requires an energy consumption of 8.33  $\mu\text{Wh}$  (i.e. 10 mW for a period of 3 s every hour) could only be powered by the cells studied under certain conditions. Cell #1 could only power it when operated at 700 °C, as the total peak power would barely reach the 10 mW. In the case of cell #2, it could power the device both at 600 °C and 700 °C. Assuming operation at 700 °C for cell #2 with a total power of 10 mW, the supplied current density is  $\approx 17 \text{ mA/cm}^2$ , which translates into a hydrogen consumption of  $\approx 75 \mu\text{L/min}$ . Then, considering a hypothetical device volume of 1  $\text{cm}^3$ , this consumption rate would translate in a continuous operation time of  $\approx 13 \text{ min}$ , or taking into account the actual operation of 3 s every hour, a total operation time of  $\approx 260 \text{ h}$ .

### 5.3.2 Characterization in electrolysis mode

The two reversible SOCs fabricated were characterized in electrolysis mode under the same range of temperatures with a mixed atmosphere of 50%  $\text{H}_2\text{O}:\text{H}_2$  in the hydrogen chamber and synthetic air in the oxygen chamber. Figure 5-9 shows the overall electrochemical characterization performed on both cells. In the case of cell #1, the  $j$ - $V$  curves (Figure 5-9a) showed progressive improvement on the performance when increasing the temperature. Differences in the OCV were also observed, presenting higher OCV values the higher the temperature, in the range of 0.72-0.94 V for this particular cell. This behavior goes in the opposite direction of what is expected from the theoretical point of view –lower OCVs for higher temperatures, taking into account Nernst equation (equation (1-4) in Chapter 1)– and is ascribed to the presence of small leakages in the cell. Current densities of the order of tens of  $\text{mA/cm}^2$  were obtained for the production of  $\text{H}_2$ . Additionally, slight deviations in the linearity of the curves is observed. Figure 5-9b shows the impedance spectra measured at each temperature under OCV conditions and under a DC bias of 1.2 V. Two clear contributions can be differentiated in the Nyquist plots irrespectively of the set temperature nor the DC bias applied, similar to the observations made in SOFC mode. At 700 °C the total ASR measured was  $\approx 14 \Omega\cdot\text{cm}^2$  and  $\approx 17 \Omega\cdot\text{cm}^2$  with 1.2 V of bias and under OCV, respectively. Figure 5-9c shows the  $j$ - $V$  curve obtained for cell #2, with differences in OCV also observed. In this case, the values obtained ranged from 0.84-1.02 V, showing a decreasing trend in OCV as the temperature increased. The current density measured varied in the order of up to 60  $\text{mA/cm}^2$  at 700 °C. Figure 5-9d shows the EIS spectra measured at 500-600 °C. Two main arc contributions can be distinguished in the Nyquist, similar to the observations made for cell #1 but with lower values of ASR. It should be pointed out that the cells present slightly worse performance –in terms of ASR and density current– in electrolysis mode than the observed in fuel cell mode. This is coherent with what has been observed in reversible cells employing mixed ionic electronic conducting (MIEC) electrodes

like  $\text{La}_{0.6}\text{Sr}_{0.4}\text{Co}_{0.2}\text{Fe}_{0.8}\text{O}_3$  (LSCF)<sup>28</sup>, where the materials performance in fuel cell mode is generally higher than in electrolysis operation.

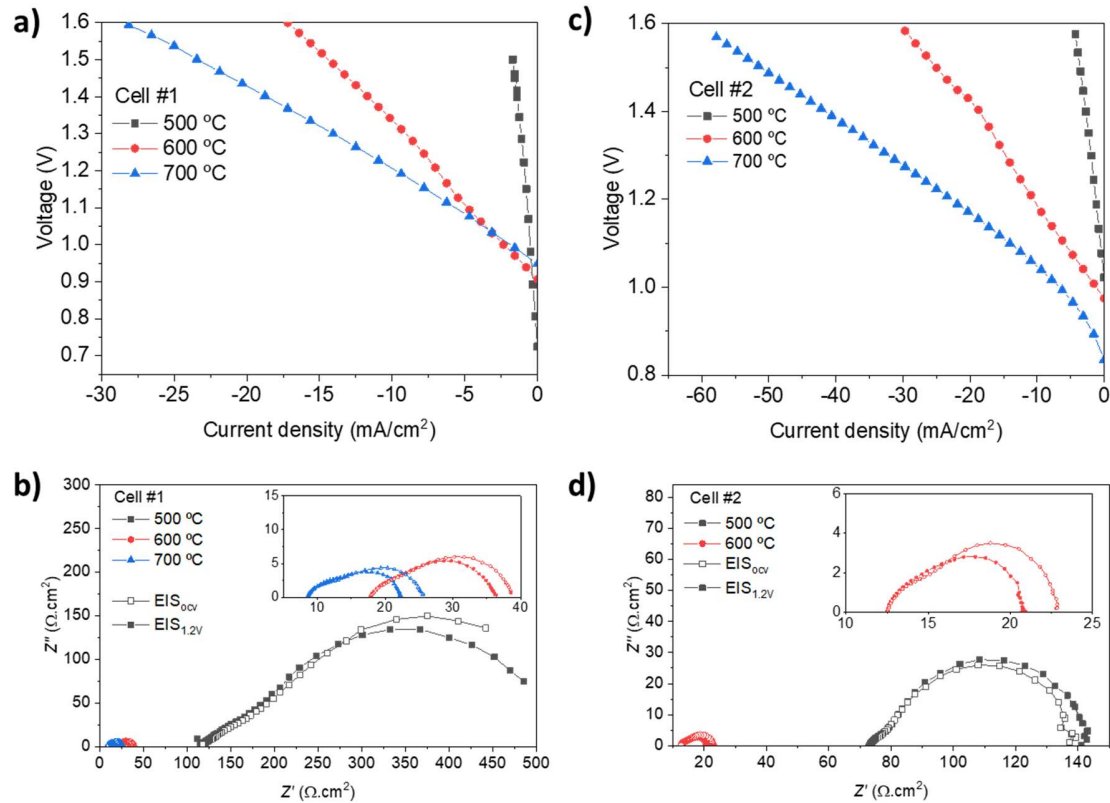


Figure 5-9. Electrochemical characterization in SOEC mode:  $j$ - $V$ / $P$  and Nyquist plots measured in OCV and under 1.62V of bias for cell #1 (a-b) and cell #2 (c-d).

The current density obtained for each of the cells under an operation voltage of 1.3 V (typical operational point for SOEC devices) is represented in Figure 5-10. It can be clearly seen that maximum current density is achieved for cell #2 with almost a 3-fold factor with respect to cell #1. This highlights the importance of achieving proper current collection when employing porous ceria electrodes. Similar to the analysis made for SOFC operation, it would be interesting to calculate an estimation on the hydrogen production rates that could be achieved with these cells. In the case of cell #2, if we assume a final hypothetical hydrogen storage volume of 1  $\text{cm}^3$  for a portable device and an operation voltage of 1.3 V, the measured current density values would yield a maximum hydrogen evolution rate of approximately 145  $\mu\text{L}/\text{min}$  at 700 °C, resulting in  $\approx 7$  minutes to reach a full capacity of hydrogen. Similarly, for the characterization performed at 600 °C the hydrogen production would be  $\approx 62 \mu\text{L}/\text{min}$  (16 minutes for full capacity), while at 500 °C a flow of  $\approx 8.6 \mu\text{L}/\text{min}$  would result in 76 minutes for full hydrogen storage.



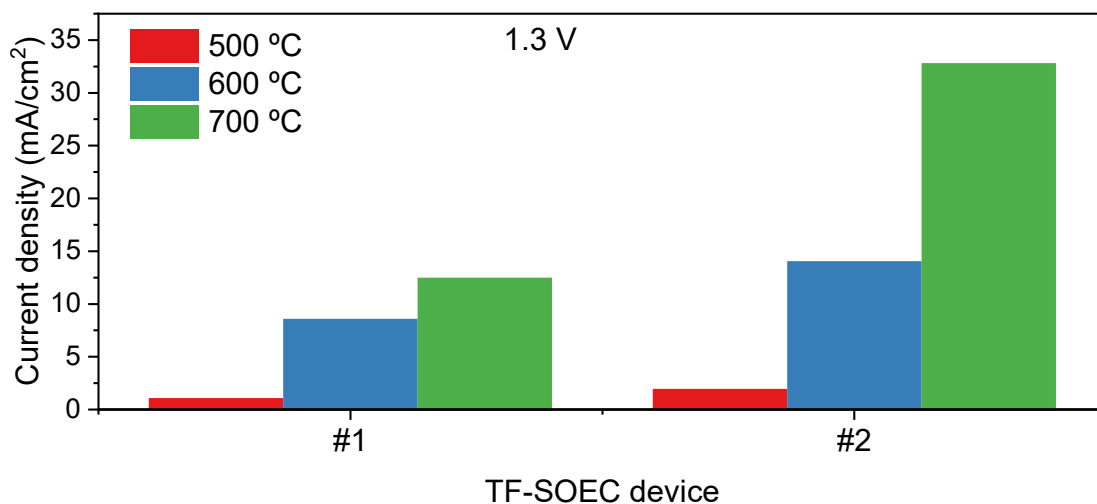


Figure 5-10. Current density obtained at 1.3 V of operation for the two TF-SOECs fabricated.

Figure 5-11 shows the results obtained for the electrochemical characterization of cell #1 when operated for a time period of  $\approx 65$  hours. Particularly, Figure 5-11a shows the evolution of the cell voltage while the cell is operated in galvanostatic mode. Three main steps can be distinguished: step #1 under operation of 10.9 mA/cm<sup>2</sup>, step #2 under operation of 3.1 mA/cm<sup>2</sup> and step #3, under operation at 3.9 mA/cm<sup>2</sup>. It can be clearly seen that the cell shows fast degradation in step #1, while for the rest the degradation is not so evident. In the case of step #2, progressive increase in voltage for the first 10 hours of the step can be observed, while continuous decrease is visualized right after. In the case of step #3, the cell keeps the voltage values for a certain period of  $\approx 10$  h, while right after the voltage decreases until reaching a plateau close to 0.95 V. Figure 5-11b shows the j-V curves obtained at different stages of the degradation test. The j-V measurement performed right before starting the galvanostatic operation showed an OCV of  $\approx 1.0$  V and current densities up to 30 mA/cm<sup>2</sup> at 1.6 V, similar to the observations made in Figure 5-9a. For the j-V measurement carried out between step #1 and #2 ( $\approx 5.8$  h of analysis), the performance of the cell decreases, showing values of 0.5 V of OCV and current below 10 mA/cm<sup>2</sup>. Recovery of the cell in terms of OCV was seen for the j-V measured between steps #2 and #3 ( $\approx 24.7$  h), with a value of 0.72 V. This improvement was not followed by an increase on the current density generated through hydrogen evolution, suggesting worsened electrochemical behavior. By the end of the experiment ( $\approx 64$  h), the cell shows the lowest OCV registered, i.e. 0.27 V, although the current density generated seems to have been partially recovered, measuring up to 15 mA/cm<sup>2</sup>. These differences could be attributed mostly to the large variability in the OCV values measured along the experiments (i.e. in the 0.27-1.0 V range).

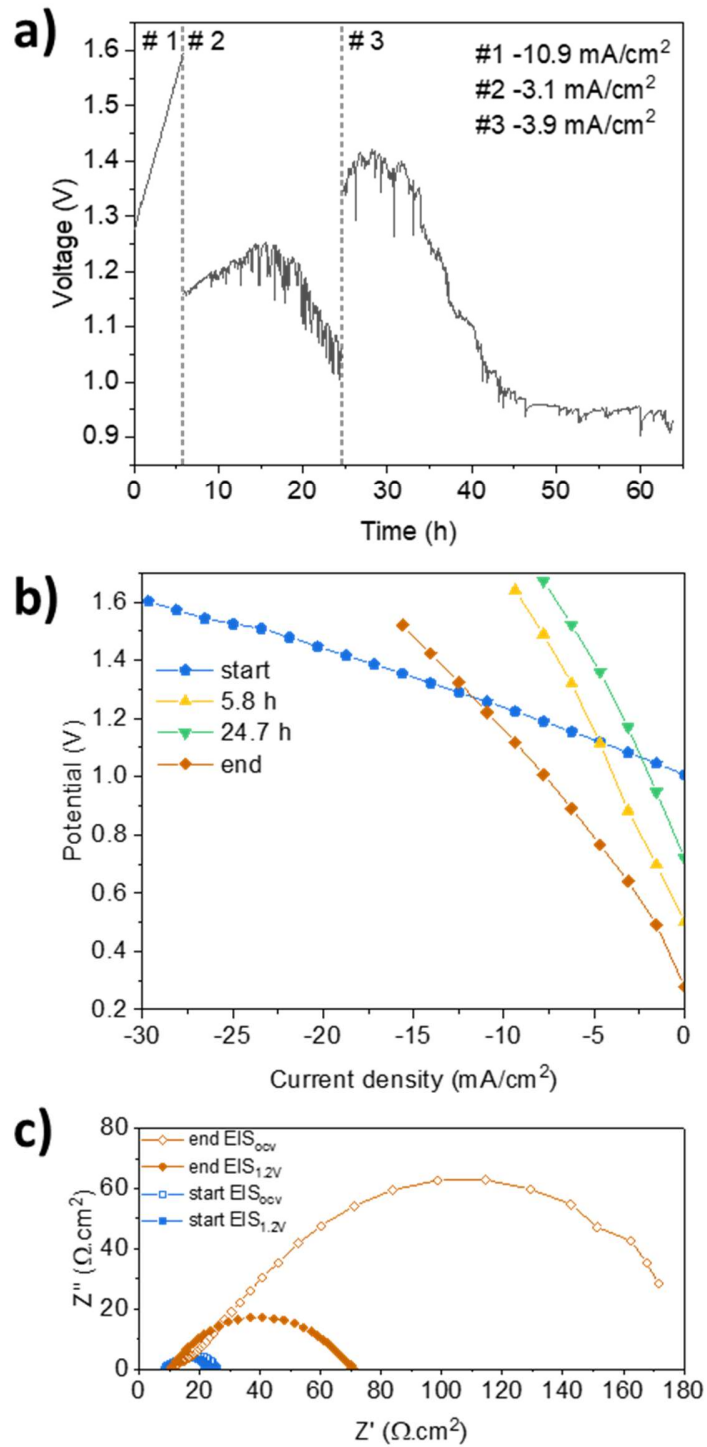


Figure 5-11. Degradation measurement in SOEC mode for cell #1: Measurement of the voltage during SOEC degradation in galvanostatic conditions (a), j-V curves obtained measured at different times during the test (b), impedance spectroscopy arcs obtained before and after the degradation test (c).

Figure 5-11c additionally shows the Nyquist plots obtained by impedance spectroscopy before and after the degradation analysis. It should be pointed out that the Nyquist plots corresponding to the stage before the degradation test coincide with the spectra reported in Figure 5-9b and are repeatedly represented for comparison purposes with the results obtained after the degradation test. It can be seen that the ASR increases substantially after the experiment performed. Specifically, the ASR measured under 1.2 V of DC bias is  $\approx 60 \text{ } \Omega \cdot \text{cm}^2$  while under OCV conditions the ASR shows a much higher value of  $\approx 170 \text{ } \Omega \cdot \text{cm}^2$ . Such large difference in the ASR values before and after the degradation test, and also for the measurements under OCV and under bias can be explained by the behavior observed in the  $j$ -V curve. The shape of the  $j$ -V curve by the end of the measurement points to unstable electrochemical behavior due to the low OCV registered –i.e. gas leakage in the cell chambers– and high cell resistance. This is observed through the large variation in voltage needed in order to increase the current density. There are works that have shown faster degradation of reversible SOCs in electrolysis mode than in fuel cell operation<sup>4,29,30</sup>, which might explain the rapid change in the  $j$ -V curves and the large increase in the ASR. Some of the mechanisms suggested for the rapid degradation in electrolysis mode are faster  $\text{SrZrO}_3$  formation at the electrolyte/electrode interface and accelerated Sr segregation phenomena due to depletion of oxygen vacancies as reported in Ref.<sup>30</sup> In this work, the authors present simulated data on the evolution of the concentration of incorporated oxygen in LSCF, showing an increase on the oxygen content under electrolysis conditions. They relate the increase in the oxygen content as a possible driving force for the precipitation of SrO towards the surface. In addition to that, they propose a mechanism in which SrO interacts with steam forming  $\text{Sr}(\text{OH})_2$  in gas form, which then can be transferred to the electrolyte interface through the gas carrier, leading to the formation of the strontium zirconate species. Nonetheless,  $\text{SrZrO}_3$  formation is unlikely to happen in the device under study in this chapter, given the dense nature of the oxygen electrode. A systematic study on the degradation of dense thin film SOECs would be of potential interest in order to shed light on the different degradation mechanisms that these materials can experience.

#### 5.4 Integration of thin film solid oxide fuel cells in silicon supported devices: micro solid oxide fuel cells

$\mu$ SOFCs have been fabricated in order to study them as suitable power devices in systems in combination with microelectronics technologies. As it has been discussed in the previous section, the need of reducing the electrolyte contribution to the overall ASR is critical for reducing overpotential losses. Reducing the electrolyte thickness and integrate the cell in a microdevice is a promising strategy for achieving this goal. Additionally, integrating the ceramic cells with silicon technologies makes the final device more feasible to realistic scenarios of application in this sector.

#### 5.4.1 Cell architecture and device setup

The  $\mu$ SOFCs were fabricated by combining the deposition of thin film oxide layers by PLD with microfabrication processing techniques employed for the release of the ceramic membranes, as described in Chapter 2. Two different microcells were successfully fabricated and electrochemically characterized as part of the work presented in this thesis. Details on the cells fabricated and characterized can be found in Table 5-4.  $\mu$ SOFC #1 was fabricated by employing LSC82 as the oxygen electrode and porous SDC as the hydrogen electrode, similar to the material architecture employed in the TF-SOFCs characterized in section 5.3. Additionally,  $\mu$ SOFC #2 was fabricated with LSC64 as the oxygen electrode, while the hydrogen electrode was fabricated by depositing a heterostructure of a dense film of LSCrMn and a porous SDC layer, like the one studied in Chapter 3. Both cells presented a dense thin film YSZ electrolyte layer fabricated according to the procedure described in Chapter 2 for the deposition of large area thin films and based in previous experience from the group<sup>31-34</sup>.

Table 5-4. Description of the components of the  $\mu$ SOFCs characterized.

Sample	CC	Hydrogen Electrode	Electrolyte	Oxygen Electrode	CC
$\mu$ SOFC #1	Pt <sub>sput</sub>	Porous SDC	YSZ/CGO <sub>buff</sub>	LSC82	Pt <sub>sput</sub>
$\mu$ SOFC #2	Pt <sub>sput</sub>	LSCrMn + porous SDC	YSZ/CGO <sub>buff</sub>	LSC64	Pt <sub>sput</sub>

Figure 5-12 shows SEM cross-section microstructures for both  $\mu$ SOFC #1 –panel (a)– and #2 –panel (b)–, with the different layers present indicated in each case. The micrographs were obtained after the electrochemical characterization was performed.

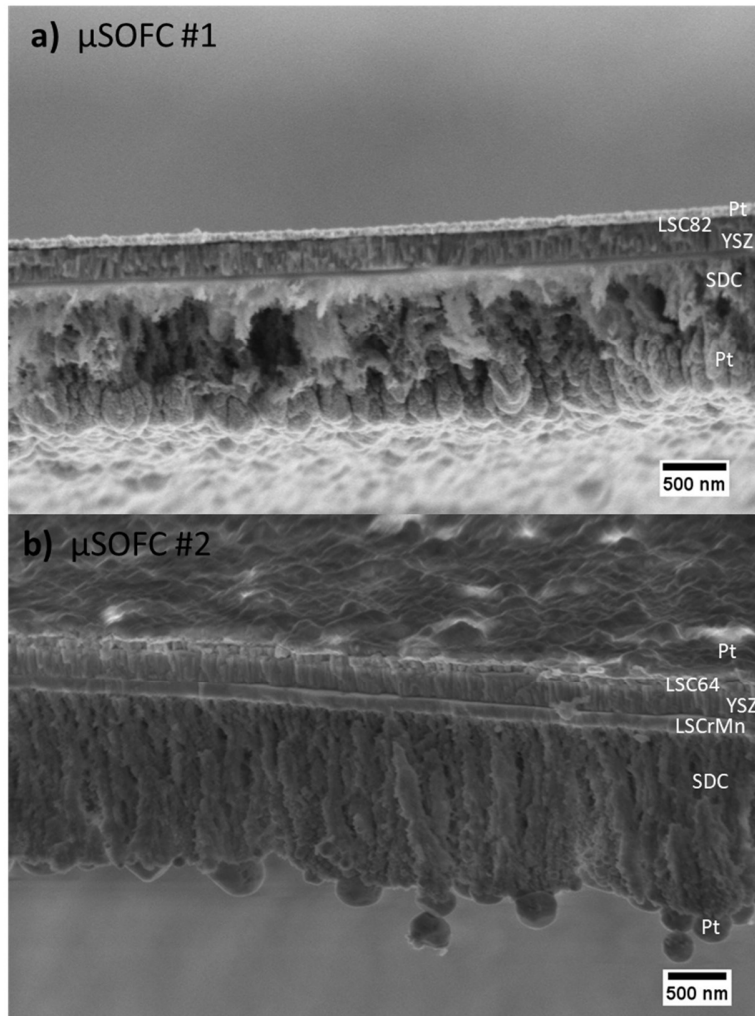


Figure 5-12. SEM cross-section micrographs showing all the functional layers of  $\mu$ SOFC #1 (a) and #2 (b).

Columnar growth of a dense YSZ electrolyte with  $\approx 200$  nm in thickness can be observed in both cases. The oxygen electrode (either LSC82 or LSC64) was about  $\approx 100$  nm thick while the LSCrMn hydrogen electrode layer in  $\mu$ SOFC #2 was  $\approx 150$  nm thick. The porous SDC layer was  $\approx 800$  nm thick in  $\mu$ SOFC #1 and  $\approx 1.3$   $\mu$ m in  $\mu$ SOFC #2. Platinum layers were deposited by a sputtering process as current collectors on top of the electrode materials for both microcells. It can be seen that the layers fully cover the dense LSC-based electrodes as

well as the porous SDC layer in  $\mu$ SOFC #1, whereas for  $\mu$ SOFC #2 the platinum does not cover the film homogeneously (cf. later discussion in section 5.4.3).

#### 5.4.2 Electrochemical characterization

Figure 5-13 shows the results obtained for the electrochemical characterization of  $\mu$ SOFCs #1 –panels (a-b)– and #2 –panels (c-d)– under wet hydrogen gas (3 % H<sub>2</sub>O in H<sub>2</sub>) in the fuel chamber and synthetic air in the oxygen chamber. In the case of  $\mu$ SOFC #1, Figure 5-13a shows the j-V and j-P plots obtained at 640 °C. The OCV was 0.75 V, a relatively low value most likely indicative of the presence of gas leakages in the system. The current densities measured were up to 30 mA/cm<sup>2</sup>, considering the dimensions of the membrane (400x400  $\mu$ m<sup>2</sup>). The resulting power density extracted was  $\approx$  14 mW/cm<sup>2</sup> at the maximum value measured. This value is lower than in other works reported by the group<sup>33,34</sup>, although comparable performance could be expected with respect to Ref.<sup>33</sup> taking into account the temperature factor (much lower in the case presented here) and the differences in the oxygen electrode employed –i.e. LSC64 in contrast to the LSC82 electrode employed in this work. In any case, the performance is also lower when compared to literature values like the studies from Evans<sup>35</sup> or Baek<sup>36</sup> et al, which show higher power densities at temperatures below 500 °C. Figure 5-13b shows the evolution of the OCV with time measured right after the j-V curve characterization. It can be seen that the values recorded were quite unstable. The oscillations and step-like variations observed in the voltage values correspond to changes in the gas flow of the fuel and oxidizing chambers, carried out with the aim of adjusting the OCV towards higher values. The instability of the electrochemical activity of the cell did not allow to perform further characterization on this  $\mu$ SOFC. Regarding  $\mu$ SOFC #2, the current and power densities obtained (see Figure 5-13c) were much lower than the values expected –i.e. values up to 0.3 mA/cm<sup>2</sup> and 0.16 mW/cm<sup>2</sup>, respectively–. These values are at least two orders of magnitude less with respect to the results obtained for  $\mu$ SOC #1 and even lower than from the literature values discussed before<sup>33–36</sup>. Such low performance was unexpected since  $\mu$ SOFC #2 employs LSC64 instead of LSC82 as the oxygen electrode, which is expected to show better performance due to the increased amount of dopant in the phase<sup>29</sup>. The limited electrochemical activity observed for the microcell was then attributed to poor current percolation. A possible reason might be the degradation of the platinum used for collecting the current in the electrodes. This is further discussed in the next session, focused in the post-mortem characterization carried out on the cells. It can also be observed that, despite the low performance observed in terms of current and power densities, the OCV value recorded for  $\mu$ SOFC #2 was  $\approx$  1 V, indicating higher stability in terms of gas leakages. This is further observed in Figure 5-13d, which shows the evolution of the OCV recorded for a period of 50 min. In the plot, a much more stable OCV signal close to 1 V is observed, with some spikes towards higher values. The OCV progressively decreased to  $\approx$  0.95 V by the end of the measurement. Due to the low performance observed for  $\mu$ SOFC #2 no further electrochemical characterization was performed on this cell.

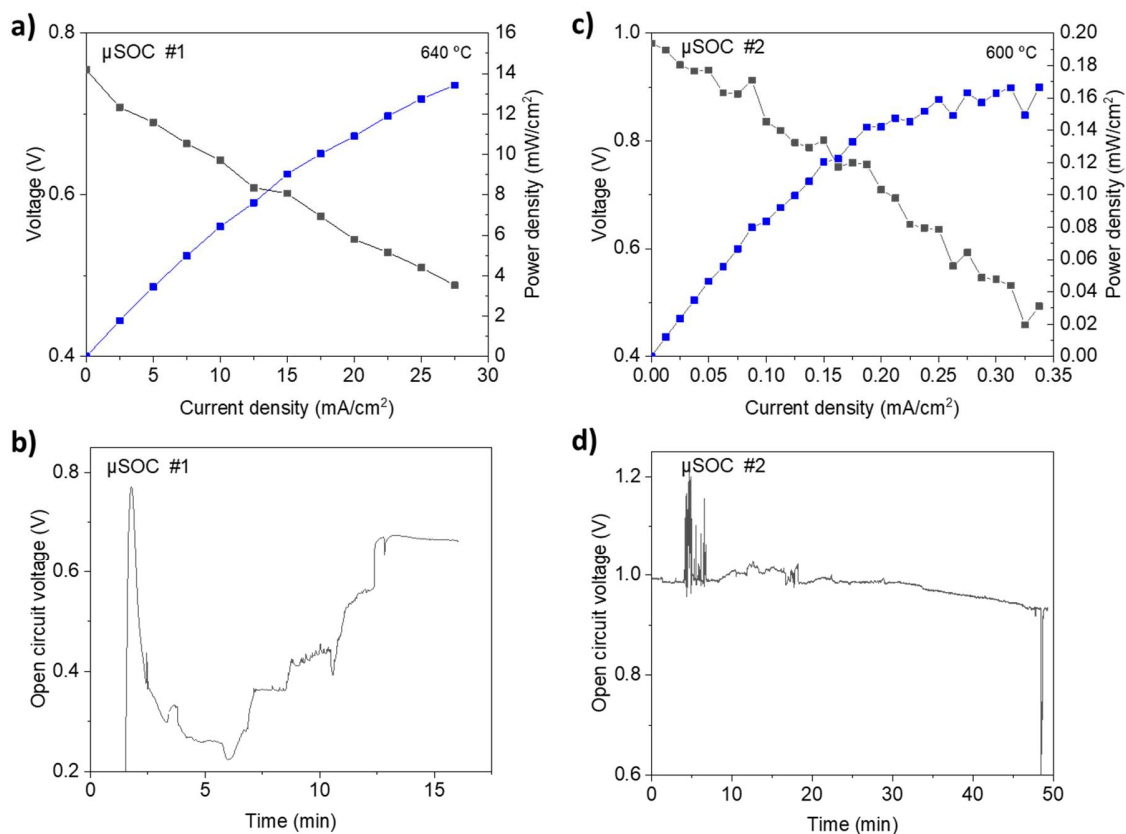


Figure 5-13. Electrochemical characterization of the  $\mu$ SOFCs characterized:  $j$ - $V$ / $P$  plots and measurement of the OCV evolution with time after the measurement for  $\mu$ SOFC #1 (a-b) and  $\mu$ SOFC #2 (c-d), respectively.

### 5.4.3 Post-mortem structural characterization

In order to make a proper evaluation on the behavior observed during the electrochemical analysis of  $\mu$ SOFC #1 and #2, post-mortem observations and structural characterization were performed on the devices. Figure 5-14 collects part of the analysis performed on  $\mu$ SOFC #1. In particular, Figure 5-14a-b show photographs of the setup before the measurement and right after the cell was set back to room temperature, respectively. The top side of the chip (oxygen electrode side) can be visualized from the central hole of the ceramic spring holder piece. Evolution of the surface morphology of the chip is confirmed by visual observation when compared to the as deposited cell, characterized by a homogeneous and reflective surface. This evolution is more evident in Figure 5-14c-d, which show optical micrographs of the top side of the sample before and after operation. From these micrographs it is clear that the surface morphology of the sample evolves considerably after the electrochemical characterization performed at high temperature. The conductivity of the chip surface after the measurement was checked with a multimeter, observing a large increase in the resistance of the current collector.

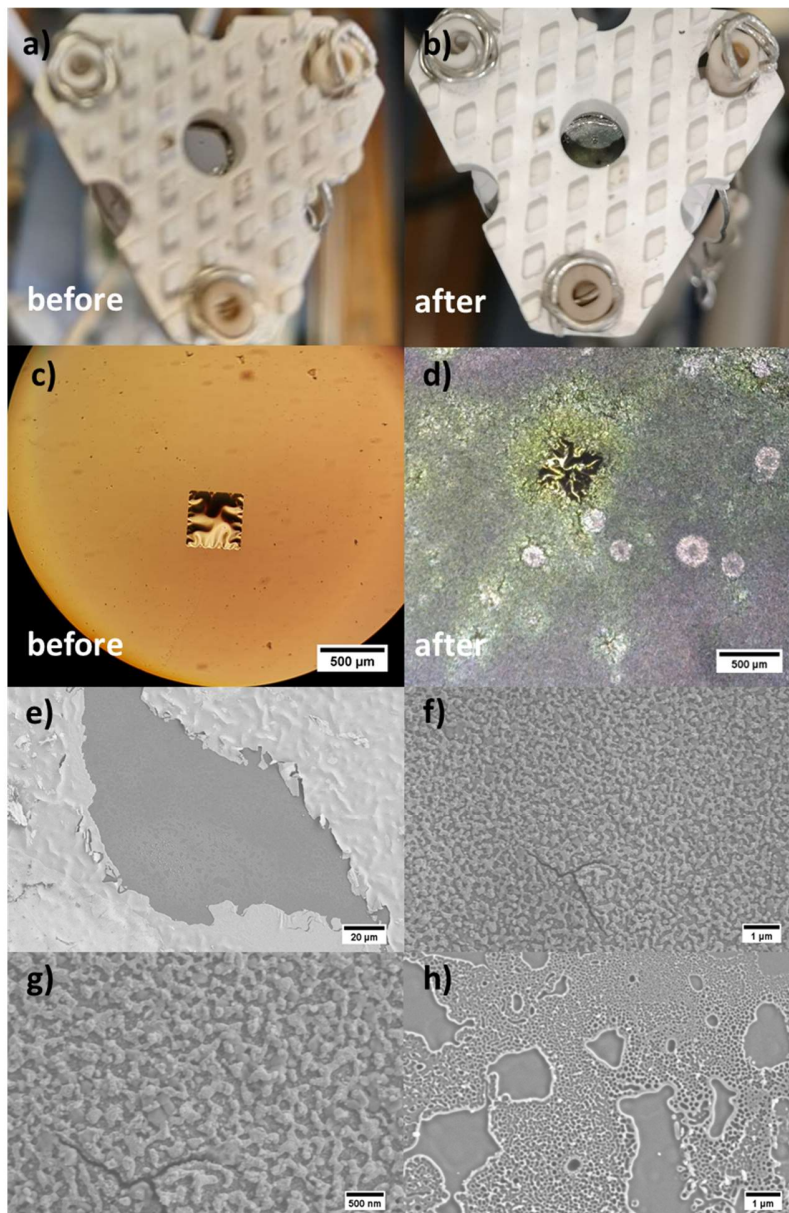


Figure 5-14. Post-mortem characterization of  $\mu$ SOFC #1. Pictures of the setup before (inset) and after the electrochemical characterization (a-b). Optical micrograph of the oxygen electrode side of the chip (c-d). SEM micrographs at different magnifications of the oxygen electrode side (e-f).

Additional information can be found in Figure 5-14e-f, which show two SEM micrographs obtained at different magnifications of this region of the sample. In panel (e) partial delamination of the platinum layer can be visualized, probably generated by the mechanical stresses induced during sample removal. Zoomed-in regions of the platinum layer are represented in Figure 5-14f-g. Evolution of the platinum can be observed, with clear signs of dewetting, resulting in loss of layer homogeneity. Moreover, a micrograph of the central region of panel (e) –i.e. the delaminated surface– is shown in panel (h). In here, signs of



dewetting can also be observed in the platinum layer, shown by the appearance bubble-like features and spherical open spaces. The morphology evolution of the surface is then attributed to the degradation of the platinum layer employed for collecting the current through the dewetting process. Most interestingly, the ceramic membrane –i.e. the functional  $\mu$ SOFC component– was seemingly intact after the experiment, proving that the mechanical stability of the membrane was not a limiting factor in the performance and lifetime of this sample.

Figure 5-15 Figure 5-15a-f shows several SEM micrographs obtained at different magnifications and in different regions of the backside (hydrogen electrode side) of the  $\mu$ SOFC. From the micrographs it can be clearly observed that the platinum layer evolves after the experiment performed. While the membrane side –central square-like region in panel (a)– seems to preserve the interconnection along the platinum layer despite the microstructure evolution, the platinum in the walls seem to show higher degree of dewetting resulting the observation of more open space areas –panels (c-f)–. This is probably caused by the deposition of a thinner layer of metal during the sputtering process, due to the vertical geometry of the wall. Some cracks are also observed in the membrane region, possibly causing current percolation losses. Nevertheless, these cracks might have also appeared during the mechanical extraction of the cell from the ProboStat station, so the correlation with the low performance is not straightforward. Moreover, some regions seem to lack the presence of the platinum layer –panel (c)–, with isolated porous SDC areas exposed. Most interestingly, the notch between the membrane and the silicon chip backbone was analyzed –panels (d-f)–. It can be seen that the notch does not show full coverage of neither SDC nor platinum. Although some presence of platinum interconnections can be observed in localized positions, the overall spatial separation observed might cause the loss of a significant contribution of electrical current resulting from the hydrogen oxidation reaction, hence deriving in the low performance observed. These observations highlight the need of employing specialized current collectors that withstand the experimental conditions set for the operation of  $\mu$ SOFCs.

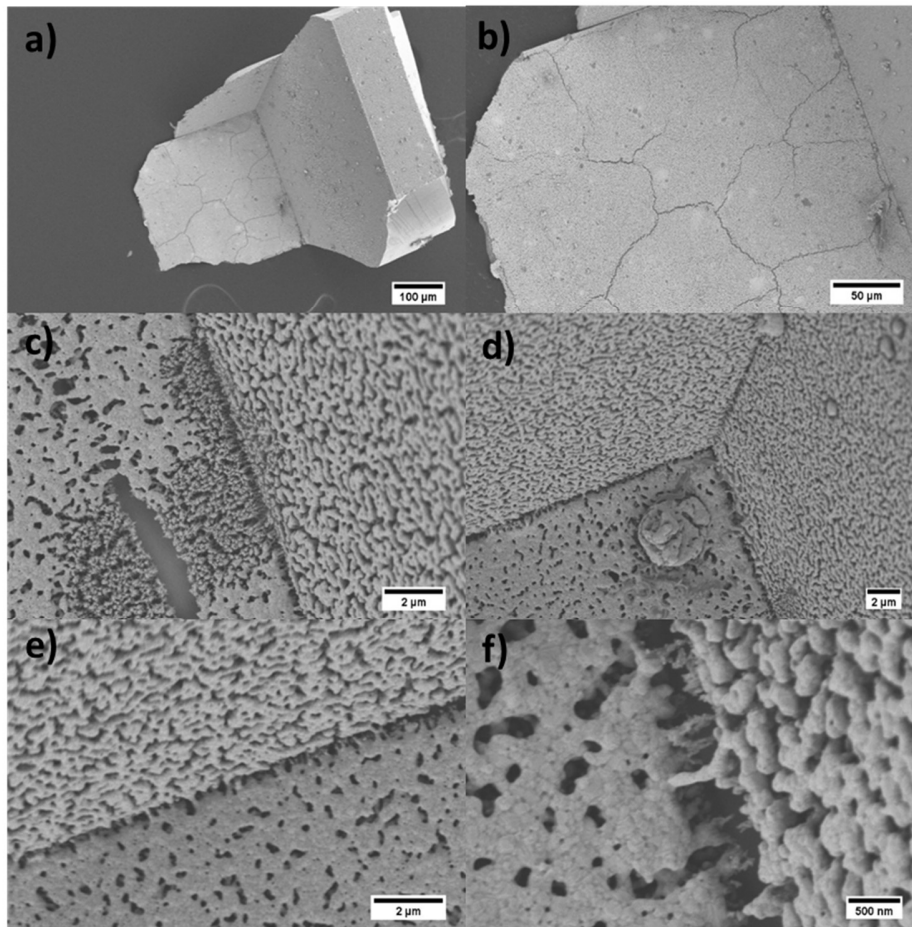


Figure 5-15. Post-mortem characterization of  $\mu$ SOFC #1: SEM micrographs at different magnifications of the hydrogen electrode side of the free-standing membrane (a-f).

Regarding  $\mu$ SOFC #2, Figure 5-16 shows the post-mortem characterization performed on the cell. Panel (a) shows the  $\mu$ SOFC setup before and after the characterization of the cell. The ceramic paste was applied until obtaining a smooth layer that may lead to a sealing free from imperfections during the curing process. No major cracks or fractures of the sealant were observed after coverage of the silicon-supported  $\mu$ SOFC sample. Platinum paste was brushed in the surroundings of the membrane in order to facilitate lateral current percolation. This was done to minimize the detrimental effects caused by dewetting processes like the ones observed in  $\mu$ SOFC #1. It can be clearly seen that the membrane withstood the thermomechanical stresses –panels (b-c)– derived from the operation at high temperature and the exposure in fuel cell atmospheres –i.e. the presence of hydrogen and oxygen in both the anode and cathode chambers, respectively–. Furthermore, there seems to be some evolution in the surface layer morphology, probably caused by dewetting of the platinum current collector, similar to the case with  $\mu$ SOFC #1. This is further analyzed in Figure 5-16d-f, in which cross-section SEM micrographs corresponding to different regions of the  $\mu$ SOFC tested are depicted. In Figure 5-16d a region of the membrane cross-section

close to the notch with the silicon wall is observed. The micrograph shows the presence of the different layers, as described in Table 5-4, and their morphology in this area –please note that a high magnification micrograph taken in this region was employed to describe the cell architecture in Figure 5-12. It is of particular interest the discontinuity observed in LSCrMn –highlighted with the dotted rectangle. The absence of this layer in the junction with the silicon wall might cause the loss of current percolation, which was one of the limitations that were expected to be solved with the addition of LSCrMn. Interestingly, a seemingly continuous platinum layer on top of the LSC64 is observed, though the visible roughness in panel (f) may indicate the appearance of the dewetting process previously discussed. In the side containing the porous SDC electrode, the platinum initially deposited on top of it presents a spherical microstructure, observed as a scattered distribution of Pt particles along the surface, as shown in Figure 5-16e and in the dotted area in Figure 5-16f.

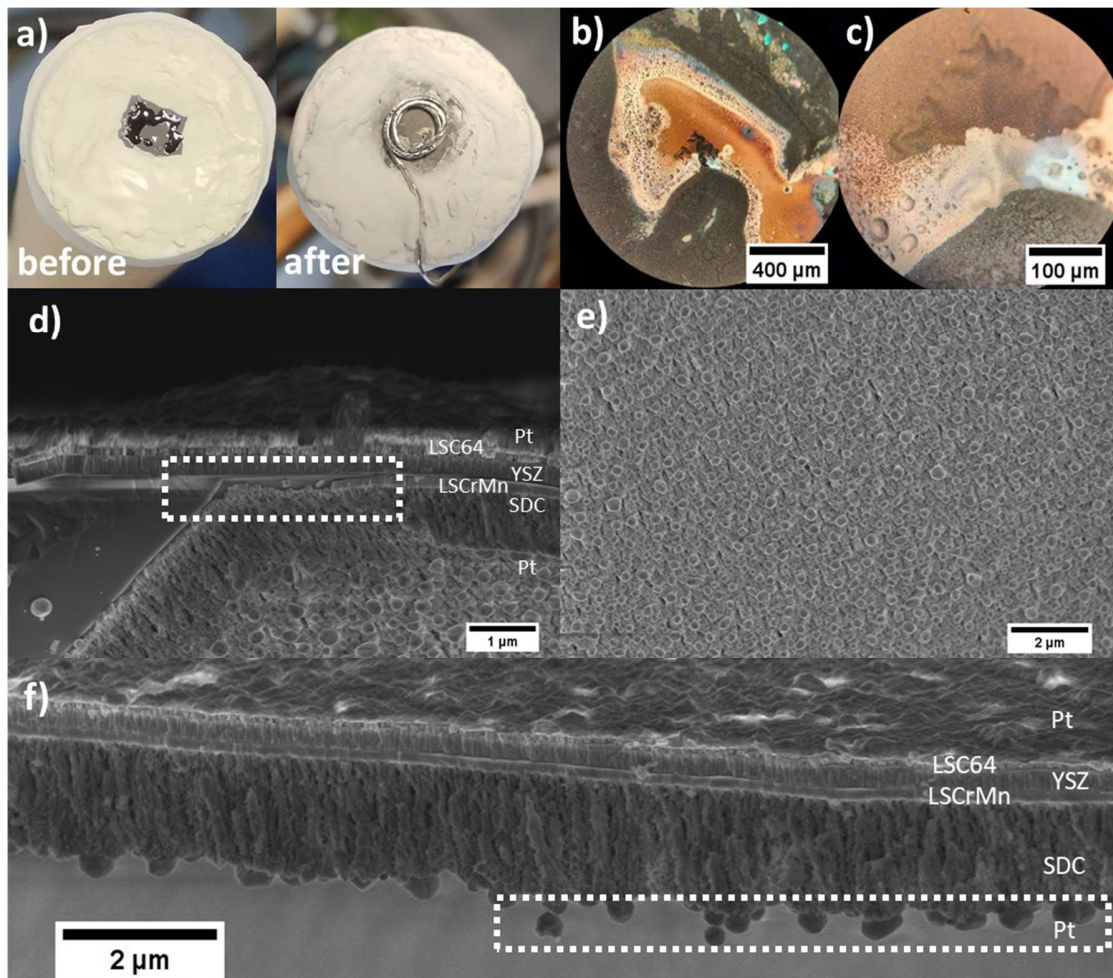


Figure 5-16. Post-mortem structural characterization of  $\mu$ SOFC #2. Picture of the cell setup after the measurement (a). Optical micrographs of the oxygen electrode side of the chip (b-c). SEM cross-section micrographs with focus on the hydrogen electrode side (d-f).

This resulted in the complete loss of percolation in the electrode (i.e. absence of any interconnection between the platinum particles), which might raise from the fact that the deposition of the platinum layer might not had been thick enough in the first place due to experimental limitations, or that the platinum layer suffered from dewetting. Given the differences observed with respect to  $\mu$ SOFC #1, which showed enough coverage of platinum in the hydrogen electrode site, a combination of both effects is more likely. It should be noted that the porosity of the SDC implies that the platinum deposited on top presents higher roughness and surface energy, potentially being easier to degrade than the planar counterpart on the cathode side. The need of reaching a critical thickness of platinum that results in proper current percolation has been proven to be a determining factor in the performance of the  $\mu$ SOFCs fabricated in this thesis. This is likely to be the main reason responsible of the poor performance observed for  $\mu$ SOFC #2.

## 5.5 Remarks on the experimental limitations for the operation of thin film-based solid oxide cells

The findings described in this chapter are the result of dedicated efforts for exploring different thin film based SOCs. Several architectures were employed –i.e. electrolyte supported cells (symmetric and asymmetric) and free-standing  $\mu$ SOFC membranes–. For this reason several experimental setups needed to be tested in order to properly characterize the cells under operation conditions. This resulted in performing a set of trials that allowed to identify some of the most important limitations for operating TF-SOCs and specifically,  $\mu$ SOFCs. With regard to single crystal electrolyte-supported devices, the major limiting factor observed has been the instability of the OCV, likely caused by the presence of partial leakages, as commented in sections 5.2 and 5.3. Despite this limitation, in general terms the TF-SOCs studied in this thesis have presented far less difficulties for their electrochemical characterization than for the case of  $\mu$ SOFCs.

Figure 5-17 depicts an overview of  $\mu$ SOFC assemblies other than  $\mu$ SOFCs #1 and #2 discussed in the previous section, that resulted in unsuccessful electrochemical characterization tests. An example of the application of the sealant and the setup for the electrochemical characterization of a  $\mu$ SOFC is presented in Figure 5-17a. The setup included the incorporation of gold paste and a platinum grid in order to facilitate the collection of current, as well as some alumina felt to alleviate possible mechanical stresses affecting the stability of the silicon substrate. Despite this, the appearance of imperfections and cracks in both the ceramic sealant and on the silicon substrate was observed (highlighted by dotted circles in the picture and optical micrographs). Other tests involved changing the ceramic sealant formulation to a different one based on zirconia (see specifics in Chapter 2) characterized by less viscosity and a curing process carried out at higher temperatures than for the previous alumina based formulation. Examples of the application of this sealant are found in Figure 5-17b-c (in addition to the case of  $\mu$ SOFC #2). Although

this sealant seemed to ease the application of a smoother layer, the appearance of cracks in the sealant –panel (b)– and in the silicon substrate was observed after placing the cell at the temperature of operation, even leading to membrane breaking –panel (c)–.

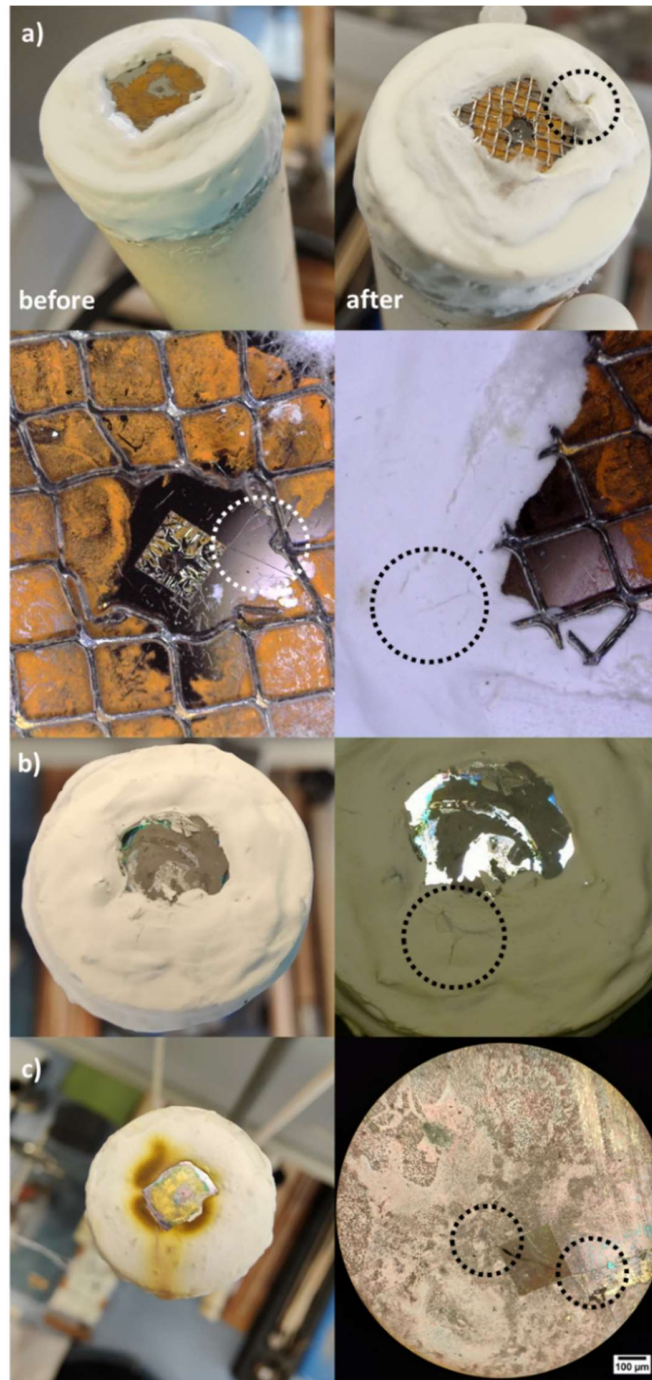


Figure 5-17. Examples of different unsuccessful trials for characterizing  $\mu$ SOFCs under operation conditions.

Possible causes for the formation of these cracks might be in the application of an inhomogeneous layer of sealant, although this does not seem to be the case for the latter examples exposed. Most likely, the cracks might appear due to the mismatch in the coefficient of thermal expansion between the ceramic layers and the silicon chip<sup>37-39</sup>. Additionally, sudden changes in temperature due to the appearance of hot spots due to partial combustion coming from leakages in the system might favor the appearance of these cracks, as observed in Figure 5-17c. In order to minimize these effects, a variation of the design of the alumina sample holder was performed, as described in Chapter 2. The new design on the holder was expected to ease the application of the sealant, as well as to facilitate setting up the electrical contacts for to the cell. No practical difference was observed when trying to set up new  $\mu$ SOFC samples with the new design though.

In summary, during the process of the work presented in this chapter several approaches were followed in order to set up and characterize the electrochemical performance of  $\mu$ SOFCs. Major limitations were met when trying to translate conventional methodologies established in the functional ceramics field into single crystal and more specifically silicon-based technologies. The limitations discussed could be reduced to a single issue, i.e. integration of both metallic and ceramic components in a single device with application at relatively high temperatures. This lead to the observation of two main experimental inconveniences when trying to measure the devices under operation conditions:

- Differences in the thermal expansion coefficient between the silicon substrate and the ceramic sealant lead to the formation of cracks in the ceramic and metallic phases ultimately provoking sample fracture.
- Microstructure evolution of the metallic phases (sputtered platinum) employed as current collectors as a consequence of the exposure to high temperatures (dewetting) resulted in the loss of current percolation in the device.

These phenomena translated into the electrochemical characterization measurements in the form of OCV instabilities and poor current collection, critically hindering the performance of the  $\mu$ SOFCs.

## 5.6 Conclusions

This chapter has focused on the study of thin film based SOC systems and their characterization in full device under different cell architectures. In the first part of the chapter, the characterization of a symmetric cell based on thin film LSCr electrodes and its evolution upon redox cycling is reported. The cell was tested in the 650-750 °C range with several cycles performed at each temperature, for which the atmosphere gases set in the chambers were reversed. The results showed promising self-healing behavior, observing performance recovery after carrying out the exchange. This was less evident in the first part of the analysis due to OCV instability, but it was clearly observed in the last cycles performed at 750 °C. Microstructure characterization after the analysis showed evolution of the surface and current collector degradation.

The second part of the chapter presents the electrochemical characterization of prototypical reversible thin film SOCs, operated both under SOFC and SOEC modes. Two cells were fabricated, with porous SDC as the hydrogen electrode and dense LSC82 as the oxygen electrode. Additionally, gold (cell #1) and platinum (cell #2) sputtered layers were applied to the hydrogen electrode in order to analyze the differences in cell performance stemming from the current collector employed in the porous layer. The results obtained showed higher performance for the TF-SOC presenting the platinum layer. Specifically, up to  $\approx 3$ - and 2-fold enhancement factors were observed for the current density measured in SOFC and SOEC modes, respectively. Degradation measurements carried out in SOEC mode for cell #1 during  $\approx 60$  hours showed cell degradation manifested as decrease in the OCV values, increase of the slope in the  $j$ -V curve and increase of the ASR measured under both OCV and 1.2 V DC bias. Likely events for the degradation observed are the appearance of cell leakages due to sample and sealing cracking, loss of current collection due to dewetting of the metallic phases and electrode material degradation. Further microstructural and chemical characterization would be needed to confirm these causes.

The third section of this chapter has focused on the integration of all-ceramic thin film electrodes in  $\mu$ SOFCs based on fabrication of free-standing membranes supported in silicon.  $\mu$ SOFCs were successfully fabricated and their performance was characterized following similar approaches than for the previous TF-SOCs. Two cells were analyzed with slight variation in the electrodes employed.  $\mu$ SOFC #1 employed the same materials and current collectors than those employed in the electrolyte supported cell #2.  $\mu$ SOFC #2 was fabricated with LSC64 and a dense LSCrMn layer deposited between the electrolyte and porous SDC. The power density obtained was lower than the initial expectations, with a maximum of  $\approx 14$  mW/cm<sup>2</sup> for  $\mu$ SOFC #1 and  $\approx 0.17$  mW/cm<sup>2</sup> for  $\mu$ SOFC #2. Post-mortem characterization analyses carried out in the  $\mu$ SOFCs after operation showed current percolation loss due to platinum dewetting. This was the most likely cause of the low performance observed, particularly severe for the case of  $\mu$ SOFC #2. Additional limitations in the form of layer

discontinuities between the membrane and the silicon wall notch were observed for the LSCrMn and platinum layers. This might have presented an additional contribution to the loss of current extracted from the electrochemical reaction. A detailed discussion on the challenges and limitations experienced when operated thin film-based SOCs with especial focus on  $\mu$ SOFCs is given in the end of the chapter.



## 5.7 Future work

The work developed in this chapter has presented promising concepts for SOC devices integrating thin film electrode materials in different cell architectures and systems. Relevant properties for performance recovery were found in symmetric cells after exchanging the chamber atmosphere. Reversible thin film-based electrolyte-supported SOCs were characterized in SOFC/SOEC modes and proof-of-concept  $\mu$ SOFCs supported in silicon were tested. Despite the promising features and properties experienced in this work, several limitations hindered the measurements carried out and the performance of the cells, as commented in section 5.5 and throughout the chapter. In addition to that, there is also room for device improvement and optimization based on the materials studied in this thesis.

In first place, reliable electrochemical setups for the characterization of fully assembled cells based on single crystal electrolyte- and silicon-supported architectures need to be further explored. This includes the optimization of the current collector and interconnects in order to prevent current losses and to guarantee the full characterization of the electrochemical activity of the materials employed. Another critical aspect to optimize would be the sealing procedure. Integration of single crystals (either YSZ or Si-based) with established ceramic setups based on alumina holders has proven to be difficult to reach, especially under the experimental conditions employed. For that reason, dedicated efforts to setup optimization with particular focus on cell assembly and sealing compatibility is a must for characterizing thin film SOCs. Some possibilities could involve the use of custom made sample holders that reduce the number of junctions to be sealed and alleviate the effect of mechanical stresses during sealant curing. Changing the sealant nature to glass-like formulation with higher curing temperatures (closer to the operational temperature) and higher robustness against gas leakage would be also advantageous.

Regarding materials optimization for the cell applications discussed in this chapter, several of the materials studied throughout this thesis have shown promising electrochemical properties. In particular, the LSCrMn-SDC dense nanocomposite reported in Chapter 3 showed enhanced electrochemical activity for symmetric applications –i.e. under both air and hydrogen atmospheres–. Because of this and its stability against degradation it would be an interesting choice for studying its behavior on redox cycling processing. With respect to the asymmetric full cell measurements performed, the NiCGO hydrogen electrode films investigated in Chapter 3 showed improved electrochemical activity while keeping a dense microstructure, which would be of potential interest for the devices studied. Additionally, part of the oxygen electrodes investigated in Chapter 4 showed high electrochemical activity and promising thermal stability. Combination of these materials could potentially result in highly performing thin film SOCs with large stability over time.

## References

- (1) Zhang, M.; Du, Z.; Zhang, Y.; Zhao, H. Progress of Perovskites as Electrodes for Symmetrical Solid Oxide Fuel Cells. *ACS Appl. Energy Mater.* **2022**, *5* (11), 13081–13095. <https://doi.org/10.1021/acsaem.2c02149>.
- (2) Zamudio-García, J.; Caizán-Juanarena, L.; Porras-Vázquez, J. M.; Losilla, E. R.; Marrero-López, D. A Review on Recent Advances and Trends in Symmetrical Electrodes for Solid Oxide Cells. *J. Power Sources* **2022**, *520*, 230852. <https://doi.org/10.1016/j.jpowsour.2021.230852>.
- (3) Gómez, S. Y.; Hotza, D. Current Developments in Reversible Solid Oxide Fuel Cells. *Renew. Sustain. Energy Rev.* **2016**, *61*, 155–174. <https://doi.org/10.1016/j.rser.2016.03.005>.
- (4) Mogensen, M. B. Materials for Reversible Solid Oxide Cells. *Curr. Opin. Electrochem.* **2020**, *21*, 265–273. <https://doi.org/10.1016/j.coelec.2020.03.014>.
- (5) Ruiz-Morales, J. C.; Canales-Vázquez, J.; Peña-Martínez, J.; López, D. M.; Núñez, P. On the Simultaneous Use of  $\text{La}_{0.75}\text{Sr}_{0.25}\text{Cr}_{0.5}\text{Mn}_{0.5}\text{O}_{3-\delta}$  as Both Anode and Cathode Material with Improved Microstructure in Solid Oxide Fuel Cells. *Electrochimica Acta* **2006**, *52* (1), 278–284. <https://doi.org/10.1016/j.electacta.2006.05.006>.
- (6) Gupta, S.; Zhong, Y.; Mahapatra, M.; Singh, P. Processing and Electrochemical Performance of Manganese-Doped Lanthanum-Strontium Chromite in Oxidizing and Reducing Atmospheres. *Int. J. Hydrog. Energy* **2015**, *40* (39), 13479–13489. <https://doi.org/10.1016/j.ijhydene.2015.07.153>.
- (7) Zamudio-García, J.; Porras-Vázquez, J. M.; Losilla, E. R.; Marrero-López, D. Efficient Symmetrical Electrodes Based on  $\text{LaCrO}_3$  via Microstructural Engineering. *J. Eur. Ceram. Soc.* **2021**, *42* (1), 181–192. <https://doi.org/10.1016/j.jeurceramsoc.2021.09.059>.
- (8) Baiutti, F.; Chiabrera, F.; Diercks, D.; Cavallaro, A.; Yedra, L.; López-Conesa, L.; Estradé, S.; Peiró, F.; Morata, A.; Aguadero, A.; Tarancón, A. Direct Measurement of Oxygen Mass Transport at the Nanoscale. *Adv. Mater.* **2021**, *33* (48), 2105622. <https://doi.org/10.1002/adma.202105622>.
- (9) Gao, Z.; Mogni, L. V.; Miller, E. C.; Railsback, J. G.; Barnett, S. A. A Perspective on Low-Temperature Solid Oxide Fuel Cells. *Energy Environ. Sci.* **2016**, *9* (5), 1602–1644. <https://doi.org/10.1039/C5EE03858H>.
- (10) Chueh, W. C.; Hao, Y.; Jung, W.; Haile, S. M. High Electrochemical Activity of the Oxide Phase in Model Ceria-Pt and Ceria-Ni Composite Anodes. *Nat. Mater.* **2012**, *11* (2), 155–161. <https://doi.org/10.1038/nmat3184>.
- (11) Jung, W.; Dereux, J. O.; Chueh, W. C.; Hao, Y.; Haile, S. M. High Electrode Activity of Nanostructured, Columnar Ceria Films for Solid Oxide Fuel Cells. *Energy Environ. Sci.* **2012**, *5* (9), 8682–8689. <https://doi.org/10.1039/c2ee22151a>.
- (12) Jankowski, A. F.; Hayes, J. P.; Graff, R. T.; Morse, J. D. Micro-Fabricated Thin-Film Fuel Cells for Portable Power Requirements. *MRS Proc.* **2002**, *730* (1), 93–98. <https://doi.org/10.1557/PROC-730-V4.2>.
- (13) Evans, A.; Bieberle-Hütter, A.; Rupp, J. L. M.; Gauckler, L. J. Review on Microfabricated Micro-Solid Oxide Fuel Cell Membranes. *J. Power Sources* **2009**, *194* (1), 119–129. <https://doi.org/10.1016/j.jpowsour.2009.03.048>.

- (14) Beckel, D.; Bieberle-Hütter, A.; Harvey, A.; Infortuna, A.; Muecke, U. P.; Prestat, M.; Rupp, J. L. M.; Gauckler, L. J. Thin Films for Micro Solid Oxide Fuel Cells. *J. Power Sources* **2007**, *173* (1), 325–345. <https://doi.org/10.1016/j.jpowsour.2007.04.070>.
- (15) Egger, A.; Bucher, E.; Yang, M.; Sitte, W. Comparison of Oxygen Exchange Kinetics of the IT-SOFC Cathode Materials  $\text{La}_{0.5}\text{Sr}_{0.5}\text{CoO}_{3-\delta}$  and  $\text{La}_{0.6}\text{Sr}_{0.4}\text{CoO}_{3-\delta}$ . *Solid State Ion.* **2012**, *225*, 55–60. <https://doi.org/10.1016/j.ssi.2012.02.050>.
- (16) Yang, Y. Characteristics of Lanthanum Strontium Chromite Prepared by Glycine Nitrate Process. *Solid State Ion.* **2000**, *135* (1–4), 475–479. [https://doi.org/10.1016/S0167-2738\(00\)00402-1](https://doi.org/10.1016/S0167-2738(00)00402-1).
- (17) Sujatha Devi, P.; Subba Rao, M. Preparation, Structure, and Properties of Strontium-Doped Lanthanum Chromites:  $\text{La}_{1-x}\text{Sr}_x\text{CrO}_3$ . *J. Solid State Chem.* **1992**, *98* (2), 237–244. [https://doi.org/10.1016/S0022-4596\(05\)80231-2](https://doi.org/10.1016/S0022-4596(05)80231-2).
- (18) Al-Shakarchi, E. K.; Mahmood, N. B. Three Techniques Used to Produce  $\text{BaTiO}_3$  Fine Powder. *J. Mod. Phys.* **2011**, *02* (11), 1420–1428. <https://doi.org/10.4236/jmp.2011.211175>.
- (19) Artini, C.; Pani, M.; Carnasciali, M. M.; Buscaglia, M. T.; Plaisier, J. R.; Costa, G. A. Structural Features of Sm- and Gd-Doped Ceria Studied by Synchrotron X-Ray Diffraction and  $\mu$ -Raman Spectroscopy. *Inorg. Chem.* **2015**, *54* (8), 4126–4137. <https://doi.org/10.1021/acs.inorgchem.5b00395>.
- (20) Lamas, D. G.; Walsöe De Reça, N. E. X-Ray Diffraction Study of Compositionally Homogeneous, Nanocrystalline Ytria-Doped Zirconia Powders. *J. Mater. Sci.* **2000**, *35* (22), 5563–5567. <https://doi.org/10.1023/A:1004896727413>.
- (21) Sha, Z.; Cali, E.; Shen, Z.; Ware, E.; Kerherve, G.; Skinner, S. J. Significantly Enhanced Oxygen Transport Properties in Mixed Conducting Perovskite Oxides under Humid Reducing Environments. *Chem. Mater.* **2021**, *33* (21), 8469–8476. <https://doi.org/10.1021/acs.chemmater.1c02909>.
- (22) Sha, Z.; Shen, Z.; Cali, E.; Kilner, J. A.; Skinner, S. J. Understanding Surface Chemical Processes in Perovskite Oxide Electrodes. *J. Mater. Chem. A* **2023**, *11*, 5645–5659. <https://doi.org/10.1039/D3TA00070B>.
- (23) Baumann, N.; Mutoro, E.; Janek, J. Porous Model Type Electrodes by Induced Dewetting of Thin Pt Films on YSZ Substrates. *Solid State Ion.* **2010**, *181* (1–2), 7–15. <https://doi.org/10.1016/j.ssi.2009.11.019>.
- (24) Yu, R.; Song, H.; Zhang, X.-F.; Yang, P. Thermal Wetting of Platinum Nanocrystals on Silica Surface. *J. Phys. Chem. B* **2005**, *109* (15), 6940–6943. <https://doi.org/10.1021/jp050973r>.
- (25) Siebenhofer, M.; Haselmann, U.; Nennung, A.; Friedbacher, G.; Ewald Bumberger, A.; Wurster, S.; Artner, W.; Hutter, H.; Zhang, Z.; Fleig, J.; Kubicek, M. Surface Chemistry and Degradation Processes of Dense  $\text{La}_{0.6}\text{Sr}_{0.4}\text{CoO}_{3-\delta}$  Thin Film Electrodes. *J. Electrochem. Soc.* **2023**, *170* (1), 014501. <https://doi.org/10.1149/1945-7111/acada8>.
- (26) Chen, K.; Ai, N.; O'Donnell, K. M.; Jiang, S. P. Highly Chromium Contaminant Tolerant  $\text{BaO}$  Infiltrated  $\text{La}_{0.6}\text{Sr}_{0.4}\text{Co}_{0.2}\text{Fe}_{0.8}\text{O}_{3-\delta}$  Cathodes for Solid Oxide Fuel Cells. *Phys. Chem. Chem. Phys.* **2015**, *17* (7), 4870–4874. <https://doi.org/10.1039/C4CP04172K>.

- (27) Jiang, S. P.; Zhen, Y. Mechanism of Cr Deposition and Its Application in the Development of Cr-Tolerant Cathodes of Solid Oxide Fuel Cells. *Solid State Ion.* **2008**, *179* (27–32), 1459–1464. <https://doi.org/10.1016/j.ssi.2008.01.006>.
- (28) Marina, O. A.; Pederson, L. R.; Williams, M. C.; Coffey, G. W.; Meinhardt, K. D.; Nguyen, C. D.; Thomsen, E. C. Electrode Performance in Reversible Solid Oxide Fuel Cells. *J. Electrochem. Soc.* **2007**, *154* (5), B452–B459. <https://doi.org/10.1149/1.2710209>.
- (29) Jiang, S. P. Development of Lanthanum Strontium Cobalt Ferrite Perovskite Electrodes of Solid Oxide Fuel Cells – A Review. *Int. J. Hydrog. Energy* **2019**, *44* (14), 7448–7493. <https://doi.org/10.1016/j.ijhydene.2019.01.212>.
- (30) Laurencin, J.; Hubert, M.; Sanchez, D. F.; Pylypko, S.; Morales, M.; Morata, A.; Morel, B.; Montinaro, D.; Lefebvre-Joud, F.; Siebert, E. Degradation Mechanism of  $\text{La}_{0.6}\text{Sr}_{0.4}\text{Co}_{0.2}\text{Fe}_{0.8}\text{O}_{3-\delta}$  /  $\text{Gd}_{0.1}\text{Ce}_{0.9}\text{O}_{2-\delta}$  Composite Electrode Operated under Solid Oxide Electrolysis and Fuel Cell Conditions. *Electrochimica Acta* **2017**, *241*, 459–476. <https://doi.org/10.1016/j.electacta.2017.05.011>.
- (31) Garbayo, I.; Dezanneau, G.; Bogicevic, C.; Santiso, J.; Gràcia, I.; Sabaté, N.; Tarancón, A. Pinhole-Free YSZ Self-Supported Membranes for Micro Solid Oxide Fuel Cell Applications. *Solid State Ion.* **2012**, *216*, 64–68. <https://doi.org/10.1016/j.ssi.2011.09.011>.
- (32) Garbayo, I.; Esposito, V.; Sanna, S.; Morata, A.; Pla, D.; Fonseca, L.; Sabaté, N.; Tarancón, A. Porous  $\text{La}_{0.6}\text{Sr}_{0.4}\text{CoO}_{3-\delta}$  Thin Film Cathodes for Large Area Micro Solid Oxide Fuel Cell Power Generators. *J. Power Sources* **2014**, *248*, 1042–1049. <https://doi.org/10.1016/j.jpowsour.2013.10.038>.
- (33) Garbayo, I.; Pla, D.; Morata, A.; Fonseca, L.; Sabaté, N.; Tarancón, A. Full Ceramic Micro Solid Oxide Fuel Cells: Towards More Reliable MEMS Power Generators Operating at High Temperatures. *Energy Environ. Sci.* **2014**, *7* (11), 3617–3629. <https://doi.org/10.1039/c4ee00748d>.
- (34) Bianchini, M. Integration of Ceramic Thin Films in Silicon Technology for Energy Conversion and Oxygen Sensing, Universitat Autònoma de Barcelona, 2022.
- (35) Evans, A.; Martynczuk, J.; Stender, D.; Schneider, C. W.; Lippert, T.; Prestat, M. Low-Temperature Micro-Solid Oxide Fuel Cells with Partially Amorphous  $\text{La}_{0.6}\text{Sr}_{0.4}\text{CoO}_{3-\delta}$  Cathodes. *Adv. Energy Mater.* **2015**, *5* (1), 1400747. <https://doi.org/10.1002/aenm.201400747>.
- (36) Baek, J. D.; Liu, K.-Y.; Su, P.-C. A Functional Micro-Solid Oxide Fuel Cell with a 10 Nm-Thick Freestanding Electrolyte. *J. Mater. Chem. A* **2017**, *5* (35), 18414–18419. <https://doi.org/10.1039/C7TA05245F>.
- (37) Wincewicz, K.; Cooper, J. Taxonomies of SOFC Material and Manufacturing Alternatives. *J. Power Sources* **2005**, *140* (2), 280–296. <https://doi.org/10.1016/j.jpowsour.2004.08.032>.
- (38) Ralph, J. M.; Schoeler, A. C.; Krumpelt, M. Materials for Lower Temperature Solid Oxide Fuel Cells. *J. Mater. Sci.* **2001**, *36* (5), 1161–1172. <https://doi.org/10.1023/A:1004881825710>.
- (39) Garbayo, I.; Tarancón, A.; Santiso, J.; Peiró, F.; Alarcón-LLadó, E.; Cavallaro, A.; Gràcia, I.; Cané, C.; Sabaté, N. Electrical Characterization of Thermomechanically Stable YSZ Membranes for Micro Solid Oxide Fuel Cells Applications. *Solid State Ion.* **2010**, *181* (5–7), 322–331. <https://doi.org/10.1016/j.ssi.2009.12.019>.



## 6. Conclusions

This thesis has been devoted to the investigation of novel electrode materials based on thin film approaches and their suitability to be implemented in solid oxide cells (SOCs). Three main research areas have been explored with this purpose: i) the development of nanostructured materials with application as fuel and symmetric electrodes, ii) the use of combinatorial methods for studying the functional properties of a materials library for oxygen electrode application and iii) integration of thin film electrodes in different model device architectures. A more detailed description of the main findings obtained throughout this thesis is given below.

- **Fabrication of nanostructured doped-ceria and lanthanum chromite-manganite-based thin film materials for application as fuel and symmetric electrodes in SOCs (Chapter 3):**
  - Low metal-containing Ni-Ce<sub>0.9</sub>Gd<sub>0.1</sub>O<sub>2</sub> (NiCGO) cermet nanocomposites with tailored microstructures were studied as a potential electrode material for hydrogen oxidation. The microstructure of the films was varied tuning pulsed laser deposition (PLD) parameters for the fabrication of films with increased level of porosity. The best performing NiCGO electrode was deposited at 500 °C and 200 mTorr of oxygen partial pressure. The film presented a microstructure characterized by crystallites in the range of 25-40 nm in size and mesoporous-like surface microstructure. The increase in the surface area along with microstructure stability were attributed to be the main reasons behind the enhanced performance. The rest of the films studied presented either dense or highly porous microstructure, resulting in less surface area and mechanical instability, respectively, hindering the overall electrochemical activity.
  - Dense LSCrMn-SDC heterostructures in the form of a bilayer and an intermixed nanocomposite were investigated as all-ceramic fuel electrode materials. The results obtained showed improvement of the performance for both heterostructures, in terms of electrochemical activity and in-plane conductivity with respect to the individual materials. Remarkable performance was also obtained for the LSCrMn-SDC intermixed nanocomposite also under oxidizing conditions and for a testing period of over 400 hours, unveiling its suitability to be employed in symmetric electrode applications. This was attributed to a synergistic effect caused by the presence of both SDC and LSCrMn along the film and exposed to the surface. The two distinguished phases were confirmed by HRTEM-ASTAR

analysis while elemental characterization by EDX showed highly cationic intermixing throughout the film.

- Further studies of the LSCrMn-SDC heterostructures were carried out in order to optimize the layer microstructure. PLD parameters were tuned with the aim of maximizing the surface exposed area of the deposited heterostructures, resulting in different films with variable roughness and porosity. The obtained heterostructured materials showed varied electrochemical performance either comparable or higher than the dense film counterparts, depending on the case. The observed higher performance was attributed to the increase of the open-volume porosity of the films, while the rest of cases were confirmed to present evolution of the surface microstructure after the electrochemical characterization. The best performing material consisted in a dense LSCrMn thin film with a top layer of porous SDC.
- **Full characterization of the LSMCF perovskite library for oxygen electrode application by means of high throughput methodologies and study of the behavior on thermal degradation (Chapter 4):**
  - The LSMCF perovskite library was successfully fabricated by means of combinatorial PLD. High throughput methodologies were employed for the characterization of the library elemental distribution, the crystallographic and structural properties, the oxygen mass-transport kinetics and the electrochemical activity under oxidizing conditions. The results obtained confirmed the elemental distribution and perovskite phase of the material library. Additionally, the functional characterization performed unveiled the promising properties in terms of oxygen kinetics of the thin film LSMCF library, particularly for increased Fe- and Co- rich regions. The experiments performed also allowed to extract the activation energy, pre-exponential factor and area specific resistance (ASR) of a large set of LSMCF compounds. A particularly promising low activation energy was observed in several of the intermixed compounds studied.
  - The evolution of the electrochemical performance on thermal degradation was investigated for the parent materials and two representative LSMCF compounds for a period of 100 h. While the single materials showed the largest degradation rates –i.e. highest for LSC and less pronounced for LSF and LSM, respectively–, the slowest degradation rates were found for the co-doped LSMCF with high Fe-content while the more intermixed LSMCF sample even showed enhancement over the degradation experiment.

- A series of LSMCF compounds were selected for performing a systematic degradation analysis representative of the LSMCF library. Pristine and annealed LSMCF samples were characterized and compared to the parent materials with focus on dopant segregation and evolution of the surface and subsurface regions. The results unveiled the promising performance of the highly co-doped LSMCF cathode materials with respect to the parent materials. Particularly, LSMCF compounds showed apparent stabilization on segregation with low evolution after performing the thermal treatment. The observations made were evident when compared to single LSC and LSF, which showed drastic evolution of the surface, with appearance of large segregated particles. This was confirmed by LEIS and XPS, showing a drastic increase of strontium segregated species in the surface, while for LSMCF compounds the increase was more alleviated. Specifically, sulfate species were found to be the ones increasing the most their relative presence after thermal degradation. These results suggest that Mn-addition facilitates the prevention of segregation phenomena in LSMCF-based perovskites.
  - Additional analyses carried out by LEIS profiling and PAS in the region deeper from the subsurface revealed the presence of local highly off-stoichiometric regions with increase of overall defect size and density.
- **Integration of thin film electrode materials in full SOC devices under different cell architecture and operation conditions (Chapter 5):**
    - Fabrication of symmetric SOCs (SSOCs) based on dense LSCr thin films and electrochemical characterization on fuel cell operating conditions under redox cycling processes. The cell was operated in the 650-750 °C temperature range and the gas chambers were reversed for a total of 7 cycles for a period over 70 h. The results showed self-healing behavior suggested by the recovery of the electrochemical performance after operation under reversed atmosphere. Microstructural characterization carried out after cell operation showed evolution of the surface morphology and partial degradation of the current collector layers.
    - Two prototypical reversible SOCs with dense LSC82 and porous SDC thin films as oxygen and hydrogen electrodes, respectively, were operated under fuel cell and electrolysis modes in the 500-700 °C range. Approximate 3- and 2-fold enhancement factors were observed for the current density measured in SOFC and SOEC modes between the two cells studied. This difference is attributed to the difference in the current collector layer employed in the porous electrode, confirming the sensitivity of this type of material to the collection of current. The degradation measurements performed showed



- increased ASR and lowered OCV, suggesting the presence of cell leakages, electrode degradation and most likely loss of current percolation.
- Fabrication of all-ceramic thin film  $\mu$ SOCs was successfully achieved following a free-standing membrane architecture supported in silicon. Two cells were fabricated and characterized: one containing LSC82 and porous SDC as the oxygen and hydrogen electrodes, and a second one containing LSC64 as the oxygen electrode and a thin film layer of LSCrMn in combination with porous SDC as the hydrogen electrode material. The operation of the  $\mu$ SOCs in fuel cell mode showed poor performance with a maximum power density of  $\approx 14$  mW/cm<sup>2</sup> for the best performing cell and  $\approx 0.17$  mW/cm<sup>2</sup> for the worst performing. This was mostly attributed to poor current collection due to dewetting processes undergoing in the metallic layers, confirmed in the post-mortem characterization of the devices.

## *Appendix*

*Direct observation of Sr segregated species in oxygen electrodes by Tip-Enhanced Raman Spectroscopy*



A.1 Motivation .....	245
A.2 Characterization of strontium species in $\text{La}_{0.8}\text{Sr}_{0.2}\text{Mn}_{0.42}\text{Co}_{0.19}\text{Fe}_{0.39}\text{O}_3$ by Tip-Enhanced Raman Spectroscopy.....	246
A.3 Conclusions and future work.....	249
References.....	250



## A.1 Motivation

Part of the work developed in this thesis has focused on the study of the performance of perovskite-based electrode materials facing thermally-driven degradation. In Chapter 4, strontium segregation has been studied in a series of  $\text{La}_{0.8}\text{Sr}_{0.2}\text{Mn}_x\text{Co}_y\text{Fe}_{1-x-y}\text{O}_3$  (LSMCF) thin films by means of Atomic Force Microscopy (AFM), Low Energy Ion Scattering (LEIS) and X-Ray Photoelectron Spectroscopy (XPS). As discussed in the chapter, these techniques allowed to identify Sr-rich segregated particles present in the surface of the thin films. Additionally, the relative presence of  $\text{SrSO}_4$  species in contrast to  $\text{SrCO}_3$ ,  $\text{Sr}(\text{OH})_2$  and SrO-like compounds was analyzed. Nonetheless, correlating the chemical species identified by XPS with the presence of the segregated particles in the microstructure is not a trivial task and therefore was not explored during the core work of the thesis. Among the extensive literature dealing with dopant segregation as a degradation phenomenon in solid oxide cell (SOC) electrodes, there are not many cases that properly identify the chemical species involved. In most cases the analysis is restricted to Sr (or the corresponding dopant) elemental detection on ceramic pellets<sup>1</sup>. More interestingly, Tripkovic et al.<sup>2</sup> showed the presence of Sr- and S-enriched particles by Scanning Electron Microscopy-Energy-dispersive X-ray Spectroscopy (SEM/EDX) analyses in a pellet of  $\text{La}_{0.6}\text{Sr}_{0.4}\text{FeO}_3$ , suggesting the formation of  $\text{SrSO}_4$  particles. Additionally, Siebenhofer et al. identified the presence of Sr- and S-enriched particles in  $\text{La}_{0.6}\text{Sr}_{0.4}\text{CoO}_3$  thin films<sup>3</sup>, following a similar analysis based on EDX and confirming it by XPS characterization. Hence, direct confirmation of the actual chemical species involved in electrode degradation and surface evolution remains a challenge. This appendix introduces the use of Tip-Enhanced Raman Spectroscopy (TERS) as a promising characterization technique for the analysis of strontium segregation in oxygen electrodes for SOCs.

TERS is a relatively new surface-sensitivity technique that overcomes the spatial resolution limitations of conventional Raman (~500 – 1000 nm) reaching even single molecule detection<sup>4-7</sup>. While it is widely used to study organic materials, its application to complex oxides is not yet widespread. Essentially, TERS combines the spectroscopic power of Raman Spectroscopy with the spatial resolution of Scanning Probe Microscopy. This is achieved by carefully focusing the laser at the apex of a tip coated with a thin metal able to generate surface plasmon resonances and lightning-rod effect to enhance the Raman signal.<sup>8</sup> In this work, preliminary TERS analysis is employed for the differentiation of the chemical nature of Sr-enriched particles present in the surface of a  $\text{La}_{0.8}\text{Sr}_{0.2}\text{Mn}_{0.42}\text{Co}_{0.19}\text{Fe}_{0.39}\text{O}_3$  thin film.

## A.2 Characterization of strontium species in $\text{La}_{0.8}\text{Sr}_{0.2}\text{Mn}_{0.42}\text{Co}_{0.19}\text{Fe}_{0.39}\text{O}_3$ by Tip-Enhanced Raman Spectroscopy

Figure 0-1 shows the Raman spectra obtained during the characterization procedure. Specifically, Figure 0-1a shows two Raman spectra measured both with and without the tip contacting the sample surface. While both spectra show similar shape, the spectra obtained with the tip in contact presents an overall increase in the signal intensity, confirming TERS enhancement on the acquired Raman signal. A main peak in the  $600\text{-}700\text{ cm}^{-1}$  region is observed. This peak is characteristic of the M-O-M' bonds of the perovskite phase, as described in Chapter 4 (section 4.3.1.3). It should be noted that additional contributions from the electrolyte substrate are also active in this region, so some peak overlap is expected<sup>9,10</sup>. The sharp peak located at  $520\text{ cm}^{-1}$  and the smaller peak at  $\approx 300\text{ cm}^{-1}$  are attributed to partial Si signal coming from the tip contribution to Raman emission. This peak is partially overlapped by a broad peak smaller in intensity, which can be attributed to the  $\text{Ce}_{0.8}\text{Gd}_{0.2}\text{O}_2$  buffer layer placed between the perovskite and the substrate<sup>11</sup>. Once TERS amplification was confirmed, a map was measured throughout the surface of the LSMCF thin film.

Figure 0-1b shows the average Raman spectrum obtained throughout the topography scan performed –i.e. result of the contribution of the spectra obtained at each position of the  $500 \times 500\text{ nm}^2$  area scanned-. While the main peaks are equivalent to those observed in panel (a), additional features can be observed in the proximity of the  $1000\text{-}1400\text{ cm}^{-1}$  region. This is more evident in the zoomed in present in the inset figure. Here, peaks centered at  $\approx 1000\text{ cm}^{-1}$ ,  $1065\text{ cm}^{-1}$ ,  $1150\text{ cm}^{-1}$ ,  $1270\text{ cm}^{-1}$  and  $1370\text{ cm}^{-1}$  can be observed. Regarding the peaks at  $\approx 1000\text{ cm}^{-1}$  and  $1150\text{ cm}^{-1}$ , these can be attributed to the  $\nu_1$  and  $\nu_3$  vibration modes of  $\text{SrSO}_4$ , respectively<sup>12,13</sup>. The peak located at  $\approx 1065\text{ cm}^{-1}$  can be ascribed to the presence of the  $\nu_1$  vibration mode of  $\text{SrCO}_3$  species, according to literature<sup>14,15</sup>. The rest of the peaks are more difficult to identify. The broad peak area located in the  $1250\text{-}1300\text{ cm}^{-1}$  range is high likely related to the presence of carbon-containing species<sup>16</sup>. The peak located at  $1370\text{ cm}^{-1}$  can be explained by the presence of  $\text{Sr}(\text{NO}_3)_2$  species through the  $\nu_3$  vibration mode<sup>17</sup>. Note that the  $\nu_1$  vibration mode of  $\text{Sr}(\text{NO}_3)_2$  is located at  $\approx 1055\text{ cm}^{-1}$  so an overlap with  $\text{SrCO}_3$  could also be present in this region. For the analysis of the relative presence of  $\text{SrSO}_4$  and  $\text{SrCO}_3$  species along the film surface the areas of the peaks centered at  $\approx 1000\text{ cm}^{-1}$  and  $1065\text{ cm}^{-1}$  were considered, as indicated by the color highlight in the inset figure.

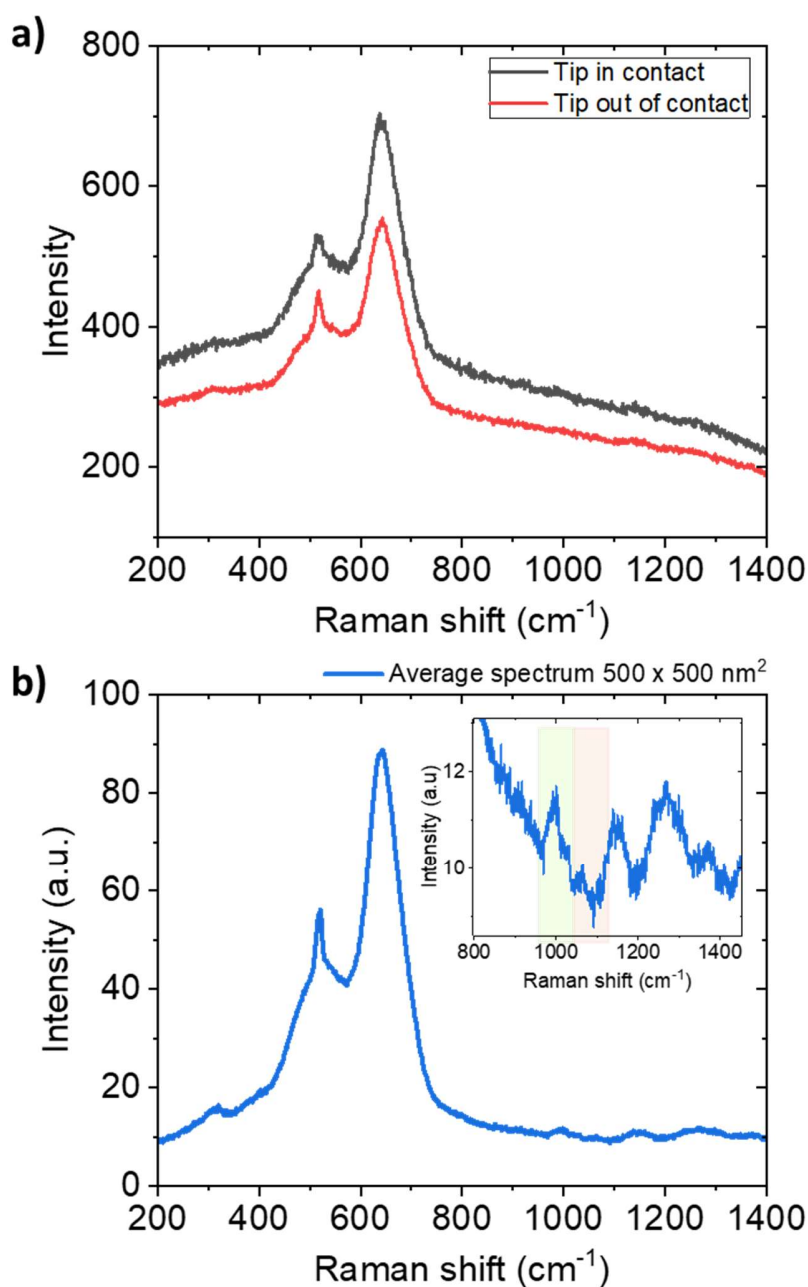


Figure 0-1. Raman spectra obtained initially showing the presence of TERS enhancement (a). Average spectra obtained after analyzing the surface of the film (b) with a zoom (inset) in the 800-1400  $\text{cm}^{-1}$  region. Sulfate and carbonate associated peaks are highlighted in green and red colors, respectively.

Figure 0-2 shows the overall TERS mapping results obtained for the  $\text{La}_{0.8}\text{Sr}_{0.2}\text{Mn}_{0.42}\text{Co}_{0.19}\text{Fe}_{0.39}\text{O}_3$  sample. Specifically, panel (a) shows the topographical micrograph obtained during the TERS scan, while Figure 0-2b shows the topography measured right after the finishing the map analysis. While some drift can be observed in the first micrograph, particularly in the upper region, most of the film features are recognizable



in both micrographs. In this sense, the presence of scattered particles of up to approximately 50 nm in size can be distinguished, as it has been discussed in Chapter 4. Panel (c) shows the spatial distribution of the peak contributions located at  $\approx 1000\text{ cm}^{-1}$  and  $\approx 1065\text{ cm}^{-1}$  associated to the presence of  $\text{SrSO}_4$  and  $\text{SrCO}_3$ , as discussed. One can see that both signals are present in most of the film surface, with some regions presenting higher signal (brighter color) and some others showing absence of it (dark regions). For a better visualization of the correspondence between topography and the Raman features, Figure 0-2d shows the 3D-view of the topography in panel (b), with the spatial distribution of the Raman features identified in panel (c) projected on top of it.

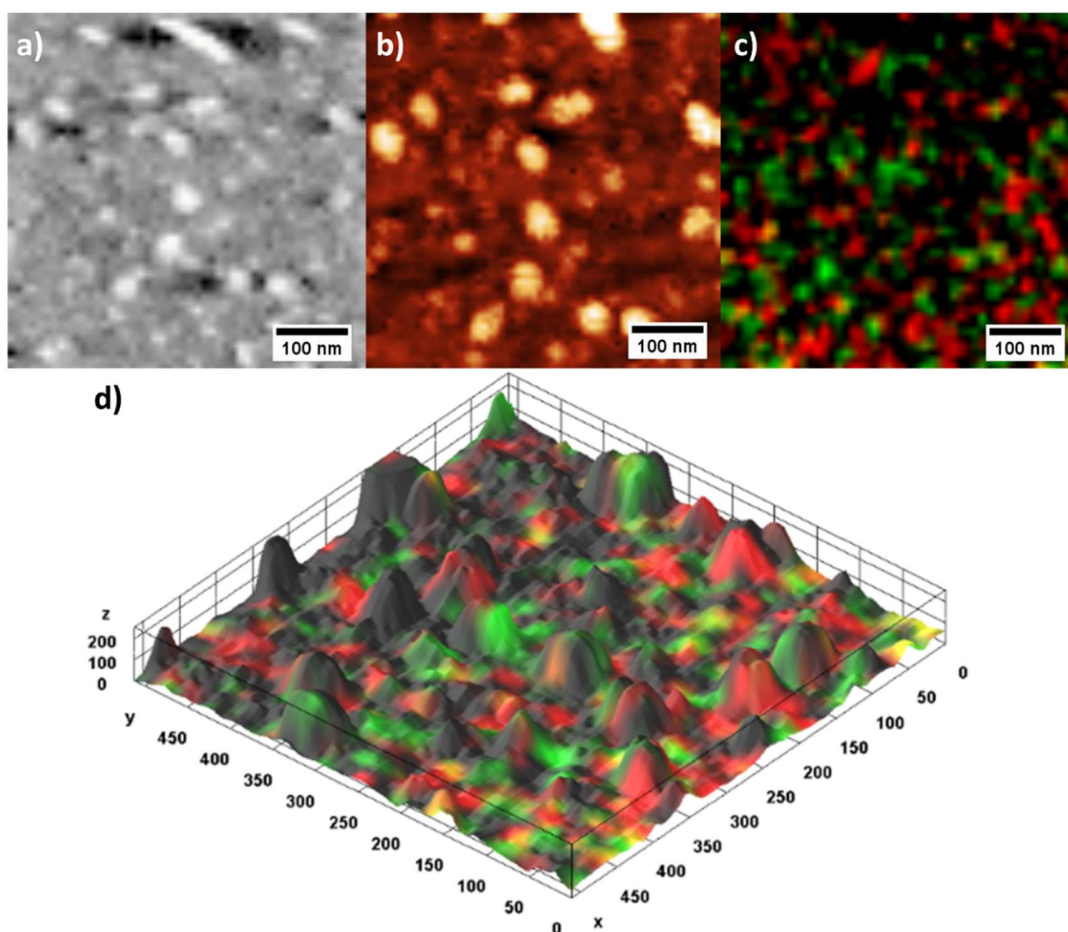


Figure 0-2. AFM micrograph of the film surface during (a) and after (b) the TERS map. Sulfate (green) and carbonate (red) Raman signal present in the film surface (c).

Despite the overall presence of both signals along the surface, one can see certain degree of differentiation around the particles, which seem to present either the carbonate or the sulfate signal. It should be also noted that the upper half of the film seems to present lower Raman signal of these phases. This could be attributed to the presence of some other features (e.g. carbon or strontium nitrate species, as previously commented). Certain shift and lowering in the signal might also come from the drift observed in this region. Another effect that

should be taken into account when analyzing these results is the variation of the TERS signal with topography. Zhang et al. evaluated the change in the TERS signal in different positions of a SrTiO<sub>3</sub> nanoisland, revealing higher intensity around the edge of the particle<sup>18</sup>. Although some other effects might be playing a role, this could explain the relative increase in the Raman signal observed in the vicinity of most of the particles visualized. Granted that further analysis would be needed to further clarify on the distribution of sulfate and carbonate species along the aged LSMCF film, direct visualization of the presence of such species has been achieved.

### A.3 Conclusions and future work

This appendix has presented TERS as a promising characterization technique for studying segregation phenomena in aged SOC electrodes. The concept has been proven in a thin film sample of La<sub>0.8</sub>Sr<sub>0.2</sub>Mn<sub>0.42</sub>Co<sub>0.19</sub>Fe<sub>0.39</sub>O<sub>3</sub>, complementing the work discussed in Chapter 4. The analysis performed allowed to identify the presence of carbonate and sulfate phases along the film topography. This represents preliminary data of direct visualization of SrSO<sub>4</sub> and SrCO<sub>3</sub> phases in the surface of the LSMCF film. This also serves as further validation of the differentiation made during the XPS analysis in Chapter 4 between these two contributions. Both phases are generally present along the surface of the film, with a seemingly more visible differentiation in the positions where the bigger segregated particles are present. Full understanding on the correspondence between the Raman signal acquired and the film position is still to be achieved. Hence, further studies would be needed to make a full analysis on the viability of the technique for the study of dopant segregation driven by thermal ageing in electrode materials.

There are several approaches that would be worth exploring for achieving a deeper understanding of segregation phenomena by TERS. First, comparison with the signal present in pristine samples would be fairly interesting for analyzing the relative enrichment of the segregated phases and evaluating the detection capabilities of TERS comparing it with the results obtained by LEIS and XPS. Additional measurements on LSC, LSF and LSM might also shed light on the differences observed among these materials for facing segregation of strontium carbonates and sulfates. This could facilitate confirmation on the partial sensitivity observed by XPS on the formation of sulfate species (both for LSC and LSF) with respect to carbonate formation (critical for LSC). Beyond the experimental conditions set in this work, studying the nature of dopant segregated species under different conditions of temperature, atmosphere (e.g. hydrogen, humidified air or with variable pO<sub>2</sub>), or applied current would be interesting topics for research. All considered, TERS suppose a promising a tool for the characterization of surface degradation phenomena occurring in SOC electrodes at the nanoscale level.

## References

- (1) Niania, M.; Podor, R.; Britton, T. B.; Li, C.; Cooper, S. J.; Svetkov, N.; Skinner, S.; Kilner, J. In Situ Study of Strontium Segregation in  $\text{La}_{0.6}\text{Sr}_{0.4}\text{Co}_{0.2}\text{Fe}_{0.8}\text{O}_{3-\delta}$  in Ambient Atmospheres Using High-Temperature Environmental Scanning Electron Microscopy. *J. Mater. Chem. A* **2018**, *6* (29), 14120–14135. <https://doi.org/10.1039/C8TA01341A>.
- (2) Tripković, Đ.; Wang, J.; Küngas, R.; Mogensen, M. B.; Yildiz, B.; Hendriksen, P. V. Thermally Controlled Activation and Passivation of Surface Chemistry and Oxygen-Exchange Kinetics on a Perovskite Oxide. *Chem. Mater.* **2022**, *34* (4), 1722–1736. <https://doi.org/10.1021/acs.chemmater.1c03901>.
- (3) Siebenhofer, M.; Haselmann, U.; Nenning, A.; Friedbacher, G.; Ewald Bumberger, A.; Wurster, S.; Artner, W.; Hutter, H.; Zhang, Z.; Fleig, J.; Kubicek, M. Surface Chemistry and Degradation Processes of Dense  $\text{La}_{0.6}\text{Sr}_{0.4}\text{CoO}_{3-\delta}$  Thin Film Electrodes. *J. Electrochem. Soc.* **2023**, *170* (1), 014501. <https://doi.org/10.1149/1945-7111/acada8>.
- (4) Schmid, T.; Opilik, L.; Blum, C.; Zenobi, R. Nanoscale Chemical Imaging Using Tip-Enhanced Raman Spectroscopy: A Critical Review. *Angew. Chem. Int. Ed.* **2013**, *52* (23), 5940–5954. <https://doi.org/10.1002/anie.201203849>.
- (5) Verma, P. Tip-Enhanced Raman Spectroscopy: Technique and Recent Advances. *Chem. Rev.* **2017**, *117* (9), 6447–6466. <https://doi.org/10.1021/acs.chemrev.6b00821>.
- (6) Langer, J.; Jimenez De Aberasturi, D.; Aizpurua, J.; Alvarez-Puebla, R. A.; Auguie, B.; Baumberg, J. J.; Bazan, G. C.; Bell, S. E. J.; Boisen, A.; Brolo, A. G.; Choo, J.; Cialla-May, D.; Deckert, V.; Fabris, L.; Faulds, K.; García De Abajo, F. J.; Goodacre, R.; Graham, D.; Haes, A. J.; Haynes, C. L.; Huck, C.; Itoh, T.; Käll, M.; Kneipp, J.; Kotov, N. A.; Kuang, H.; Le Ru, E. C.; Lee, H. K.; Li, J.-F.; Ling, X. Y.; Maier, S. A.; Mayerhöfer, T.; Moskovits, M.; Murakoshi, K.; Nam, J.-M.; Nie, S.; Ozaki, Y.; Pastoriza-Santos, I.; Perez-Juste, J.; Popp, J.; Pucci, A.; Reich, S.; Ren, B.; Schatz, G. C.; Shegai, T.; Schlücker, S.; Tay, L.-L.; Thomas, K. G.; Tian, Z.-Q.; Van Duyne, R. P.; Vo-Dinh, T.; Wang, Y.; Willets, K. A.; Xu, C.; Xu, H.; Xu, Y.; Yamamoto, Y. S.; Zhao, B.; Liz-Marzán, L. M. Present and Future of Surface-Enhanced Raman Scattering. *ACS Nano* **2020**, *14* (1), 28–117. <https://doi.org/10.1021/acsnano.9b04224>.
- (7) Cao, Y.; Sun, M. Tip-Enhanced Raman Spectroscopy. *Rev. Phys.* **2022**, *8*, 100067. <https://doi.org/10.1016/j.revip.2022.100067>.
- (8) Huang, T.-X.; Huang, S.-C.; Li, M.-H.; Zeng, Z.-C.; Wang, X.; Ren, B. Tip-Enhanced Raman Spectroscopy: Tip-Related Issues. *Anal. Bioanal. Chem.* **2015**, *407* (27), 8177–8195. <https://doi.org/10.1007/s00216-015-8968-8>.
- (9) Pomfret, M. B.; Stoltz, C.; Varughese, B.; Walker, R. A. Structural and Compositional Characterization of Yttria-Stabilized Zirconia: Evidence of Surface-Stabilized, Low-Valence Metal Species. *Anal. Chem.* **2005**, *77* (6), 1791–1795. <https://doi.org/10.1021/ac048600u>.
- (10) Zhu, W.; Nakashima, S.; Marin, E.; Gu, H.; Pezzotti, G. Microscopic Mapping of Dopant Content and Its Link to the Structural and Thermal Stability of Yttria-Stabilized Zirconia Polycrystals. *J. Mater. Sci.* **2020**, *55* (2), 524–534. <https://doi.org/10.1007/s10853-019-04080-9>.

- (11) Schmitt, R.; Nanning, A.; Kraynis, O.; Korobko, R.; Frenkel, A. I.; Lubomirsky, I.; Haile, S. M.; Rupp, J. L. M. A Review of Defect Structure and Chemistry in Ceria and Its Solid Solutions. *Chem. Soc. Rev.* **2020**, *49* (2), 554–592. <https://doi.org/10.1039/C9CS00588A>.
- (12) Chen, Y.-H.; Huang, E.; Yu, S.-C. High-Pressure Raman Study on the BaSO<sub>4</sub>–SrSO<sub>4</sub> Series. *Solid State Commun.* **2009**, *149* (45–46), 2050–2052. <https://doi.org/10.1016/j.ssc.2009.08.023>.
- (13) Böhme, N.; Hauke, K.; Neuroth, M.; Geisler, T. In Situ Hyperspectral Raman Imaging of Ternesite Formation and Decomposition at High Temperatures. *Minerals* **2020**, *10* (3), 287. <https://doi.org/10.3390/min10030287>.
- (14) Eror, N. G.; Loehr, T. M.; Balachandran, U. Carbonate Adsorption on Perovskite Surfaces. II. Raman Spectroscopic Evidence for Non-Adsorption on Cubic SrTiO<sub>3</sub>. *Ferroelectrics* **1982**, *40* (1), 71–73. <https://doi.org/10.1080/00150198208210599>.
- (15) Kaabar, W.; Bott, S.; Devonshire, R. Raman Spectroscopic Study of Mixed Carbonate Materials. *Spectrochim. Acta. A. Mol. Biomol. Spectrosc.* **2011**, *78* (1), 136–141. <https://doi.org/10.1016/j.saa.2010.09.011>.
- (16) Pardanaud, C.; Cartry, G.; Lajaunie, L.; Arenal, R.; Buijnsters, J. G. Investigating the Possible Origin of Raman Bands in Defective Sp<sup>2</sup>/Sp<sup>3</sup> Carbons below 900 Cm<sup>-1</sup>: Phonon Density of States or Double Resonance Mechanism at Play? *C – J. Carbon Res.* **2019**, *5* (4), 79. <https://doi.org/10.3390/c5040079>.
- (17) Brooker, M. H.; Irish, D. E.; Boyd, G. E. Ionic Interactions in Crystals: Infrared and Raman Spectra of Powdered Ca(NO<sub>3</sub>)<sub>2</sub>, Sr(NO<sub>3</sub>)<sub>2</sub>, Ba(NO<sub>3</sub>)<sub>2</sub>, and Pb(NO<sub>3</sub>)<sub>2</sub>. *J. Chem. Phys.* **1970**, *53* (3), 1083–1087. <https://doi.org/10.1063/1.1674101>.
- (18) Zhang, J.; Youssef, A. H.; Dörfler, A.; Kolhatkar, G.; Merlen, A.; Ruediger, A. Sample Induced Intensity Variations of Localized Surface Plasmon Resonance in Tip-Enhanced Raman Spectroscopy. *Opt. Express* **2020**, *28* (18), 25998. <https://doi.org/10.1364/OE.403345>.



## Scientific contributions

### Publications

#### Peer-reviewed scientific journals

- Sirvent, J. de D.; Carmona, A.; Rapenne, L.; Chiabrera, F.; Morata, A.; Burriel, M.; Baiutti, F.; Tarancón, A. Nanostructured  $\text{La}_{0.75}\text{Sr}_{0.25}\text{Cr}_{0.5}\text{Mn}_{0.5}\text{O}_3\text{-Ce}_{0.8}\text{Sm}_{0.2}\text{O}_2$  Heterointerfaces as All-Ceramic Functional Layers for Solid Oxide Fuel Cell Applications. *ACS Appl. Mater. Interfaces* 2022, 14 (37), 42178–42187. <https://doi.org/10.1021/acsami.2c14044>

#### Chapters in books

- Sirvent, J. de D.; Buzi, F.; Baiutti, F.; Tarancón, A. Advances in Nanoengineered Air Electrodes: Towards High-Performance Solid Oxide Cells. In *Nanoengineered Materials for Solid Oxide Cells*; Develos-Bagarinao, K., Ed.; IOP Publishing, 2023; pp 1-1-1–35. <https://doi.org/10.1088/978-0-7503-4064-9ch1>

## Contributions in meetings and conferences

### Conferences

- J. Sirvent, G. Cordaro, D. Thiaudière, M. Núñez, A. Morata, G. Dezanneau, F. Baiutti, A. Tarancón, High-throughput methodologies for the study of cathodes in solid oxide cells: the  $\text{La}_{0.8}\text{Sr}_{0.2}\text{Co}_x\text{Mn}_y\text{Fe}_{1-x-y}\text{O}_3$  perovskite family, European Materials Research Society (E-MRS) Fall meeting 2022, Warsaw (Poland), Oral presentation.
- J. Sirvent, A. Carmona, L. Rapenne, F. Chiabrera, A. Morata, M. Burriel, F. Baiutti, A. Tarancón, All-ceramic functional layers based on nanostructured LSCrMn-SDC heterointerfaces for electrode application in solid oxide cells, European Materials Research Society (E-MRS) Fall meeting 2022, Warsaw (Poland), Oral presentation.
- J. Sirvent, M. Burriel, L. Rapenne, A. Morata, F. Baiutti, A. Tarancón, Development of nanostructured ceramic thin films for micro solid oxide cell applications, European Materials Research Society (E-MRS) Spring meeting 2021, Virtual Conference, Poster presentation.
- J. Sirvent, F. Baiutti, I. Monterroso, A. Hornés, A. Tarancón, Development of nanostructured ceramic thin films for micro solid oxide cell applications, Electronic Materials and Applications (EMA) 2021, Virtual Conference, Oral presentation.

### Meetings

- J. Sirvent, G. Cordaro, D. Thiaudière, M. Núñez, A. Morata, G. Dezanneau, F. Baiutti, A. Tarancón, High-throughput methodologies for the study of cathodes in solid oxide cells: the  $\text{La}_{0.8}\text{Sr}_{0.2}\text{Co}_x\text{Mn}_y\text{Fe}_{1-x-y}\text{O}_3$  perovskite family, The Power of Interfaces Workshop 2022, Mallorca (Spain), Oral presentation.
- J. Sirvent, A. Hornés, G. Dezanneau, P. Gemeiner, M. Burriel, L. Rapenne, I. Monterroso, A. Morata, F. Baiutti, A. Tarancón, Development of nanostructured ceramic thin films for micro solid oxide cell applications, The Power of Interfaces Workshop 2021, Virtual Meeting, Oral presentation.
- J. Sirvent, A. Carmona, F. Baiutti, A. Tarancón, Development of nanostructured ceramic thin films as hydrogen electrode for micro solid oxide cell applications, The Power of Interfaces Workshop 2020, London (UK), Poster presentation.